# PROCEEDINGS
# OF INTERNATIONAL SCHOOL-SEMINAR
# «ACTUAL PROBLEMS OF PARTICLE PHYSICS»

*Accelerator Physics,*
*LHC Program,*
*Physics (in) and (out) the Framework of Standard Model*
*Soft and Hard QCD Processes,*
*Quantum Field Theory,*
*Relativistic Nuclear Physics*

Vol. I

# PROCEEDINGS of INTERNATIONAL SCHOOL-SEMINAR «ACTUAL PROBLEMS OF PARTICLE PHYSICS»

Joint Institute for Nuclear Research (Dubna, Russia),
National Center of Particle and
High Energy Physics (Minsk, Belarus),
Institute of Physics (Minsk, Belarus) &
Institute of Metal Polymer Systems (Gomel, Belarus)
of National Academy of Sciences of Belarus,
Gomel State Univiversity,
Gomel Polytechnic Institut



August 8-17, 1997 Gomel, Belarus



**Accelerators physics,**
**LHC program,**
**Physics «in» and «out» the framework of Standard Model,**
**Soft and Hard QCD Processes,**
**Quantum Field Theory,**
**Relativistic Nuclear Physics**

edited by P. Kuzhir

Vol. I

**Dubna, 1998**

ISBN 5-85165-516-x (т. I)
ISBN 5-85165-519-4

# CONTENTS

## Volume I



* — poster

** — copies of transparences

## Volume II



* — poster
** — copies of transparences

## Preface

The International Symposia, Conferences, Workshops on different fields of science which are organized in the Republic of Belarus contribute significantly to the development of the Byelorussian science. The international School-Seminars on the actual problems of microworld physics carried out in the hotel "Golden Sands" in 1971, 1973, 1977 become traditional. The idea and the organization of the present (in 1997) and previous Gomel Schools connects with the names of the famous scientists such as A.Bogolubov, F.Fedorov, V.Kadyshevsky, V.Belyi, B.Bokut' and their followers.

Particle and High Energy Physics plays an important role both as a way of understanding of the fundamental structure of matter and in the development and practical using of the newest technologies in the microelectronics, computers, physics and technique of deep vacuum and super low temperatures and other closely related fields. The main goals of this School are education of young scientists, discussion of the recent results in the fields of modern physics developing intensively, the exchange of information and experience of the modest methodology, establishment and extending of the cooperation between the leading scientists of international and national scientific centers.

The International School-Seminar "The Actual Problems of Particle Physics" was organized by the Joint Institute for Nuclear Research (Dubna, Russia) together with the National Center of Particle and High Energy Physics (Minsk, Belarus), and with participation of Institute of Physics & Institute of Metal Polymer Systems of National Academy of Sciences of Belarus, Gomel State University of F. Skarina & Gomel Polytechnic Institute of P.Sukhoi.

The scientific program of the School includes lectures and talks on physics and technique of accelerators, relativistic nuclear physics. Special attention was given to the experiments on the new accelerators and to the experimental status of the fundamental interactions at high energy. The new lines of investigations in quantum field theory were also discussed. The lectures and talks were presented by the scientists from the world-famous centers of the USA, Germany, Switzerland, France, Great Britain, Austria and Russia, Belarus and some other countries of the Former Soviet Union. The fact that one of the lecturers of 1977 Gomel School Professor Carlo Rubbia (Harvard University & CERN) was awarded Nobel Prize demonstrates the high scientific level of the series of these Schools.

The organizers of Gomel School, Byelorussian scientific society give a great importance to this good tradition of carrying out the meetings of physicists at the banks of the beautiful river Sozh and we hope for new meetings in the next years of current and future centuries.

We are grateful to the Administration of Gomel region and hotel "Golden Sands" for kind hospitality and support.

We owe many thanks to all those who made this Gomel School possible.

Chairman of the Local Organizing Committee
Professor N. Shumeiko

Vice-Chairman of the Local Organizing Committee
Correspondent Member of the National Academy of Science of Belarus Yu. Pleskachevsky

# 1. THE HISTORY OF PARTICLE PHYSICS AND TOOLS OF ITS STUDY

## Discovery of Electron, New Physical Theories and Fedorov's Approach

A.A. Bogush

*B.I. Stepanov Institute of Physics,*
*National Academy of Sciences of Belarus, Minsk*

In this short lecture important role of the discovery of electron as the first elementary particle in forming of new physical theories, first of all of special relativity and quantum mechanics, is outlined. Some topics related to the development of the quantum relativistic field theory of free and interacting elementary particles in Belarus are also briefly considered.

I. **Introduction.** One hundred years ago, in 1897, the first elementary particle, electron, was discovered by J.J. Thomson. This discovery has given rise to the transition of the studies of the structure of matter to the subatomic level. It led to the new physics, the physics of the XX-th century, and, as a consequence, to new techniques. The new, quantum relativistic physical picture of the world was also formed.

Of course, it is impossible to review here all the richest scientific and practical consequences of the electron discovery. Only some topics related to the role of electrons in the formation of special relativity theory and quantum mechanics will be outlined in this talk. In addition, the general covariant approach to the modern theoretical physics which has been developed in Belarus by F.I. Fedorov (1911 – 1994) and was generated, in fact, by the Dirac's theory of the electron will be also briefly indicated.

II. **Electron and special relativity theory.** It is well known that, on the one hand, the discovery of electron was mostly due to the study of physical nature of electricity and, in particular, of electroconductivity phenomena in liquids, solids (metals) and, especially, in gases. A detailed description and analysis of this history have been given in many publications (see, for example, [1-3]) and will be here omitted.

On the other hand, the discovery of electron has brought to the final stage in the formation of the classical (microscopic and macroscopic) electrodynamics as logically closed, contemporary physical theory. First

of all, the closed system of the basic equations in the framework of the Lorentz-Maxwell microscopic electrodynamics was formulated. In addition to the Maxwell-like microscopic equations for electromagnetic field with sources it includes the Newton-like equation for the electron moving in the electromagnetic field under the action of the Lorentz force. Nevertheless, the supposed by H. Lorentz (see [4]) microscopic structure of source of the electromagnetic field in the Lorentz-Maxwell electrodynamics was only later satisfactorily explained and found its adequate mathematical mapping in the theory. As a result, the modern formulation (see, for example, [5], 1972) of the classical (microscopic and macroscopic) electrodynamics was given in fact only about 100 years after the elaboration of the original Maxwell theory (1873).

A principal role of electrodynamics of moving media and physics (dynamics) of electron in the formation of special relativity theory, one of the two most fundamental theories (alongside with quantum mechanics) of the XX-th century, follows directly from the titles and contents of the basic publications of creators of this theory (see [6]):

*J. Larmor.* Aether and matter (1900).

*H.A. Lorentz.* Electromagnetic phenomena in a system moving with any velocity smaller than that of light (1904).

*H. Poincare.* To the dynamics of electron (1905, 1906).

*A. Einstein.* To the electrodynamics of moving media (1905). Does the inertia of body depend on the matter contained in it? (1905).

*M. Planck.* The relativity principle and the basic equations of mechanics (1906).

*H. Minkowski.* Space and time (1909).

First of all, namely the microscopic Lorentz-Maxwell equations for electromagnetic field which is generated, in fact, by moving electrons have been main subjects of study in most of above original works. As a starting point for the following investigations, the non-invariance of these equations with respect to the ordinary (non-relativistic) Galilei transformations has been used. As a consequence, the new space-time symmetry transformations, the Lorentz transformations, have been introduced. Thus, the invariance of the existing equations for electromagnetic field with sources with respect to all transitions from one to any other inertial reference frames in the space-time, realized by the Lorentz transformations, has been ensured. The mathematical formulation of new physical requirements to any relativistic physical theory postulated by Einstein who

determined the main content of the special relativity theory has been incorporated namely in the relativistic invariance conditions and in the own structure of the Lorentz transformations (or, in more general case, of the Poincare transformations).

The Lorentz-invariance requirements considered as the requirements of general meaning are, naturally, also imposed on the equation of motion of electron in the electromagnetic field, i.e. on the second constituent part of the microscopic classical electrodynamics. Since the previously existing equation turned out to be explicitly Lorentz-non-invariant, the new, relativistic invariant equation of motion for the electron has been introduced (M. Planck, 1906).

Thus, one can now say, that namely the need of solution of the problem of physical nature of electrons, which have been considered as the primary sources of the electromagnetic field, as well as its reagents, which can move with great velocities, has led, at last, to the creation of the special relativity theory.

Simultaneously the classical (microscopic and macroscopic) electrodynamics turned out to be an essentially relativistic physical theory. Additionally, a new mechanics, the relativistic classical one, more general than Newton's mechanics, has been also constructed.

III. **Electron and quantum mechanics.** Electron was found to be also the first particle of matter, whose description led to appearance of the second of the two most fundamental physical theories of the XX-th century, the quantum (wave) mechanics (L. de Broglie, V. Heisenberg, E. Schrödinger, M. Born and others; 1924–1928).

Electron has played in fact a crucial role in the formation of the theoretical and experimental foundations of non-relativistic quantum mechanics. The wave nature of matter was actually first assigned to electron (L. de Broglie, 1924). These properties of massive microobjects have been also firstly verified in diffraction experiments with electrons (C.J. Davisson, L.H. Germer; G.P. Thomson; 1927). The most of the basic statements of the non-relativistic quantum mechanics as well as of its first applications are mainly connected with the electrons and with corresponding, real or imaginary, experiments. Moreover, for solving the one-electron Kepler problem on the quantum level, the basic Schrödinger wave equation (1926) has been introduced (see [7]).

Thus, to describe the specific physical properties of electron, both relativistic and quantum ones, two new different physical theories were

constructed. Namely the need to elaborate the contemporary physical theory of electron has generated, as the natural next stage in development of modern theoretical physics, the synthesis of both above theories and, as a result, the formation of a new physical theory, the relativistic quantum mechanics.

A first step in this direction was done by E. Schrödinger himself. On solving the problem of description of electron as a constituent part of the hydrogen atom (see [7]), he introduced in 1926, as a by-product, a second order relativistic invariant (covariant) quantum mechanical wave equation. During 1926 a series of publications belonging to the various known authors have there appeared in which such second order relativistic wave equation was also introduced and studied in detail. However, this equation, called now the Klein-Fock-Gordon wave equation:

$$(\partial_\mu^2 - m^2)\varphi_0(x) = 0 \tag{3.1}$$

turned out to be unsuitable for description of electron (see, for example, [8]) and is now used in the quantum relativistic theory of free scalar (spinless) particles (fields).

Later, in 1928 P.A.M. Dirac, starting from the Klein-Fock-Gordon equation, has derived for the free electron an appropriate first order relativistic wave equation:

$$(\gamma_\mu \partial_\mu + m)\psi_0(x) = 0. \tag{3.2}$$

On the basis of the Dirac equation (3.2), existence of spin equal to 1/2 for electron has been justified for the first time. Simultaneously, a first antiparticle, positron, which was discovered experimentally just in 1932, was predicted by Dirac. So, electron was found to be the first carrier of two principally new specific inherent properties of all the elementary particles.

The Dirac's theory of electron has generated in following the quantum electrodynamics describing the interaction between the secondly quantized electromagnetic (photon) and electron-positron fields and remaining up to now the self-consistent theory of electromagnetic interactions. Moreover, at present, the quantum electrodynamics is the constituent part of the general relativistic theory of secondly quantized fields, i.e., the relativistic quantum field theory forming theoretical foundation of the one-hundred years old physics of elementary particles and their interactions.

Thus, elaboration of the non-relativistic and relativistic quantum mechanics and, later, of the quantum electrodynamics, as well as general relativistic quantum field theory, are closely connected with electron.

IV. **Dirac equation for electron and general theory of linear and nonlinear relativistic wave equations.** Shortly after introduction of the Dirac equation (3.2) for electron, it has been found that description of all free elementary particles may be given with help of the first order relativistic wave equations in the universal (Dirac-like) matrix form (see, for example, [9,10])

$$(\alpha_\mu \partial_\mu + \alpha_0)\psi_0(x) = 0. \tag{4.1}$$

In the framework of theory of the relativistic wave equations (4.1) the general method of the projective operators has been worked out in Belarus by F.I. Fedorov ([11], see [10]). This method allowed to find all the solutions of equation (4.1) with physical meaning, i.e. those describing all possible physical states $\psi_0 = \psi_p^s(x)$ of a free particle in a covariant (indexless) form. It means that these solutions may be found independently of choice of basis in the wave function space, by using only invariant properties of the matrices $\alpha_\mu$ and $\alpha_0$ (mass matrix), in the compact form of projective dyadic matrices $\Lambda_0 = \psi_0 \cdot \bar{\psi}_0$.

Moreover, within the projective operator approach the square of the interaction matrix elements $M_{1\to 2} = \bar{\psi}_2 Q \psi_1$ can be calculated with help of the following general formula [11]:

$$\mid M_{1\to 2} \mid^2 = Sp\{Q\Lambda_1 \bar{Q} \Lambda_2\}. \tag{4.2}$$

Here the dyadic matrices $\Lambda_1 = \psi_1 \cdot \bar{\psi}_1$ and $\Lambda_2 = \psi_2 \cdot \bar{\psi}_2$ determine the elementary particle states before ($\psi_1$) and after ($\psi_2$) interaction, $Q$ is the interaction operator.

It turned out that the number of terms in expression for the trace of matrix product (4.2) increases rapidly when polarization states of the interacting particles are being taken into account. In order to overcome this obstacle the following covariant method of direct calculation of matrix elements themselves, rather than of squares of their modules, has been proposed ([12], see [10]):

$$M_{1\to 2} = Sp\{Q\psi_1 \cdot \bar{\psi}_2\} = Sp\{Q\Lambda_1 T^{-1}\}. \tag{4.3}$$

Here $T = T(\hat{1})$ are the Lorentz group representation operators, which realize the transition

$$T\psi_1 = \psi_2 \qquad (\bar{\psi}_1 T^{-1} = \bar{\psi}_2). \tag{4.4}$$

These operators were constructed in the framework of Fedorov's vector parametrization to be discussed below.

Now, the similar methods of direct calculation of scattering amplitudes are predominantly used in modern high-energy physics.

F.I. Fedorov introduced also the general nonlinear wave equation for arbitrary interacting fields in the following universal matrix form [13] :

$$(\alpha_\mu \partial_\mu + m)\psi(x) + \Lambda\psi(x)\psi(x) = 0. \qquad (4.5)$$

Here the quadratic $(\alpha_\mu, \alpha_0)$ and cubic $(\Lambda)$ matrices are expressed in a very compact algebraic form in terms of the basic elements ($e^{AB}$ and $e^{ABC}$) of matrix algebras defined by the generalized Kroneker symbols $\delta_{AB}$ [14,15] in space of joint field wave function $\psi = \{\psi_A(x)\}$ [16]. During 1968-1988 all the existing basic field theories of gravitational, electromagnetic, weak (electroweak) and strong interactions were reformulated on the unique mathematical foundation formed by Fedorov's universal nonlinear equations (4.5) (see reviews in [17,18]). The general rules based on gauge (supergauge) invariance conditions have been established to transfer the linear wave equations (4.1) for free fields to the nonlinear equations (4.5) for interacting fields [19].

In all such investigations, for description of 6 leptons and 6 quarks as primary sources of all fundamental interactions the Dirac equation (3.2), first introduced for electron, is used (with $m \neq 0$ and $m = 0$) as a starting point. It should be also underlined that the gauge field concept forming now a base of modern theory of fundamental interactions has been introduced and exploited in constructive, correct way only after quantum relativistic description of the electron , particularly, in the work of V.A. Fock under following title: "Geometrisation of Dirac's theory of electron"(1929).

V. **Finite symmetry transformations and Fedorov's vector parameters.** Nowadays, it is well known that formation of the above new physical theories, which were mainly evoked by the discovery of electron, was essentially based on the constructive use of ideas and principles of physical symmetry. For example, a crucial role in the construction of the special relativity theory belongs to the space-time symmetry (Lorentz or Poincare transformations).

The usefulness of the general finite symmetry transformations, in contrast to the infinitesimal ones, depends essentially on the convenient choice of the group parameters and, as a consequence, on the simplicity of their composition rules. An example of such an efficient parametrization

was given by F.I. Fedorov (1958-1962) for the rotation $SO(3.R)$ and Lorentz $SO(3.1)$ groups (see [10]). In the framework of this vector parametrization, an isomorphic correspondence between the group of transformations and the group of three-dimensional vector parameters with the simplest possible group operation (composition law) was explicitly formulated. That all allows to operate in most cases just with vector parameters, avoiding usage of the explicit expressions for related finite transformation matrices. Now, one can say that namely the Fedorov's vector parametrization became a base for for elaboration of the general finite geometrical (global) and dynamical (local) symmetry transformation approach.

To apply the finite symmetry transformations to relativistic kinematics, the Lorentz matrices and group representation operators as well as the corresponding vector parameters have been expressed in terms of the physical quantities to be transformed [12]. On this basis, the covariant spin description of moving elementary particles and the above mentioned (see (4.3),(4.4)) covariant approach to the direct computation of scattering amplitudes of polarized particles were worked out. Many other general problems of relativistic kinematics have been also solved[1] (see [10,20]).

Later, it was found that in the framework of the vector parametrization of the group $SU(2)$ ($SO(3.R)$) a transition from the global finite transformations $U = U(\boldsymbol{n}) \in SU(2)$, ($O = O(\boldsymbol{n}) \in SO(3.R)$) to the corresponding local (gauge) finite transformations $U(x)$ ($O(x)$) reduces to an obvious redefinition of the vector parameters $\boldsymbol{n} \to \boldsymbol{n}(x)$ [17]. There have been obtained the relations:

$$\boldsymbol{b}'_\mu(x)\boldsymbol{t} = U(x)\boldsymbol{b}_\mu(x)\boldsymbol{t}U^{-1}(x) - i(\partial_\mu U(x))U^{-1}(x) =$$

$$= \{O(x)\boldsymbol{b}_\mu(x) + f(\boldsymbol{n}(x))\partial_\mu \boldsymbol{n}(x)\}\boldsymbol{t}, \qquad (5.1)$$

$$f(\boldsymbol{n}(x)) = 2(1 - \boldsymbol{n}^\times(x))/(1 + \boldsymbol{n}^2(x)), \quad (n^\times_{ac} = \varepsilon_{abc}n_b), \qquad (5.2)$$

which define explicitly the transformation properties of the Yang-Mills vector potentials $\boldsymbol{b}_\mu = (b^a_\mu(x))$ under the finite (rather than usual infinitesimal ones) gauge transformations $O(x) = O(\boldsymbol{n}(x))$ [17,18]. As a consequence, an explicit expression for the vacuum connection $\boldsymbol{a}_\mu(x) =$

[1]It should be noted that the main information about the Fedorov's vector parametrization as well as its numerous physical applications have been earlier presented at the three previous Gomel schools (1971 [21], 1973 [22] and 1977 [23]). That is why just several new results which were obtained during the last twenty years are listed here.

$f(\boldsymbol{n}(x))\partial_\mu \boldsymbol{n}(x)$ and a non-linear equation for the principal chiral fields $+\boldsymbol{n}^0(x)$ and $-\boldsymbol{n}^0(x)$ on the $SO(3.R)$ group [24] were introduced. It was shown, particularly, that the last equation becomes solvable in the two-dimensional space-time and allows the existence of soliton-like solutions [25]. The differential Cartan form $dU(x)U^{-1}(x)$ has been also expressed in terms of the local vector parameters $\underline{n}(x)$ of the gauge group $SU(2)$ (see (5.1), (5.2))

$$dU(x)U^{-1}(x) = id\boldsymbol{n}'(x)\boldsymbol{t}, \quad d\boldsymbol{n}'(x) = f(\boldsymbol{n}(x))d\boldsymbol{n}(x),$$

with help of the composition law alone [26]. Some of these results were later generalized for the wide set of gauge (supergauge) groups and effectively used in study of popular nonlinear field models (see [27,28]).

During the last years the theory of quantum ($q$-deformed) groups is being developed very intensively. These groups are connected with noncommutative geometry and reflect the new symmetry of the quantum physical systems (see, e.g. [29]).

The effectiveness of the Fedorov's vector parametrization was recently used as a motivation for the introduction of quantum vector parameters into the theory of quantum groups. Such an extension allows to establish some new properties of the vector parametrization. For instance, it was shown that a transition from the classical groups $SL(2.C)$, $SU(2)$ to the $q$-deformed $SL_q(2.C)$, $SU_q(2)$ may be reduced to the simple $q$-deformation of the corresponding classical vector parameters themselves. Moreover, the simple composition law for the obtained quantum vector parameters, which remains to be the same as in the classical case allows to derive the basic commutation rules for the quantum group parameters in a direct and natural way [30].

The general method of projective operators in the theory of first order relativistic wave equations, the universal nonlinear wave equations for interacting fields and the three-dimensional vector parametrization of the physical symmetry groups form now the main content and meaning of the Fedorov's covariant approach to the theory of elementary particles. Namely this very general and effective approach, generated mainly by the Dirac's theory of electron, has allowed to obtain a series of new physical results in Belarus, which were impossible or very difficult to get in other way or in the other places.

## VI. Dirac's theory of electron and classical field theory.

The advances of the quantum electrodynamics in describing the electromagnetic pheromena on the microscopic level are now known. Therefore the concept of secondly quantized fields was found to be for a long time the dominant concept in the field theory of elementary particles and their interactions. At the same time, the possibilities of relativistic quantum mechanics in solving many problems of the above theory have not been used fully.

The new, in some sense, situation has been formed in the last three decades. Within the gauge field theory it was established that many problems of this theory, that especially arose in the beginning of its elaboration, may be solved in a more simple and natural way within the frameworks of non-quantized relativistic quantum mechanical field theory, called now the classical (semiclassical) field theory. Moreover, the use of the Feynman's continual (functional) path-integration methods in the gauge field theory allows to overcome substantially the barriers existing previously between classical and quantized field theories.

An essential progress in the development of the classical field theory has been achieved in Belarus, in the framework of Fedorov's covariant approach (see [31] and [10]). Here the theory of electromagnetic interactions has been worked out within the concept of the classical fields, that means, without making direct use of the second quantization procedure and without building the quantum electrodynamical scattering matrix (see [32]).

First of all, the quantum mechanical one-particle interpretation of the general solutions of the relativistic wave equations for free Dirac and electromagnetic fields has been developed. Then, the closed system of the wave equations for the above interacting fields have been derived using local (gauge) $U(1)$ invariance conditions. The solutions of these nonlinear field equations have been obtained with help of the familiar quantum mechanical methods of the causal Green functions and of the perturbation theory taken, naturally, in their relativistic form.

Particularly, the general solution of the Dirac equation for electron (see (4.2)) in electromagnetic field $A_\mu(x)$ (see [32,18])

$$(\gamma_\mu \partial_\mu + m)\psi(x) = ie\hat{A}(x)\psi(x), \quad (\hat{A} = A_\mu\gamma_\mu) \tag{6.1}$$

is presented in the integral form

$$\psi(x) = \psi_0(x) + ie \int G_c^{1/2}(x - x')\hat{A}(x')\psi(x')d^4x'$$

and then is rewritten as perturbation series

$$\psi_n(x) = \sum_{k=0}^{n} \psi^{(k)}(x),$$

where

$$\psi^{(k)}(x) = (ie)^k \int\int \dots \int G_c^{1/2}(x - x')\hat{A}_0(x')G_c^{1/2}(x' - x'')\hat{A}_0(x'') \dots$$

$$\dots G_c^{1/2}(x^{(k-1)} - x^{(k)})\hat{A}_0(x^{(k)})\psi_0(x^{(k)})d^4x'd^4x'' \dots d^4x^{(k)}. \qquad (6.2)$$

Here $G_c^{1/2}(x - x')$ is the causal Green function defined as the solution of Dirac equation (6.1) with point-like source

$$(\gamma_\mu \delta_\mu + m)G_c^{1/2}(x - x') = \delta(x - x'),$$

whereas $\psi_0(x)$ and $A_{\mu o}(x)$ are the known free state functions of electron and electromagnetic field, respectively.

As a next step, the Fourier decomposition for arbitrary function $\psi^{(k)}(x)$ (6.2)

$$\psi^{(k)}(x) = \sum_q c_q^{(k)}(t)\psi_0(x, q)$$

is introduced. The full set of orthonormalized wave functions $\psi_0(x, q)$

$$(\psi_0(x, q), \psi_0(x, q')) = \delta_{qq'}$$

is used, where $q$ defines the energy, momentum and spin projection values of free electron.

Now, by taking into account the given initial conditions, for example, as

$$\psi(x)/_{t=-\infty} = \psi_0(x) = \psi_0(x, q_1) = \psi_1,$$

$$\psi(x)/_{t=+\infty} = \psi_0'(x) = \psi_0(x, q_2) = \psi_2,$$

fixing the asymptotically free states of the electron before ($t = -\infty$) and after ($t = +\infty$) interaction, one can find the scattering amplitude with help of a following simple rule:

$$c_{q_2,q_1}^{(k)}(t = +\infty) = (\psi_0(x, q_2), \psi^{(k)}(x)/_{t=+\infty}) \rightarrow \qquad (6.3)$$

$$\rightarrow M_{1\to 2}^{(k)} = \bar{\psi}_2 Q^{(k)} \psi_1.$$

The obtained in such a way interaction matrix element $M^{(k)}_{1\to 2}$ (6.3) defines a probability amplitude (in $k$-th order of the perturbation theory) for transition of the electron from in-state $\psi_1$ to out-state $\psi_2$ in the electromagnetic process determined by the vertex operator $Q^{(k)}$.

Such calculation schema allows one to obtain for many concrete electromagnetic scattering amplitudes the same results that may be derived within the quantum electrodynamics, but with essentially smaller expenditures of labour and time.

An analogous approach and related calculation schema have been also elaborated within the gauge field theory of electroweak interactions [18].

There are known only several books and monographs which are specially devoted to the concept of classical fields in their connection with elementary particles theory (see [5,9,33-36]). Main topics associated with the classical field theory are also included as an introduction into some monographs on the general quantum field theory (see, for example, [37]) and , naturally, in the most of monographs published during last decades which are dealing with the gauge field concept (see [38-44]).

Nevertheless, only in Belarus the development of the classical field theory was brought to its concluding stage, namely, to the description not only of free but also interacting elementary particles up to the calculation of the effective cross sections for concrete interaction processes.

VII. **Conclusion.** Like at the beginning of its 100 years history, the electron remains up to now a difficult for complete understanding unit of the structure of matter. The main aim of all the above mentioned new physical theories, elaborated in XX century, to give the satisfactory and full description and explanation of the all unordinary physical properties of electron remains to be in fact not achieved. So, for instance, the known values of the mass, electrical charge and spin of electron are the empirical parameters of the existing theory.

The history of electron is being continued and will bring, undoubtedly, many new surprising results.

# References


[1] Anderson D.L. *The Discovery of Electron.* N.-Y. 1964.

[2] Thomson G.P. *The septuagenarian electron.* Phys. Today. 1967. V.20. N 5. P. 55.

[3] Weinberg S. *The Discovery of Subatomic Particles.* N.-Y. 1983.

[4] Lorentz H.A. *The Theory of Electrons and its Applications to the Phenomena of Light and Radiant Heat.* Leipzig. 1916.

[5] De Groot S.R. and Suttorp L.G. *Foundations of Electrodynamics.* Amsterdam. 1972.

[6] *Relativity Principle. Works in Special Relativity Theory.* M. 1973. (In Russian).

[7] Schrödinger E. *Selected Works on the Quantum Mechanics.* M. 1976. (In Russian).

[8] Pauli W. *Die allgemeinen Prinzipen der Wellenmechanik.* Berlin. 1958.

[9] Corson E. *Theory of Tensors, Spinors and Wave Equations.* N.-Y. 1953.

[10] Fedorov F.I. *Lorentz Group.* M. 1979. (In Russian).

[11] Fedorov F.I. *Projective operators in theory of elementary particles.* JETP. 1958. V.35. N 2. P.493-500. (In Russian).

[12] Bogush A.A., Fedorov F.I. *Covariant spin description and its application.* Vesti AN BSSR. Ser. fiz.-tech.nav. 1962. N 2. P.26-37. (In Belarussian).

[13] Fedorov F.I. *First order equation for gravitational field.* Dokl. AN SSSR. 1968. V.179. N.4. P.802-805. (In Russian).

[14] Bogush A.A., Fedorov F.I. *Generalized Kroneker symbols.* Dokl. AN BSSR. 1968. V.12. N.1. P.21-24. (In Russian).

[15] Bogush A.A. *Universal matrix form of the joint field equations in the standard electroweak interaction theory.* Rep. Math. Phys. 1987. V.25. N 3. P.27-42.

[16] Kuvshinov V.I., Fedorov F.I. *Nonlinear equations in electrodynamics of scalar mesons.* Vesti AN BSSR. Ser. fiz.-mat.nav.1970. N.5. P.69-75. (In Russian).

[17] Bogush A.A. *Introduction to the Field Theory of Elementary Particles.* Mn. 1981. (In Russian).

[18] Bogush A.A. *Introduction to the Gauge Field Theory of Electroweak Interactions.* Mn. 1987. (In Russian).

[19] Babich A.A., Kuvshinov V.I., Fedorov F.I. *Local gauge and relativistic invariance conditions for first order universal nonlinear equations in theory of fundamental interactions.* Dokl. AN SSSR. 1982. V.267. N.5. P. 1093-1097. (In Russian).

[20] Bogush A.A., Fedorov F.I. *Finite Lorentz transformations in quantum field theory.* Rep.Math.Pys. 1977. V.11. Pp.37-52.

[21] Fedorov F.I. *Some methods of relativistic kinematics.* In: International School on High Energy Physics for Young Scientists (Gomel - 71). Dubna. Pp. 3-37. (In Russian).

[22] Bogush A.A., Fedorov F.I. *Complex Lorentz group and its applications in quantum field theory.* Ibid. (Gomel - 73). Dubna. 1973. Pp. 5-35. (In Russian).

[23] Bogush A.A., Kurochkin Yu.A., Fedorov F.I. *Biquaternions and relativistic kinematics.* Ibid. (Gomel - 77). Dubna. 1979. Pp. 467-479. (In Russian).

[24] Bogush A.A., Zhirkov L.F. *Composition law of vector parameters and chiral field on group $SO(3.R)$.* In: Cov.Meth. in Theor.Phys. Elem.Part.Phys. a. Relat.Theory. (I) Minsk. 1981. Pp.5-26. (In Russian).

[25] Doktorov E.V. *Solitons of rotation group vector parameters.* Ibid. (III). 1991. Pp. 64-68. (In Russian).

[26] Berezin A.V., Kuvshinov V.I., Tho N.V. *Cartan form and lagrangians of nonlinear fields in vector parametrization of group manifold.* Ibid. (III). 1991. Pp. 21-27. (In Russian).

[27] Bogush A.A., Fedorovych A.M., Zhirkov L.F. *Some properties of local gauge transformation parameters in non-abelian field theory.* In: Group Theoretical Methods in Physics. London, N.-Y. 1987. Pp. 271-277.

[28] Kuvshinov V.I., Tho N. *A new method for calculating the Cartan forms and applications to the gauge and chiral field theories.* J. Phys. A.: Math. Gen. 1993. V.26. Pp. 631-645.

[29] Pittner L. *Algebraic Foundations of Non-Commutative Differential Geometry and Quantum Groups.* Berlin. 1995.

[30] Bogush A.A. *Transition $SL(2.C)$ $(SU(2), SO(3.R)) \to SL_q(2.C.)$ $(SU_q(2), SO_q(3.R))$ and q-deformation of vector parameters.* In: VII International Conference. Symmetry Methods in Physics. V.I. Dubna. 1996. Pp.58-62.

[31] Fedorov F.I. *To the problem of solution of relativistic wave equations.* Dokl. AN SSSR. 1949. V.65. N6. P.813. (In Russian).

[32] Bogush A.A., Moroz L.G. *Introduction to the Theory of Classical Fields.* Mn. 1968. (In Russian).

[33] Ivanenko D., Sokolov A. *Classical Field Theory.* M. 1947. (In Russian).

[34] Barut A. *Introduction to the Theory of the Electromagnetic and Classicul Fields.* N.-Y. 1964.

[35] Rohlich F. *Classical Charged Particles.* Mass. 1964.

[36] Das A. *The Special Theory of Relativity. Mathematical Exposition.* N.-Y. 1993.

[37] Bogolyubov N.N., Shirkov D.V. *Introduction to the Theory of Quantized Fields.* M. 1957. (In Russian).

[38] Konoplyova N.P., Popov V.N. *Gauge Fields.* M. 1972, 1980. (In Russian).

[39] Itzykson C., Zuber J.-B. *Quantum Field Theory.* N.-Y. 1980.

[40] Ramond P. *Field Theory.* London. 1981.

[41] Cheng T.-P., Li L.-F. *Elementary Particle Physics.* Oxford. 1984.

[42] Halzen F., Martin A.D. *Quarks and Leptons: An Introductory Course in Modern Particle Physics.* N.-Y. 1984.

[43] Ryder L.H. *Quantum Field Theory.* Cambridge. 1985.

[44] Sterman G. *An Introduction to Quantum Field Theory.* Cambridge. 1993.

# Particle Accelerators in Particle Physics (from electron to higgs)

I.N. Meshkov
JINR, Dubna

## Content



## Introduction: Electron Centenary

This year we, physicists, celebrate a remarkable event in the history of our science — Hundredth Anniversary of the experiment performed by J.J. Thomson with cathode rays, which proved the existence of electron as an independent particle, i.e. the particle travelling in a free space (vacuum) without any connection with an atom, which contained this electron before.

Not every physicists realises that the Thomson's experiment was the very first event of artificial "creation" of a basic natural particle. Therefore,

this creation plays in modern physics the role analogous to the well known event of human person origination in Christian religion.

Actually, the Thompson's device was *very first particle accelerator* with particle energy of a few keV.

In this lecture the author has a goal to analyse an influence of particle accelerators as an experimental tool on the development of particle physics and to discuss present status and trends in the accelerator technique progress.

Discribing the scientific progress during the centure followed to the electron discovery we do not pretend to give a full description. The events related to the accelerator development are mostly mentioned.

# 1 In The Very Beginning

1911 — the famious **Rutherford's experiment** was the very first attempt of an use of fast particle, as a projectile penetrating a medium to examine the characteristics of the last one. Since that moment scattering of fast particles by an object became the most fruitful method in experimental physics (to study this object). Rutherford used in his experiment $\alpha$ – particle from a radioactive source.

1913 — the **Bohr's hypotesis** of atom structure opened the era of quantum mechanics (E.Schrodinger, W.Heisenberg, W.Pauli, P.Dirac, L.De-Brogle).

1922 — E. Rutherford introduces the word "**proton**" indicating the charge particle cotaining in atomic nuclei.

1928 — R. Wideroe formulates the idea and constructs first *linear accelerator*.

# 2 The First Subatomic Particles (1930–1942)

1930 — W.Pauli analysing electron spectrum in beta–decay proposes the hypothesis of **neutrino** (electron neutrino in modern understanding).

1931 — R.van-de-Graaf constructs first *electrostatic accelerator* by his principle and reaches voltage of 1.5 MV.

1932 — J.Cockroft and E.Walton construct another kind of *electrostatic accelerator*, the "cascade" rectifier, and obtain the voltage of 0.6 MV.

J.Chadwick accelerates $\alpha$–particles with Cocroff–Walton machine and discovers **neutron** in the reaction

$$\alpha + {}^9 Be \Longrightarrow 3\alpha + n.$$

Soon W. Heisenberg and D. Ivanenko formulate (independently) the hypotesis of **nuclei structure** as combination of neutrons and protons.
1930–32 — E.O. Lawrence proposes the method of *resonant acceleration*, designs and constructs first *cyclotron* and resonant *linear accelerator*.
1935 — H.Yukawa introduces new hypothetic particle with intermediate, between electron and proton mass — **meson** responsible for nuclear force or, as we say now, the "strong interaction". He writes the formula of the nuclear potential, the famious **"Yukawa potential"**, and calculates with it using nuclei size the meson mass: $m_{meson} \sim 100\ MeV$
1936 — K. Andersen and S. Neddermeer find in *cosmic rays* light particle of the mass of 105 MeV, but .... it penetrares a medium without an efficient interaction with nuclei. The triumph of Yukawa hypothesis is postponed for 10 more years. 1st European cyclotron was put in operation in Radium Institute at Leningrad.
1940 — D. Kerst demonstrated the *betatron*.
1942 — after one dozen years of expectation the fact of **neutrino** exsistence was proved by J. Allen: he observed in the reaction of K–capture

$${}^7 Be + e^- \Longrightarrow {}^7 Li + \nu_e$$

the recoil of Li–nuclear due to momentum transfer from neutrino. The idea of this experiment was proposed by A. Alikhanian in 1938.

# 3 The Breakthrough In Accelerators (1945–1947)

The limitation of particle energy in cyclotron machines connected with relativistic increase of the particle mass and desynchronisation was overcome with discovery of the *phase stability principle* by V. Veksler (1944) and E. McMillan (1945). Soon first small electron *synchrotrons* of the energy of 300–500 MeV were constructed, and one of them — in Lebedev Physics Institute at Moscow.

Unfortunately, the authors of the principle missed the Nobel prize they definitely deserved, because Soviet officials did not satisfy the Nobel

committee requirements, when refused to answer the traditional question, posed in accordance with the committee regulations — where the proposed principle was applied. At that time the LPI synchrotron was a "top secret" object!

And the next "harvest" of new accelerator appearence was taken by J. Blewett and Huber (USA), when they observed *synchrotron radiation* of relativistic electrons rotating in magnetic field.

# 4 Success With Cosmic Rays (1947)

Nevertheless cosmic rays at that time remained very effective source of fast particle, and the next double success was reached with them in 1947: G. Rochester and G. Butler observed particles heavier of nucleon — **hyperons**, and S. Powell, G. Lattes and H. Muirhead discovered the long awaited "Yukawa particle" — $\pi$ – **meson** (or **pion**, the modern name).

# 5 Progress In, With and Without Accelerators (1948–1957)

The principle of Veksler-McMillan permitted to increase significantly the energy of accelerators.

1948–49 — first *synchrocyclotrons* were constructed at Berkeley and Dubna, and, as result, the generation of pions in collisions of accelerated protons with a target was obtained. From this moment accelerators became the most effective sources of pions.

During this ten years the series of *protons synchrotons* in relativistic energy range was constructed: "Cosmotron" at Brookhaven (3 GeV, 1952), "Bevatron" at Berkeley (6.3 GeV, 1954) and "Synchrophazotron" at Dubna (10 GeV, 1957). They were "the last mogikans" among the weak focusing machines, because at the same time in USA N. Kristofilos (1950, not published) and independently E. Courant, M. Livingston and H. Sneider (1953) suggested *the strong focusing principle,* which really was the next breakthrough in accelerator technology.

The "Bevatron" was constructed especially to exceed the threshold energy of **antiproton** generation in $pp$–collisions. And soon (1955) the first antinucleon was obtained by O. Chamberlain, E. Segre, C. Wiegand

and T. Ypsilantis. It was first *great success* in particle physics achieved with accelerators!

Another remarkable result was obtained in 1955 by Hofstadter's group at Stanford University in deep inelastic scattering of electrons from linear accelerators on protons (hydrogen target). It was actually continuation of the Rutherford experiment but with relativistic electrons at the energy of the order of several hundreds MeV. This permitted to examine the electric charge distribution in proton in the range of $10^{-13}$ cm.

Also in 1955 A.Pais and O.Piccioni discovered the effect of **kaon oscillations** – the transition of $K^0$ in $\bar{K}^0$ and back. This effect, named for the authors, opened the new category of phenomena in particle physics.

One should underline, that these experiments performed with accelerator beams were accompanied by remarkable achievements in nonaccelerator studies. So, in 1953–1956 the group of F. Reines and C. Kowan registered at first time the **interaction of neutrinos** with another particles, namely protons, in reaction of the "reversed" $\beta$–decay:

$$\tilde{\nu}_e + p \Longrightarrow n + e^+.$$

They used neutrinos from a nuclear reactor, and it was a real challenge for accelerator physicists to repeat this success.

1956 — T.D. Lee and C. Yang formulate the hypothesis of **non – conservation of parity** and one year later Chien–Shiung Wu, R.W. Hayword, D.D. Hoppes and R.P. Hudson at US Nat. Bureau of Standards proved it experimentally in beta–decay. In the 1957 year, the group leaded by L.Lederman using muons from decay of pion generated with protons from "Cosmotron", performed the experiment on parity violation test in muon decay.

At the end of this decade the idea of *colliding beams* was suggested by D.W. Kerst with colleguaes (1956).

# 6 The Beginning of The Era of Big Machines (1959–1966)

The construction of two large machines — Proton Synchrotron (PS) at CERN (26 GeV, 1959) and Alternative Gradient Synchrotron (AGS) at Brookhaven (28 GeV, 1960) opened the new Era of *cyclic accelerators with strong focusing systems.* Soon both machines have brought remarkable

achievement — the discovery of new kind of **neutrino**, the **muonic** one. In 1962 two groups — one of L. Lederman at Brookhaven and another one of M. Schwarz and J. Steinberger at CERN using the beam of fast neutrinos from muon decay:

$$p + p \longrightarrow p + p + \pi^+ + \pi^-, \quad \pi^\pm \longrightarrow \mu^\pm + \nu_\mu(\tilde{\nu}_\mu)$$

have observed the reaction

$$\tilde{\nu}_\mu + n \longrightarrow p + \mu^-.$$

An absence of electrons from the probable reaction

$$\tilde{\nu} + n \longrightarrow p + e^-$$

proved the specific characteristic of $\tilde{\nu}_\mu$, different from "conventional" $\tilde{\nu}$, which was called $\tilde{\nu}_e$ since that time. It was the beginning of the **2nd Generation** of the particles and the beginning of the formation of the **"Standard Model"** (Table 1). Two years later (1964) M. Gell–Mann and G. Zweig suggested the hypothesis of **quarks** — the constituents of strong interacting particles **hadrons**. And P. Higgs introduced his **"Higgs particles"**, responsible for the supersymmetry breaking and formation of particle masses.

During this period a significant progress in accelerators was achieved. In 1964 2 GeV linear accelerator was put into operation at Kharkov Physics and Technique Institute, and in 1966 much more powerful *Stanford Linear Accelerator* of 2 miles length reached the project energy of 20 GeV.

1965 was official year of the birth of the *colliding beams*: two groups — of INP Novosibirsk and Stanford/Princeton Universities reported the realisation of the electron–electron colliding beams project. The first *colliders* had energy 2×180 MeV (VEP INP) [1] and 2×500 MeV (SLAC) and luminosity of the order of $1 \times 10^{29} cm^{-2} \cdot c^{-1}$ (see Fig. 1). The main goal of these experiment set–ups was to test quantum electrodinamics at small distance between interacting particles or to find, does electron have a finite size? The answer was : electron behaves itself as a pointlike charge up to $1 \cdot 10^{-14} cm$.

[1] VEP – abbriviation from Russian "colliding electron beams" = "vstrechnie electronnie puchki"

Table 1: "The Standard Model." The Fundamental Particles and Their Mass ($MeV/c^2$)

| Family | Electric Charge (e) | Generation | | |
|---|---|---|---|---|
| | | 1 | 2 | 3 |
| 1.Neutrino (Neutral lepton) | 0 | electron neutrino $\nu_e$ ($< 5 * 10^{-6}$) | muon neutrino $\nu_\mu$ ($< 0.3$) | $\tau$–lepton neutrino $\nu_\tau$ ($< 24$) |
| 2.Charged Leptons | $-1$ | electron $e^-$ (0.511) | muon $\mu^-$ (105.7) | $\tau$–lepton $\tau$ (1784) |
| 3.Quarks | $+2/3$ | Up (u) (5) | Charm (c) (1270) | Top (t) (176000) $\pm$ 8 $\pm$ 10 |
| 4.Quarks | $-1/3$ | Down (d) (8) | Strange (s) (175) | Bottom (b) (175) |

Table 1, continue. Interaction Carriers and Their Masses ($GeV/c^2$)

| Interaction | electric charge | particle |
|---|---|---|
| strong | 0 | gluon g |
| electromagnetic | 0 | photon $\gamma$ |
| weak | $\pm e$ | intermediate vector bozons $W^{\pm}$, (80.22) |
| | 0 | $Z^0$, (91.187) |

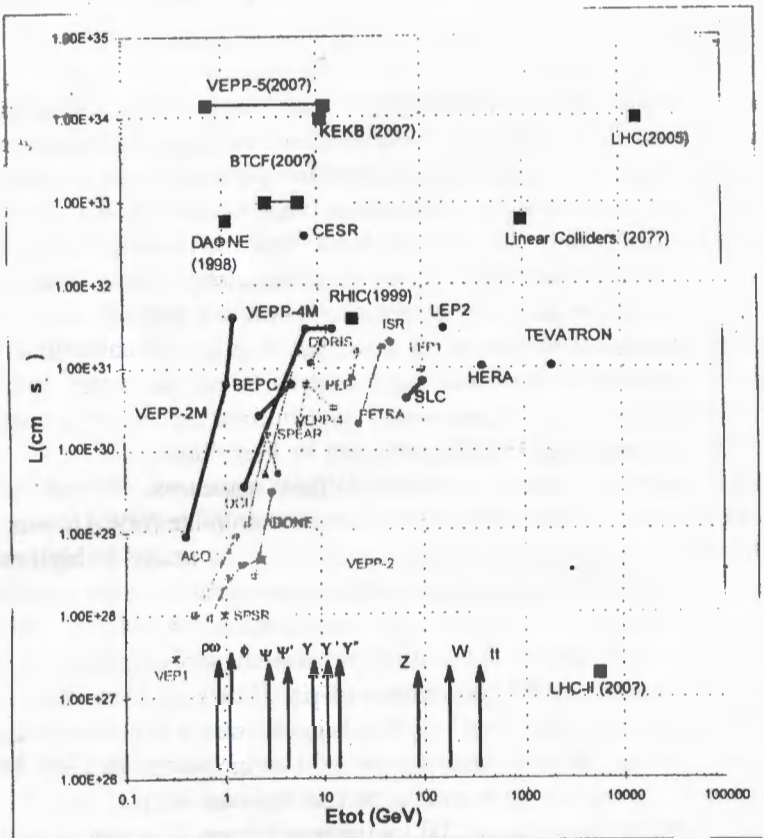


* - first e-e- colliders VEP1 Novosibirsk and Stanford/Princeton storage ring

colliders now in operation: VEPP2M, BEPC, CESR, VEPP4M, , LEP2, - symmetric $e^+e^-$ -colliders; HERA - 820 GeV protons x 30 GeV electrons; Tevatron - 2x0.9 TeV proton-antiproton collider

, colliders to be built: VEPP5, DAΦNE, BTCF - symmetric $e^+e^-$ collider, KEKB - asymmetric 3.5x8 GeV $e^+e^-$ collider, VEPP5 - asymmetric $e^+e^-$ collider; LHC - 2x7 TeV pp- and 2x2.76 TeV/u ii- collider; RHIC - ii- 2x100 GeV/u and pp- 2x250 GeV/u collider; VLEPP (and also JLC, TESLA, NLC, CLIC) - linear colliders

closed colliders: ACO, VEPP2, ADONE, SPEAR, VEPP4 - symmetric $e^+e^-$ -colliders, DCI - 2 rings symmetric $e^+e^-$ -collider, ISR - two rings pp collider.

Figure 1: The colliders

# 7 New Ideas And Further Progress (1966–1970)

In 1966 G. Budker formulates his idea of *electron cooling method* opens a new page oi particle beam physics: the method, which permits to overcome the limitation posed by Liouville theorem for a heavy particle beam, was proposed. From now accelerator physicists begin to think how to introduce a sufficient friction inside the heavy particle beam to decrease significantly its emittance and momentum spread (6–dimensional phase space size). The only kind of the particle "cooling" was known before: synchrotron radiation of electrons circulating in a storage ring (or synchrotron). Soon the idea of *stochastic cooling* was suggested by S. van der Meer at CERN (1968). The experimental studies and development of the both methods began in Novosibirsk and CERN and later in Fermilab.

In 1967 the first *electron–positron collider* appeares. It was *VEPP2* storage ring at INP Novosibirsk. Soon similar collider *SPEAR* was built at SLAC. Both machines were used, particularly, to study at high resolution $\rho, \omega, \varphi$–mesons discovered before with accelerators generating particle beams to bombard fixed targets. One should mention, that $\varphi$–meson by its structure is a "pure" quark–antiquark system and contains **s-quark,** the first quark from the $2^{nd}$ Generation of particles (see Table 1).

In the same year the "flag" of the biggest world accelerator moved from USA (AGS at Brookhaven) to Soviet Union, where 76 GeV proton synchrotron *U–70* was set in operation at Institute for High Energy Physics in Protvino near Serpukhov, in 100 km to south from Moscow. It kept the energy record until 1971 and brought many remarkable results including so called **"Serpukhov effect"** — an increase with energy of total cross-section of strong interaction.

The operation of the biggest linear accelerator at SLAC in 1967–69 gave very important effect in studies of deep inelastic scattering of electrons on protons, interpreted as an existence inside of proton of pointlike scattering centres, which were called by R. Feynmann **"partons"** (from the world "part").

Soon the idea of **u** and **d–quarks** forming nucleons appeared. The 1967th was also the birth year of the theory of **electroweak interaction,** constructed mainly by A. Salam and S. Weinberg.

# 8 The Fruitful 70ties

1971 — the first *hadron collider* is set in operation at CERN: *Intersecting Storage Rings (ISR)*, where two proton beams collide at energy 25 GeV per particle. 1972 — the "Flag" returns to USA, when *Main Ring*, the proton synchrotron at Fermilab, reaches its project energy of 500 GeV. One should name here the leader of the project and the founder of Fermilab — a distinguished accelerator physicist R. Wilson. Four years later, in 1976, CERN draws near this mark, setting in operation *"Super Proton Synchrotron" (SPS)* with particle energy of 400 GeV.

1973 — the top point competition between "fixed targetry accelerators" and colliders: two groups leaded by S. Ting at Brookhaven and B. Richter at SLAC discovered an unexpected particle — **J/Ψ meson.** The first group used proton beam from *AGS,* the second one — $e^+e^-$–collider *SPEAR* (see Fig. 1). The double title of the new particle corresponds to the double authorship, and, evenmore, each letter in it repeats the forms of the particle tracks recorded by detectors of each experiment: the first one dealt with extracted beam, where reaction products fly mainly forward, and the second one used colliding beams, where the centre mass reference frame coincides with the laboratory one.

This discovery was remarkable by several reasons. First of all, it was a "pure experimental fact", which was not predicted by the theory. Then, cross–section of $J/\Psi$ generation was by a few orders of magnitude larger of that one corresponding to $e^+e^-$ scattering. And at last this particle, as it was realised immediately, consists of two new, unknown before, quarks called the "charm" ones, or **c–quark.** So, the **second quark of the 2nd Generation** was discovered.

Two years later, in 1975, the group of M.L. Perl at SLAC discovered the first member of the **3d Generation** of particles — **$\tau$–lepton**, the analog of electron from $1^{st}$ generation and muon from the $2^{nd}$ one. It was observed in reaction

$$e^+ + e^- \Longrightarrow \tau^+ + \tau^-$$

with $e^+e^-$ colliding beams in *SPEAR.*

Two years more and one more remarkable discovery: L. Lederman with colleguaes at Fermilab have found in $pp$–collisions on fixed target the appearence of another new particle — **Y–meson**, consisting of **b–quark** ($b\bar{b}$). It was the next step in exploration of the $2^d$ Generation.

# 9 The Proof of The Standard Model (1983–1996)

To the beginning of the eighties the successful development of the particle physics theory including QED, QCD, electro-weak interaction etc. has formed finally so called "Standard Model" (Table 1) which corresponds in the particle physics to the Periodic Mendeleev Table of chemical elements in atomic physics and chemistry. One needed "only" to fill in two windows — of the **top–quark (t)** and of the carriers of the weak interaction, so called **intermediate vector bosons**. One believed also that existence of **gluon** was proved by many experimental facts from strong interaction reactions.The problem was, as often, very high energy of particles to be used for generation of these "members" of the table. The only candidate for such a high collision energy level, of order of 200 GeV, could be at that time a *proton–antiproton collider*. This idea was under discussion since Budker proposal of the electron cooling method in 1966 and its realization at INP in 1974.Then the first project of $\bar{p}p$*–collider* was developed in Novosibirsk. Later the idea of $\bar{p}p$–collider based on SPS (CERN) as a storage ring was suggested by D.Cline, P.McIntyre and C.Rubbia. It was accepted officially and realized in 1983. The critical point of the project was the use of *stochastic cooling* for storing of antiprotons. Two groups leaded by C. Rubbia and Dariuallat provided the detector part. The first group succeeded in discovery of long awaited $\mathbf{W^{\pm}}$ and $\mathbf{Z^0}$–bosons (see Table 2).

During 1976–1986 years a significant progress was achieved in studies of particle physics at $e^+e^-$– colliders. Among them one can point out the precise measurements of masses of so called **"quarkoniums"** — $\phi$, j and Y–mesons, performed at Novosibirsk INP at VEPP2M and VEPP4 using a special technique of resonant depolarization of the circulating beams.
1989 — the second $\bar{p}p$–collider, named *"Tevatron"*, 2×0.9 TeV energy, was set in operation at Fermilab. And again the stochastic cooling was a key point of the project.
1992 — the project of the *Large Electron–Positron collider (LEP)* was realized at CERN (see Fig.1). Having particle energy upto 50 GeV the LEP collider was dedicated to precise studies of physics related to $Z^0$-boson (the mass of 91.2 GeV).

In 1996 the particle energy in the LEP collider was almost doubled, 2×85 GeV. Thus, the *LEP2* collider became able to generate in $e^+e^-$ – collisions the $W^{\pm}$ pairs. Correspondingly, the physics related to the charged carriers of electroweak interaction became accessible.

And the last step in the proof of the Standard Model was made also

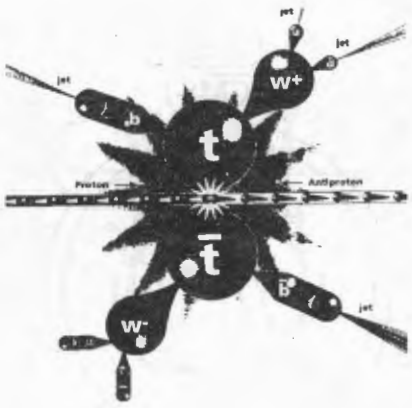


Figure 2: The chematics of the reaction of top–quark generation: $\bar{p}p \rightarrow t,\ \bar{t} \rightarrow$ cascade of particle.

in 1996, when the discovery of (also long awaited) "top", or **t-quark** was announced officially at Fermilab after several months analysis of data taken from $\bar{p}p$–collisions in Tevatron (Fig. 2)

# 10 Which Accelerators We Have and Which Ones We Need

The first part of this question is well defined.

One can give a rough classification of the existing accelerators being used in particle physics. They can be divided in 6 groups, which have rather diffuse borders (Table 2).

*10.1. Big Proton Accelerators* like SPS, Main Ring, and U–70. They are used presently as sources of extracted proton beam at energy of several tens or hundreds GeV and/or injectors (boosters) for colliders.

*10.2. Hadron Colliders.* Only facility of this type existing now is the "Tevatron" at Fermilab.The Large Hardron Collider ( *LHC* ) at CERN will be assembled to 2005 year in the tunnel of 27 km length occupied presently by LEP2 collider. LHC is double ring *pp*-collider with four intersections–collision points (Fig. 3) and its project energy is 7 TeV per particle (Ta-

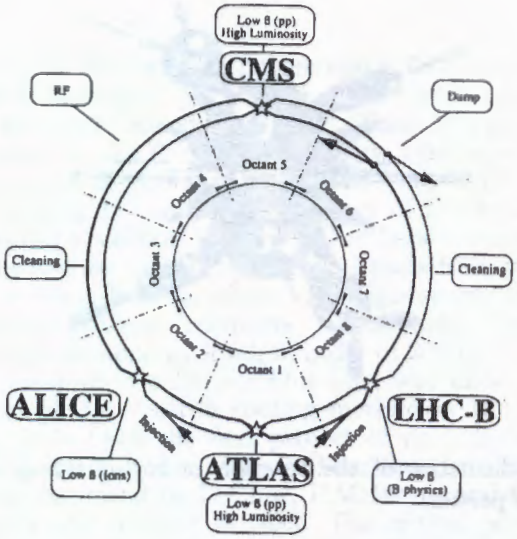


Figure 3: Chematics layout of the LHC. The collision points in the middle of the regionsof low beta–function values are indicated by stars. The detectors are planned to be placed in these points.

ble 2). The second stage of the project is the beams of lead nuclei $^{208}Pb^{82+}$ (completely stripped lend ions) at energy of 4 TeV per nucleon.

*10.3 Lepton Colliders.* Nowadays the family of *circular* $e^+e^-$ *– colliders* is very numerous. They cover a wide energy range providing rather light luminosity (Fig.1, Table 2). In the nearest future one expects the construction of such collider of new generation, so called $\phi$, C$\tau$, and b–factories with luminosity of order of $10^{34} cm^{-2} \cdot s^{-1}$. The next step will be construction of first *linear* $e^+e^-$*–colliders* (Fig. 4). The concept of such a collider was formulated in the middle of the seventies by V. Balakin and G. Budker at INP Novosibirsk. Main goal of linear colliders use is to avoid particle energy limitation in circular colliders related to strong dependence of particle energy loss with particle energy due to synchrotron radiation (SR): proportional to $E^4/R$, where E is the particle energy, R — curvature radius of the particle trajectory. Namely SR limits particle energy in LEP2, for instance. Since that time the development of the concept had

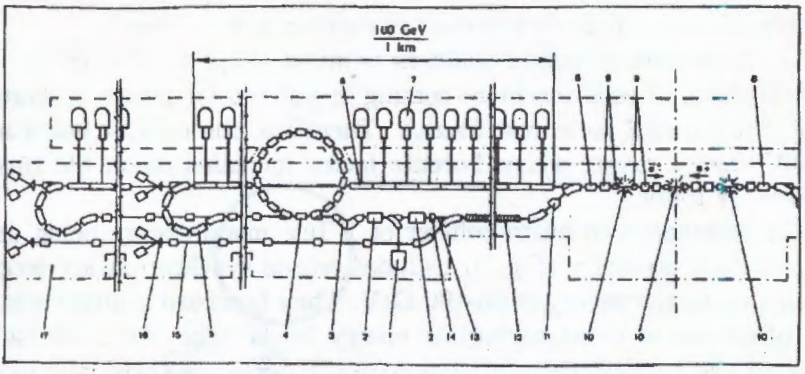


Figure 4: The general lay–out of the VLEPP facility: 1–initial injector; 2–intermedeiate accelerator; 3–debuncher–monochromatizer; 4–storage ring; 5–buncher; 6–accelerating sections; 7–RF–generator; 8–pulse detector; 9–focusing lenses; 10–collision points; 11–spectrometr; 12–helical ondulator; 13–the beam of $\gamma$–quanta; 14–conversion target; 15–residal electron·(positron) beam; 16–electron (positron) beam experiments; 17–the second stage.

a significant progress. However, the realization of any project of linear collider requires to solve two main problems — high acceleration rate and high luminosity average in time. A solution of the first problem is supposed to be solved by two different approaches: pulsed RF system with copper cavities where superhigh strength of the accelerating electric field, up to 100 MV/m in average (35 MV/m is the level reached today), and another one — superconducting cavities, where the field strength achieved now is of about the same of magnitude. Correspondingly, the collider length is of order of 2×10 km at particle energy 250 GeV chosen for first projects (Table 3). The solution of the second problem requires to form very intense $e^+e^-$ beam with emittances of order of 10 $\pi$ nm. To obtain such beam parameters special methods are used: cooling via synchrotron radiation in a storage ring, as shown on Fig. 4, beam formation as a short bunch, strong focusing in collision point etc.

As future development of $e^+e^-$– colliders the idea of *photon ($\gamma\gamma$) colliders* was proposed [1]. One suggests to generate photons of high energy and in sharply directed streams in collision of electrons and positrons with laser beam in $e^+e^-$– colliders. This hard roentgen radiation of high inten-

sity and density provides suffisient luminosity of the photon colliders. *The electron–photon collider* is a variant of independent interest.

The next kind of lepton colliders is *muon ($\mu^+\mu^-$) colliders* [2]. The main problem of such machines coming in not too far future is short life time of muon (2.2 $\mu$s in rest frame). Therefore, the collider has a sense in TeV energy range, where Lorentz–factor increases muon life time in Laboratory frame.

The schematics of muon collider of 1 TeV muon energy being under consideration presently (Fig. 5) includes proton synchrotron accelerating protons up to the energy of 30-100 GeV. They bombard a target and the part of generated pions having the energy in the rage of 0.1-100 GeV is collected and transmitted into pion–to–muon decay channels. Muons generated in pion decays undergo *ionization cooling* passing through a gaseous or solid targets and accelerate and enter into collider ring. Special technique permits (hopefully) to select the muons of certain polarization — parallel or antiparallel to the muon momentum [2].

*10.4. Intermediate energy accelerators.* It is agreed recently by the particle physicists community that the *high energy accelerators* are those which able to generate charm quarks ($J/\Psi$). It means the particle energy available with these accelerators is above 1.5 GeV for lepton and hadron colliders and 11.2 GeV for proton accelerators operating with extracted beams and fixed target ($pp$–collisions). Correspondingly, *intermediate energy accelerators* have to have the capability of producing of the particles with mass from pions up to $\eta$–meson. The energy borders are certainly very conventional. Nevertheless, the physics which can be studied with these accelerators is rich and important.

One can classify four categories among accelerators of this group:
1) proton synchrocyclotrons and synchrotrons, like "Phasotron" and "Synchrophasotron" (JINR, Dubna), "Saturne" (Sacley) and others;
2) linear proton and electron accelerators, like LAMPF (Los–Alamos), proton linac at INR of RAS, Troitsk, electron linac at Kharkov;
3) "coolers"— proton and ion storage rings with electron cooling [3]— COSY (Juelich), SELSIUS (Uppsala), IUCF (Bloomington);
4) $e^+e^-$– colliders — VEPP2M (Novosibirsk), DAΦNE (Frascati) and others (Fig. 1)

Very important requirement to the beams generated by these accelerator is particle *polarization*. From this point of view the most distinguished hadron accelerators today are the "old" 10 GeV "Synchrophasotron" at

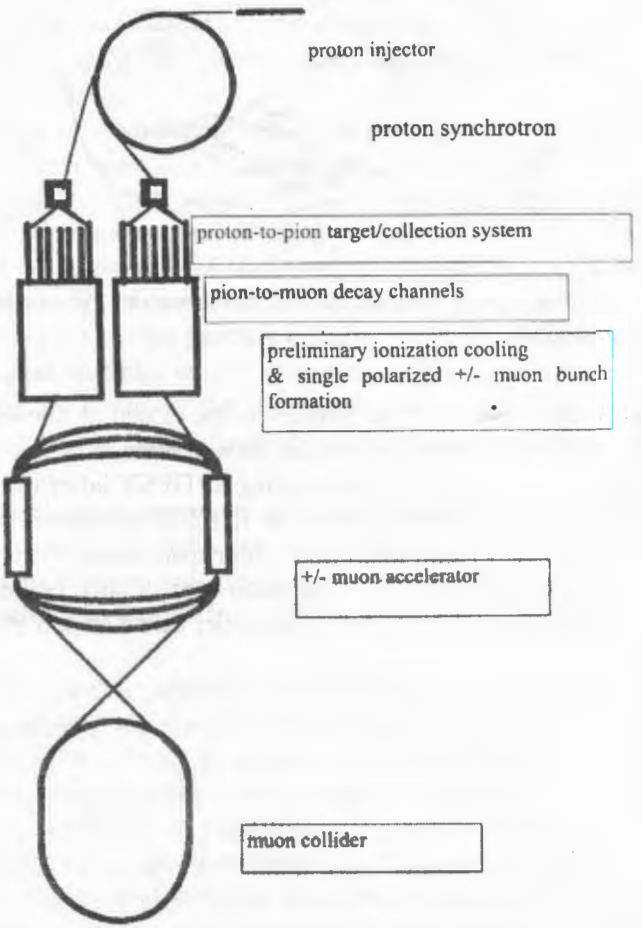


Figure 5: The chematics of muon collider complex.

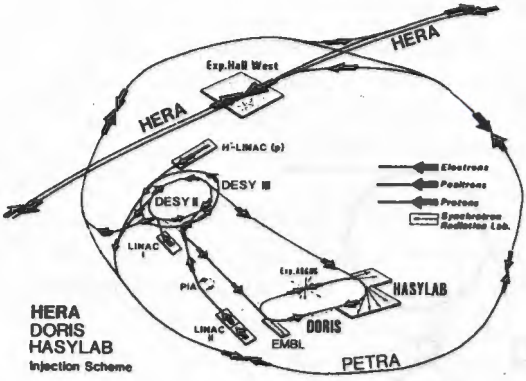


Figure 6: The accelerator complex of DESY laboratory (the collider HERA is shown only partially).

Dubna and 3 GeV "Saturne" at Saclay (to be closed at the end of 1997).

*10.5 Electron–ion colliders* is rather new tendency in particle and nuclear physics, and the first one is operating at DESY laboratory (Fig. 1,7). Under realization is MUSES project of RIKEN laboratory in Japan [4] (2.5 GeV $e^- \times$ 3.5 GeV/amu ions) and under discussion is the next project of i–e collider in GSI and DESY. The main idea of such colliders is to use "pencil" electron beam for studying of nuclei and nucleon structure at a quark–gluon level.

*10.6 Generators of exotic beams* are considered to mean an accelerator or an accelerator complex, which allows to produce quasiatomic systems consisting of artificially created and electromagnetically bound particles, for instance protonium ($\bar{p}p$), muony ($\mu^+e^-$), antihydrogen ($\bar{p}e^+$), positronium ($e^+e^-$), hadronic atoms and so on. One can use different accelerators for generation of such "atoms". So, under realization at CERN presently the project of "Antiproton Decelerator" [5] is dedicated to generation and studies of antihydrogen and "antiprotonic helium" (*He* atoms where one electron is replaced by antiproton)

To answer the second part of the question posed in title of the section 10 that need to determine the goals of future studies — the nearest ones and the far ones. Very roughly one can point out at least 10 problems of different significance, of course, which attract an attention of physicists

today (Table 2).

1) The completion of the Standard Model with discovery of **Higgs–particles**. They are "responsible" for virtual breaking of electroweak symmetry and particle mass appearance. The latest results of the Standard Model show that the most likely place to find the Higgs is at 150 GeV. An obvious question can be posed: why the Higgs–particle *was not* found in Tevatron experiments, where t–quark of mass of 176 GeV *has been* discovered? It seems reasonable to say that the problem lies not only in the colliding particle energy.

It is pertinent to note the difference between lepton and hadron colliding beams. By the modern ideas, the first one are the "pointlike–particles" and, as a consequence, full particle energy in $e^+e^-$–collisions, for instance, can be converted in generation of another particles. The nucleon is a different matter — it consists of three quarks and gluons (at least, three). Therefore, the energy of quark–antiquark interaction in $\bar{p}p$–collisions does not exceed 1/6 part of the particle energy. However, the summary mass of new generated particles can be somewhat higher due to collective phenomena — see, for instance, the top–quark case.

The candidates for Higgs discovery are Tevatron (as before), LHC and $e^+e^-$ linear colliders.

2) **Quark–gluon plasma**, as one might expect, will be created and observed in collisions of relativistic ions (RHIC, LHC in lead ion collision mode). The first hints of this phenomena can be obtained in fixed target experiments with ions beams from SPS at CERN and (may be) Nuclotron at JINR.

3) **Quarkoniums** — the mesons consisting of "pure" pair of certain quark and its antiquark (no mixture of another quark–antiquark pairs), are of great interest for further development of the Standard Model. These studies are and will be performed mainly on colliders (Table 2). Very intriguing here is the task of **toponiun** ($\bar{t}t$–meson) search.

4) "Old particle" — **pion** remains the very attractive object and tool for studies of strong interaction at nucleon (overquarkial) level. For this reason the proton accelerators, especially of high intensity, like LAMPF or synchrocyclotron at PSI, are exploited actively.

5) **Nucleon spin** nature is a puzzle of modern particle physics: recent experiments at HERA collider demonstrated, that nucleon spin is not equal to the sum of spins of quarks forming the nucleon. There are several hypotheses, however all they need further experimental investigations.

6) Similar "puzzling" situation takes place with **proton (nucleon) strangeness**. So called effect of "Okuba–Zweig–Izuka (OZI) rule violation" discovered in experiments on $\bar{p}p$ interaction at LEAR CERN, has demonstrated, that these particles, which do not contain s ("strange") quark are capable to generate in their collisions much greater number of $\varphi$ - mesons ($\bar{s}s$) than predicted by theory. By present understanding this effect does not contradict to the Standard Model, however it proves more complicated structure of nucleon, containing some "cloud" of virtual quarks and antiquarks.

7) **Neutrino** experiments are a traditional field of activity in particle physics, and directed and well controlled fluxes of fast neutrinos generated with proton beams at accelerators are used in experimental studies of weak interaction. Extension of these experiments in the area of ultra – high energy (LHC) is very important.

8) $\tau$**–lepton** — the heaviest "quasielectron" particle belonging to the $3^d$ Generation (Table 1) is not so well studied, and a possibility of $\tau$–lepton generation in directed fluxes appears with creation of asymmetric $e^+e^-$–colliders, like VEPP5, KEKB and BCTF (Fig. 1). Thus, new quality of experiments on electroweak interaction studies with $\tau$–leptons can be obtained.

9) The problems of **symmetries violation** is among most basic ones in particle physics since 1956 (see above). And this wide area requires an involvement of all the accelerator "bouquet", to generate very different kinds of particles and quasiatomic systems, mentioned in section 10.6. And first phenomenon should be pointed out is famous particle–antiparticle oscillations (see Sec.5). It is expected (B. Pontecorvo, 1957), that such a phenomenon takes place also with neutrinos ($\nu \leftrightarrow \tilde{\nu}$, $\nu_e \leftrightarrow \nu_\mu$), neutrons ($n \leftrightarrow \tilde{n}$), muony ($e^-\mu^+ \leftrightarrow e^+\mu^-$) and others. These oscillations appearence means nonconservation of certain quantum numbers, for instance, the lepton charge in $\nu$ and muony–oscillations.

Most fundamental principle — CPT theorem can be tested with antihydrogen atoms in high precision spectroscopy experiments [5,6].

10) And an eternal problem of the researcher — "what is beyond the horizon of existing knowledge", requires settings up of experiments on a search of new particles, test of the sypersymetries models etc.

Some of the experimental problems listed above lie in the frames of the Standard Model and provide additional insights into it, some give hints of its violation. However, radically new knowledge can be obtained above

all with further increase of particle collision energy. Therefore, the development of accelerator technique, elaboration of new principles of particle accelerations remain always a challenging goal for accelerator physicists.

The very first step in this direction, "beyond the horizon" will be done apparently with coming generation of lepton and hadron colliders (Sec. 10.2 and 10.3).

Nevertheless, any success at this stage should not decrease the level of activity on elaboration of new *acceleration methods*. And here we are pinning the main hopes on the *plasma accelerators* of new principle, which is as follows. A beam of a laser radiation or of low energy particles excites in a plasma, preliminary prepared and confined in a magnetic field, travelling or standing waves, which create an electric field of very high strength. This field can be used for particle acceleration. The level of the acceleration rate achieved today in laboratory experiments lies in the range of 20 MeV/m–5 GeV/m depending on the length of the acceleration section (Sec. [7] and References there).

# Conclusion

The centennial jubilee of the electron discovery is a good reason for examination of the status–quo of high energy physics. And this examination demonstrates a remarkable progress in this field of knowledge. A further development of the experimental studies here requires an increase in accelerators energy. And, despite the fact that conventional methods of accelerator technique are close to the practical limit of their potentialities, the new methods coming soon promise a further progress.

# References

1. V.Telnov, Nucl. Instr. And Meth., A355 (1995) 3.
2. A.Skrinsky, Nucl. Instr. And Meth., A391 (1997) 188.
3. I.Meshkov, Fiz. Elem. Chastits At. Yadra, 25 (1994) 1487; Phys. Part. Nucl. , 25.
4. Collected Papers on the RIKEN RI Beam Factory Project, RIKEN, August 1996.
5. http//:www.cern.ch; http//:www.cern.ch/anthena

6. I.Meshkov, Fiz. Elem. Chastits At. Yadra, 28 (1997) 495; Phys. Part. Nucl. 28 (1997) 198.
7. A.Ogata, Beam Dynamics Newsletter 12 (1996) 34.

Table 2: Which accelerators we have and which one we need

| Physics Problem | Type of accelerator | Collision energy | Facility | | |
|---|---|---|---|---|---|
| | | | Existing | Constructing | R and D |
| 1.Higgs particle | Hadron colliders | $\geq$ 0.9 TeV | Tevatron | LHC | Linear colliders |
| 2.Quark-gluon colliders | Hadron Accelerators and colliders | > 5 GeV/amu | SPS CERN, Nuclotron JINR (?) | LHC, RHIC | ion-ion colliders |
| 3.Quarkoniums | $e^-e^-$, $\bar{p}p$ and $pp$ colliders | 0.6-12 GeV | VEPP2M, BERC, VEPP4M, CESR, Tevatron | KEKB, VEPP5, LHC, DA$\Phi$NE | BCTF |
| 4.Physics with $\pi$ions | Proton accelerators | > 0.3 GeV | PSI, INR RAS, LAMPF, TRISTAN(?) Phasotron, Sinchrophasotron JINR | | |
| 5.Nucleon spin | e-p and p-p colliders | > 100 GeV | HERA | LHC | |
| 6.Proton Strangeness | proton coolers, antiproton generators | > 2 GeV | COSY, CELSIUS U-70 | AD CERN | |
| 7.Neutrino physics (proton extracted beam) | proton accelerators | > 15 GeV | U-70, SPS, Tevatron | LHC | |
| 8.Symmetries: CP-violation physics; CPT-theorem | Colliders, proton accelerators Antiproton generators | > 1 GeV | | LHC-B, HERA-B AD CERN | $\phi$, C$\tau$ and $b$ factories Antihydrogen generators |
| 9.Supersymmetries and search for "new particle" | Lepton and hadron colliders | $e^-e^-$ $E$ > 500 GeV pp $E$ > 10 TeV | | LHC | Linear colliders Photon colliders |

Table 3: The Linear Colliders (Project Parameters)

| Laboratory | DESY | | KEK | | | SLAC | BINP | CERN |
|---|---|---|---|---|---|---|---|---|
| Project | TESLA | SBLC | JLC(S) | JLC(C) | JLC(X) | NLC | VLEPP | CLIC |
| Energy (GeV) | 500 (2×250) | | | | | | | |
| Luminosity ($10^{33} cm^{-2} s^{-1}$) | 6.0 | 5.3 | 4.6 | 6.1 | 5.1 | 5.5 | 9.3 | 6.4 |
| RF frequency of main linac (GHz) | 1.3 | 3 | 2.8 | 5.7 | 11.4 | 11.4 | 14 | 30 |
| Beam Power (MW) | 8.2 | 7.25 | 1.3 | 3.2 | 3.67 | 4.8 | 2.4 | 4.5 |
| Damping ring energy (GeV) | 3.2 | 3.15 | 2 | 2 | 1.98 | 2 | 3 | 2.15 |
| Two-linak length (km) | 29 | 33 | 22.1 | 18.8 | 10.5 | 17.6 | 7 | 7.5 |

# The Antihydrogen and Positronium Problem in Particle Physics

I.N. Meshkov

*Joint Institute for Nuclear Research, Dubna*

**Abstract**

The importance of experimental studies of antihydrogen and positronium extremely high precision reletes to the fundamental problems of matter properties – its symmetry (CPT theorem) and nature of basic interactions (quantum electrodynamics).

Generation of antihydrogen and positronium atoms "in-flight", especialy in a form of rather intense and well directed streams, opens new advantages for experiment performance discussed in this report.

## 1 Introduction

The physics of antihydrogen is of great interest from the viewpoint of understanding the fundamental properties of matter, and, in particular, its symmetry properties. A specific problem which was suggested by the authors of the first studies on antihydrogen production [1], [2] is that of veryfying the CPT theorem. This has become quite feasible since the first synthesis of antihydrogen atoms in December 1995 at the LEAR antiproton ring at CERN [3]. Alhough this experiment was essentially just a demonstration, it can now be claimed that antihydrogen exists as a physics object.

Currently, there are two quite different approaches in antihydrogen physics. The first is the production of antihydrogen atoms one by one in antiproton and antipositron traps at ultralow energies, followed by confinement of the atoms in magnetic traps with the minimum magnetic field and cooling down to a temperature of order 1 K by means of laser radiation [4].

The second approach is the use of anriproton and positron storage rings [1], [2]. A variant of this idea suggested recently [5] would allow the production of intense pencil beams of 30–3 $\times$ $10^4$ antihydrogen atoms per second with velocities in the range 0.03–0.3 times the speed of light, respectively (antiproton energies of 0.5–50 MeV). This setup would simultaneously produce pencil beams of orthopositronium (30–1.7 $\times$ $10^4$ $sec^{-1}$), which are of independent interest as an object of study.

The purpose of the present report is to discribe the possibilities offered by experiments using of antihydrogen and positronium.

# 2 Problems in the physics of antihydrogen and positronium

## 2.1 Antihydrogen and CPT invariance

The principle of CPT invariance (CPT theorem) can be verified by comparing particle and antiparticle parameters: their masses, absolute values of electric charges and magnetic moments, and gyromagnetic ratios. Of course, it is interesting to perform measurements at a level of accuracy exceeding that attained at present. The latter can be judged from the data, given in Table 1.

Although at present there is no experimental evidence calling the validity of CPT invariance into question, there is also no reason not to verify CPT invariance. In this respect, CPT invariance is just as much an axiom of modern physics as are other axioms. The high accuracy attained by inderect comparison of the masses of neutral kaons

$$\left|\frac{m\left(K^0\right)-m\left(\bar{K}^0\right)}{m(K^0)}\right| \leq 5 \cdot 10^{-19}$$

cannot serve as absolute proof of the theorem, because, in general, any particle "has the right" to be asymmetric relative to its antiparticle. Therefore, the experimental verification of the symmetry of each of the known particles is of independent importance. It is most important for the "most fundamental" particles, i.e., the proton and electron.

The use of antihydrogen atoms as a test object allows direct and highly accurate comparison of the electric charges of the antiproton and positron (See 4.1). The measurement of the hypefine structure and the Lamb shifts

TABLE I. Parameters of the fundamental particles.

| Parameter | Value | Accuracy |
|---|---|---|
| **Electron and positron** | | |
| Electron mass, MeV | 0.510 099 906(15) | $3 \cdot 10^{-7}$ |
| Mass difference $\lvert m^+ - m^- \rvert / m^-$ | $< 4 \cdot 10^{-8}$ | $< 4 \cdot 10^{-8}$ |
| Charge inequality $\lvert e^+ - e^- \rvert / e^-$ | $< 4 \cdot 10^{-8}$ | $< 4 \cdot 10^{-8}$ |
| Difference of the charge to mass ratios | $< 3 \cdot 10^{-8}$ | $1 \cdot 10^{-8}$ |
| Electron magnetic moment (in Bohr magnetons) | 1.011 159 652 193(10) | $1 \cdot 10^{-11}$ |
| Gyromagnetic ratios $\lvert g^+ - g^- \rvert / g^-$ | $(-0.5 \pm 2.1) \cdot 10^{-12}$ | $2.1 \cdot 10^{-12}$ |
| **Proton and antiproton** | | |
| Proton mass, MeV | 938.2723(28) | $3 \cdot 10^{-7}$ |
| Mass difference, $\Delta M/M$ | $< \pm 4 \cdot 10^{-8}$ | $< 4 \cdot 10^{-8}$ |
| Inequality of the proton and electron charges, $\lvert e_p - e^- \rvert / e^-$ | $< 1 \cdot 10^{-21}$ | $< 1 \cdot 10^{-21}$ |
| Inequality of the proton and antiproton charges, $\lvert e_p - e_a \rvert / e_p$ | $< 2 \cdot 10^{-5}$ | $< 2 \cdot 10^{-5}$ |
| Inequality of the proton and antiproton charge-to-mass ratios | $< 1.5 \cdot 10^{-9}$ | $< 1.1 \cdot 10^{-9}$ |
| Proton magnetic moment (in nuclear magnetons) | 2.792 847 39(6) | $2 \cdot 10^{-8}$ |
| Antiproton magnetic moment (in nuclear magnetons) | −2.8005(90) | $3 \cdot 10^{-3}$ |

of the optical spectrum of antihydrogen is just as interesting. As is well known, the hyperfine splitting of levels is proportional to a combination of fundamental constants

$$\Delta\omega_{HFS} \propto \mu_p \mu_e (e_p e)^3,$$

where $\mu_p$ and $\mu_e$ are the proton (antiproton) and electron (positron) electric charges. Since the parameter known at present with least accuracy is $\mu_p$ (while for the antiproton this has not been measured at all), a precise measurement of $\Delta\omega_{HFS}$ would first of all allow the determination of the

magnetic moment – both its absolute value and, with much higher accuracy, the relative difference between the proton and antiproton magnetic moments.

The Lamb shift is proportional to

$$\Delta\omega_L \propto me^6e_p^4$$

where $m$ is the electron (positron) mass. Therefore, measuremenr of $\Delta\omega_L$ gives information about the value of three fundamental constants [in the combination (1.3)] for particles and antiparticles.

Of couse, the precise determination of $\Delta\omega_{HFS}$ and $\Delta\omega_L$ is important not only because it provides more accurate knowledge of the antiproton and positron parameters. If these values were found for differ for atoms and antiatoms, this would in itself be an indication of symmetry breaking in the fundamental interactions. In particular, the Lamb shift, which is calculated in quantum electrodynamics including radiative corrections, a parameter of the atomic spectrum-measured with a high degree of accuracy. Accordingly, by comparing its value for hydrogen and antihydrogen it becomes possible to judge the symmetry of the interactions.

## 2.2 Positronium and QED

Positronium, being a very simple quantum system, has been described quite well theoretically and perhaps plays the same role in quantum electrodynamics as the hydrogen atom in nonrelativistic quantum mechanics. Experiments involving positronium, which so far have been carried out under rather complicated conditions in which it is not easy to isolate the effect of the target, have, as a rule, produced rather inaccurate results, and even results which in some cases are ambiguous [6], [7]. A precise measurement of the positronium parameters is therefore of great interest.

Among experiments of this type are the following:

– the measurement of the *orthopositronium lifetime and the parapositronium lifetime;*

– *the positronium spectrum;*

– the search for orthopositronium annihilation with violation of momentum conservation and charge invariance:

$$\text{o-Ps} \rightarrow 2n\gamma,$$

where $n$ is an integer;

– the search for exotic and rare decay channels of parapositronium:

$$\text{p-Ps} \rightarrow n\gamma, \quad n > 2;$$

– search for a light, neutral, short-lived boson, via which o-Ps annihilation can occur

$$\begin{array}{c} \text{o-Ps} \rightarrow b + \gamma; \\ \downarrow \\ 2\gamma \end{array}$$

– Perhaps, the most intriguing problem in positronium physics is the search for the *"mirror world"* (see Section 5.4).

# 3 Antihydrogen production

## 3.1 The first experiment producing antihydrogen

In the experiment [3] performed at the LEAR antiproton storage ring at CERN, a circulating antiproton beam of energy 1.2 GeV (momentum 1.94 GeV/c) interacted with the xenon atoms of an internal cluster (jet) target. The target thickness reached $3 \times 10^{13} atoms/cm^2$, and the intensity of the antiproton beam was $1.7 \times 10^{10}$ particles for a lifetime of 3 min. The integrated luminosity for September and October of 1995 was $5 \times 10^{33}(\pm 50\%) cm^{-2}$.

Atoms of antihydrogen $\left(\bar{H}^0\right)$ appeared inside the target when antiprotons interacted with xenon nuclei: an antiproton interacting with a nucleus generates an $e^+e^-$ pair (Fig. 1) and captures a positron if the momentum of the latter is close in magnitude and direction to that of the antiproton (an energy difference of less than 13.6 eV). The cross section for this process is

$$\sigma \sim 2Z^2 pb \sim 6 \cdot 10^{-33} cm^2,$$

where $Z = 54$ is the atomic number of xenon. Therefore, for the given luminosity, it could be expected that 30 atoms of $\bar{H}^0$ would be obtained. The fast, neutral $\bar{H}^0$ atoms (antiproton energy equal to 1.217 GeV and positron energy equal to 0.663 MeV), which were not deflected in the magnetic field of the storage ring, traveled into the detection channel (Fig. 2). Passing through the two of three silicon counters Si (of thickness 700 $\mu$ m,

respectively), the $\bar{H}^0$ atoms lost the positron, which was stopped in one of the counters, producing a $\gamma$ pair. The third counter recorded $dE/dx$ from the remaining antiproton. The annihilation $\gamma$ pair was recorded by a cylindrical NaI calorimeter (with energy resolution 14%), which covered 91% of the entire solid angle, thereby ensuring a total efficiency of 82%.

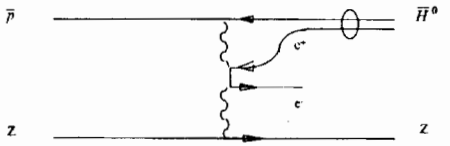


Figure 1: Graph of two-proton $e^+e^-$ production pair in the interaction of an antiproton with a nucleus and production of an antihydrogen atom.

The antiprotons appearing after the stripping of the $\bar{H}^0$ atom passed through three start scintillators Sc (each 4 mm thick) and a hodoscope H of 16 fibers ($2 \times 2 \times 32$ mm), and then a group of four stop scintillators Sc (Fig. 2). The three drift chambers D with corresponding readout delays recorded the passage of antiprotons deflected in the dipole magnetic field $B$. The needed calibrations were performed using cosmic rays.

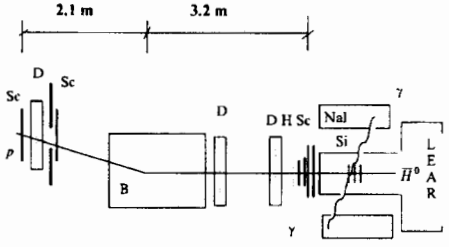


Figure 2: Scheme for antihydrogen generation: Si–three silicon counters; Sc–silicon counter-trigger and scintillators; D–proportional chambers; NaI– 6-section calorimeter; H–scintillation hodoscope; B–dipole magnet.

The experiment recorded 11 $\bar{H}^0$ atoms for a background contribution of no more than $2 \pm 1$ with 95% probability.

The main result of the experiment, namely, the proof of the "existence theorem", i.e., of the possibility of synthesizing antihydrogen atoms under terrestrial conditions, is certainly of fundamental importance.

Later, in 1996 similar experimentwas performed at Fermilab and 30 $\bar{H}^0$ atoms were recorded.

## 3.2 Antihydrogen production and storing in magnetic traps. AD and Athena project

The first experiment where physics parameters of $\bar{H}^0$ will be measured is under preparation now at CERN. After closing in Desember 1996 of the LEAR accelerator specialists and "users" of antiproton beam at CERN began to look for a chance to reactivate $\bar{p}$-source and proposed "Antiproton Decelerator" (AD) project [8]. which was approved this year. It will be new $\bar{p}$ -storage ring, assembled on the base of elements of the "old" AC ("Antiproton Collider") storage ring (Fig. 3).

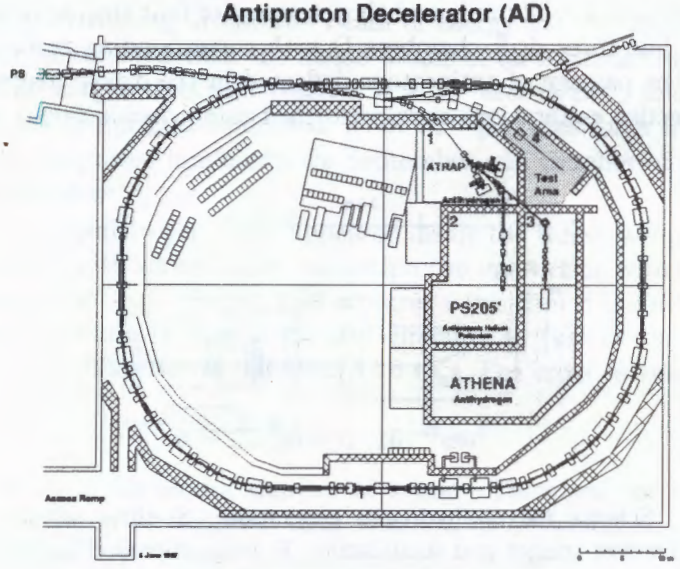


Figure 3: The Layout of AD storage ring.

AD will accumulate and decelerate antiprotons generated on existing targer system: the proton beam from Proton Synchrotron at 26 GeV/c proton momentum produces on the target $\bar{p}$-bunch, and 5 $10^7 \bar{p}'s$ with momentum 3.57 GeV/c are collected by pulsed lense (so called "magnetic horn") and injected into AD. After deceleration (in several steps) up to 100 MeV/c momentum (about 5.9 MeV kinetic energy) and cooling $\bar{p}'s$ are extracted in one or several bursts with a length ranging from 200 to 500 ns. Such a pulsed beam will be used in several experiments, and among them the ATHENA project (AnTiHydrogEN Apparatus) [9] is dedicated to antihydrogen generation and study.

ATHENA (Fig. 4) consists of several traps, where $\bar{p}'s$ and $e^+$ are to be stored, cooled down and recombined to form $\bar{H}^0$-atoms. Antiprotons and positrons meet and recombine in the Central (Recombination) Trap (Fig. 4), but before they pass a long way and preparation procedure.

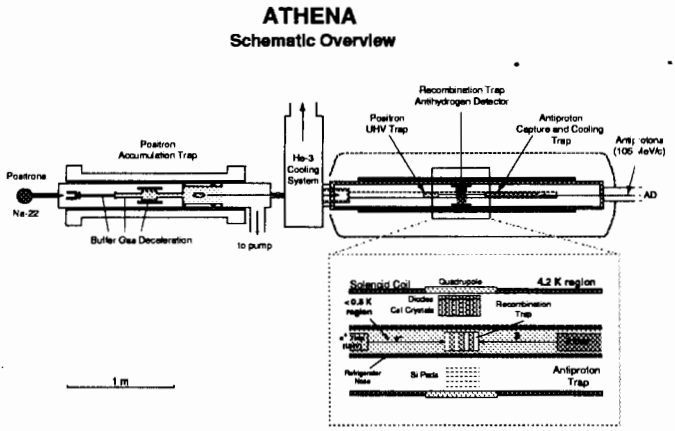


Figure 4: Athena Schematic Overview

Antiprotons extracted from AD at kinetic energy 5.88 MeV, enter the Antiproton Trap, decelerating in the Degrader due to ionization energy losses (Fig. 5, stage 1). The Trap has longitudinal magnetic field of 3 T. After bunch passing of degrader a negative potential is applied to it and $\bar{p}'s$ are trapped in the potential well, oscillating in space between Ring Electrodes of negative potential and Degrader (Fig. 5, stages 2, 3). Prelimenary an electron cloud is injected from an electron gun in the central

part of the Trap, catched in another potential well formed by additional rings, and cooled via emission of synchrotron radiation due to rotation in longitudinal magnetic field applied in parallel to the trap axis. This radiation (which actually is classic dipole radiation, or "cyclotron radiation" at low electron energy) cools electrons for characterictic time about 0.1 s at B=6 T. Penetrating the cloud of cold electrons the trapped antiprotons reduce their kinetic energy until it equilizes with the electron one. Then $\bar{p}$-bunch is transfered (by pulsing of ring potentials) into the Recombination Trap.

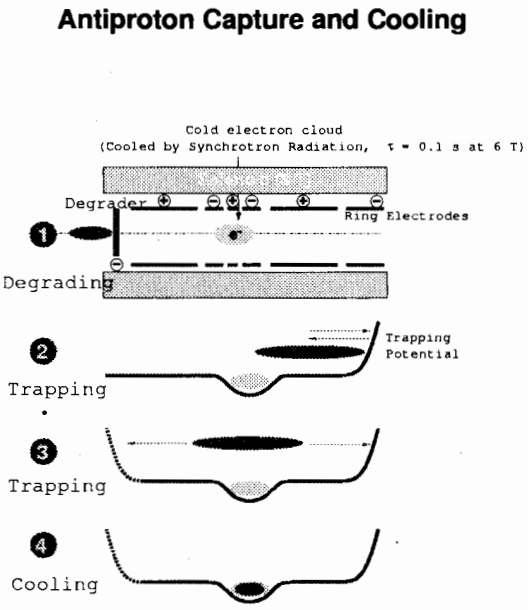


Figure 5: Antiproton Capture and Cooling

*Positrons* are generated by $Na^{22}$ radioactive source and collected in the Positron Accumulation Trap (Fig. 4), loosing their energy in collisions with Buffer Gas molecules. Such a cooling method provides low positron temperature and accumulation. After storing and cooling positron bunch is transfered through the channel with differential vacuum pumping to Positron Ultra High Vacuum Trap where several positron bunches are to

be stored to get a necessary number of positrons. Both bunches – $e^+$ and $\bar{p}$ ones – merge in the Recombination Trap, where *antihydrogen atoms* bear in $e^+ - \bar{p}$ recombination. Some ways of intensification of this process are under studying, for instance, stimulation of recombination by laser radiation.

*The Recombination Trap* has a system of current coils, which form special nonhomogenious magnetic field with minimum in the central point of the Trap – so called "Ioffe–trap". It consists of pair of ring coils, generating magnetic field of opposite direction,, and the windings of transverse quadrupole field. Antiproton atoms experience the focusing action of the field gradient and can not leave free the Trap. Thus, some certain number of $\bar{H}^0$-atoms can be stored and kept in the Trap.

The Trap walls are cryogenically cooled below 4.2 K, so ultrahigh vacuum, of the order of $10^{-12}$ Torr or better, is expected in central zone. Being thermoequilibrium with walls (via a thermoradiation) $\bar{H}^0$-atoms get the same low temperature, which brings significant gain in the precision of spectroscopic measurements.

The final goal of the experiment is "Doppler free spectroscopy" of two-photon 1S-2S transition in antihydrogen (see description in Sec. 4.4) with expected precision better than

$$\frac{\Delta\omega}{\omega} \leq 1 \cdot 10^{-12}.$$

## 3.3 Generation of antihydrogen in-flight

The idea of producing beams (fluxes) of antihydrogen atoms is closely related to the technique of electron cooling [1]. For antihydrogen ($\bar{H}^0$) generation, the antiproton source, one like the antiproton installations at CERN or Fermilab, must be provided with two storage rings. The first is used to store low-energy antiprotons ($\bar{p}$) and has a traditional system with strong focusing. The second is a positron ($e^+$)storage ring of the racetrack type with four straight sections. The storage rings are combined such that in one of the straight sections the beams pass through each other (Fig. 6). This is where the $\bar{p}$ and $e^+$ particles recombine, forming $\bar{H}^0$ atoms. Each storage ring has its own electron cooling system, allowing dense, cold beams of recombining particles to be obtained. *Positronium (Ps) production* also occurs on the section of electron cooling of positron. Its long-lived component, orthopositronium, can be extracted from the

focusing system into the detection channel, similar to the $\bar{H}^0$ atoms.

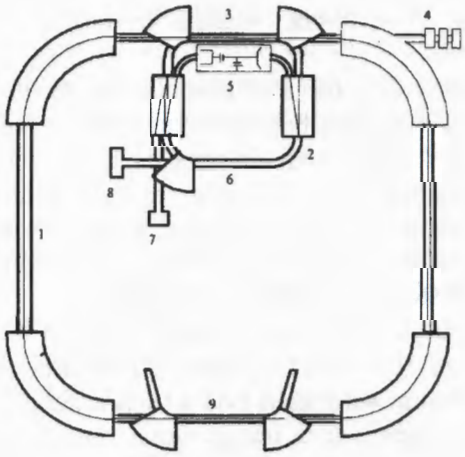


Figure 6: Scheme for generating antihydrogen and positronium: 1–antiproton storage ring; 2–positron storing ring; 3–$\bar{p}e^+$ -recombination section; 4–$\bar{H}^0$ detection channel; 5–source and collector of the electron beam; 6–section of electron cooling of positrons; 7–positron injection channel; 8–positronium detection channel; 9–system for electron cooling of antiprotons.

The proposed variant of positron storage ring [5], [10] has a special focusing system with longitudinal quasiuniform and helical quadrupole magnetic fields. A bending magnetic field consistent with the positron energy is also applied to the toroidal segments of this storage device. Such a focusing system of the "stellarator" type ensures stability of the beam of circulating electrons.

The fundamental feature of this scheme distinguishing it from those proposed earlier for low antiproton energies [1], [2] is the magnetization of the positrons, whose source is also inmersed in the longitudinal field. This complicates the injection of positron into the ring, making it necessery to use a special injection system. However, the magnetization leads to several important advantages (see details in Ref. 5)

The design with magnetized beam is only weakly sensitive to retuning of the particle energy, which suggests that it might also be applicable for stabilizing the positron beam down to very low positron energies of the

order of hundreds of eV (accordingly, antiproton energies of hundreds of keV) at rather high beam intensity. Such a storage ring is equivalent to a ring with very strong focusing, because the role of the betatron function in it is played by the Larmor helix, the period of which is of the order of several centimeters for the highest energy planned.

The electron cooling of the two beams of recombining particles, antiprotons and positrons, ensures low temperatures of each (small spread and velocity), thereby leading to a high recombination rate. Therefore, the low temperature of cooled beams makes it possible to obtain rather intense *fluxes of $\bar{H}^0$ and Ps atoms with small angular and velosity spreads.*

Positron production and storing is a special problem, and the proposed schematics allows to resolve it effectively (see Ref. 5, 10).

Table II lists the design values of the parameters of storage rings and estimates of the intensities of antihydrogen and orthopositronium fluxes made in the radiative recombination approximation.

Yet another extremely important advantage of systems with electron cooling, which follows from the quality of the average velocities of the cooling and cooled particles, is the possibility of *absolute calibration* of the $\bar{H}^0$-atom velosity (using the voltage at the cathode of the electron gun) and the possibility of smooth, controlled *tuning* of this velocity within a broad range (using the same voltage or the potential of a "suspended" cooling segment).

To obtain very slow $\bar{H}^0$-atoms the proposed scheme does not fit because, when the positrons energy is of the order of hundred eV, the life time of circulating positrons is too short (or, in other words, the vacuum conditions are nonrealistic) – about 1 s, when vacuum pressure is of order of 100 pTorr. As a result, the lowest energy of antihydrogen atoms available in such a scheme is of the order of a few hundred keV. One can avoid this problem and produce very slow antihydrogen atoms using electrostatic deceleration of the antiprotons and positrons in the recombination section [5], [10]. Several limitations do not allow to get an intense $\bar{H}^0$ flux with this scheme. However, one can hope to generate several atoms per second at energy of the order of 10 eV (see details in Ref. 6).

TABLE II. Antiproton and positron storage ring parameters.

| | | |
|---|---|---|
| Antiproton storage ring | | |
| Circumference, m | 80 | |
| Antiproton energy, MeV | 50 | 0.5 |
| Density of cooling electron beam, $A/cm^2$ | 1.0 | 0.02 |
| Electron longitudinal temperature, $\mu eV$ | 120 | 70 |
| Number of stored antiprotons | $1 \cdot 10^{11}$ | $1 \cdot 10^{9}$ |
| Antiproton current, mA | 20 | 2.0 |
| Positron storage ring | | |
| Circumference, m | 20 | |
| Positron energy, keV | 27.2 | 0.272 |
| Longitudinal magnetic field, $T$ | 0.1 | 0.05 |
| Number of stored positrons | $1 \cdot 10^{9}$ | $1 \cdot 10^{8}$ |
| Positron beam current, $\mu A$ | 800 | 80 |
| Density of cooling electron beam, $A/cm^2$ | 1.0 | 0.002 |
| Antiproton flux | | |
| Intensity, $sec^{-1}$ | $3 \cdot 10^{4}$ | 30 |
| Angular spread, $\mu rad$ | 1.1 | 8.5 |
| Velocity spread, $10^{-6}$ | 1.1 | 8.5 |
| Doppler spread, $\Delta v/c, 10^{-7}$ | 3.5 | 2.7 |
| Orthopositronium flux | | |
| Intensity, $sec^{-1}$ | $1.7 \cdot 10^{4}$ | 35 |
| Angular spread, mrad | 1.5 | 16 |
| Velocity spread, $10^{-5}$ | 5.1 | 40 |
| Doppler spread, $10^{-5}$ | 1.5 | 1.2 |

# 4 Experiments with $\bar{H}^0$ in-flight

*4.1. Direct comparison of particle electrical charges* can be produced by measuing the diplacement of the beam of atomic particles – antihydrogen, hydrogen, and positronium – emitted from the storage ring and deflected in the transverse magnetic field. It is possible to obtain an upper limit on the difference of the electric charges $\delta e$ [6], [11] at the resolution $(\delta e/e)_{\bar{H}^0} \sim$

$2 \cdot 10^{-9}$.

For positronium the value of $B_\perp$ is limited owing to interference between its ortho- and para-states accompanied by rapid annihilation of the *p-Ps* component. Nevertheless, even in fields of order 1 T we can count on $(\delta e/e)_{Ps} \sim 1 \cdot 10^{-8}$. Of course, this value decreases the present limit $4 \cdot 10^{-8}$ only insignificantly. Nevertheless, by performing an experiment of this design with antihydrogen and positronium and using the high accuracy with which the charges $e_p$ and $e^-$ coincide, it is possible to "close" (via positronium!) the chain of charges of all four particles with an accuracy of at least $10^{-8}$, i.e., to improve the inequality of $e_p$ and $e_a$ by three orders of magnitude (see Table III below). Further improvement is determined by the limit on the inequality of $e^+$ and $e^-$.

We should stress the fact that the proposed experiment gives the *difference of the electric charges* of the particles, and so it differs from the experiment of Ref. 12, where $e/m$ is measured. The results of the two experiments allow the upper limit on the inequality of $m_p$ and $m_a$ to be improved.

*4.2. Microwave spectroscopy of the 2S-2P states of antihydrogen.* The methods of radiospectroscopy and atomic interferometry developed in measurements of the hyperfine structure and the Lamb shift of the hydrogen spectrum [11]–[17] can be used in these experiments [6], [11]. These methods are based on the interference of two nearby states of an atom in an external electromagnetic field.

The first method developed in precision measurements of the hyprefine structure of the hydrogen atom [13],[14] can also be used in experiments involving an antihydrogen flux. The idea of the method is that an external perturbation can be used to excite transitions between hyperfine levels of the metastable $2^2S_{1/2}$ state (whose lifetime is 1/7 sec), and then the resonance frequency of the transition can be measured. The atoms which have undergone this transition are detected by exciting the next transition from the $2S$ state to one of the short-lived $2^2P_1/2$ states (whose lifetime is about 1.5 nsec) with the decay of this state detected using the $2P \to 1S$ transition (Fig. 7). The frequencies of $2S - 2P$ transitions lie in the centimeter wavelength region, and those of $2P \to 1S$ transitions lie in the vacuum ultraviolet (10.2 eV).

The main difference between the experiment discussed here and the pioneering one of Ref. 12 is the relativey high velocity of the atoms, $v_0$. This affects the resolution of the method, and also makes it necessary to

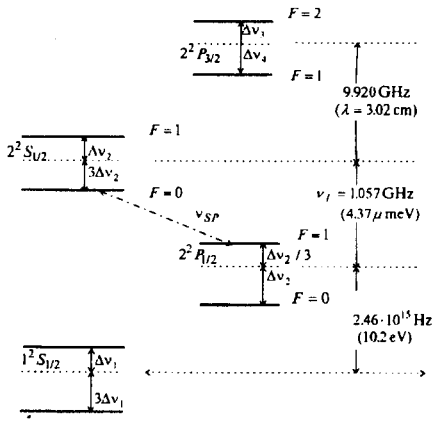


Figure 7: Structure of the low-lying levels of the hydrogen atom. $\Delta\nu_1 = 355.1014\ MHz$, $\Delta\nu_2 = \Delta\nu_1/8$, $\Delta\nu_3 = \Delta\nu_2/10$, $\Delta\nu_4 = (13/30)\Delta\nu_2$, $\nu_L$ =1057.8514(19) MHz is the Lamb shift.

take into account the Doppler frequency shift:

$$\omega_{Lab} = \frac{\omega'}{\gamma\left(1 - \beta\cos\theta\right)}, \quad \gamma = \left(1 - \beta^2\right)^{-1/2}, \quad \beta = v_0/c. \tag{1}$$

Here $\omega'$ is the frequency in the atomic rest frame and $\theta$ is the angle between the directions of the atomic velocity and the cavity axis.

The accuracy (resolution) can be improved by many orders of magnitude by using the technique of the *atomic interferometer* [13]–[15], [17].

The operating principle of such an interferometer, which was apparently first proposed in Ref. 11, is the following. Two short electromagnetic field pulses, separated in space and time by a relatively long interval $L$, are applied, where the atom moves in free space. In the radiospectroscopic version of this interferometer these pulses are generated by the electromagnetic field of two cavities $P$ and $A$ (Fig. 8) excited at the same frequency $\omega$. The first cavity $P$ induces, as before, transitions between initial "lower" $2^2S_{1/2}\,(F = 0)$ states and final "upper" $2^2S_{1/2}\,(F = 1)$ states. The phase of the wave function at the output of $C_1$ depends on the cavity length $l$ and the frequency. After passing through the free segment $L$, the atom

enters the second cavity $A$, where it again undergoes transitions between the same states. The atoms leaving the interferometer in the "upper" state undergo transitions to the $2P$ state in the cavity $C_2$ and deexcite to the $1S$ state with some probability $P(\omega)$. The photons of the UV radiation are recorded by the detectors $DET$.

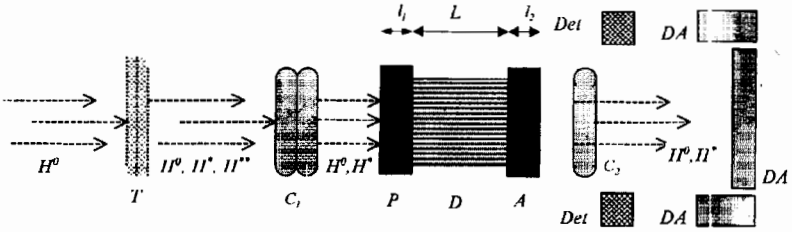


Figure 8: Scheme for an atomic interferometer: $\bar{H}^0$, $H^*$, $\bar{H}^*$ are antihydrogen atoms in the ground and excited states; $T$ is a thin target; $C_1$ and $C_2$ are cavities for purification and analysis. The interferometer:$l$ is the length of cavities $P$ and $A$; $L$ is the length of free space ($D$); $Det$ are UV-radiation detectors; $DA$ are annihilation detectors.

The accuracy of determining the transition frequency $\omega_0$ can be raised considerably if the dependence $P(\omega)$ is measured. By fitting the experimental data to the theoretical function (see Ref. 8), it is possible to raise the accuracy to nearly $\sqrt{N}$, where $N$ is the total number of experimental points.

The best accuracy is achieved in this manner in Ref. 12. The authors of that study obtained a resolution of order 50 Hz, which allows measurement of the hyperfine structure of the $2S_{1/2}$ state with an accuracy of order $\delta\omega/\omega \sim 3 \cdot 10^{-7}$. Zeeman splitting and double fitting were used for this.

Determination of the values of the hyperfine splitting of the $2S_{1/2}$ level of hydrogen and antihydrogen allows comparison of the proton and antiproton magnetic moments at a level $10^{-6} - 3 \times 10^{-7}$.

A variant of the atomic interferometer with static electric fields (the $\nu_{SP}$ transition, Fig. 7) was succesfully used in experiments [15] involving hydrogen atoms of low energy of order 20 keV. The first measurements

of the Lamb shift with a flux of fast ($v_0/c \approx 0.35$) hydrogen atoms were performed at a proton storage ring with electron cooling, NAP-M [16].

*4.3. The atomic interferometer and the Stern-Gerlach method. Spectroscopy of the 1S state.* The use of the atomic interferometer in the classical Stern-Gerlach method made it possible to perform high-precition measurements of the hyperfine structure of the ground $1^2S_{1/2}$ state of the hydrogen atom [17]. This scheme can be applied nearly without change in experiments involving antihydrogen fluxes. For this the polarizer and analyzer of the atomic interferometer must be realised as ordinary EPR spectrometers: each must consist of a dipole magnet with a uniform field $B_\perp$ directed across the beam, and a cavity in which an electromagnetic field is produced. Its magnetic component $B_g(t) = B_g \sin \omega t$ excites EPR transitions. In addition, a sorting system composed of two gradient magnets, one before and one after the analyzer, is provided. The magnets separate atoms with different polarization (the Stern-Gerlach method), and guide atoms in a given state to the detector. The transition from one state to another is accompanied by change of the polarization, as a result of which the atom is sent to the detector by the second sorting magnet. In the current version, the gradient sorting magnets are made in the form of sextupoles as, for example, in the hydrogen maser – the time standard.

It can be hoped that this method will allow the Doppler-broadening limit (see Table III) to be exceeded by an order of magnitude, giving $\delta\omega/\omega_0 \leq 3 \cdot 10^{-8}$. Knowledge of the frequency of transitions between hyperfine levels of the ground state makes it possible to determine the value of the antiproton magnetic moment which for this accuracy gives $\Delta\mu_a/\mu_a \sim 2 \times 10^{-5}$. Higher accuracy can be obtained by comparing the values of the hyperfine splitting $\Delta$ for $H^0$ and $\bar{H}^0$. It allows the difference between $\mu_p$ and $\mu_a$ to be found with an accuracy of at least $1 \times 10^{-7}$.

*4.4. The laser spectroscopy of fast antihydrogen atoms,* in spite of the low intensity of the atomic fluxes, does not seem hopeless, and is of great interest. In working with a directed flux of fast atoms, by using a laser opposing the flux it is possible to raise the proton energy in the frame of the atom by way of the Doppler shift (1):

$$\omega' = \gamma\,(1+\beta)\,\omega_{Lab}. \tag{2}$$

This means helps to compensate for the limitations in the choice of available lasers, and, as noted in Sec. 3.3, it also ensures *smooth tuning of the proton energy* in the frame of the atom, by changing the energy of

the cooling electrons and, accordingly, the atomic velocity. This method, fairly simple and routine in the electron cooling, eliminates the necessity of using low-power dye lasers, which are commonly used in spectroscopy to vary the wavelength of the radiation.

*The 1S-2S two-proton transition* is interesting because the small width of the metastable $2S_{1/2}$ level (a lifetime of 1/7 sec), which makes it possible, in principle, to measure the transition frequency with an accuracy

$$\frac{\delta\omega}{\omega} \leq \frac{\Gamma}{\omega} \sim 10^{-17}.$$

The possibility of a 1S-2S two-photon transition in the scattering of an opposing laser beam on a flux of hydrogen atoms has been discussed since first proposals on antihydrogen [2]. However, only in the version discussed in the present study it actually becomes feasible to perform such an experiment [6], [11]. As estimations show, the count rate at the length of the bombardment segment of 5 m, laser power density $d^2P/dSdf \sim 100W \cdot cm^{-2} \cdot sec$, atomic flux of order of $3 \times 10^4 s^{-1}$, $\beta = 0.64$ is about 30 per sec.

The experiment can be set up as follows (Fig. 9). By means of a refracting cone, an axicon, laser light is directed counter to a beam of $\bar{H}^0$ atoms. The axicon has a hole at its center. Atoms excited by the radiation arrive at the cavities $C$ tuned to the frequencies of 2S-2P transitions. After undergoing a transition to a short-lived $2P$ state, the atoms deexcite, and the rest of the procedure for detecting them is, in principle, analogous to that described in Sec. 4.2: the photons of $2P - 1S$ transitions are recorded in coincidence (with time-of-flight selection) with signals from the detectors of the annihilation and ionization chambers. Therefore, the *integrated flux* of UV photons is recorded as a function of the velocity of the $\bar{H}^0$ atoms. The background of scattered laser radiation can be lowered significantly owing to the same Doppler shift (1): the photon wavelength and flux of UV photons depend on the direction of the emission in the laboratory frame ( the angle $\theta$ on Fig. 9 and in Formula (1)). Therefore, in the laboratory frame the wavelength of the atomic radiation is shorter that of the laser radiation; they are comparable only for photons scattered strictly backward. The atomic radiation is primarily directed forward. The photon flux $\dot{N}^*$ in the forward hemisphere is

$$\frac{d\dot{N}_\gamma}{d\omega} = \frac{\dot{N}^*}{\gamma^2 (1 - \beta\cos\theta)^2}, \quad \Delta\dot{N}_\gamma = \frac{1+\beta}{2}\dot{N}^*, \quad if \quad \theta \leq \pi/2.$$

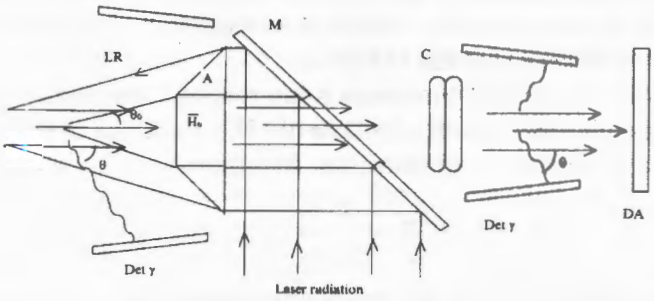


Figure 9: Scheme for an experiment on the optical spectroscopy of antihydrogen atoms: $\bar{H}^0$ is the beam of antihydrogen atoms; LR is laser radiation; M is a mirror; A is a conical "prism", an axicon; C is a resonator exciting $2S-2P$ transitions; Det $\gamma$ are UV-photon detectors; DA are detectors of the radiation arising in the annihilation of the $\bar{H}^0$ atom, an antiproton and a positron, on the detector walls.

A critical question is that of the choice of laser, because for the $1S-2S$ transition, even in two-photon excitation, a laser with wavelength near 240 nm is needed. The closest candidate is the KrCl excimer laser ($\lambda = 222\ nm$). Unfortunately, the power of excimer is low, and their continuous single-mode operation is problematic. Using Doppler shift (2) in colliding atomic-laser beams one can reach the region of the most powerful continuously operating laser, the argon laser (514 mm). Then atoms with antiproton energy of about 280 MeV are needed ($\beta = 0.64$), which is quite possible.

Finally, the resolution of the method remains the main question. It can be estimated by including in (1) the angular spreads of the $\bar{H}^0$ beam $\Delta\theta$ and laser beam $\delta\theta$ and longitudinal velocity spread of the atoms $\Delta v/v$. When $\beta \ll 1$ and the beam intersecting angle $\theta_0 \sim \Delta\theta \ll 1$, one obtains

$$\omega' = 2\,(1+\beta)\,\omega_{Lab} + \Delta\omega', \quad \frac{\Delta\omega'}{\omega'} \sim \beta \cdot \frac{\Delta v}{v} + \beta\theta_0\,(\Delta\theta + \delta\theta)\,. \qquad (3)$$

Using the parameters of $\bar{H}^0$ flux from Table I and $\delta\theta \sim 10^{-4}\ rad, \theta_0 \sim 10^{-2}\ rad$ one obtains for slow atoms ($E_p \sim 0.5\ MeV, \beta \sim 0.03$) the resolution $\Delta\omega'/\omega' \sim 3 \cdot 10^{-7}$. The fitting technique mentioned in Sec. 3.2, 3.3

allows this limit to be exceeded by at least an order of magnitude, to reach of accuracy of $3 \cdot 10^{-8}$.

*The Doppler-free scheme* can be used in this experiment if it is somehow possible to solve the laser problem. Unfortunately, its application inhibits to use the Doppler shift (2) as suggested above, because the Doppler-free scheme presupposes the excitation of a two-photon transition in an atom bombarded by two colliding beams of the same laser, one beam directed along the atomic flux, and the other opposite to it. Therefore, the Doppler shifts have different signs for each beam. This is actually the main idea of this scheme: the total energy (frequency) of two colliding photons in the frame of the atom (see Eq. (1)) is independent, in a first approximation, of the angular spread of the beam and of the velocity spread and direction:

$$\omega_1' + \omega_2' = 2\gamma\omega_{laser} + \Delta\omega', \quad \frac{\Delta\omega'}{\omega'} \sim \beta^2 \frac{\Delta v}{v} + \beta \cdot \Delta\theta\,(\theta_0 + \delta\theta)\,.$$

Thus, the resolution dependence on experiment parameters significantly differs from the preceding case (3): the angular spread of the laser beam $\delta\theta$ does not play any role when $\theta_0 \gg \delta\theta$. At the same parameters, as above, one obtains now $\Delta\omega'/\omega' \sim 1 \cdot 10^{-8}$. Reduction of $\bar{H}^0$ velocity and velocity and angular spreads (which is possible using special electron guns in electron cooling system, see Ref. 6), allows reach the resolution

$$\Delta\omega'/\omega' \sim 10^{-11}.$$

One should underline the basic advantage of experiments with $\bar{H}^0$ in-flight compared to the experiments with $\bar{H}^0$ in traps: using a directed flux of atoms and coincidence schematics of detection one can clearly distinguish the transitions in $\bar{H}^0$ from those in hydrogen atoms of residual gas.

*The 1S-2P one-photon transition* and *the 2S-4S two-photon transition* are also of great importance for the studies of antihydrogen physics. Performence of experiments on laser spectroscopy of these transitions looks realizable [6]–[11] with modern laser technique, and schematics of the experiments is similar to one discussed above.

# 5 Experiments using positronium fluxes

The use of positron storage ring described in Sec. 2 as a generator of directed flux of orthopositronium (o-Ps) opens new possibilities of exper-

imental studies of this physics object [8]. First of them is *the comparison of $e^+e^-$ charges,* considered in Sec. 3.1.

*5.1. Positronium spectroscopy.* When the o-Ps fluxes of high intensity and small velocity spread are used, a level of precision of at least $10^{-6}$ can be expected. Both radiospectroscopic and laser-spectroscopic realization of these experiments are possible. The latter may also allow measurements on two-photon transitions with cancellation of the Doppler broadening. Among such spectroscopic experiments one can point out the measurements of the fine structure of the ground state, o-Ps – p-Ps transitions in magnetic field, transition energy of different states, fine structure of excited states. All these experimental data are of great importance for QED, where positronium is used as a test particle for theory.

The knowledge of $Ps$ spectrum parameters with high precision allows also to obtain the limit of the difference of masses $\delta m$ and charges $\delta e$ of electron and positron. So, modern experimental value of the 1S-2S transition energy in positronium is known with the precision of $1 \cdot 10^{-8}$. Even a naive conclusion, based on well known formula for Bohr atom energy levels leads to the estimation

$$\left(\frac{\delta\varepsilon}{\varepsilon}\right)_{theor} = 2\frac{\delta e}{e} + \frac{\delta m}{m} \leq \left(\frac{\delta\varepsilon}{\varepsilon}\right)_{exp} \sim 1 \cdot 10^{-8},$$

which gives

$$\delta e/e \sim \delta m/m < 1 \cdot 10^{-8}.$$

This is 4 times smaller then modern "official" level.

*5.2. $e^+e^-$ – recombinaton* is another experiment of similar significance if the high precision in measurement of the parameters of electron-positron recombination process with forming of Ps atoms can be reached. Pure and well controlled conditions are provided, when this process occurs in electron cooling section of the positron storage ring.

*5.3. Searches for exotic decay channels* of positronium is the way of experimental test of the fundamental physics law of momentum conservation. The forbidden decay modes

$$\text{o-Ps} \to 4\gamma, \quad \text{p-Ps} \to 3\gamma$$

can be detected with a probability of the order of $10^{-8}$ using pure conditions of o-Ps in-flight and o-Ps $\to$ p-Ps transition in magnetic field at well

controlled conditions (see details in Ref. 8). The same level of experiment resolution can be obtained for allowed decay modes

$$\text{p-Ps} \rightarrow 4\gamma, \quad n > 2.$$

*5.4. The lifetime of positronium. The search for "Mirror Universe.* The use of the method of p-Ps generation allows also to perform high precision measurements of p-Ps life time at pure vacuum conditions [8].

The problem of o-Ps *life time* has already some history, when discrepancy between its theoretical and experimental value (Fig. 10) gave rise to the hypothesis of short-lived neutral bosons (see details in Ref. 8 and 18). Another fascinating idea related to this problem is the hypothesis of so called "Mirror Universe", proposed by I.Yu.Kobzarev, L.B.Okun' and I.Ya.Pomeranchuk [19]. They showed that "usual" world, which consists of "left" (L) particles, can interact with the "mirror" world of right (R) particles only by exchange with photons or gravitons. In more recent times S.Glashow proposed [20] to use positronium as a test system, considering the process of exchange of L- and R-positronium atoms by photons (Fig. 11 a). Such an interaction gives a "coupling" of o-Ps and o-Ps' (R) with spliting of the coupled state in 2 ones (Fig. 11 b).

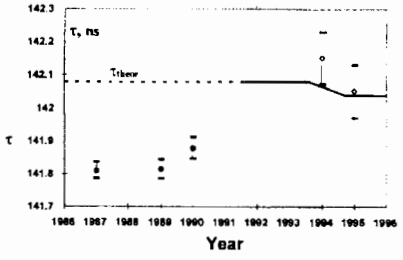


Figure 10: Theoretical and experimental values of orthopositronium life time. 1987–1990: studies by the Michigan group, 1994–1995: studies by the Tokyo group (see Ref. 18).

What can be observed? By definition, in our L-world one can detect o-Ps ("L-system"), however one can NOT detect o-Ps' ("R-system"). Then,

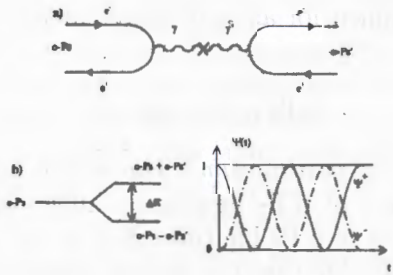

Figure 11: The diagram of the interaction between o-Ps (L) and o-Ps' (R) particles (a) and coupling of two states of positronium (b).

due to coupling, the probability of "attendance" (or "survival") of o-Ps in L-world is equal to

$$\left|\Psi^{+}_{o-Ps} + \Psi^{-}_{o-Ps}\right|^2 = e^{-\Gamma t} \cdot \cos^2 \omega t,$$

where $\Gamma = 1/\tau$ is the "usual" decay rate of o-Ps. S.Glashow has found

$$\omega = \varepsilon \cdot 2\pi f, \tag{4}$$

where $f = 87\ GHz$ is the frequency, which value follows from consideration of the one-photon annihilation diagram and the parameter, $\varepsilon$ defines the value of the split of coupled states $\Delta E = 2\pi\omega$. By his first estimation $\varepsilon < 3 \times 10^{-7}$. In more recent works this parameter value was estimated as

$$\varepsilon < 3 \times 10^{-8}[21] \quad and \quad \varepsilon < 2.8 \times 10^{-7}[22].$$

Thus, the task for experiment is to detect invisible decay of o-Ps as mirror matter by registration of violation of the classic experimental decay law:

$$N(t) = N(0)\, e^{-\Gamma t} \cdot \cos^2 \omega t \approx N(0)\, e^{-\Gamma t} \left(1 - (\omega t)^2\right), \tag{5}$$

or

$$\ln\left(N(t)/N(0)\right) \approx -\Gamma t - (\omega t)^2.$$

Therefore, measuring the dependence of o-Ps decay rate on coordinate X along vacuum channel, where positronium flux travels, one should provide

the experiment resolution, which allows to measure $N(x)$ with a precision

$$\Delta_{exp} \equiv \frac{\Delta N(x)}{N} < \left(\omega \frac{x}{v}\right)^2 \sim \left(\frac{\omega}{\Gamma}\right)^2. \quad (6)$$

The analysis of the systematic errors, related to o-Ps velocity spread and the dependence of the decay rate $\Gamma$ on the velocity (via Lorentz-factor), the accuracy of measurement of the decaying positronium position etc., shows, that the level of the resolution

$$\Delta_{exp} \sim 10^{-6}$$

is achievable. This allows to obtain the upper limit of the parameter $\varepsilon$ (see Formulae (4), (6)):

$$\varepsilon = \frac{\sqrt{\Delta_{exp}}}{2\pi f} \cdot \Gamma \leq 1 \cdot 10^{-8}.$$

One should underline the crucial advantage of the performance of this experiment with o-Ps in-flight in vacuum. It differs fundamentally this approach from the traditional one, when positronium is generated in a target (gaseous or solid one). In the latter case an interaction of o-Ps with media destroys coupling of L and R positroniums, resulting in violation of the decay law (5) [22]. Therefore, the negative result on detection of the "invisible decay" obtained by authors of Ref. 23 at the level $\varepsilon < 1 \cdot 10^{-8}$ does not exclude in principle the existence of this phenomenon.

# Conclusions

Experiments on directed monochromatic atoms of antihydrogen and positronium reveal new possibilities for the experimental testing of the CPT theorem and quantum electrodynamics. In Table III we give the accuracies of measuring the parameters of the fundamental particles and the simplest atoms which have been attained at present and which can be expected in the future on the basis of the estimates made above.

The author takes this opportunity to thank the colleagues joined him in researches used as the basis for this report – A.O. Sidorin, A.N. Skrinsky, E.A. Kuraev.

This work is supported by the Russian Foundation for Basic Research, grant No. 96–02–17211.

TABLE III. Accuracies of the experimental values of the fundamental particle parameters.

| Parameter | Accuracy | |
|---|---|---|
| | Attained | Expected |
| Difference of antiproton and positron electric charges, $\delta e/e$ | $2 \cdot 10^{-5}$ | $2 \cdot 10^{-9}$ |
| The same for the electron, positron, proton, and antiproton, $\delta e/e$ | $2 \cdot 10^{-5}$ | $2 \cdot 10^{-8}$ |
| Antirpoton magnetic moment, $\delta\mu_a/\mu_a$ | $3 \cdot 10^{-3}$ | $2 \cdot 10^{-5}$ |
| Difference of the proton and antiproton magnetic moments, $\delta\mu/\mu_N$ | $3 \cdot 10^{-3}$ | $1 \cdot 10^{-7}$ |
| Hyperfine structure of the ground state of antihydrogen, $\delta\varepsilon/\varepsilon$ | ... | $2 \cdot 10^{-5} - 1 \cdot 10^{-6}$ |
| Hyperfine structure of the $2S_{1/2}$ level and Lamb shift of the $2P_{1/2}$ level, of antihydrogen, $\delta\varepsilon/\varepsilon$ | ... | $2 \cdot 10^{-5} - 1 \cdot 10^{-6}$ |
| Energy of $1S - 2S$ transition in antihydrogen, $\delta\varepsilon/\varepsilon$ | ... | $3 \cdot 10^{-7} - 1 \cdot 10^{-11}$ |

# References


[1] G.I. Budker and A.N. Skrinsky, Usp. Fiz. Nauk, 1978, vol. 124, p. 561, [Sov. Phys. Usp., 1978, vol. 21, p. 277.

[2] H. Herr, D. Moehl, and A. Winnacker, in *Physics at LEAR with Low-Energy Cooled Antiprotons* (Plenum Press, New York, 1984), p. 659.

[3] G. Baur, G. Boero, V. Oelert *et al.,* Phys. Lett. B, 1966, vol. 368, p. 251.

[4] M. Charlton, J. Eades, D. Horvath *et al.,* Phys. Rep., 1994, vol. 241, p. 67.

[5] I.N. Meshkov and A.N. Skrinsky, Nucl. Instr. and Meth. A, 1996, vol. 379, p. 41, Preprint No. E9–95–130, JINR, Dubna, 1995.

[6] I.N. Meshkov, Fiz. Elem. Chastits At. Yadra, 1997, vol. 28, p. 495; Phys. Part. Nucl., 1997, vol. 28, p. 216; Yad. Fiz., 1996, vol. 59, No. 8 [Phys. At. Nucl., 1996, vol. 59, No. 8.

[7] I.B. Khriplovich, A.I. Mil'stein, and I.N. Meshkov, *JINR Rapid Communications,* 1997, No. 3, p. 68.

[8] AD, http://www.cern.ch

[9] "Athena" project, http://www.cern.ch/athena

[10] I.N. Meshkov and A.O. Sidorin, Nucl. Instr. and Meth. A, 1997, vol. 391, p. 216.

[11] I. Meshkov, and A. Skrinsky, Nucl. *Instr. and Meth. A,* 1997, vol. 391, p. 205.

[12] G. Gabrielse *et al., Phys. Rev. Lett.,* 1995, vol. 74, p. 35.

[13] N.F. Ramsey, *Phys. Rev.,* 1950, vol. 72, p. 695; *Molecular Beams,* (Clarendon Press, Oxford, 1950) [Russ transl., IL, Moscow 1960].

[14] J.W. Heberle, H.A. Reich, and P. Kusch, *Phys. Rev.,* 1956, vol. 101, p. 612.

[15] Yu.L. Sokolov, *Zh. Eksp. Teor. Fiz.,* 1982, vol. 83, p. 15, [*Sov. Phys. JETP*, 1982, vol. 56, p. 7].

[16] V.V. Parkhomchuk, in *Proc. of the Symp. on the Production and Investigation of Atomic Antimatter,* Karlsruhe, 1988, vol. 315.

[17] H. Kopfermann, *Kernmomente* (Akademische Verlagsgesellschaft M.B.H., Frankfurt am Main, 1996) [Russian transl., Moscow, IL, 1960].

[18] C.L. Cezar *et al., Phys. Rev. Lett.,* 1996, vol. 77, p. 255

[19] I.Yu. Kobzarev, L.B. Okun', and I.Ya. Pomeranchuk, *Yad. Fiz.*, 1996, vol. 3, p. 1154, [*Sov. J. Nucl. Phys.*, 1966, vol. 3, p. 837 .

[20] S.L. Glashow, *Phys. Lett. B,* 1986, vol. 167, p. 35.

[21] E. Carlson, and S. Glashow, *Phys. Lett. B,* 1987, vol. 193, p. 168.

[22] S. Gninenko, *Phys. Lett. B,* 1994, vol. 326, p. 317.

[23] T. Mitsui *et al., Phys. Rev. Lett.,* 1993, vol. 70, p. 2265.

# Wire Chambers. Some Problems and Limits of Gasous Detectors.

**Walter Bartl**
*Vienna Austria*

## Summary

Electronics high energy physics experiments have been made feasible mainly due to the invention of gasous detectors, in particular wire chambers. The ingenious development by G.Charpak in 1968 opened up various new possibilities for diverse detectors usable in particle physics experiments.

In this talk first some of the basic principles of wire chamber physics are described in order to make the operation of this device understandable. Green's theory for the description of the induced charge is presented as well as the main contributions to the charge on the anode. Due to the longer drifting path of the positive ions their contribution is the dominant one. Compared to the semi - proportional amplification mode, the streamer mode, requiring a bigger field volume, is faster (about 5 ns production time) and produces around 10 times more charge due to its development mechanism.

All the response of a drifting ion is compared with that of an electron under the influence of an electric field. While the velocity of the first one mainly depends linearly on the applied field, the velocity of electrons has a more complicated dependence on the electric field due to an energy dependent cross section. It rises up to about 500kV/cm and then is more or less flat depending on the gas composition. It is mentioned that electrons under the influence of an electric field of 400kV/cm will drift with about 20 ns/mm but ions drift at least two orders of magnitude slower.

The theoretical part is followed by various examples of wire chamber conceptions. First of all the application of MWPC (multiwire proportional chambers) in a spectrometer called SFM (split field magnet) at the CERN - ISR in 1973 is shown. Chambers with a total of nearly 100.000 anode wires have been an enormous amount at that time for this new technique. By exploiting the drift time of the electron an improved space resolution of about 200 - 300 micron could be reached. This type of MWDC (multiwire drift chamber) has been constructed i.e. for the EHS (european hybrid spectrometer) with dimensions of about $2 * 4m^2$. Also drift tubes take advantage of drift time measurements to get a space point. This is

demonstrated with the forward chamber A - working in the streamer mode - at the DELPHI/LEP/CERN experiment.

Cylindrical chambers for the use in colliders are also feasible and illustrated in a few examples. A segmented drift chamber is not only cylindrical, but improves also the space resolution by the evaluation of several anode wires of a track and reaches a $\sigma$ of about $60\mu m$. This is demonstrated in the KEDR/Novosibirsk and SLD/ Stanford experiment. The JET - drift chamber is a big barrel of anode and cathode wires and is used i.e. at JADE/Petra, MARCII/SLAC or OPAL/CERN/LEP. The selection is concluded with the TPC (time projection chamber). It is a gas filled barrel having on each end plate a set of wire chambers. By means of an electric field parallel to the axis of barrel the track of the ionizing particle is measured by the projection to the wire chamber on the end plates and its drift time.

An example for improving the space resolution is represented by the TEC (time expansion chamber) which reaches a $\sigma \sim 35\mu m$ and has been used i.e. for MARC - J/DESY or L3/CERN/LEP.

The report ends with the recent development of gasous detectors, the MSGC (microstrip gas counter). It is a method of putting an anode and cathode electrode arrangement on a substrate of insulating material like glass with a surface resistivity of about 10 exp 13 ohm/square. A high rate capability in the MHz range and a reasonable space resolution of about $40\mu m$ satisfy the requirements of the new collider experiments.

### Fundamental Steps

- G. Charpak Nucl. Inst. and Meth. 62 (1968) 235 Nobel price 1992
- E. Jarocci Nucl. Inst. and Meth. 152 (1978) 423
- A. Oed Nucl. Inst. and Meth. A263 (1988) 351

### Wirechambers

- What are they for?
- What can they do?

(Mostly) Detection of
- Charged (ionizing) particles
- Interaction with gas necessary

Main domains

- Tracking devices
- Particle identification
- Detectors (receiptors)

With / for other devices

**A few Chambers for Illustration!**
What can we do?

- Planar (any shape)
- Cylindric
  - jet Chamber
  - Radial Chamber
  - Vertex Detector
- TPC
- RICH
- MSGC

**Construction**

- Solid Frames
- Self Supporting
  - Tubes
    - any cross section
    - straw Tubes

## Some BASIC PRINCIPLES

### Ionisation

- elastic interaction
- inelastic interaction

Bethe, Blochi differential energy loss

$$-\frac{dE}{dx} = 4\pi N_a r_e^2 m_e c^2 \rho \frac{Z}{A}\frac{z^2}{\beta^2}\left[\ln\left(\frac{2m_e c^2\gamma^2\beta^2}{I}\right) - \beta^2 - \frac{\delta}{2} - \frac{c}{Z}\right],$$

$$\beta = v/c, \quad \gamma = \frac{1}{\sqrt{1-\beta^2}}$$

$\frac{dE}{dx}$ depends on particle velocity $v = \beta c$

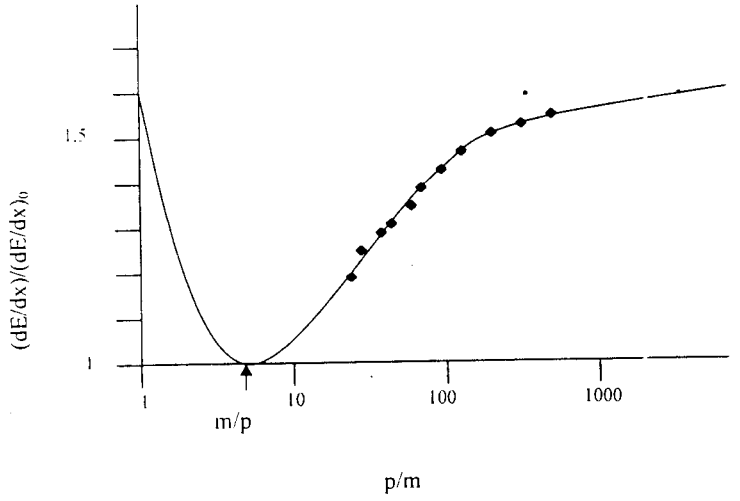


### Drift of ions in electric field

$v_D^+[\text{ion}] \approx \mu^+ E\frac{p_0}{p}$, $p_0 = 760$, mobility $\mu^+ \ldots\ldots 0.6 - 16$,
i.e. $A_r/A_r \ldots\ldots 1.7$, $A_r/isob \ldots\ldots 1.56$

### Drift of electrons in electric field

$$v_D[e^-] = \frac{2}{3}\frac{q}{m}E\frac{\lambda}{u} \sim E\frac{\lambda}{u},$$

$$u = \sqrt{\frac{2\epsilon}{m}} \quad \text{thermic velocity,}$$

$\lambda$ means free path
cross section $\sigma$ dependent

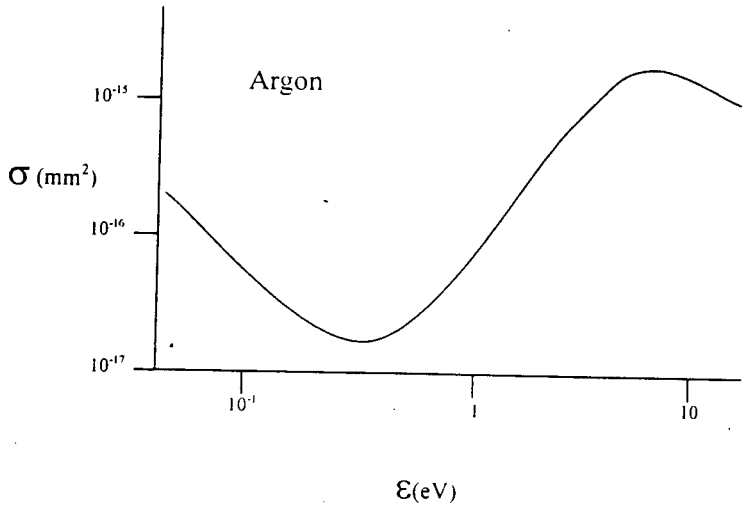


Collision cross section $\sigma$ Ramsaner

Drift velocity of electrons
in gases at normal conditions

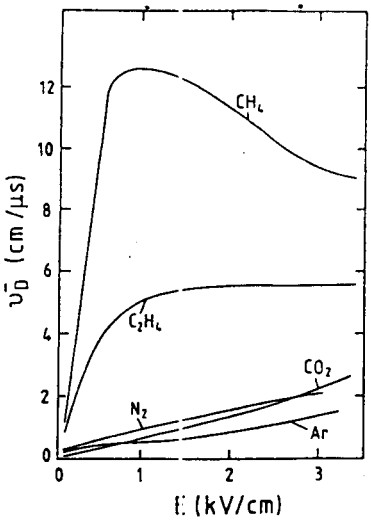


Drift velocity of electrons
in argon-isobutane mixtures

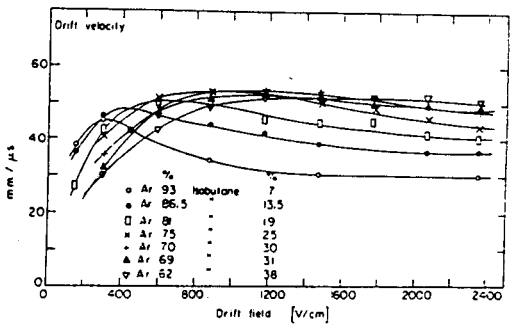

## Charges

How one gets the charge onto the electrodes → Induced charge (current)
Based ... Reciprocity Theorem (Green's Theorem)
"Relation of potentials and charges"

- General multielectrode system

$$\sum_i Q_i V_i' = \sum_i Q_i' V_i$$

$Q_i V_i, Q_i' V_i'$ - initial value and value after change

- 2 electrodes

$$V_1 \rightarrow Q_2, Q_1' \leftarrow V_2', Q_1' V_1 = Q_2 V_2', \quad \frac{Q_1'}{V_2'} = \frac{Q_2}{V_1} = C_{1-2}$$

- in WC

$Q_m, V_m$ - charge imaginar electrode, $Q_1, V_1$ - anode,

$$Q_m V_m = Q_1 V_1, Q_m \frac{V_m}{V_1} = C_{1-2}$$

induced current $i_1 = \frac{dQ_1}{dt}$, motion of $Q_m$ $v = \frac{dl}{dt}$,

$$i_1 = \frac{d\left(\frac{Q_m V_m}{V_1}\right)}{dt} = Q_m \frac{d\left(\frac{V_m}{V_1}\right)}{dl} \frac{dl}{dt}$$

charge $Q_m$ moves away from 1, $Q_m$ - constant as $C_{1-2}$ decreases, $\frac{V_m}{V_1} = V_W$ - normalized potential,

$\frac{d\left(\frac{V_m}{V_1}\right)}{dl} \rightarrow \text{grad}\left(\frac{V_m}{V_1}\right) = -E_W$ - normalized field "weighting field"

$i_1 = -Q_m * E_W v$

Total induced charge $Q_{1j}$ ($Q_m$ moves, $m_1 \rightarrow m_2$).

$$Q_1 = \int i_1 dt = -Q_m \int_{m_1}^{m_2} E_W dl = Q_m \left[V_W(m_1) - V_W(m_2)\right]$$

Induced charge is difference of weighting potentials between two positions of the moving charge.

## GAIN-MODES

Equipotential and field lines due to $V_0$ are shown. Equipotential curves correspond to $V/V_0 = 0/05, 0.10, 0.15...$

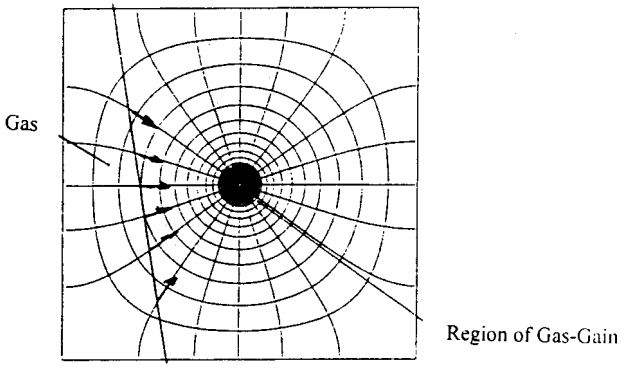


Drift time: $e^- \sim 20\mu s/mm$, ion $\sim 200\mu s/mm$

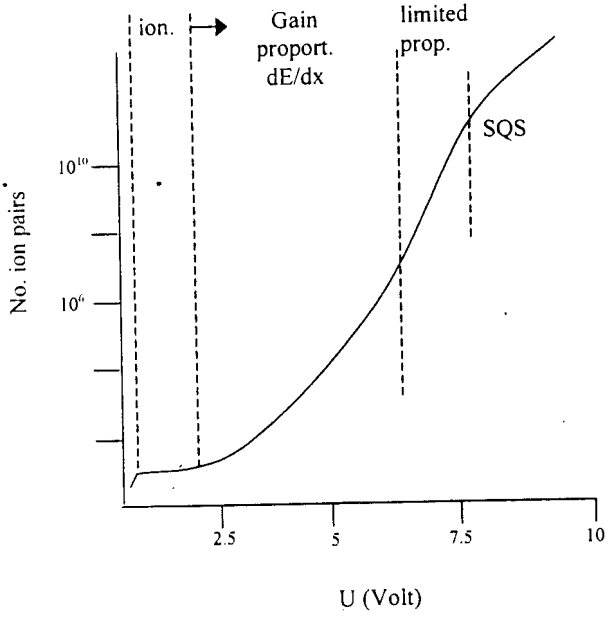

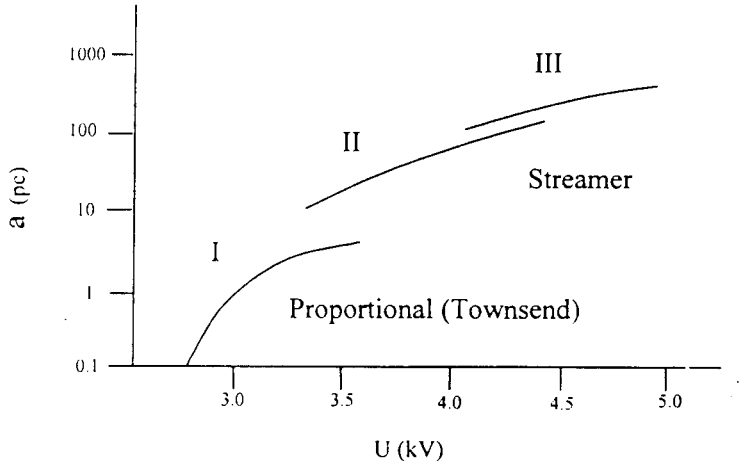


**Propotional-Limmited Prop.-Mode**

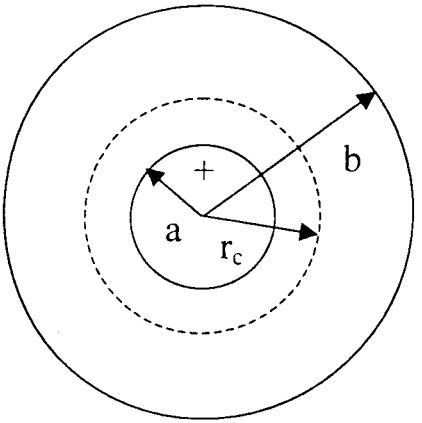


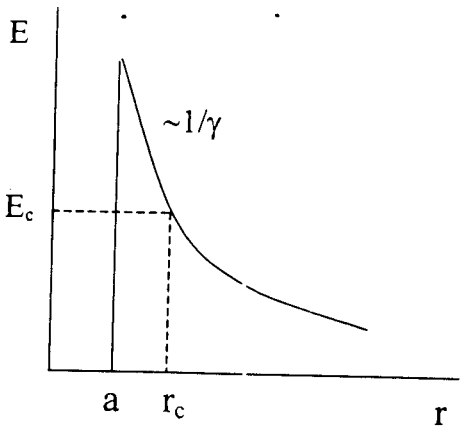


$a$ ..... wire radius, $r_c$ ..... critical distance, $a \sim 10\mu m$.

**at** $r_c$
ionization:

- inelastic
- elastic
- photoionization

$$v_D \sim 50mm/\mu s$$

than avalanche $\sim 1ms$, $dn \approx m\alpha dx$ $m \approx m_0 e^{\alpha x}$ $\alpha^{-1}$ means free path

Multiplication $M = \frac{m}{m_0} = e^{\alpha x}$

$$\alpha = \alpha(x), \quad x = a \to r_c, \quad M = exp\left[\int_a^{r_c} \alpha(r)dr\right]$$

Induced charge $q$ on electrode moving $Q$ by $dx$

$$dq = Q\frac{dx}{l} = Q\frac{dV}{V_0}$$

but for the wire $V = V(r)$, $Q = Q(r)$

$$dq = \frac{Q}{V_0}\frac{dV}{dr}dr$$

assumption: all charges MQ produced at $d < r_c$

electron

$$q^- \approx \frac{MQ}{V_0}\int_a^{a+d}\frac{dV}{dr} \sim MQ\ln\frac{a+d}{a}$$

ion

$$q^+ \approx \frac{MQ}{V_0}\int_{q+d}^{l}\frac{dV}{dr} \sim MQ\ln\frac{b}{q+d}$$

neglecting $c = \frac{2\pi\varepsilon_0}{\ln\frac{b}{a}}$

Result: most of the charge (signal) comes from $q_-$ $\sim 50\%$ of $q^+$ produced at last $\alpha$

$$\frac{q^+}{q^-} \sim 10^{-2}$$

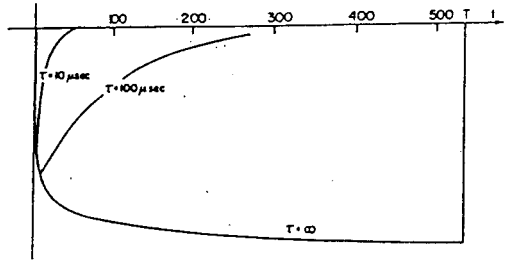


**Self-Quenching-Streamer (SQS)**

conditions:

- wire diameter $\gtrsim 30\mu m$
- field at surface $> 100kV/mm$

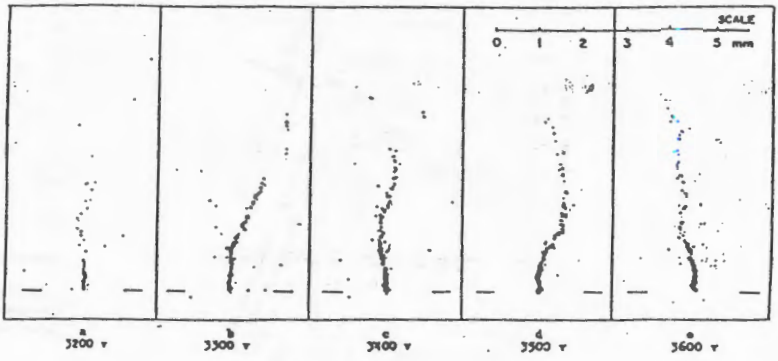


Actions
1. streamer development
2. electron displacement
3. pos. ion migration

"Preparation"

**Preparation to start (model of Zung)**

- ionization
- at wire surface multiplication
- photoionization

$$e + A \rightarrow A^{+*} + e + e$$
$$A^{+*} \rightarrow A^{+} + h_r$$
$$h_r + A \rightarrow A^{+} + e$$

- metastable Argon $A_r^m$

$$A_r^m + A_r^m \rightarrow A_r + A_r^+ + e^- + h_r$$

and

$$A_r^m + b_r \rightarrow A_r^+ + e^-$$

At critica concentration → peng.
Necessity: high field volume, wire →∼ $100\mu m$

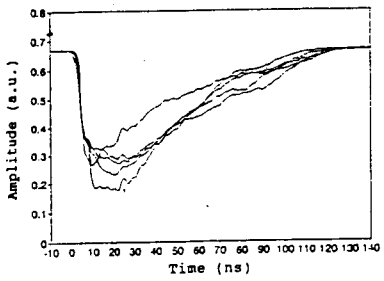


Experimental anode pulse shapes recorded with a 350 MHz bandwidth digitizing system in single-short mode. The risetime of the signal is faster than it is usually inferred from pictures taken for multiple super imposed pulses with limited bandwidth systems. The three distinct regions of the pulse are clearly seen.

1. development $3\mu s$
2. electrons $15\mu s$
3. ion fulling

### Advantage

- ∼ 10 times charge
- fast

### Disadvantage

- dead time
- higher voltage
- fast amplitudes

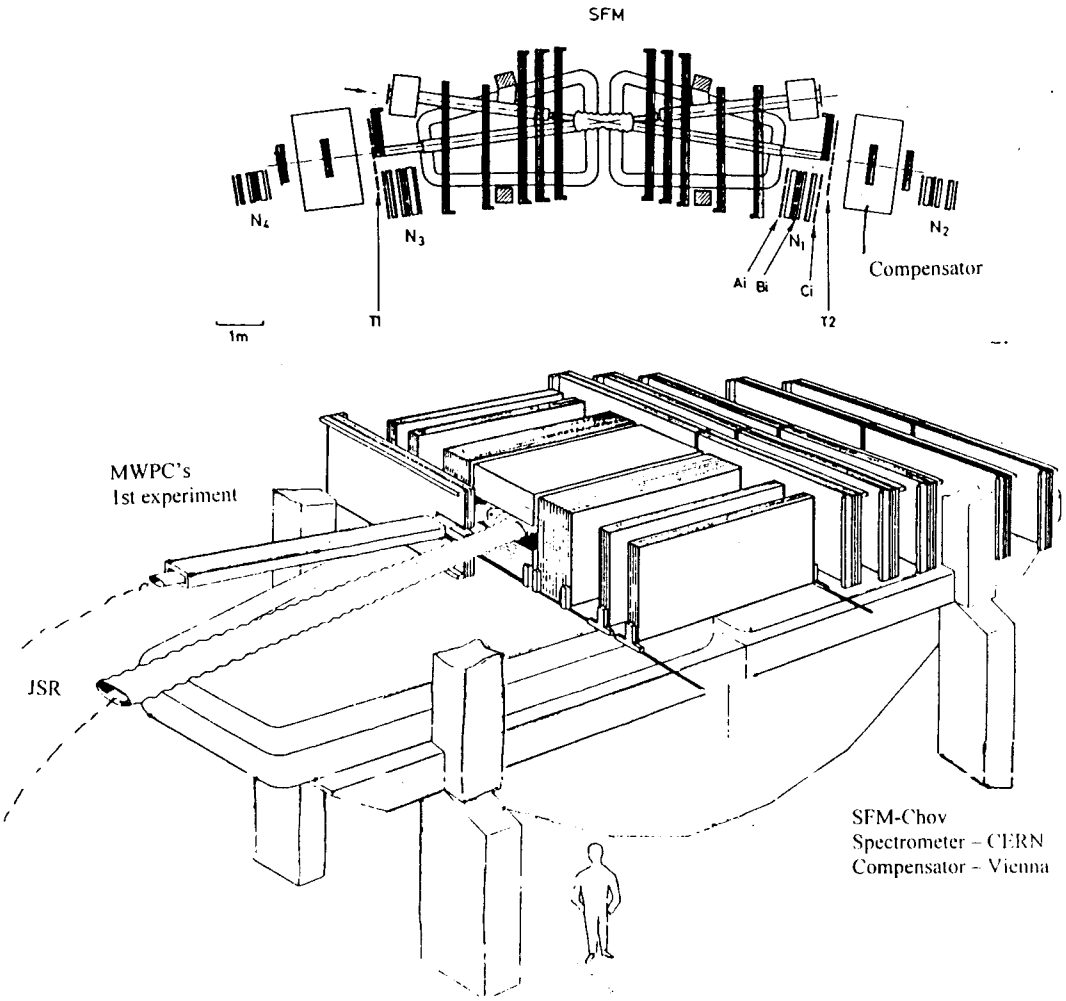
SFM
N4
N3
N1
N2
Ai
Bi
Ci
Compensator
1m
T1
T2
MWPC's
1st experiment
JSR
SFM-Chov
Spectrometer – CERN
Compensator – Vienna

MWDC EH5/CERN
Drift distance $> 10mm(15mm)$
1 chamber, 4 planes $\pm 6°$ from hor. $\pm 17°$ from hor.

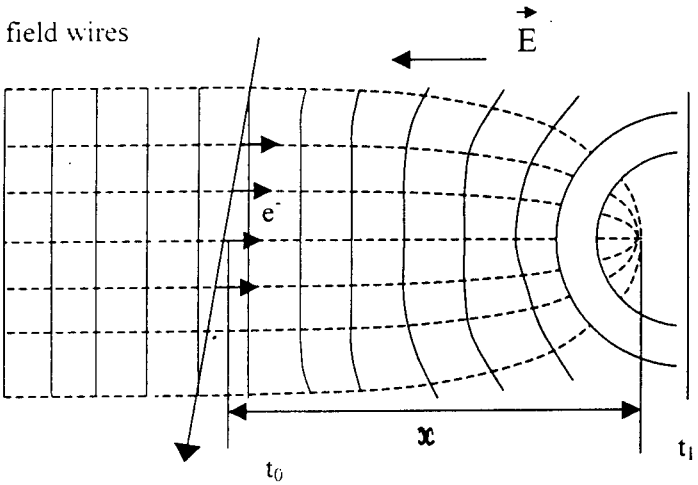


distance $x = V_D t = V_D(t_1 - t_0)$, $V_D \sim 20ms/mm$

FCA DELPHI/CERN
- streamer mode
- conductive PVC tubes
- cathode read out

3 planes, 120°, res. $\sigma \sim 120\mu m$

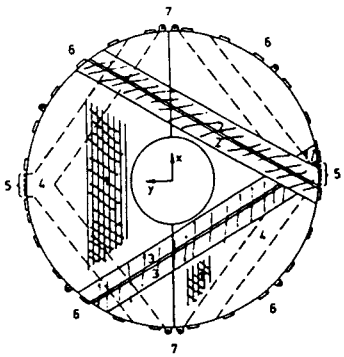

Wire and cathode strip configuration of a chamber disk (two modules): 1. Wires. 2. Cathode strip, front side. 3. Cathode strip, back side. 4. Test strip to pulse the chamber. 5. Connections (gas, HV, LV). 6. Connections for signal cables. 7. Stainless steel ring to support the chamber.

Casode resolution

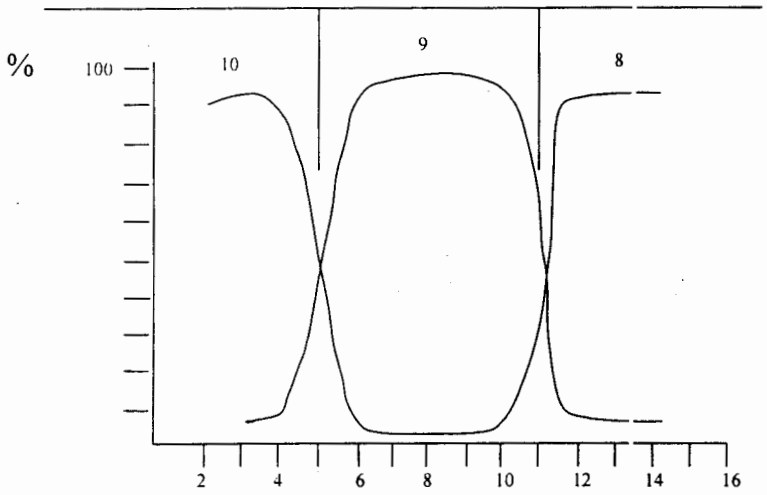


CASCADE muon-detector FZK 1000 drifttubes, 16000 channels, 4m length. tube $9 * 9mm^2$

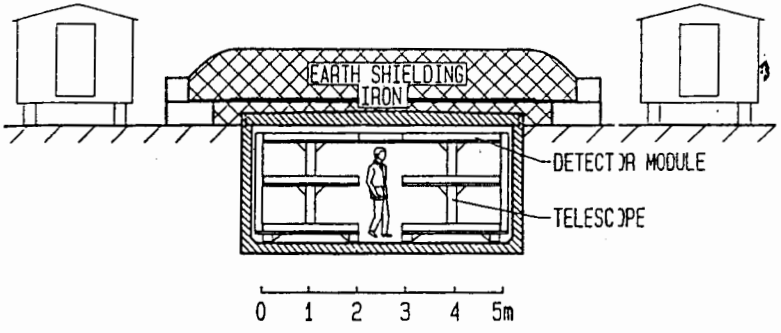


Cross section of the muon detector tunnel of 11 m length located between array detector stations

**tubes**

- PVC coathed
- mass conducting
- reliable working

- good surface

biggest qantity - Adon, Mont Blane, Delphi

**CyL DC**, KEDR/Novosibirsk. SLD/ Stanford
shaped drift field
better space resolution

$2m\phi * 2m$, $\pm$ell $\sim 60mm$ wide$*50mm$ high, $6*41$mrad stereo layers,

$\sigma_{min} \sim 60\mu m$ hit resolution (alone one cell) $\sim 1.5mm \rightarrow$ electronics

1. Wire layout of a signal cell of the CDC.
2. Global and ocal drift distance resolution.
3. The numbe· of 2d hits on a wire vs the separation between the 1st and 2d hits.

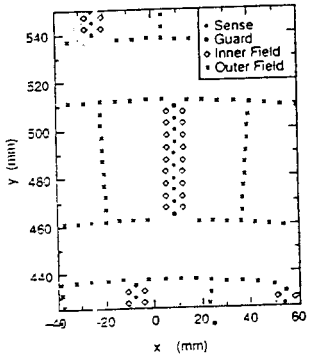


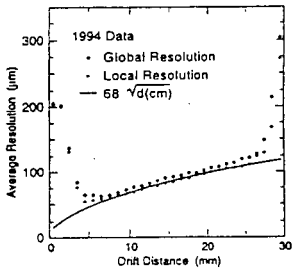


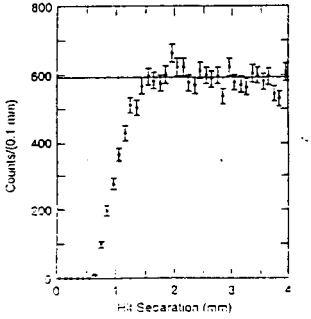


**Jet DC** Jade/Petra March/SLAC OPAL/CERN/LEP
$\sim 4m\varnothing * 4m$
gravitatior al sag $\sim 200\mu m$
gas, 4 bar (Ar/Meth/Jsob)

- 3 coordinates: R.... wire position, $\phi$..... drift time, Z ..... charge division

- particle identification $dl/dx(\sim 150$ points)

Resolution: $\sigma_{r\phi}$.....$110 - 175\mu m$, $\sigma_z$... $\sim 50mm$

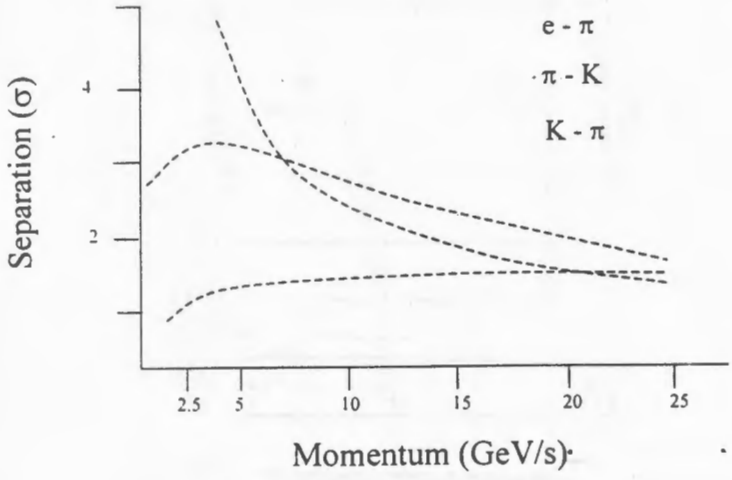


particle separation at Zents 40 hits

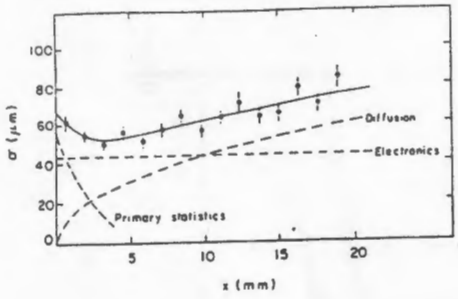


Measured intrinsic accuracy in the drift chamber as a function of drift space. The experimental results have been decomposed into three contributions: a constant electronics dispersion, a physical diffusion term function of the square root of the drift space, and a contribution of the primary ion pair statistics.

**Time expansion chamber (TEC)**
MareJ/DESY. L3/Lep/CERN, Walenta
$CO_2/iC_4H_{10}(80/20)$. $1,2bar$, $6mm/\mu s$, $res \sim 35\mu m$

The scheme of the TEC principle

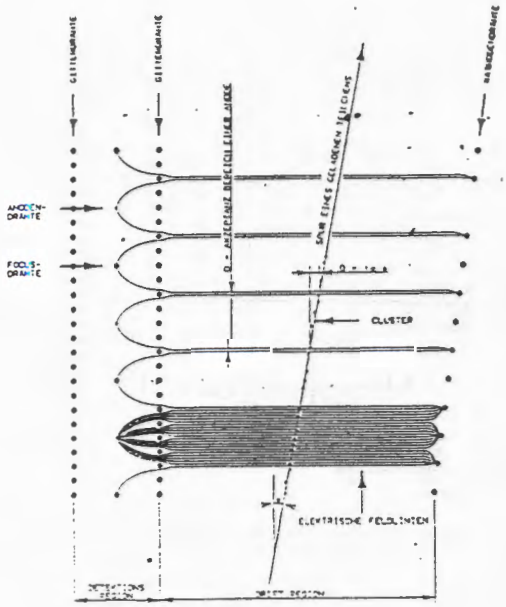

**TPC**

- Nygren. LBL Int. Rep. (1974)
- TOPAZ/KEK
- Na36/CERN
- Aleph/CERN $3.6m\phi * 4.6m$
- Delphi/CERN $2.3m\phi * 2.7m$

resolution $R_\phi... \sim 230\mu m$ $\frac{dE}{dx}$ : mips electr. 5.7%6.2%, $Z.... \sim 900\mu m$

## TPC

electron focusing $\sim \frac{1}{(1-\omega^2 c^2)}$. $\omega = \frac{eB}{m}$ – cyclotron frequency.

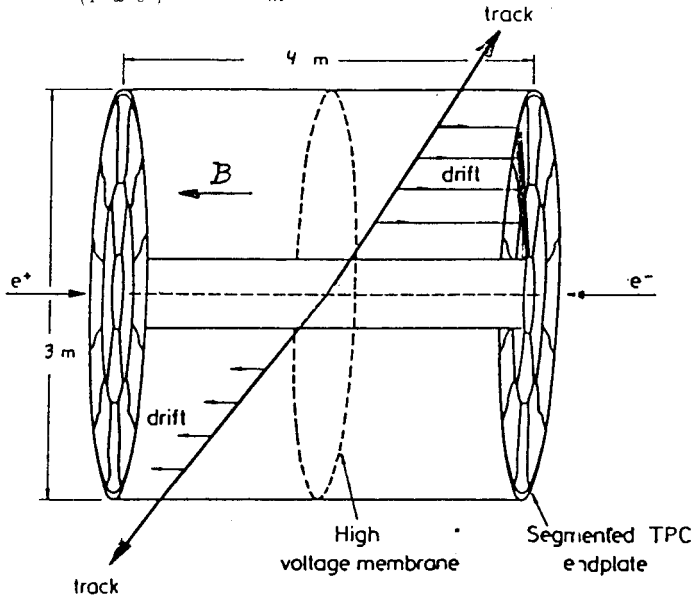


Specific energy loss $dE/dx$ in the TPC as a function of the momentum

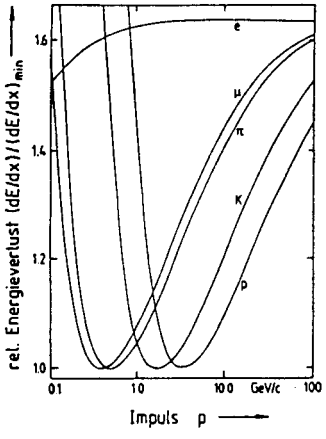


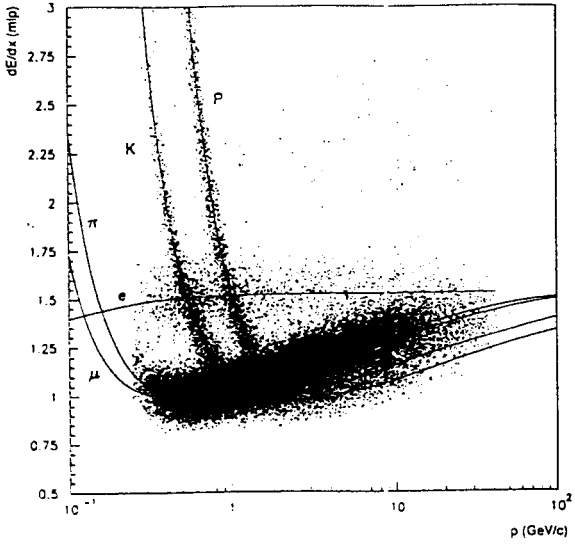

**MSGC (Mire-Strip-Gas-Counter)** Sauli/CERN
Ar/DME (50/50) %

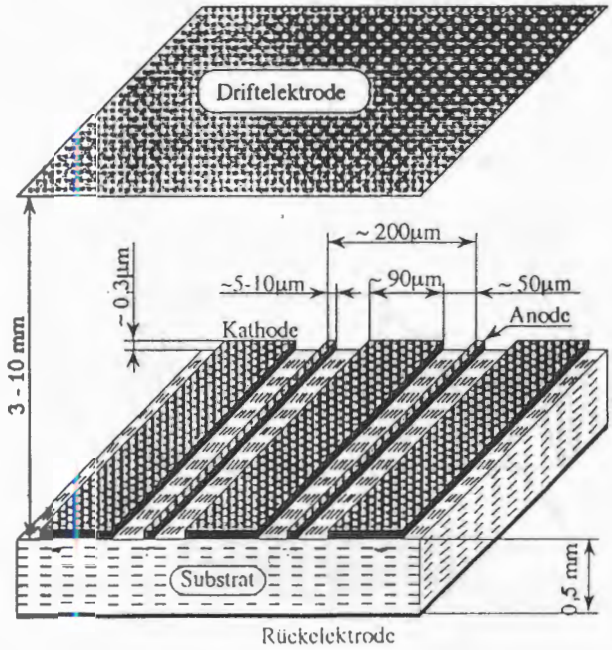


Used as $\mu-$ vertex detector DESY, CERN, etc.
LHC enviroment $\sim 10 mG/J/cmi \quad n, \gamma$, hadrons
Problems:

- rate (surface resistivity)
- surface charge (field lines)
- ageing
- polarisation (glass structure)
- discharges (radiation-rate)

Solutions:

- resistive glasses

- coating glass, bovsilicate (Sibott D263, $R > 10^{16}/\Omega$)
  over-under-coating:
  - lead silicate
  - Ni
  - DLC (diamond-like-carbon) on D263, $10^{13} - 10^{13}\Omega$
- ion implantation
  - boron
  - argon

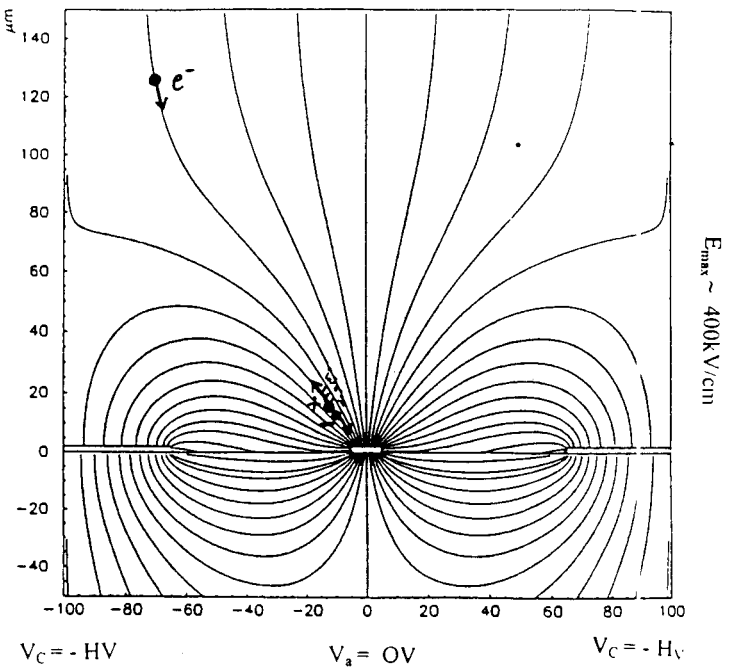

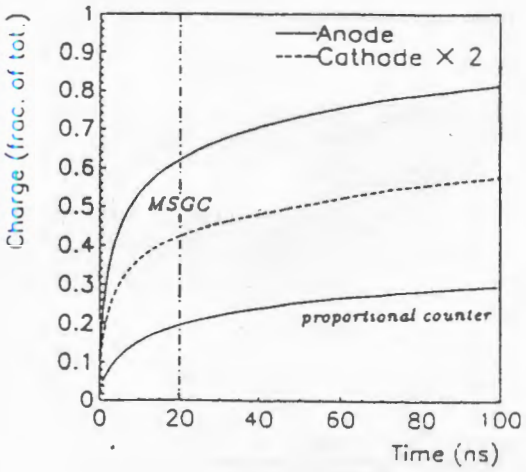


1. Comparison of gain stability for standard and boron implanted glass.
2. Rate capability of an MSGC made on sputtered lead silicate glass.
3. Improved stability at high radiation doses of MSGC made on implanted glass.
4. Rate capability of an MSGC made on diamond-like coated glass.

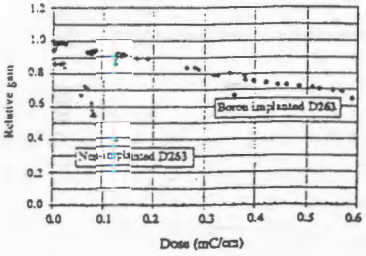


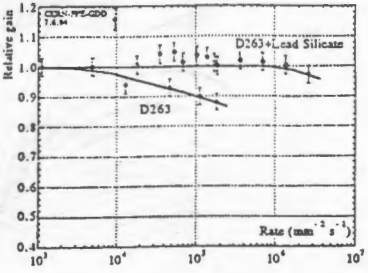


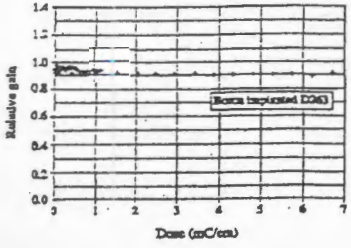


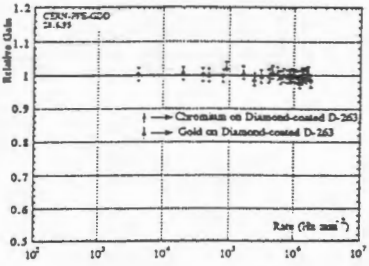

5. Long-term stability of charge gain of the over-coated MSGCs.

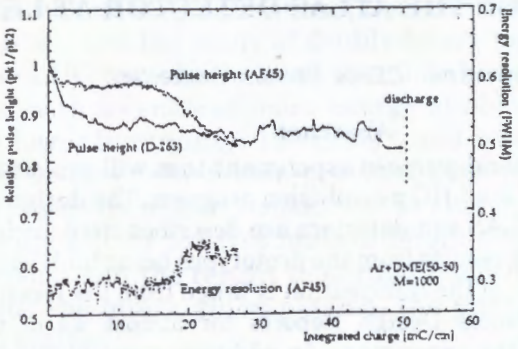


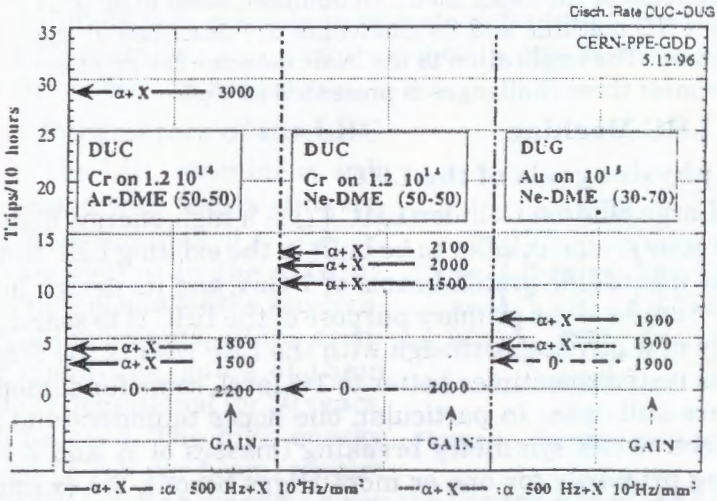


GEM, Gas-Electron-Multiplier Sauli/CERN

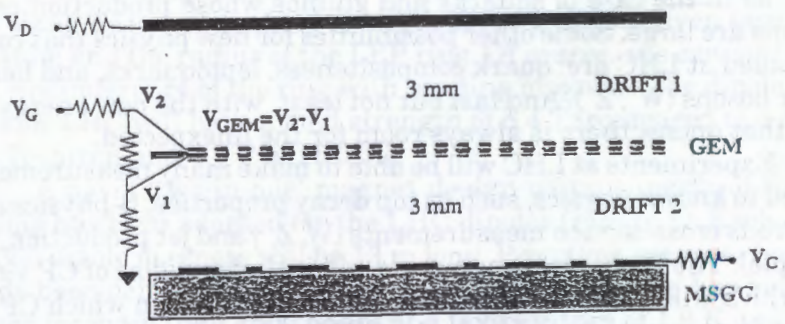

# 2. LHC PROGRAM: ATLAS, CMS

## OVERVIEW OF THE ATLAS DETECTOR AT LHC

Ilias Efthymiopoulos *CERN, Geneva, Switzerland*

**Abstract**

ATLAS is a general-purpose experiment that will exploit the full potential of the LHC p-p collision program. The design aspects of the ATLAS sub-detectors are described here, including performance results from the prototypes being built in the past years. Most of the information is taken from the recently published Technical Design Reports for almost all of the sub-systems of the experiment. In addition, some highlights of the LHC machine and its challenges are described at the beginning. The implication to the basic detector design in order to meet these challenges is presented as well.

### 1 The LHC Machine

### 1.1 The physics goals of the LHC

The Large Hadron Collider(**LHC**)[1] is a high-energy, high-luminosity proton-proton collider to be built in the existing LEP tunnel at CERN. It will collide proton beams of 7 GeV and its design luminosity is $10^{34}$ $cm^{-2}$ $s^{-1}$.The primary purpose of the LHC is to search for and to study new physics. Although with the LEP results the Standard Model is tested sometimes better to 1% level, some fundamental questions are still open. In particular, one hopes to understand the origin of electroweak symmetry breaking (masses of W and Z bosons), looking primarily for one or more Higgs bosons, for example. The LHC can also be exploited to search for Supersymmetric (SUSY) particles which, if exist, will be produced in some cases with large rates, as in the case of squarks and gluinos whose production cross sections are large. Some other possibilities for new physics that could be studied at LHC are: quark compositeness, leptoquarks, and heavy vector bosons (W , Z ). And last but not least, with the new energy regime that opens, there is always room for the unexpected.

Experiments at LHC will be able to make many measurements related to known physics, such as top decay properties, B-physics and numerous cross-section measurements (W, Z, $\gamma$ and jet production, for example). The B-physics programme will include studies of CP violation which will allow one to test the Standard Model in which CP violation is parameterized within the CKM matrix. It will also include

the measurement of $B_s^0$ oscillations, the search for rare B decays such as $B_d^0 \rightarrow \mu^+\mu^-$, and the study of doubly-heavy hadrons such as $B_c$.

The LHC can also be used to collide beams of heavy ions, e.g. lead ions, with a centre-of-mass energy of about 6TeV per nucleon, but with lower luminosity: $10^{32}\,cm^{-1}s^{-1}$ and interaction rate: $10^4 s^{-1}$, compared to $10^9 s^{-1}$ for proton-proton collisions. The heavy-ion programme has as its primary objective the search for the quark--gluon plasma. One will try to investigate different stages in the production of the plasma and the return to normal hadronic matter: the initial conditions, the quark-gluon plasma, the phase transition and the hadronic matter.

Finally it is possible to operate simultaneously the LHC and the LEP machines and produce e-p collisions, but this only if there are strong physics arguments.

## 1.2 Parameters of the LHC

The LHC machine is well integrated with the existing accelerator complex of CERN. It will be housed in the existing LEP tunnel and for the acceleration of the protons, all the existing machines, some of them already operational for 20 years, will be used. The high energy beams (7 TeV per beam) require powerful bending magnets given the limited size of the LEP ring (27 km circumference). Using $p = 0.3 \cdot B \cdot R$, where p is momentum in GeV, B is the magnetic field in Tesla and R is the radius in meters, one obtains an average field strength of 5.4 T for the given beam momentum and the radius of the LEP ring. Of course, one cannot fill the full circumference of the ring with bending magnets. The dipole magnets for LHC will have a field strength of 8.4 T (compared to 4.4 T at the Tevatron and 4.7 T at HERA).

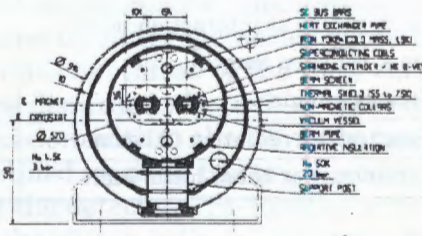

**Figure 1:** Section view of an LHC magnet.

A novel 'two-in-one' magnet design using superfluid-helium cooling has been adopted for the LHC dipoles (Figure 1). Each of the ~1,300 dipole magnets will be 13 m long. Prototype magnets have already been delivered and tested. A three-dipole 'string' has been operated for more than 1500 hours at a temperature of 1.9 K and more than 50 quenches have been induced without damage to the mag-

nets. The main parameters for the machine are summarised in Table 1.

**Table 1**: The main parameters of the LHC machine.

| | | pp | Pb-Ions |
|---|---|---|---|
| Expected operational cm energy | (TeV) | 14.0 | 1148 |
| Dipole field (max) | T | 8.4(9.0) | 8.4 |
| Luminosity | $cm^{-2}\,s^{-1}$ | $10^{34}$ | ~ $10^{27}$ |
| Number of bunches | | 2835 | 608 |
| Bunch spacing | m-ns | 7.5-25 | 37.4-124.8 |
| Particles per bunch | | $10^{11}$ | $9.4 \times 10^{7}$ |
| Particles per beam | | $2.8 \times 10^{14}$ | $4.7 \times 10^{10}$ |
| Number of experiments | | 2 | 1 |
| $\beta^*$ at interaction point | m | 0.5 | 0.5 |
| r.m.s. radius at interaction point | μm | 16 | 15 |
| r.m.s. collision length | cm | 5.4 | 5.4 |
| Crossing angle | μrad | 200 | <100 |
| Synchrotron radiation (2 beams) | kW | 7.2 | |
| Luminosity at beam-beam limit | $cm^{-2}\,s^{-1}$ | $2.5 \times 10^{34}$ | |

## 1.3 The experimental environment at LHC

In the LHC machine, bunches of protons in counter-rotating beams will be made to collide at the 'interaction points'. An important parameter of the machine is the 25 ns bunch-crossing period. The LHC will operate at very high luminosity $10^{34}$ $cm^{-1}s^{-1}$. The total inelastic, non-diffractive cross-section at LHC energies will be about 100 mb, corresponding to an interaction rate of $10^9$ Hz. The task of the LHC experiments is to identify and select the interesting events on top of this enormous background. For example, in the case of the Higgs particle with mass 500 GeV, about 17 K events will be produced per year, compared to a total of $1.7 \times 10^{16}$ events from the inelastic interactions! In addition, with the bunch-crossing rate of 40 MHz (period of 25 ns), about 25 interactions will overlap in each bunch crossing ('pile-up') with each one having on the average about 100 tracks, or in other words about $10^4$/100 ns (the typical duration of a pulse), uniformly distributed in the pseudorapidity down to $\eta \sim 5$.

All the above, impose stringent requirements to the LHC detectors:

- they must be rather fast, in order not to integrate the signals from the pile-up events over many bunch crossings,
- they must be highly granular in order to minimise the probability for pile-up in a given detector cell. For an occupancy of about 1%, detectors with $10^6$ channels are needed, or even $10^7$ channels for the most sensitive part, the inner tracker.

The high flux of particles from proton-proton interactions (and to a lesser extent from beam losses) places the detectors and associated electronics in a high-radiation environment. Only radiation resistant detectors can be used, and electronics must be `radiation hard'. One must also take into account background signals induced in the detectors by such radiation.

The high interaction rate has also implications on the trigger and data-acquisition systems. Only a tiny fraction of the interactions can be recorded for off-line analysis, requiring a trigger selectivity of about one interaction in $10^7$. Furthermore, massive amounts of data have to be transmitted to and stored in buffer-memories while the trigger system performs its calculations. (Most of the data correspond to rejected events and will be discarded.) Note that, since it is impossible to make a trigger decision within the 25 ns between bunch crossings, the so-called 'pipelined readout' has to be used, typically with electronics mounted on the detector. The functionality of pipelined readout is illustrated in the sketch bellow:

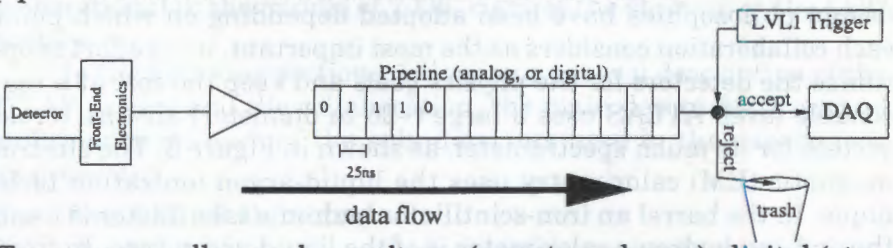


The memory cells may be analogue (e.g. store charge), digital (store the result of an analogue-to-digital conversion) or binary (store a single bit of information, e.g. discriminator output). The data must be kept in the pipeline memory for a few μs, until the first-level trigger decision is available.

## 1.4 Detectors for LHC

There will be four large-scale experiments at LHC. Two very big `general-purpose' experiments ATLAS[6] and CMS[3], a

heavy-ion experiment ALICE[4] and a B-physics experiment LHC-B[5]. The design of a 'generic' LHC detector is shown in Figure 2. The detectors have an 'onion' structure matching well the needs for particle identification and detection.

Working outwards from the interaction point, the following functions can be identified: Momenta of charged particles are measured in the inner tracker (possibly also particle identification is performed, e.g. by Transition Radiation Detection in ATLAS). Primary and secondary vertices are reconstructed from track information, including precision 'vertexing' layers close to the beams. The energies and directions of electrons and photons are measured in EM calorimeters. The energies and directions of hadrons are measured in calorimeters (EM and hadronic). Muons are identified, and their momenta are measured, in the muon spectrometer. Forward calorimetry completes the missing transverse energy measurement.

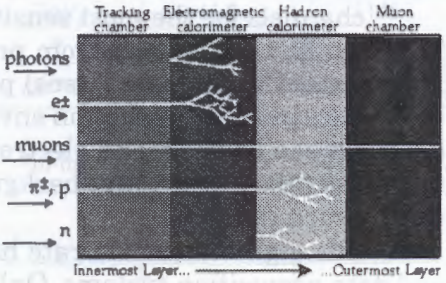


**Figure 2:** Illustration of identification of electrons, photons, hadrons and muons in a 'generic' detector.

Among the four experiments proposed for the LHC, different design philosophies have been adopted depending on which point each collaboration considers as the most important, in an effort to optimize the detectors for the physics goals and keep the cost at a reasonable level. ATLAS uses a large (~20 m diameter) air-core toroid system for its muon spectrometer, as shown in Figure 3. The electromagnetic (EM) calorimetry uses the liquid-argon ionization technique. In the barrel an iron-scintillator hadronic calorimeter is used; the end-cap hadronic calorimeter is of the liquid-argon type. In front of the barrel EM calorimeter (integrated in the same cryostat) is a superconducting-solenoid coil that provides a 2~T field for the tracker. The inner-tracking system consists of semiconductor detectors in the innermost part and straw-tubes in the outer part. The basic design considerations for the ATLAS detector can be summarised as follows: very good em-calorimetry for e, $\gamma$ identification and measurement; hermetic jet and $E_T^{miss}$ calorimetry; efficient tracking at high luminos-

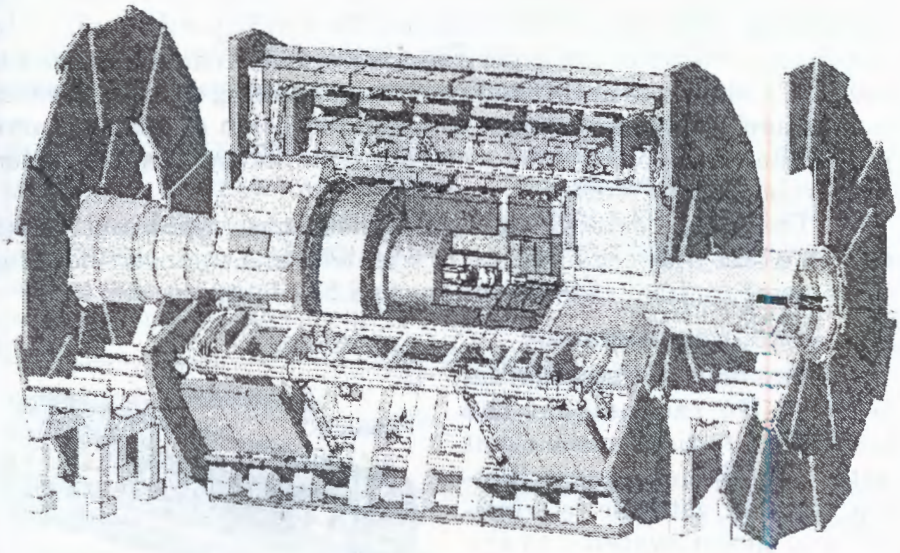

**Figure 3:** The ATLAS detector.

ity for lepton measurement, b-quark tagging and enhance e, $\gamma$ identification; $\tau$ and heavy flavour vertexing and reconstruction capability of some B decays (low luminosity running); large acceptance in $\eta$ coverage; low $p_T$ thresholds for the trigger. The detector is expected to be operational in the middle of 2005, right at the start-up of the LHC machine.

In the following sections, following a general description of the ATLAS project and the collaboration, the main design features and performance for each of the sub--detectors used in the experiment are presented.

## 2 The ATLAS Detector

The ATLAS detector concept was first presented in the Letter of Intent (LoI)[6] and later in the Technical Proposal[2]. Since then, the design has been developed much further guided by detailed physics performance studies, experience from a rigorous and broad R&D programme, and the necessity to stay within cost-effective technologies which fulfil the essential physics requirements. Open options on some of the major detector components at the stage of the LoI and TP have been resolved, and some new ideas emerging from the signifi-

cantly enlarged Collaboration have been implemented in the detector. During 1996, most of the Technical Design Reports for all of the major components of the experiment were written and presented to the LHC Committee at CERN. Since then, following a positive recommendation by the committee, the collaboration enters in a new phase, that of the production, which for some sub-systems (e.g. calorimetry) is about to start.

The ATLAS detector will be designed, constructed, and operated by a world-wide collaboration of scientists and engineers, forming 1700 members from 144 institutions and 33 countries.

## 2.1 The Inner Detector

The task of the inner detector is to reconstruct the tracks and vertices in the event with high efficiency, contributing, together with the calorimeter and muon systems to the electron, photon and muon recognition, and supplying the important extra signature for short-lived particle decay vertices. Its acceptance covers the pseudorapidity region of $|\eta| < 2.5$, matching that of the rest of the ATLAS systems for precision measurements.

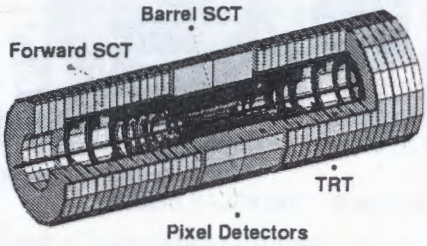


**Figure 4:** Three-dimensional cut-away view of the ATLAS inner detector.

The detectors used for the inner tracker at LHC have to meet very stringent requirements such as: be very fast, be radiation hard, have high granularity and good momentum resolution. In addition, the total amount of material should be kept as small as possible, otherwise the momentum resolution in the tracker itself will be degraded due to the multiple scattering, and the photon and electron identification and energy measurement in the calorimeters will be affected as well. ATLAS has chosen for the innermost part of the tracker the semiconductor detectors (SCT). A three-dimensional cut-away view of the layout of the Inner Detector is shown in Figure 4.The outer radius of the tracker cavity is 115 cm and the total length is 7 m. Mechanically, the Inner Detector consists of three units: a barrel part extending over 80 cm, and two identical end-caps covering the rest of the cylindrical cavity. In the barrel ($|\eta| < 1$), the high-precision detector layers are arranged on concentric cylinders around the beam axis,

while the end-cap detectors are mounted on disks perpendicular to the beam axis. The basic design parameters and the resolutions for space-point measurements are summarised in Table 2.

**Table 2:** The main parameters of the Inner Detector.

| **Pixel Detector** | | | **Semiconductor Tracker** | |
|---|---|---|---|---|
| total active area | 2.3 $m^2$ | $\sigma_{r\text{-}\phi}$= ~12 μm | total area | 61 $m^2$ |
| r/o channels | $1.4 \times 10^8$ | $\sigma_z$= ~60 μm | r/o channels | $6.2 \times 10^6$ |
| max. power dens. | 0.6 W/$cm^2$ | | module size | $123.2 \times 61.4 mm^2$ |
| no. of layers | 3(barel)+8 disks | | operating temp. | -7 °C |
| module dim. | $2 \times 6$ $cm^2$ | | radiation dose | |
| occupancy/mod. | $0.6–0.4 \times 10^{-4}$ (pile-up) | | barrel | $1.3–0.8 \times 10^{14}$ n/$cm^2$ |
| | $3–5 \times 10^{-4}$ (b-jets) | | forward | $1.4–0.9 \times 10^{14}$ n/$cm^2$ |
| | | | resolution | σ(strip) = 22 μm |
| | | | | $\sigma_{r\text{-}\phi}$ = 16 μm |
| | | | | $\sigma_z$ = 580 μm |
| **Transition Radiation Tracker** | | | occup./mod. | 0.3-0.6% (pile-up) |
| no. of straws | 372,032 | | | 1.4-1.7% (b-jets) |
| r/o channels | 424,576 | | | |
| gas mixture | 70%Xe, 20%$CF_4$, 10%$CO_2$ | | | |
| gain | $2.5–3.5 \times 10^4$ | | | |
| resolution | 170 mm (low lum.) | | | |
| occupancy | 10-40% (high lum.) | | | |

Starting from the beam pipe, in the range from 4 to 22 cm in radius, pixel detectors are used which provide up to 3 points per track. Following that, and up to 56 cm in radius, Si-strip detectors are used, providing four 2-D points per track. For improved momentum reconstruction, pattern recognition and electron identification a straw tube Transition Radiation Tracker (TRT) is used, which provides 36 points per track (>7 points/track for e-id). Although the straw hits have lower precision than the ones from the silicon layers, their large number and the fact that they come from larger average radius compensates for that, such that the overall momentum resolution is improved and no single measurement dominates. This means that the overall perform-

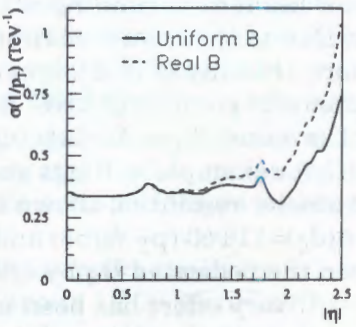


**Figure 5:** The Inner Detector momentum resolution with beam constraint, for tracks with $p_T$ = 500 GeV, for the real solenoidal field compared to a uniform 2T field.

ance is robust, even in the case that a single system does not perform to its full specification. The full momentum resolution, combining the information from the discrete precision points and the large number of drift-time measurements of the TRT in a global fit through the realistic solenoid field map, is shown in Figure 5.

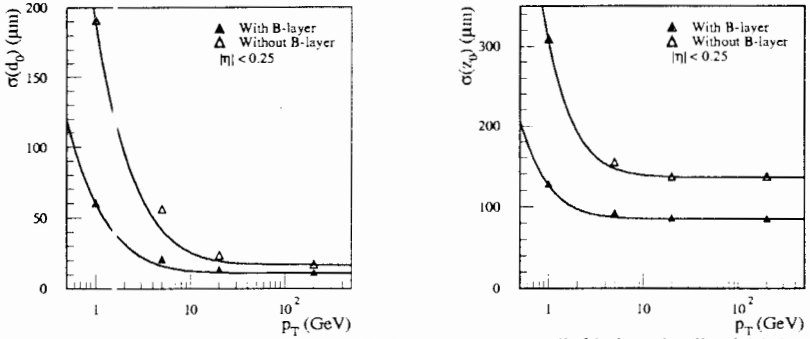


**Figure 6:** The impact parameter resolution: transverse (left), longitudinal (right).

The inner most silicon layer at about 4 cm from the IP, also called the b-layer, of the pixel detector has a substantial contribution to the secondary vertex measurement performance, during the initial lower luminosity running of LHC, in particular for the B physics sector. Due to the hostile environment at this position in terms of radiation, this layer is designed to be removable for the later high luminosity running of LHC. Recent physics studies have demonstrated the value of good b-tagging performance during all phases of the LHC, for example in Higgs and supersymmetry searches. The impact parameter resolution shown in Figure 6, can be parameterized in $R_0$ as $\sigma(d_0)=11\oplus 60/(p_T\cdot\sqrt{\sin\theta})$ and in $z$ as $\sigma(z_0)=70\oplus 100/p_T\cdot\sqrt{\sin^3\theta}$ (in μm) when the dedicated B-physics layer is present.

Every effort has been made to keep the material in the tracking volume to a minimum, by careful design of the active detectors and by the use of low-Z materials (such as aluminium for the power cables, and carbon-fibre reinforced plastic for the support structures). The distribution of material, in radiation lengths, as a function of $|\eta|$ is shown in Figure 7. The level corresponds to an average of 43% $X_0$, with a peak at ~60%. The effect of material, studied in many physics processes (such as $H \rightarrow \gamma\gamma$, $H \rightarrow e^+e^-e^+e^-$), can be clearly identified in the ATLAS performance, but it does not create unacceptable problems for physics studies.

However less material would clearly be of great benefit in many areas, if this can be achieved without compromising the inner detector in other ways. Work is in progress to attempt to reduce the material budget still further, by detailed optimization of the active detectors, and by further integration of the overall support structure.

More details on each subsystem of the inner detector are given below.

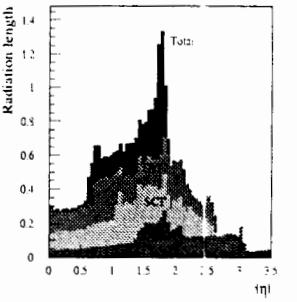


**Figure 7:** The total material budget in the Inner Detector.

*2.1.1 The Pixel detector*

The pixel detector system provides critical tracking information for pattern recognition near the collision point and largely determines the ability of the Inner Detector to find secondary vertices. The ATLAS pixel detector system is composed of modular units. Read out integrated circuits are mounted on a detector substrate to form barrel and disk modules. The detector substrate is silicon, and the current baseline is an $n^+n$-bulk sensor. The read out integrated circuits are mounted on the silicon sensor using bonding techniques. An additional integrated circuit for control and clock distribution and data compression is mounted on each module, and flexible cables connect each module to data transmission/control circuitry located within the detector volume.

The modules are overlapped on the support structure in order to give hermetic coverage. There are about 1,500 identical barrel modules and about 1,000 disk modules in the system. Both the barrel and disk modules are mounted on special supporting structures and the resulting mechanical structure is very stable and provides the cooling capability to maintain the silicon temperature at $\leq 6$ °C even with the large heat load from the electronics. Special attention is made to the radiation hardness of the detectors, since they have to withstand over 300kGy of ionising radiation and over $5\times10^{14}$ neutrons per $cm^2$ in ten years of operation.

*2.1.2 The Semiconductor Tracker (SCT)*

The system is an order of magnitude larger in surface area than previous generations of silicon microstrip detectors, and in addition, it must face radiation levels which will alter the fundamental characteristics of the silicon wafers themselves. The barrel SCT uses four layers of silicon microstrip detectors to provide precision points in the $R_\phi$ and $z$ coordinates, using small angle stereo to obtain the $z$ measurement. Each silicon detector is $6.36 \times 6.40$~cm$^2$ with 768 read out strips each with 80 μm pitch. The spatial resolution is 16 μm in $R_\phi$ and 580 μm in $z$. Tracks can be distinguished if separated by more than ~200 μm.

Solutions have been found to the critical issues in the system, and prototype modules have been successfully tested in beams in a magnetic field, showing the required performance in resolution, signal-to-noise and speed. Modules containing both front-end electronics and detectors, irradiated to the level expected for 10 years of LHC operation, have also been shown to function within specifications.

*2.1.3 Transition Radiation Tracker (TRT)*

The TRT is based on the use of straw detectors, which can operate at the very high rates needed by virtue of their small diameter and the isolation of the sense wires within individual gas envelopes. Electron identification capability is added by employing xenon gas to detect transition-radiation photons created in a radiator between the straws.

Each straw is 4 mm in diameter, giving a fast response and good mechanical properties for a maximum straw length of 150 cm. The barrel contains about 50,000 straws, each divided in two at the centre in order to reduce the occupancy and read out at each end. The end-caps contain 320,000 radial straws, with the read out at the outer radius. The total number of electronic channels is 420,000. Each channel provides a drift-time measurement, giving a spatial resolution of 170 μm per straw, and two independent thresholds. These allow the detector to discriminate between tracking hits, which pass the lower threshold, and transition-radiation hits, which pass the higher.

A primary concern in the design of this sub-system has been to obtain good performance at high occupancy and high counting rate. In the barrel, the rate of hits above the lower threshold varies with radius from 6 to 18 MHz, while in the end-caps the rate varies with

$z$ from 7 to 19 MHz. The maximum rate of hits above the higher TR-threshold is 1 MHz. Within a single drift-time bin, the occupancy is about one third of that in the entire straw active time window. A fast, low-noise preamplifier-shaper circuit with active baseline restoration has been developed to process the signals, using a radiation hard bipolar process. Position accuracies of about 170 μm have been achieved in tests at average straw counting rates of about 12 MHz. At these rates, only about 70% of the straws give correct drift time measurements because of shadowing effects, but the large number of straws per track guarantees a measurement accuracy of better than 50 μm averaged over all straws at the LHC design luminosity, including errors from alignment.

## 2.2 Calorimetry

The calorimeters will play a crucial role at LHC. They are required to measure the energy and direction of photons, electrons, isolated hadrons and jets, as well as the missing transverse energy. At LHC the calorimeters will be the leading detectors in many measurements for the reconstruction of physics channels of prime interest. Combined with the inner tracker, calorimeter measurements are used for electron and photon identification and isolation measurements. Fast detector response (<50 ns) and fine granularity are required to minimise the impact of the pile-up on the physics performance. High radiation resistance is also needed, given the high particle fluxes expected over a period of operation of at least ten years.

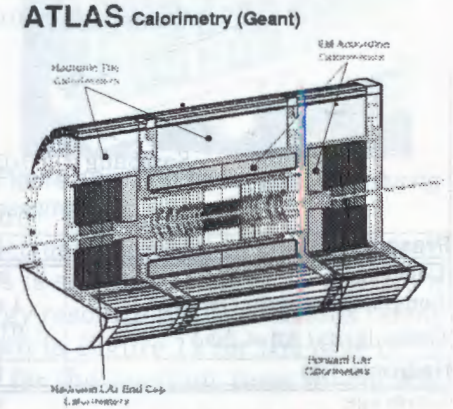


**Figure 8:** View of the ATLAS calorimetry.

The ATLAS calorimetry covers the range $|\eta|<5$ using different techniques and devices as best suited for the different requirements and radiation environment. A view of the ATLAS calorimetry is presented inFigure 8. It consists of an electromagnetic calorimeter covering the rapidity region $|\eta|<3.2$, a barrel hadronic calorimeter covering $|\eta|<1.7$, hadronic end-cap calorimeters in $1.5<|\eta|<3.2$, and

forward calorimeters covering $3.1<|\eta|<4.9$. The em calorimeter system is contained in a cylinder of outer radius 2.25 m and total length spanning 6.65 m along the beam axis. The barrel hadronic calorimeter system has an outer radius of 4.23 m and a total length spanning ~12 m. The total weight of the calorimeter system is about 4,000 tons. The rapidity coverage, granularity and longitudinal segmentation of the ATLAS calorimetry is summarized in Table 3.

**Table 3:** Rapidity coverage, granularity and longitudinal segmentation of the ATLAS calorimetry.

| **EM calorimeter** | **barrel** | **end-cap** | |
|---|---|---|---|
| Coverage | $\|\eta\|<1.475$ | $1.375<\|\eta\|<3.2$ | |
| Longitudinal segmentation | 3 samplings | 3 samplings | $1.5<\|\eta\|<2.5$ |
| | | 2 samplings | $1.375<\|\eta\|<1.5$ |
| | | | $2.5<\|\eta\|<3.2$ |
| Granularity($\Delta\eta \times \Delta\phi$) | | | |
| Sampling 1 | $0.003 \times 0.1$ | $0.025 \times 0.1$ | $1.375<\|\eta\|<1.5$ |
| | | $0.003 \times 0.1$ | $1.5<\|\eta\|<1.8$ |
| | | $0.004 \times 0.1$ | $1.8<\|\eta\|<2.0$ |
| | | $0.006 \times 0.1$ | $2.0<\|\eta\|<2.5$ |
| | | $0.1 \times 0.1$ | $2.5<\|\eta\|<3.2$ |
| Sampling 2 | $0.025 \times 0.025$ | $0.025 \times 0.025$ | $1.375<\|\eta\|<2.5$ |
| | | $0.1 \times 0.1$ | $2.5<\|\eta\|<3.2$ |
| Sampling 3 | $0.05 \times 0.025$ | $0.05 \times 0.025$ | $1.5<\|\eta\|<2.5$ |
| **Presampler** | **barrel** | **end-cap** | |
| Coverage | $\|\eta\|<1.52$ | $1.5<\|\eta\|<1.8$ | |
| Longitudinal segmentation | 1 sampling | 1 sampling | |
| Granularity($\Delta\eta \times \Delta\phi$) | $0.025 \times 0.1$ | $0.025 \times 0.1$ | |
| **Hadronic Tile** | **barrel** | **extended barrel** | |
| Coverage | $\|\eta\|<1.0$ | $0.8<\|\eta\|<1.7$ | |
| Longitudinal segmentation | 3 samplings | 3 samplings | |
| Granularity ($\Delta\eta \times \Delta\phi$) | | | |
| Samplings 1 and 2 | $0.1 \times 0.1$ | $0.1 \times 0.1$ | |
| Sampling 3 | $0.2 \times 0.1$ | $0.2 \times 0.1$ | |
| **Hadronic LAr** | | **end cap** | |
| Coverage | | $1.5<\|\eta\|<3.2$ | |
| Longitudinal segmentation | | 3 samplings | |
| Granularity ($\Delta\eta \times \Delta\phi$) | | $0.1 \times 0.1$ | $1.5<\|\eta\|<2.5$ |
| | | $0.2 \times 0.2$ | $2.5<\|\eta\|<3.2$ |
| **Forward calorimeter** | | **end-cap** | |
| Coverage | | | |
| Longitudinal segmentation | | 3 samplings | |
| Granularity ($\Delta\eta \times \Delta\phi$) | | ~$0.2 \times 0.2$ | |

*2.2.1 The electromagnetic calorimeter*

The EM calorimeter is a lead-Liquid-Argon (LAr) detector with accordion geometry, (Figure 9)[9]. In the pseudorapidity range $|\eta| < 1.8$ it is preceded by a presampler detector, installed immediately behind the cryostat cold wall, and used to correct for the energy lost in the material (inner detector, cryostats, coil) upstream of the calorimeter. The lead absorber thickness is above 24 $X_0$ in the barrel and 26 $X_0$ in the end-caps. The total number of channels is about 200,000.

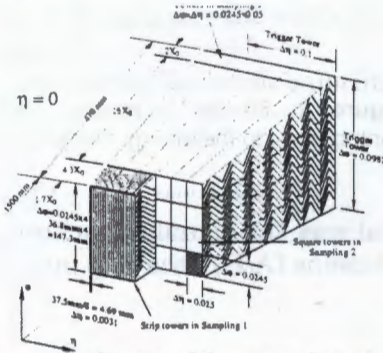


**Figure 9:** Sketch of the accordion structure of the electromagnetic calorimeter.

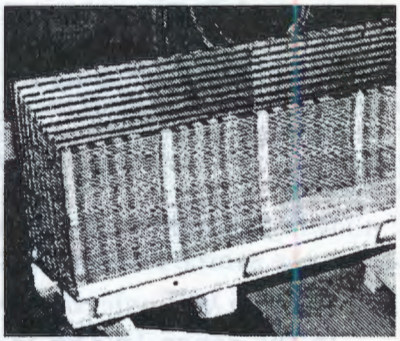

**Figure 10:** EM barrel prototype during assembly.

The energy resolution for electrons achieved in the test beam with large scale detector prototypes is shown in Figure 11 for two $\eta$ values. The contribution to the energy resolution of the various terms as a function of the rapidity is shown in Figure 12 for the case of 50 GeV $E_T$ photons. The target figure for the constant term in the ATLAS detector is below 0.7%.

Beyond energy measurement, the EM calorimeter will provide, thanks to its high granularity, powerful electron/photon identification and rejection of the jet background. The thin strips in the first sampling will allow $\pi^0$ rejection, by a factor larger than 3 at 50 GeV $E_T$. In total, the jet rejection, at 20 GeV or above, is expected to be about 5,000. Such a rejection is required to eliminate huge QCD backgrounds in the $H \rightarrow \gamma\gamma$. The narrow strips contribute also to the photon angular measurement in the $\eta$ direction, with an accuracy of about $50\text{mrad}/\sqrt{E}$, an essential information in the reconstruction of the channel mentioned above. The calorimeter is also an essential tool in identifying $\tau$ decays into hadrons. Combined with the tracker, a rejection of about 400 against jets is possible for about 30% efficien-

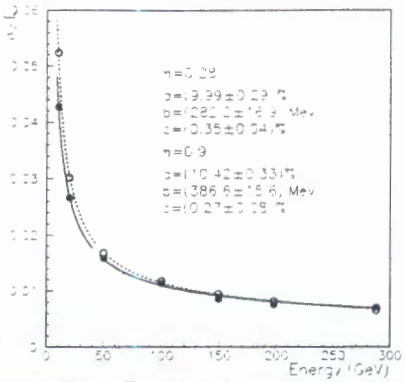

**Figure 11:** Fractional energy resolution of the beam energy for electrons incident at $\eta$=0.28 (closed circles) and at $\eta$=0.9 (open circles).

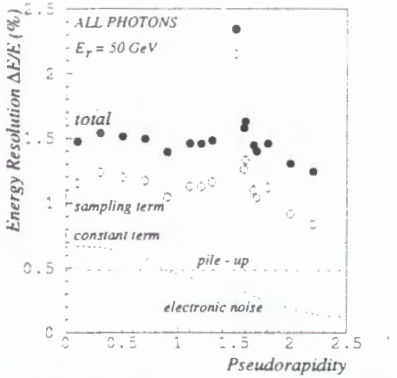


**Figure 12:** 50~GeV $E_T$ photons. Various contributions to the energy resolution.

cy, allowing to improve in an essential way the signal to background ratio in the search for MSSM Higgs bosons (A/H) decaying into $\tau\tau$.

### 2.2.2 *The Tile hadronic calorimeter*

In the range $|\eta|<1.6$ the iron scintillating tiles technique is used for the barrel and extended barrel hadron calorimeters. The hadronic barrel calorimeter is a cylinder with an inner radius of 2.28 m to an outer radius of 4.23 m. It is divided in three sections: the central barrel and two extended barrels. It is based on a sampling technique with plastic scintillator plates (tiles) embedded in an iron absorber and read out by wave length shifting fibres. The tiles are placed in plane perpendicular to the beam axis and staggered in depth, simplifying the mechanical construction and the fibre routing. In Figure 13 a barrel calorimeter module constructed according to the ATLAS dimensions is shown.

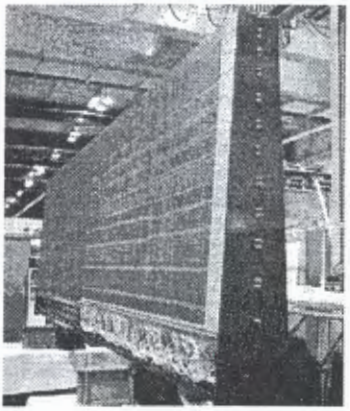

**Figure 13:** Photo of a barrel module prototype constructed in ATLAS dimensions.

The calorimeter is segmented in three layers, approximately 1.4, 4.0 and 1.8 λ thick at η=0. Azimuthally, the barrel and extended barrels are divided into 64 modules. In η, the read-out cells, built by grouping fibres into a photomultiplier, are pseudo-projective to the interaction region. The resulting granularity of the Tile calorimeter is given in Table 3. The total number of channels is of the order of 10,000. The calorimeter is placed behind the EM calorimeter (~1.2 λ) and the solenoid coil. So the total active calorimeter thickness (EM + Tile) is 9.2 λ at η=0. The amount of material in front of the muon system, that includes the support structure of the Tile calorimeter, is 11 λ at η=0.

For the hadronic calorimeter the guidelines for the energy res-

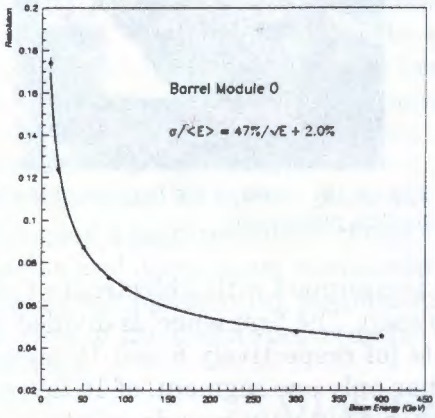


**Figure 14:** The standalone Tile calorimeter pion resolution for the barrel Module 0.

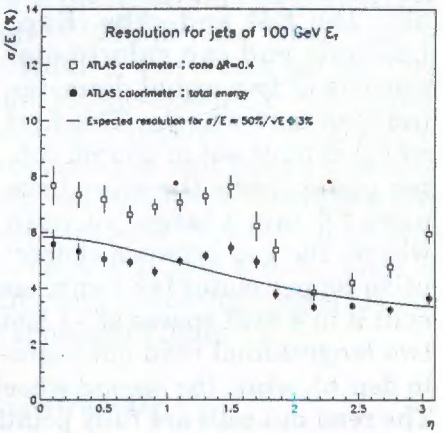


**Figure 15:** Resolution for 100 GeV $E_T$ jets as a function of η

olution performances are set requiring a jet energy resolution at different levels in different η regions: $\Delta E/E=50\%/\sqrt{E}\oplus 3\%$ for $|\eta|<3$ and $\Delta E/E=100\%/\sqrt{E}\oplus 10\%$ for $3<|\eta|<5$. Such resolutions are adequate to the tasks of providing jet reconstruction and the jet-jet mass reconstruction as well as missing $p_T$ measurement for physical process of interest. Figure 14 shows the pion energy resolution in the case of the standalone Tile calorimeter modules, while Figure 15 shows the expected jet resolution in the full rapidity range, when the information from the various calorimeters is used. From test beam runs with the em and hadronic prototype modules the pion resolution obtained are $\Delta E/E=((38.3\pm4.6)\%/\sqrt{E}+(1.62\pm0.29)\%)\oplus(3.06\pm0.18)\%/E$, well within the specifi-

cations for ATLAS.[8]

*2.2.3 The LAr hadronic calorimeters*

In the range $1.5<|\eta|<4.9$ the Liquid Argon calorimetry takes over: the end-cap hadronic calorimeter extends till $|\eta|<3.2$ while the range $3.1<|\eta|<4.9$ is covered by the high-density forward calorimeter. Both the hadronic end-cap and the forward calorimeters are integrated in the same cryostat housing also the EM end-caps. Each hadronic end-cap calorimeter consists of two, equal diameter, independent wheels. The first wheel is built out of 25 mm copper plates, while the second one uses 50 mm plates; in both wheels the gap between consecutive copper plates is 8.5 mm, and is equipped with 3 electrodes that split it in 4 drift spaces of ~1.8 mm each. The first wheel is divided in two longitudinal read-out segments (of respectively 8 and 16 layers in depth), while the second wheel has only one segment, of 16 layers. The read-out cells are fully pointing in $\phi$ but only 'pseudo-pointing' in $\eta$. The thickness of the active part of the end-cap calorimeter is ~12 $\lambda$.

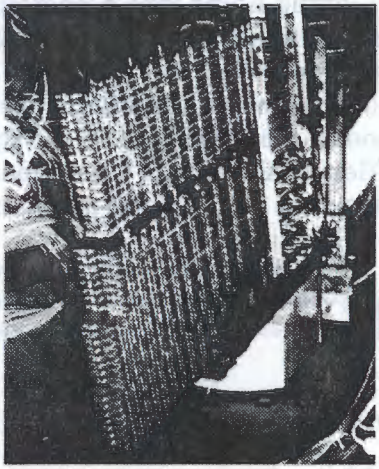

**Figure 16:** View of the hadronic end-cap module prototypes.

In ATLAS the forward calorimeter is integrated in the end-cap cryostat, with the front face at about 5 meters from the interaction point. This makes the forward calorimeter a particularly challenging detector due to the high level of radiation, however providing a clear benefit in terms of uniformity of coverage, reducing to the minimal possible level the effects of the crack and dead space in the transition region around $\eta$=3.1, with advantages for the efficiency of forward jet tagging and for the reduction of the tails in the distribution. The forward calorimeter has to accommodate at least 9 $\lambda$ of active detector in a rather short longitudinal space, and thus it is a high density detector, consisting of three longitudinal sections: the first one is in copper, while the other two are tungsten. In each of them the calorimeter consists of a metal matrix with regularly spaced longitudinal chan-

nels filled with rods. The sensitive medium is Liquid Argon and fills the gap between the rod and matrix: the gaps are 250 microns wide in the first section and 375 (500) microns in the second (last) one. In the forward calorimeter the electronic noise in a jet cone of $\Delta R=0.5$ is ~1 GeV $E_T$ at $\eta=3.2$ and drops quickly to 0.1 GeV in $E_T$ at $\eta=4.6$.

## 2.3 The Muon Spectrometer

High-momentum final-state muons are amongst the most promising and robust signatures of physics at the Large Hadron Collider (LHC). The discovery potential of the spectrometer has been optimized on the basis of selected benchmark processes, in particular Standard Model and supersymmetric Higgs decays and new vector bosons. To obtain a good performance of the apparatus for transverse momenta which are small on the scale of LHC physics, beauty physics and CP violation have also been studied. Important parameters that need to be optimized for maximum physics reach are: resolution, second-coordinate measurement, rapidity coverage of track reconstruction, trigger selectivity, trigger coverage and bunch-crossing identification. To exploit this potential, the ATLAS collaboration has designed a high-resolution muon spectrometer with stand-alone triggering and momentum measurement capability over a wide range of transverse momentum, pseudorapidity, and azimuthal angle[11]. An *rz* view of the muon spectrometer is shown in Figure 17.

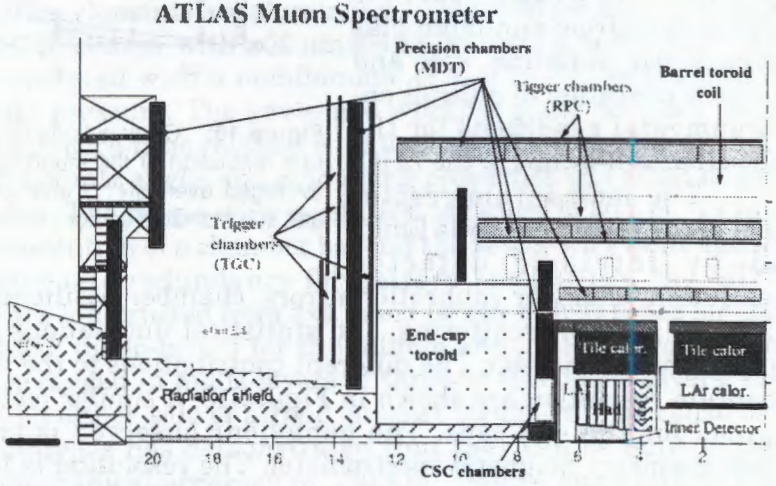


**Figure 17:** View of the ATLAS muon spectrometer.

The muon spectrometer is based on the magnetic deflection of muon tracks in a system of three large superconducting air-core toroid magnets instrumented with separate-function trigger and high-precision tracking chambers. In the pseudorapidity range $|\eta|<1.0$, magnetic bending is provided by a large barrel magnet constructed from eight coils surrounding the hadron calorimeter. For $1.4<|\eta|<2.7$, muon tracks are bent in two smaller end-cap magnets inserted into both ends of the barrel toroid. In the interval $1.0<|\eta|<1.4$ referred to as transition region, magnetic deflection is provided by a combination of barrel and end-cap fields. This magnet configuration provides a field that is mostly orthogonal to the muon trajectories, while minimising the degradation of resolution due to multiple scattering [12].

The design and performance of the muon spectrometer must satisfy exacting, and sometimes conflicting, requirements of three different kinds: the largest possible discovery reach for expected and unexpected new physics, with minimal systematic biases; good discrimination against high levels of charged and neutral particle background from minimum-bias events and radiation; safe and reliable operation in difficult environmental conditions for the anticipated life-time of the LHC.

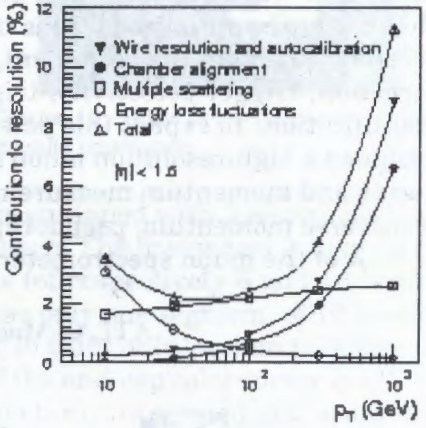


**Figure 18:** Contributions to the momentum resolution of the muon spectrometer, averaged over $|\eta|<1.5$ and azimuthal angle, in a standard sector.

The momentum resolution of the spectrometer is limited by intrinsic detector resolution, chamber calibration errors, chamber positioning uncertainties, multiple scattering, and statistical fluctuations of energy loss in the calorimeter. The different contributions to the barrel momentum resolution are shown in Figure 18; a similar picture is obtained for the end-caps. The behaviour observed is typical for open-geometry magnetic spectrometer. The resolution is limited by energy loss fluctuations at small momenta and by detector resolution

at high momenta, whereas the multiple scattering effect is approximately momentum-independent.

The momentum resolution is typically 2-3% over most of the kinematic range apart from very high momenta, where it increases to ~10% at $p_T$=1 TeV. The momentum resolution is shown in Figure 19 as a function of pseudorapidity for $p_T$=100 GeV muons. The resolution is largely constant over the $\eta$ range of the spectrometer, with the exception of some spikes at pseudorapidities obstructed by barrel magnet elements, and of an enhancement around $\eta$=1.5 owing to a degraded bending power in the transition region between barrel and end-cap magnets.

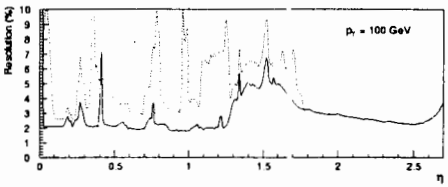


**Figure 19:** Momentum resolution for $p_T$=100 GeV as a function of $\eta$, averaged over all azimuth angles. The solid curve applies to a standard sector; the dotted curve corresponds to one of the bottom sectors, where barrel toroic coils are captured inside the support structure for the inner parts of the detector.

*2.3.1 Monitored Drift Tubes (MDT)*

Over most of the pseudorapidity range, a precision measurement of the track coordinates in the principal bending direction of the magnetic field is provided by Monitored Drift Tubes (MDTs). The basic detection elements are aluminium tubes of 30 μm diameter and 400 μm wall thickness, with a 50 μm diameter central W-Re wire. The tubes are operated with a non-flammable Ar-$CH_4$-$N_2$ mixture at 3 bar absolute pressure. The envisaged working point provides for a highly linear space-time relation with a maximum drift time of ~500 ns, a small Lorentz angle, and good aging properties due to small gas amplification. The single-wire resolution is typically 80 μm. To improve the resolution of a chamber beyond the single-wire limit and to achieve adequate redundancy for pattern recognition, the MDT chambers are constructed from 2×4 mono-layers of drift tubes for the inner and 2×3 mono-layers for the middle and outer stations. The tubes are arranged in multi-layers of three or four mono-layers, respectively, on either side of a rigid support structure. The construction of prototypes has demonstrated that they can be built to the required mechanical accuracy of ~30 μm. Table 4 summarises the

main parameters of the muon spectrometer.

**Table 4:** Overview of the muon chamber instrumentation. 'area covered' refers to chamber modules which normally contain several detector layers.

| | Precision chambers | | Trigger chambers | |
|---|---|---|---|---|
| | CSC | MDT | RPC | TGC |
| Number of chambers | 32 | 1194 | 596 | 192 |
| Number of r/o channels | 67,000 | 370,000 | 355,000 | 440,000 |
| Area covered ($m^2$) | 27 | 5,500 | 3,650 | 2,900 |

*2.3.2 Cathode Strip Chambers (CSC)*

In the first station in the end-cap region and for pseudorapidities $|\eta|>2$, Cathode Strip Chambers (CSCs) are used to provide a finer granularity which is required to cope with the demanding rate and background conditions in this region of the apparatus. The CSCs are multi-wire proportional chambers with cathode strip read-out and with a symmetric cell in which the anode-cathode spacing is equal to the anode wire pitch. The precision coordinate is obtained by measuring the charge induced on the segmented cathode by the avalanche formed on the anode wire.

Good spatial resolution is achieved by segmentation of the read-out cathode and by charge interpolation between neighbouring strips. The cathode strips for the precision measurement are oriented orthogonal to the anode wires. The anode wire pitch is 2.54 mm and the cathode read-out pitch is 5.08 mm; r.m.s. resolutions of better than 60~mm have been measured in several prototypes. Other important characteristics are small electron drift times (30 ns), good time resolution (7 ns), good two-track resolution, and low neutron sensitivity. A measurement of the transverse coordinate is obtained from orthogonal strips, i.e. oriented parallel to the anode wires.

The CSCs are arranged in 2×4 layers. The design uses low-mass construction materials to minimise multiple scattering and detector weight. The present baseline CSC gas is a non-flammable mixture of 30% Ar, 50% $CO_2$ and 20% $CF_4$, with a total volume of about 1.1 $m^3$. The fact that this gas contains no hydrogen, combined with the small gap width, explains the low sensitivity to neutron background. In general, the CSC performance is less sensitive to variations of the gas parameters than that of the MDTs.

*2.3.3 Trigger chambers (RPCs and TGCs)*

The trigger chambers for the ATLAS muon spectrometer serve a threefold purpose, and must therefore fulfil the following basic re-

quirements: bunch crossing identification, requiring a time resolution better than the LHC bunch spacing of 25 ns, a trigger with well-defined $p_T$ cut-off in moderate magnetic fields, requiring a granularity of the order of 1 cm, measurement of the second coordinate in a direction orthogonal to the one measured in the precision chambers with a typical resolution of 5-10 mm.

The proposed system employs two different types of detectors, Resistive Plate Chambers (RPCs) in the barrel ($|\eta|<2.4$) and Thin Gap Chambers (TGCs) in the end-cap region. Both types of trigger chambers also provide a 'second-coordinate' measurement of track coordinates orthogonal to the precision measurement, in a direction approximately parallel to the magnetic field lines. The second-coordinate capability of the trigger chambers is designed to match the acceptance of the precision chambers. The RPC is a gaseous detector providing a typical space-time resolution of 1 cm × 1 ns with digital read-out. The basic RPC unit is a narrow gas gap formed by two parallel resistive bakelite plates, separated by insulating spacers. The primary ionization electrons are multiplied to form avalanches by a high, uniform electric field of typically 4.5 kV/mm. Amplification in avalanche mode produces pulses of typically 0.5 pC. The candidate gas mixture is based on tetrafluoroethane ($C_2H_2F_4$), a non-flammable and environmentally safe gas that allows for a relatively low operating voltage. The signal is read out via capacitive coupling by metal strips on both sides of the detector. A trigger chamber is made from two rectangular detector layers, each one read out by two orthogonal series of pick-up strips: the '$\eta$ strips' are parallel to the MDT wires and provide the bending view of the trigger detector; the '$\phi$ strips', orthogonal to the MDT wires, provide the second-coordinate measurement which is also required for the off-line pattern recognition.

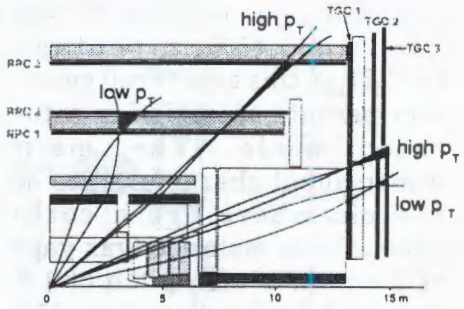


**Figure 20:** Schematic representation of the muon trigger.

The TGC chambers are designed in a way similar to multiwire proportional chambers, with the difference that the anode wire pitch

is larger than the cathode-anode distance. Signals from the anode wires, arranged parallel to the MDT wires, provide the trigger information together with read-out strips arranged orthogonal to the wires.

The read-out strips also serve to measure the second coordinate. Using a highly quenching gas mixture of 55% $CO_2$ and 45% n-pentane (n-$C_5H_{12}$), this type of cell geometry permits operation in saturated mode. The main dimensional characteristics of the chambers are a cathode-cathode distance (gas gap) of 2.8 mm, a wire pitch of 1.8 mm, and a wire diameter of 50 μm. The operating high voltage foreseen is 3.1 kV. The electric field configuration and the small wire distance provide for a short drift time and thus a good time resolution. As the angle increases, the tracks pass closer to the wire, thus reducing the maximum drift distance and improving the time resolution. In the ATLAS chamber layout, all muons passing through TGCs with transverse momenta above the required threshold have incident angles greater than 10°.

**Figure 21:** View of the test beam installation with the muon detector prototypes

## 3 Trigger and DAQ

The ATLAS trigger is organized in three trigger levels (LVL1, LVL2, LVL3), as shown in Figure 22. At LVL1, special-purpose processors act on reduced-granularity data from a subset of the detectors (calorimeters and muon system). The LVL1 trigger accepts data at the full LHC bunch-crossing rate of 40 MHz (every 25 ns). The latency is about 2 μs, and the maximum output rate is limited to 100 kHz by the capabilities of the subdetector read-out systems and the LVL2 trigger. During the LVL1 processing, the data from all parts of the ATLAS detector are held in pipeline memories. Requirements on the LVL1 trigger are such that it must identify unambiguously the bunch crossing containing the interaction of interest and introduce negligible dead time. The information from the LVL1 trigger system is used to identify the 'regions of interest' (ROI) in the detector, containing interesting features such as high $p_T$ electromagnetic clusters (elec-

trons or photons), jets and muons.

The LVL2 trigger uses full-granularity, full-precision data from most of the detectors, but examines only the 'regions of interest'. The LVL2 trigger reduces the rate from to about 1 kHz. The LVL2 trigger then has to access and process only a small fraction of the total detector data, with corresponding advantages in terms of the required processing power and data-transfer capacity. The total LVL2 latency is variable, up to about 10 ms.

At LVL3, the full event data are used to make the final selection of events to be recorded for off-line analysis. The LVL3 system must achieve a data-storage rate of 10-100 MB/s by reducing the event rate and/or the event size. For some triggers, for example Higgs boson candidates, the full event data will be recorded with an event size of about 1 MB, corresponding to a maximum event rate of about 100 Hz. Algorithms that will be used at LVL1 and LVL2, rates and efficiencies for signals and backgrounds have been evaluated with detailed physics and detector Monte Carlo simulations. It is to be noted that the trigger processors at all three levels will be programmable, so that the trigger criteria can be adapted according to the experience from initial running, and to increasing luminosity of LHC.

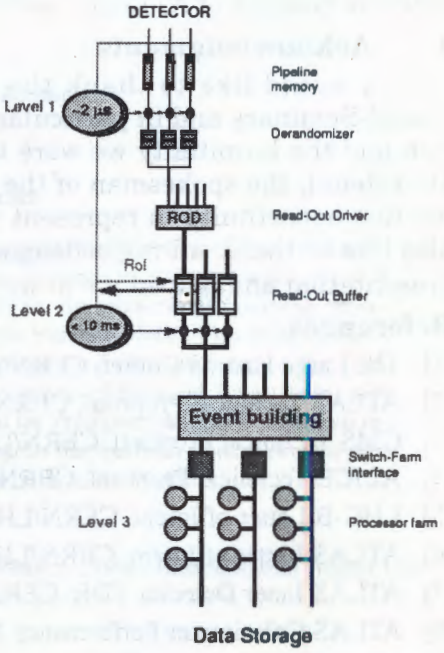


**Figure 22:** The ATLAS trigger and DAQ architecture.

The full data of each event accepted by LVL2 are assembled and transferred to a farm of processors that perform full-event analysis and make the LVL3 selection before permanent recording. The data-merging stage will be based on a high-speed switching network, interconnecting Data Acquisition (DAQ) memories and LVL3 processing units, supervised by data-flow manager components. It is

too early at this stage to freeze the technological implementation of the DAQ system. The architecture of technology-independent implementations of DAQ models is being investigated with detailed system performance simulations using front-line software tools.[13]

Pre-prototype hardware for the LVL1 and LVL2 trigger processors and clock distribution system has been developed. The processors have been successfully tested in connection with subdetector test beam data-taking. Trigger and DAQ prototyping and testing is an integral part of the test beam activities with complete prototype detector systems of ATLAS.

## 4 Acknowledgments

I would like to thank the organizers of the International School-Seminars and in particular Prof. N. Shumeiko for the invitation and the hospitality we were treated. I would also like to thank Dr. P.Jenni, the spokesman of the ATLAS collaboration, for offering me this opportunity to represent the collaboration. Finally I would also like to thank all my colleagues who provided material for this presentation and helped me in writing these proceedings.

## References

[1] The Large Hadron Collier, CERN/AC/95--05.

[2] ATLAS Technical Proposal, CERN/LHCC/94--43, 15 December 1994.

[3] CMS Technical Proposal, CERN/LHCC/94--38, 15 December 1994.

[4] ALICE Technical Proposal, CERN/LHCC/95--71, 15 December 1995.

[5] LHC-B Letter of Intent, CERN/LHCC/ 95--5, 25 August 1995.

[6] ATLAS Letter of Intent, CERN/LHCC/92--4, LHCC/I2 (1992).

[7] ATLAS Inner Detector TDR, CERN/LHCC 97-16/17 (1997).

[8] ATLAS Calorimeter Performance TDR, CERN/LHCC/96-40 (1996).

[9] ATLAS Liquid Argon Calorimeter TDR, CERN/LHCC 96-41 (1996).

[10] ATLAS Tile Calorimeter TDR, CERN/LHCC 96-42 (1996).

[11] ATLAS Muon Spectrometer TDR, CERN/LHCC 97-22 (1997).

[12] ATLAS Magnet System TDR, CERN/LHCC 97-18/19/20 (1997).

[13] ATLAS Computing Technical Proposal, CERN/LHCC/96-43 (1996).

# A Pedagogical Introduction to the CMS Electromagnetic Calorimeter

D. Barney

*CERN, Geneva, Switzerland*

***ECAL Group***

***CMS collaboration***

**Abstract**

Physics at the LHC requires extremely high performance detectors. The CMS electromagnetic calorimeter ('ECAL') has been designed to facilitate the discovery of the Higgs boson, thought to be responsible for the spontaneous symmetry breaking observed in the electroweak sector of the Standard Model. This report outlines the particular physics requirements that govern the choice and design of the CMS ECAL and describes in some detail the properties of the Lead Tungstate crystals used in the ECAL, the readout system and the Preshower detectors. Testbeam results are presented which illustrate the progress that has been made during the past few years and which highlight the features of the CMS ECAL.

Presented at *The Actual Problems of Particle Physics*, Gomel, Belarus 8-16th August 1997

# 1 Introduction

This report is intended to be a pedagogical introduction to the design features of the CMS ECAL. The target audience was a group of theoretical particle physics students from the Commonwealth of Independent States. With a view to this audience, an introduction (section 2) to the basics of electromagnetic calorimetry is first given, which introduces the physical quantities important for the choice of a good calorimeter medium. Section 3 then outlines the physics goals of CMS, in particular the discovery of the Higgs boson. Attention is paid to the possibility of an 'intermediate mass' Higgs (between about 80 GeV and 135 GeV) as its 'gold-plated' discovery channel is the decay to two photons; this decay imposes strict criteria on the design of the ECAL. Section 4 describes the physical and optical characteristics of the lead tungstate ($PbWO_4$) crystals, whilst section 5 briefly overviews the photodetectors and readout electronics. There are two Preshower detectors in CMS, one in the barrel and one in the endcaps, although only the endcap preshower is a baseline item; they have similar structures but perform different functions: photon angular measurement in the barrel; neutral pion rejection in the endcaps. These detectors are described in section 6. Finally, testbeam results showing progress during the past few years are given in section 7.

The majority of the information found in this report can also be found, in more detail, in the CMS ECAL Technical Design Report [1].

# 2 Introduction to Electromagnetic Calorimeters

Each sub-detector in a high energy physics experiment is optimized for the detection and measurement of a specific type of particle. Electromagnetic calorimeters measure the *energy* of electrons and photons. They also aid in particle identification (specifically electron/charged-pion separation in conjunction with the tracker) and help to measure the energy of high energy hadrons (in conjunction with the hadron calorimeter - HCAL).

## 2.1 Detection Mechanism

When a high energy photon or electron is incident upon a dense medium it may initiate an 'electromagnetic shower', via the processes of bremsstrahlung, pair-production and, at low energies, Compton scattering. The electrons/positrons in the shower may produce either ionization or 'light' (or both), depending on the material in which the shower occurs. Calorimeters based upon ionization detection are not discussed in this report.

Light may be produced in three different ways:

1. Separate shower media and scintillators - e.g. lead+scintillator 'sandwich' [2]. The shower develops in the lead and the produced electrons/positrons create scintillation in layers of scintillator.
2. Čerenkov light [3] inside a dense medium such as lead glass [4] or lead fluoride ($PbF_3$).
3. Scintillation light [5] inside the shower medium - e.g. caesium iodide or lead tungstate.

The produced light is then passed, perhaps via light-guides, to photodetectors such as photomultiplier tubes (PMTs) or silicon photo-diodes.

Figure 1 shows a simulation of a typical electromagnetic shower produced inside lead tungstate crystals from an incident 10 GeV electron. The spread of the shower in both the longitudinal and transverse directions is dependent upon many factors, including some physical properties of the shower medium and the energy of the incident particle. In this diagram three crystals are shown; each measures about 23cm in length and has a transverse dimension of just over 2cm - see section 4. The 'produced' scintillation light is not shown.

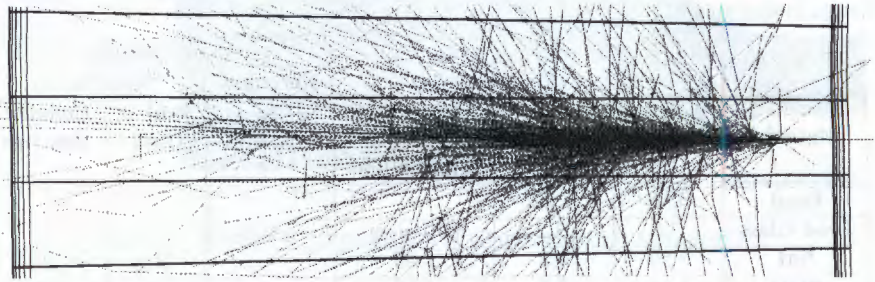

Figure 1: Simulation of a 10 GeV electron incident (from the right) on lead tungstate crystals. The photodetectors would be on the left (but not shown). The dashed lines represent photons produced by electron/positron bremsstrahlung; short solid lines represent the electrons and positrons created by pair-production.

## 2.2 Physical Quantities Relevant for Shower Media

A variety of different shower media have been used in high energy physics experiments. The appropriate choice depends upon the particular application - resolution, cost, space requirements etc. The principle physical characteristics which govern the choice are as follows:

- **Radiation length - $X_0$** - the longitudinal distance over which an electron loses (1-1/e) of its energy by bremsstrahlung; about 25 $X_0$ of material is required in order to longitudinally contain about 99% of the shower. An approximate form relating $X_0$ to a specific element with atomic number $Z$, atomic mass $A$ and density $\rho$ is given in equation 1.

$$X_0(cm) = \frac{716.4A}{\rho Z(Z+1)ln(287/\sqrt{Z})} \tag{1}$$

  For a mixture or compound this becomes:

$$1/X_0 = \sum w_j/X_j \tag{2}$$

  where $w_j$ and $X_j$ are the fraction by weight and the radiation length for the $j$th element.

- **Molière radius - $R_M$** - the scale for the transverse spread of an electromagnetic shower. It is related to $X_0$ by equation 3 below.

$$R_M = X_0 E_s/E_c \tag{3}$$

  where $E_s \approx 21$ MeV and $E_c$ is the *critical energy* defined by Rossi [6] as the energy at which ionization loss per radiation length is equal to the electron energy.

- $N_{pe}$ - Amount of detected light per unit energy deposited.
- **Wavelength(s) of light emitted in shower** - important for the choice of photodetector.
- $T_{scint}$ - Scintillation emission time (if relevant).

Table 1 gives the values of these quantities for some shower media. These will be discussed further in section 4.

| | | | | Light Emission | | |
|---|---|---|---|---|---|---|
| | | | | Čerenkov | Scintillation | |
| Material | $X_0$ (cm) | $R_M$ (cm) | Light output (relative for scintillators) | Peak $\lambda$ (nm) | Peak $\lambda$ (nm) | Emission time (ns) |
| Lead | 0.56 | 1.22 | - | - | - | - |
| Lead Glass | 2.8 | 3.2 | 290 $\gamma$/cm | >500 | - | - |
| NaI | 2.59 | 4.8 | 1.00 | - | 410 | 230 |
| BGO | 1.12 | 2.3 | 0.18 | - | 480 | 300 |
| CsI | 1.85 | 3.5 | 0.20 | - | 315 | 16 |
| $CeF_3$ | 1.68 | 2.6 | 0.08 | - | 340 | 25 |
| $PbWO_4$ | 0.89 | 2.2 | 0.01 | - | 440 | 5-15 |

Table 1: Physical characteristics of some shower media used in electromagnetic calorimeters.

## 2.3 Types of Electromagnetic Calorimeter

The two principle types of light-detecting electromagnetic calorimeter are shown in figures 2 and 3.

**Sampling:** The calorimeter is divided into alternate 'sheets' of dense shower media and light producer. For example, a common setup is to use layers of lead (or depleted uranium) interspersed with plastic scintillator. The shower develops in the lead layers; electrons/positron from the shower which pass through the plastic produce scintillation light which is then detected.

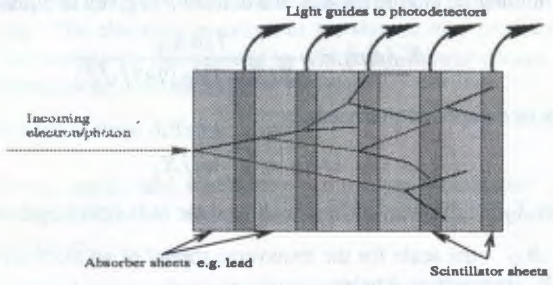


Figure 2: Schematic representation of a sampling calorimeter, comprising lead sheets (shower media) and scintillators (light producers)

**Homogeneous:** One substance acts as both shower medium and light producer. The light may be either scintillation (as in CsI and $PbWO_4$ for example) or Čerenkov. This light can then be detected.

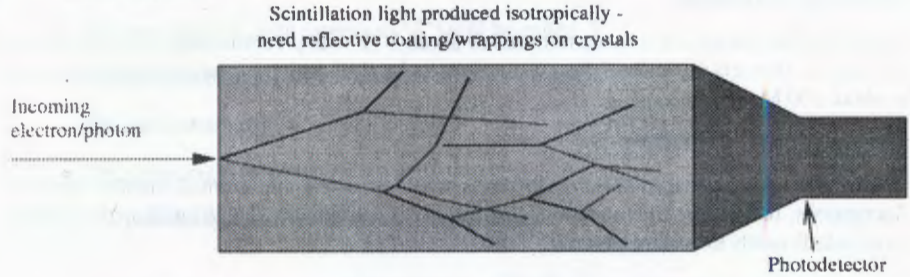


Figure 3: Schematic representation of a homogeneous calorimeter

## 2.4 The Energy Resolution Equation

The ultimate aim of an electromagnetic calorimeter is to measure the energy of photons/electrons as well as possible. The energy resolution can be approximated by equation 4.

$$\frac{\sigma_E}{E} = \frac{a}{\sqrt{E}} \oplus \frac{\sigma_N}{E} \oplus c \tag{4}$$

where:

$E$ is the energy, usually in GeV

$\frac{\sigma_E}{E}$ is the energy resolution

$a$ is the "stochastic" term - mainly governed by photostatistics and sampling fluctuations

$\sigma_N$ is the "noise" term - electronics noise and pileup

$c$ is the "constant" term - mainly from shower containment limitations and calorimeter non-uniformities

$\oplus$ implies a quadratic sum

For optimum calorimeter performance each term should be small and of the same order at the relevant electron/photon energies.

## 2.5 Relative Merits of Sampling and Homogeneous Calorimeters

If we assume a Higgs mass of about 100 GeV (relevant for $H \longrightarrow \gamma\gamma$ searches) then the typical photon energy will be of the order of about 50 GeV (in the barrel) and about 180 GeV (in the

endcaps - due to the Lorentz boost). The average photon energy of relevance may then be approximated to about 100 GeV.

**Sampling Calorimeters**

It is difficult to obtain a stochastic term below about 10% without demanding strict mechanical tolerances. This sets the scale of the constant term to be $\leq 1\%$ and the noise term to be equivalent to about 500 MeV.

**Homogeneous Calorimeters**

These have the potential to achieve stochastic terms of $\approx 2\%$ due to much smaller sampling fluctuations. In this case the limitation is the control of systematics which build up the constant term, which needs to be around 0.5%.

The expected energy resolution of a $PbWO_4$ calorimeter is:

$$\frac{\sigma_E}{E} = \frac{2\%}{\sqrt{E}} \oplus \frac{\approx 200 MeV}{E} \oplus 0.5\% \tag{5}$$

# 3 Physics Requirements

In this section the design requirements of the electromagnetic calorimeter are summarised. The design is driven by the physics goals of CMS which will be reviewed briefly. Particular attention is paid to the two-photon decay of the intermediate Higgs boson as this channel is extremely demanding of the electromagnetic calorimeter.

## 3.1 Reminder of CMS Design Philosophy

At this point it is useful to recall the CMS design goals [7]:

1. A very good and redundant muon system
2. The best possible electromagnetic calorimeter consistent with 1.
3. A high quality central tracker to complement 1. and 2.
4. A financially affordable detector

The detector should thus be optimized for leptons and photons, facilitating the detection of the Higgs through various decay channels.

## 3.2 Terminology

The following definitions will be used throughout the remainder of this section and those subsequent:

- 1 year at low luminosity $(10^{33} \mathrm{cm}^{-2} \mathrm{s}^{-1}) \equiv 10^4 \mathrm{pb}^{-1}$
- 1 year at high luminosity $(10^{34} \mathrm{cm}^{-2} \mathrm{s}^{-1}) \equiv 10^5 \mathrm{pb}^{-1}$

and for the co-ordinate system:

- The beam axis will be called '$Z$'
- The vertical axis (with respect to '$Z$') will be called '$Y$'
- The horizontal axis (with respect to '$Z$') will be called '$X$'
- The azimuthal angle is '$\phi$'
- The polar angle is '$\theta$'
- The pseudorapidity ('$\eta$') is in the '$Z-\theta$' plane

## 3.3 Physics Goals

### 3.3.1 Standard Model (SM) Higgs

The principle goal of both CMS and ATLAS is the discovery (or not) of the Higgs boson. The Standard Model Higgs should have a mass between about 80 GeV/c$^2$ [1] and 1 TeV/c$^2$ [2]. Figure 4 shows diagramatically the 'gold-plated' decays of the Standard Model Higgs as a function of its mass.

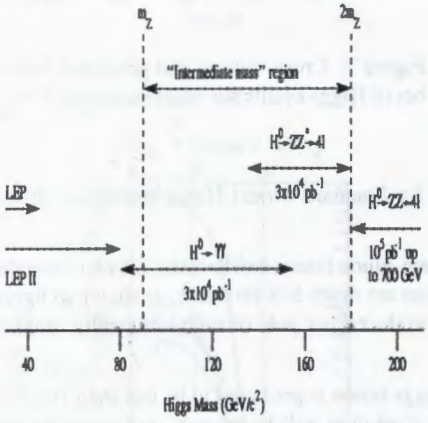


Figure 4: The 'gold-plated' decays of the Standard Model Higgs

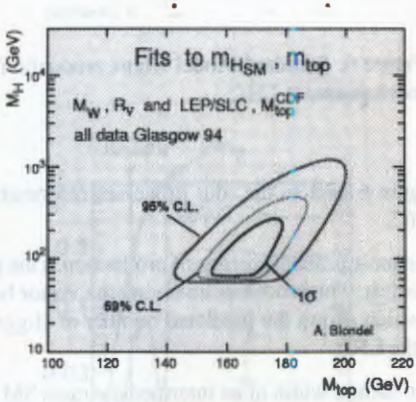


Figure 5: $\chi^2$ as a function of $m_H$ ($m_{top}$ = 165 GeV/c$^2$) for precision electroweak data interpreted within the SM radiative corrections framework

The discovery range for the Standard Model Higgs can be extended up to the 1 TeV limit by detecting forward jets from WW and ZZ fusion and exploiting decay channels with large branching ratios (e.g. $H^0 \longrightarrow WW \longrightarrow l\nu jj$ and $H^0 \longrightarrow ZZ \longrightarrow lljj$).

[1] This lower limit is due to the reach of the current colliders - the Tevatron at Fermilab and LEP at CERN

[2] Set by the constraints of unitarity

It is important to note that many of the decay channels involve leptons and/or photons; consequently the electromagnetic calorimeter will play a leading rôle in the discovery of a Standard Model Higgs.

Current electroweak measurements point to a Standard Model Higgs with a relatively low mass, around 100 GeV/$c^2$. Figure 5 shows the $\chi^2$ of various measurements as a function of the Higgs mass. The data are a few years old now, as exemplified by the mass of the top quark used (165 GeV/$c^2$), but are still consistent with the most recent measurements.

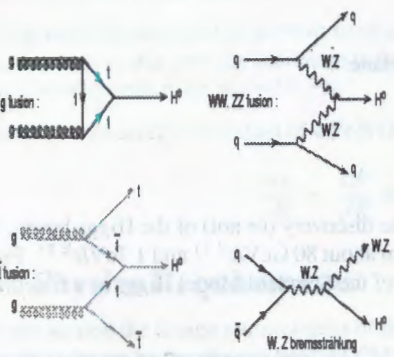


Figure 6: Standard Model Higgs production mechanisms at LHC

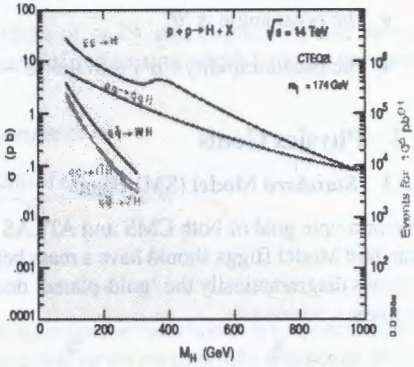


Figure 7: Cross-section and predicted number of Higgs events per years running at LHC

Figure 6 depicts the four processes responsible for Standard Model Higgs production at the LHC.

The most probable means of production is the gluon-gluon fusion mechanism, which is also the cleanest. The processes involving the vector bosons are much less probable, as shown in figure 7 which shows the predicted number of Higgs' produced per year of high luminosity running at the LHC.

The natural width of an intermediate mass SM Higgs boson is predicted to be less than 10 MeV (see figure 8). This means that the Higgs mass resolution will be entirely dominated by the detector resolution.

The most stringent requirements imposed on the ECAL are from the two-photon decay of the intermediate mass Higgs boson.

Figure 8 shows the natural width of the Higgs as a function of its mass, together with three simple Feynman diagrams depicting the two-photon and four-lepton decay modes [3] which are relevant for Higgs masses below about 200 GeV/$c^2$. The branching ratios for various decay modes are shown in figure 9 as a function of the Higgs mass.

[3] for a Higgs mass above about 140 GeV/$c^2$ and below $2m_Z$ one of the $Z$ bosons in the four-lepton diagram should be replaced by a $Z^*$

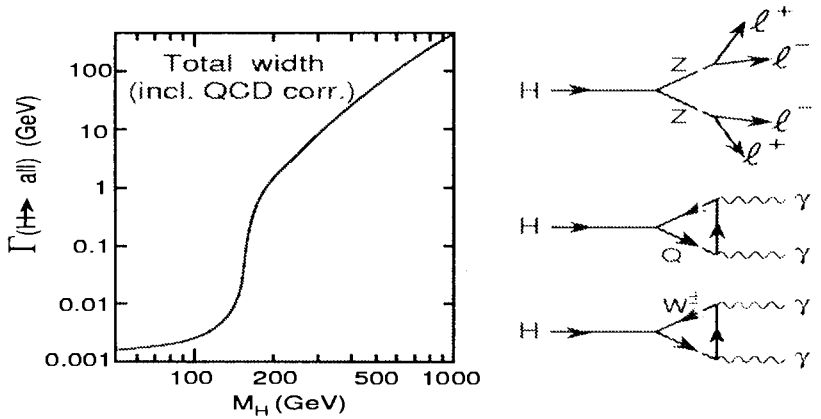


Figure 8: The natural width of the Standard Model Higgs as a function of its mass. Also shown are Feynman diagrams depicting the decays to two photons and four leptons.

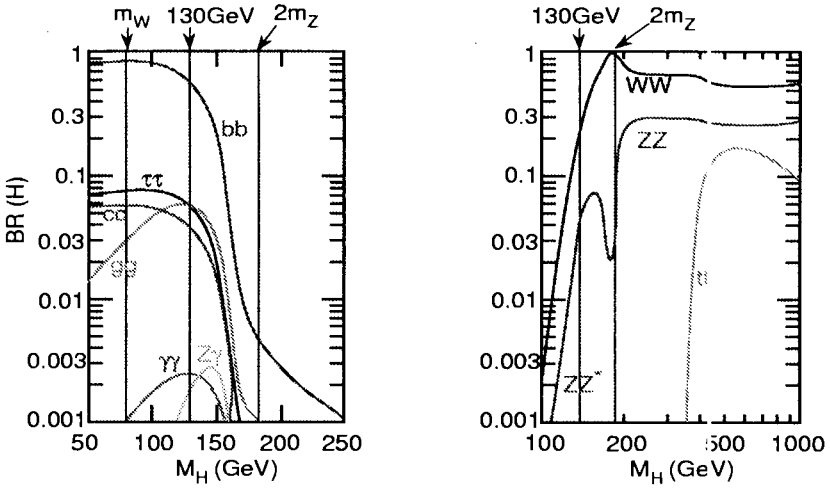


Figure 9: Branching ratios for the main decay channels of the Standard Model Higgs as a function of its mass.

It is clear that the dominant decay mode is to $b\bar{b}$ pairs but this is extremely difficult to detect efficiently. The two-photon decay (relevant for Higgs masses between about 90 GeV/$c^2$ and 160 GeV/$c^2$) is rare but is very clean. For Higgs masses above about 140 GeV/$c^2$ the decay to $ZZ^*$ (subsequently decaying to four leptons) becomes important (and above $2m_Z$ the decay to two real $Z$'s).

### 3.3.2 Minimal Supersymmetric Model (MSSM) Higgs

Figure 10 shows the CMS '$5\sigma$' contours in the $m_A - tan\beta$ plane for a variety of decays of supersymmetric Higgs particles. It is apparant that a large region of the parameter space will be covered - the shaded area shows the region of parameter space which cannot be covered.

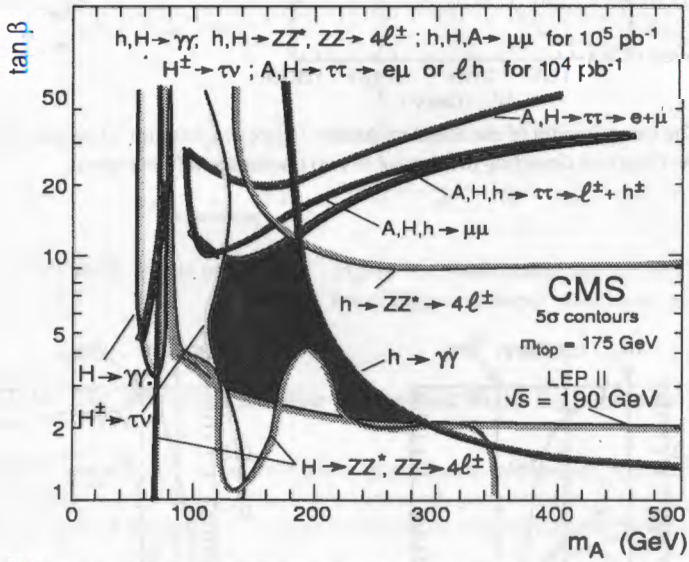


Figure 10: CMS $5\sigma$ contours for various decays of a Higgs particle within the Minimal Supersymmetric Model

Again it should be emphasised that many of the decay channels involve leptons and/or photons.

### 3.3.3 Other SUSY Searches

Events with many high energy jets and missing transverse energy ($E_t$) are the most obvious (and model independent) signatures in searches for squarks and gluinos. Hermeticity of the calorimeters is thus of the utmost importance.

### 3.3.4 B Physics

With an integrated luminosity of about $10^4 pb^{-1}$ CMS is sensitive to values of $\sin 2\beta \geq 0.05$ and $\sin 2\alpha \geq 0.06$. These should be measured via the decay channels $B_d^0 \longrightarrow J/\psi K_s^0$ and $B_d^0 \longrightarrow \pi\pi$ respectively. Time development of $B_s^0 \Longleftrightarrow \bar{B}_s^0$ oscillations will enable the mixing parameter $x_s$ to be measured for values up to 20-25.

### 3.3.5 Heavy Ion Physics

In addition to colliding protons, the LHC will also be able to collide heavy ions at $\sqrt{S} = 5.5$ TeV per nucleon pair. A strong suppression of the production of $\Upsilon'$ and $\Upsilon''$ relative to $\Upsilon$ (when compared to $pp$ collisions) will signal the formation of the quark-gluon plasma.

## 3.4 The Intermediate Mass Higgs - 85 GeV/c$^2$ $< m_H <$ 180GeV/c$^2$

As mentioned previously, the measured width of an intermediate mass SM Higgs boson is entirely dominated by the detector performance.

In this case the mass resolution is given by:

$$\frac{\sigma_m}{m} = \frac{1}{2}[\frac{\sigma_{E1}}{E1} \oplus \frac{\sigma_{E2}}{E2} \oplus \frac{\sigma_\theta}{\tan(\theta/2)}] \quad (6)$$

where:

- $\frac{\sigma_m}{m}$ is the mass resolution
- $\frac{\sigma_{E1}}{E1}$ and $\frac{\sigma_{E2}}{E2}$ are the energy resolutions for the two photons
- $\theta$ is the angle (in radians) between the two photons
- $\sigma_\theta$ is the angular resolution

In addition to the requirement that the terms in the mass resolution be kept small the design of an appropriate ECAL is also dictated by the necessities of background rejection, geometric acceptance and radiation tolerance.

### 3.4.1 Energy Resolution Requirements

For illustration purposes we can assume a Higgs mass of 100 GeV/c$^2$. In this case the following kinematic cuts would be applied to two-photon events in CMS:

$$P_t^{\gamma_1} > 40GeV \qquad P_t^{\gamma_2} > 25GeV \qquad |\eta| < 2.5 \quad (7)$$

The mean photon energy in the central barrel region ($|\eta| < 0.5$) would thus be around 50 GeV. If we require the ECAL constant term to be 0.5% then the stochastic and noise terms in the barrel should be around $2\%/\sqrt{E}$ and 150 MeV respectively.

In the outer part of the endcaps ($1.5 < |\eta| < 2.0$) the mean photon energy is around 140 GeV, whilst the minimum photon energy is around 80 GeV. This means that, keeping the same noise and constant terms, a higher stochastic term is acceptable (around $5\%/\sqrt{E}$).

### 3.4.2 Angular Resolution

In order to not dominate the mass resolution, the angular resolution should be around $50mrad/\sqrt{E}$. The angular measurement requires the photon incidence positions on the ECAL to be measured accurately, and for the primary vertex position to be known. The photon incidence positions can be measured by the ECAL itself to a good accuracy (see section 7). The largest uncertainty is in the measurement of the primary vertex position along the beam axis ('Z'): the bunches of protons have very small lateral dimensions but have a longitudinal rms spread of about 5.3cm.

In the low luminosity phase of CMS the hard tracks associated with the production of the Higgs allows the primary vertex position (along 'Z') to be measured.

However, in the high luminosity running there will be around 17 events per bunch crossing, which may make the measurement of the primary vertex position virtually impossible. If the primary vertex position is not known, the contribution to the mass resolution could be around 1.5 GeV for a 100 GeV/$c^2$ Higgs, a factor of about 3 higher than the mass resolution at low luminosity. In this case it may be necessary to install a barrel preshower for the angle measurement at high luminosity - see section 6.

### 3.4.3 Backgrounds to $H \longrightarrow \gamma\gamma$

As shown in section 3.3.1, $H \longrightarrow \gamma\gamma$ is a relatively rare decay (branching ratio $\approx 10^{-3}$ for $m_H < 150$ GeV/$c^2$) and has some large backgrounds. Diagrams depicting the four most important backgrounds are shown in figure 11.

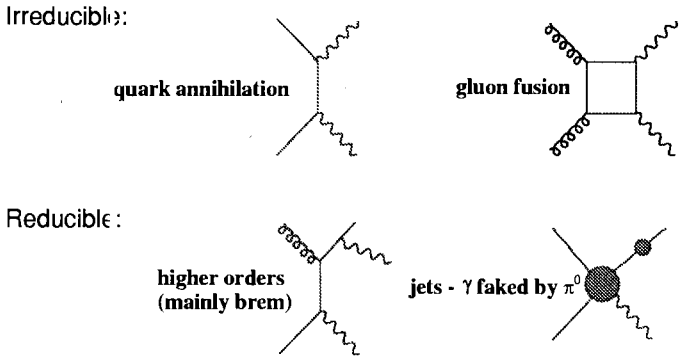


Figure 11: The principle backgrounds to the two-photon decay of the Higgs

Isolation cuts can reduce the bremsstrahlung and jet backgrounds by a large factor, but an additional rejection factor of about 3 is required for the jet background so that it does not dominate the irreducible backgrounds. In the barrel of CMS the rejection of $\pi^0$s in jets which fake single photons can be performed by the crystals due to the relatively large separation between the two photons from the $\pi^0$. In the endcaps the separation is much smaller, necessitating a fine-granularity preshower detector - see section 6.

Table 2 summarises the signal and background cross sections for the $H \longrightarrow \gamma\gamma$ decay channel, assuming an ECAL with the energy resolution terms given in section 2.5.

| **Signal** | $m_H$ **110 GeV** | $m_H$ **130 GeV** | **Background** $d\sigma/dm_{\gamma\gamma}$ **(fb/GeV)** | $m_{\gamma\gamma}$ **110 GeV** | $m_{\gamma\gamma}$ **130 GeV** |
|---|---|---|---|---|---|
| $\sigma.B(H \rightarrow \gamma\gamma)$ **(fb)** | 75.9 | 68.3 | **Quark annihilation** | 61.0 | 41.2 |
| **Acceptance** | 57% | 63% | **Gluon fusion** | 72.4 | 42.4 |
| $\sigma_m low\mathcal{L}$ **(MeV)** | 475 | 600 | **Isolated bremsstrahlung** | 84.4 | 50.4 |
| $\sigma_m high\mathcal{L}$ **(MeV)** | 870 | 960 | **TOTAL (isolated)** | 217.8 | 134.0 |

Table 2: (a) Signal cross-section, acceptance and mass resolution at $m_H$=110 and $m_H$=130 GeV/$c^2$, (b) background cross-sections after cuts.

The degradation in mass resolution in going from low to high luminosity is mainly due to the necessary presence of the barrel preshower which degrades the energy resolution somewhat.

The background due to jets, specifically $\pi^0$s in jets faking single photons, was not included in the table. There are very large theoretical uncertainties in calculating the magnitude of this background such that we require the predicted level (after cuts) to be less than the irreducible background. As mentioned previously, isolation cuts can reduce this background by a factor of about 3, and a highly segmented ECAL can provide a further factor of 3 in the barrel.

### 3.4.4 Geometric Acceptance and Radiation Dose

It should be noted that several important physics channels, particularly the SM Higgs decays and various SUSY channels, require an extremely hermetic ECAL. The coverage at high $\eta$ is limited by the radiation dose which would be received. At $|\eta| > 2.6$, for an integrated luminosity of $5 \times 10^5 pb^{-1}$ (corresponding approximately to the first ten years of running at the LHC) the ECAL would receive a dose of $> 7$ Mrad and a neutron fluence of $> 2 \times 10^{14}$n/cm$^2$. The calorimeter medium, electronics, readout etc. have to be able to survive in this extremely hostile environment.

## 3.5 Contributions to the Di-photon Mass Resolution

Assuming that an electromagnetic calorimeter can be made to fulfill the criteria mentioned in the previous sections, the contributions to the di-photon mass resolution for a Higgs of 110

GeV/$c^2$ are as given in table 3.

| Effect | Contribution, in MeV, to mass resolution for $m_H$ = 110 GeV | | | |
|---|---|---|---|---|
| | Low Luminosity $\mathcal{L} = 10^{33} cm^{-2} s^{-1}$ | | High Luminosity $\mathcal{L} = 10^{34} cm^{-2} s^{-1}$ | |
| Stochastic Term | 2.0% | 150 | 0.5% | 400 |
| Constant Term | 0.5% | 350 | 0.5% | 350 |
| Energy equivalent of noise | | 200 | | 200 |
| Angular measurement in range $\|\eta\| < 1.1$ | using tracks | 200 | 50 mrad/$\sqrt{E}$ | 625 |
| Energy pileup | | - | | 200 |
| **TOTAL** | | **475** | | **870** |

Table 3: Contributions to the di-photon mass resolution at low and high luminosity

An homogeneous electromagnetic calorimeter made from single crystals can achieve these goals.

Figure 12 shows the background subtracted di-photon spectra for Higgs masses of 90, 110, 130 and 150 GeV/$c^2$ for one years running at high luminosity.

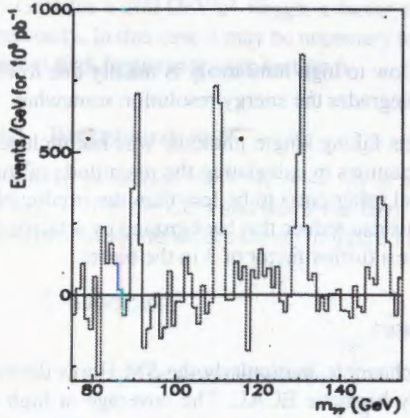


Figure 12: Background subtracted di-photon mass plot for $10^5 pb^{-1}$ with signals at $m_H$ = 90, 110, 130 and 150 GeV/$c^2$ in the CMS $PbWO_4$ calorimeter

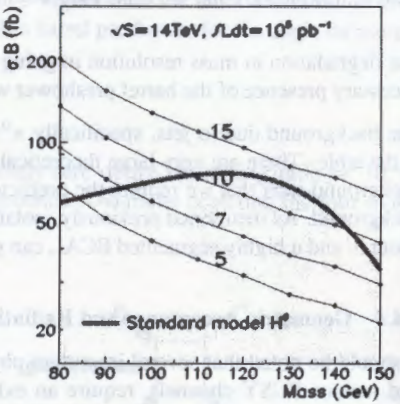


Figure 13: Signal significance contours for $10^5 pb^{-1}$ taken at high luminosity

Also shown, in figure 13 are signal significance contours: it is apparent that the signal will have a significance greater than 5 for a majority of the intermediate mass range.

# 4 The CMS $PbWO_4$ Crystal Calorimeter

This section describes the physical and optical properties of lead tungstate - $PbWO_4$ - crystals, which have been chosen as the active medium for the CMS electromagnetic calorimeter. Some recent measurements concerning light yield, radiation tolerence and energy resolution are given. A brief description of the current mechanical construction is also presented.

## 4.1 Shower Media Physical Quantities Revisited - with Reference to $PbWO_4$

Section 2.2 described how the physical properties of a shower medium affect the performance of an electromagnetic calorimeter. The following is a summary of the attractive properties of $PbWO_4$.

- $X_0$ - this should be as short as possible to allow a compact calorimeter. For $PbWO_4$ the radiation length is 0.89cm which means only 23cm of crystal are needed for 'full' longitudinal shower containment. This results in:
  - lower cost per unit area (c.f. $CeF_3$ which would need 42cm long crystals and which costs approximately the same as $PbWO_4$ *per unit volume*)
  - ability to place the whole calorimetry (including the hadron calorimeter) inside the superconducting solenoid of CMS
- $R_M$ - a small Molière radius allows a high granularity detector to be made at a small radius. For $PbWO_4$ this is about 2.2cm.
  - less crystals needed to laterally contain a shower - improves isolation efficiency and reduces pileup
  - excellent spatial precision - useful for angular resolution

Figure 14 shows a view of the CMS detector. The compact design is a direct consequence of the short length of the $PbWO_4$ crystals.

- **Light emission time** - should be as short as possible. Most of the light from $PbWO_4$ is emitted within 25ns, as demonstrated in figure 15. This is advantageous since we require that as few time samples are used as possible to reduce noise.
- **Amount of light output** - as much as possible. This is relatively low for $PbWO_4$
  - amplification can introduce noise
  - standard amplifying photodetectors (e.g. PM tubes) cannot operate satisfactorily in a magnetic field of 4T

  These problems have been largely overcome with the progress made on silicon avalanche photodiodes (APDs) - see section 5.

  Figure 16 shows the light yield in photoelectrons per MeV (p.e./MeV) deposited for 20 crystals produced in Bogoroditsk in 1997. The mean value of 12.5 p.e./MeV (measured with a PM tube which covers the whole of the rear surface of a crystal) is equivalent to about 2.5 p.e./MeV into a $5x5mm^2$ APD and about 5 p.e./MeV into a pair of APDs - as planned for the final CMS barrel ECAL.

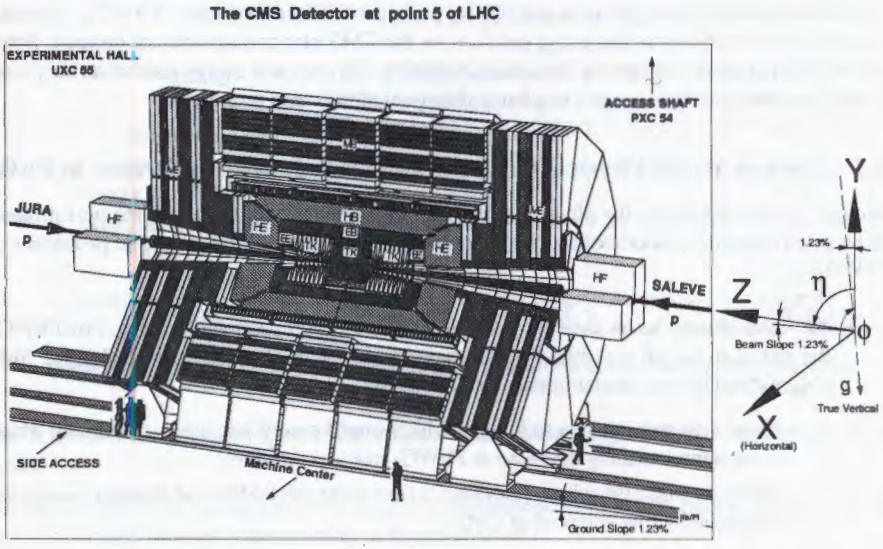


Figure 14: The CMS detector

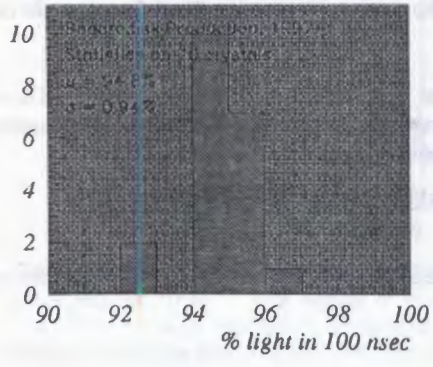


Figure 15: Percentage of light in 100nsec compared to 1$\mu$sec

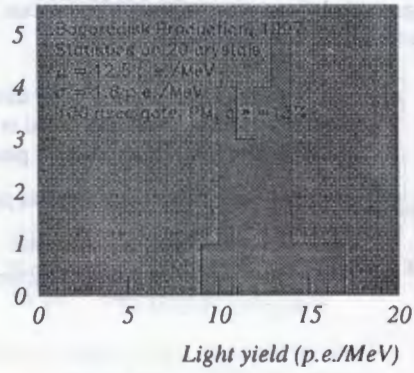


Figure 16: Light yield 2.5cm from the PM

- **Wavelength of light emitted.** Peak for $PbWO_4$ is around 450nm.
  - UV light is difficult to detect with silicon devices
  - transmission of light through the crystal depends on wavelength

  Figure 17 shows the radioluminescence spectrum for $PbWO_4$ crystals, together with the transmission curve. It is apparent that the complete scintillation spectrum can be transmitted through $PbWO_4$. However, impurities and non-uniformities in the crystals may result in absorption centres which will reduce this transmission, as described in the next section.

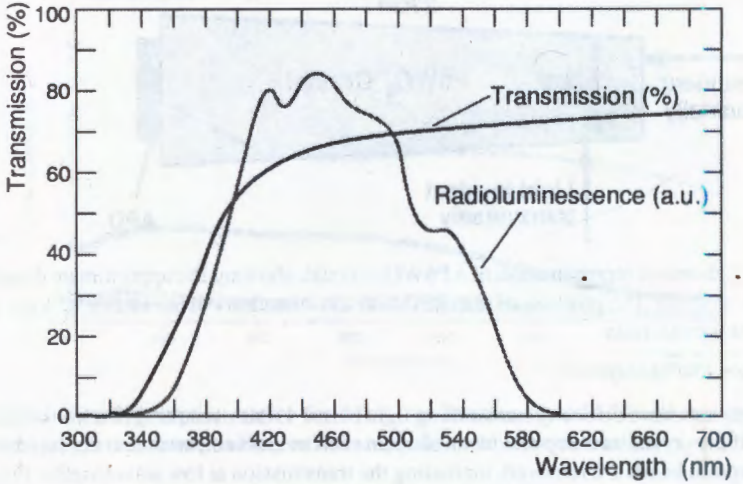


Figure 17: Radioluminescence and transmission spectra for $PbWO_4$ crystals

- **Radiation hard** - to neutrons, photons and charged particles see section 4.3
- **Substantial production capacity already exists**
  - Bogoroditsk - Russia
  - Shanghai Institute of Ceramics (SIC) - China
  - Kharkov - Ukraine
  - Crytur - Czech Republik
  - Carat - Ukraine

During the production period (5 years) we expect to be able to make around 1500 crystals per month. The total number of crystals will be around 120000.

## 4.2 Optical Characteristics of the $PbWO_4$ Crystals

Figure 18 shows a schematic representation of a $PbWO_4$ crystal of the approximate dimensions to be used in the CMS barrel ECAL. The crystals are tapered such that they present a constant solid angle to particles coming from the interaction point.

In CMS the particles will be incident longitudinally (from the 'left' in the diagram) and this is also the standard way of testing the crystals in a testbeam. However, for some studies, such as measuring the transverse transmission or longitudinal uniformity the light or particles may be incident transversely, as shown.

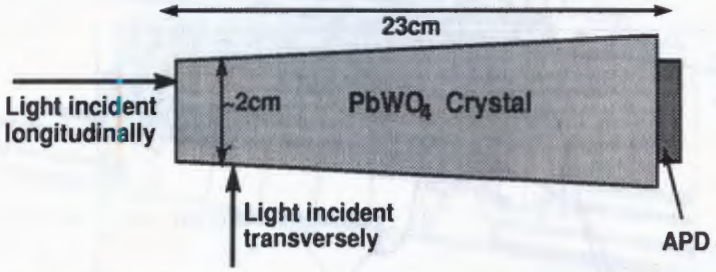


Figure 18: Schematic representation of a $PbWO_4$ crystal, showing the approximate dimensions to be used in CMS, the position of the APD and the directions of incidence of light and/or particles for various tests

*Transmission and absorption*

Undoped crystals have difficulty transmitting light below 450nm, resulting in a loss of scintillation light. If the crystals are doped with an element such as niobium, lanthanum or lutetium then some absorption bands are removed, increasing the transmission at low wavelengths. Figure 19 shows transmission curves for undoped and doped crystals.

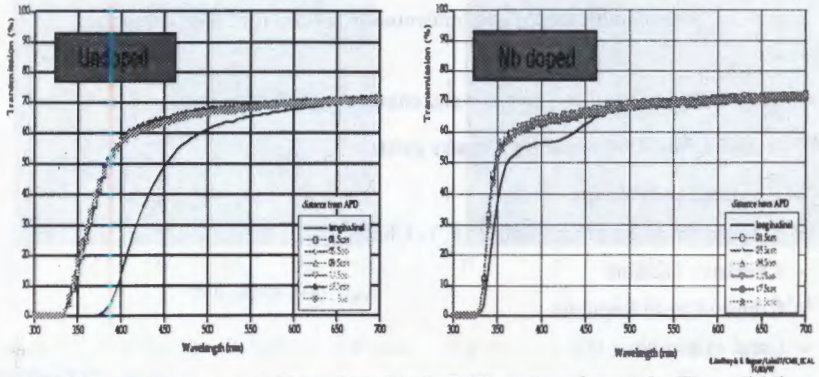


Figure 19: Transmission curves for undoped and niobium-doped crystals. The solid line shows the longitudinal transmission whilst the data points are transverse transmission measured at various points along the crystal.

The transmission edge for the niobium-doped crystals is much steeper, and the longitudinal transmission (light passes through 23cm of crystal) is virtually the same as the transverse transmission in this case.

These dopants are particularly important for the control of induced absorption (after irradiation), as demonstrated in figure 20 which shows the induced absorption as a function of wavelength for four full-size Russian crystals. The doped crystals are between a factor of 2 and 5 better (longer absorption length) than the undoped crystal.

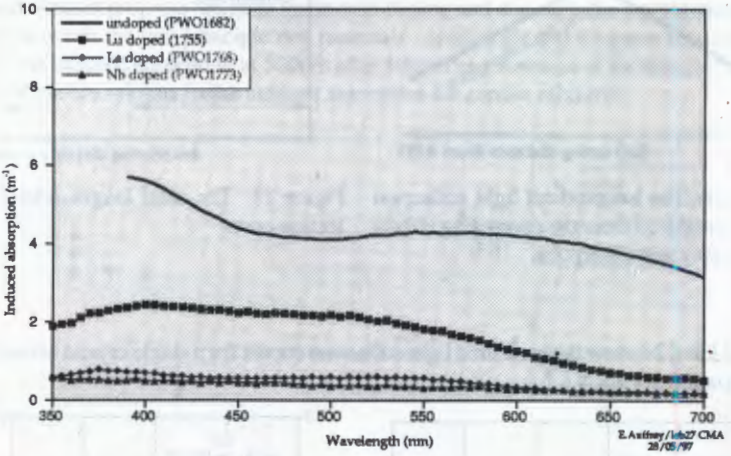


Figure 20: Induced absorption curves for 4 full-size Russian crystals. The longer the induced absorption length (i.e. lower on the vertical scale) the more 'transparent' the crystal.

*Longitudinal Uniformity*

The tapered shape of the crystals has a focussing effect on any light inside a crystal: light produced at the front of the crystal (farthest from the photodetector) is focussed more, and thus has more chance of being detected by the photodetector, than light produced towards the back of the crystal. However, if the absorption length of the crystal is relatively short, light produced at the front of the crystal has more chance of being absorbed than that produced at the back. The light collection efficiency is thus a function of position along the crystal, as illustrated in figure 21. The shape of the longitudinal light collection curve can contribute to the constant term. The ideal shape is shown in figure 22.

The most important region is around the shower maximum. This region should have a flat response. It is useful for the curve to show an increase towards the back of the crystal such that late developing showers are enhanced - this reduces low energy tails.

Recent crystals have shown a marked increase in their absorption lengths, resulting in the light collection curves being dominated by the focussing effect. This is far from the ideal case as the light collection decreases towards the back of the crystal. There is thus a need for crystal 'uniformization': systematic depolishing of parts of the crystal can change the light collection curve to be closer to the ideal case, thus reducing the contribution to the constant term.

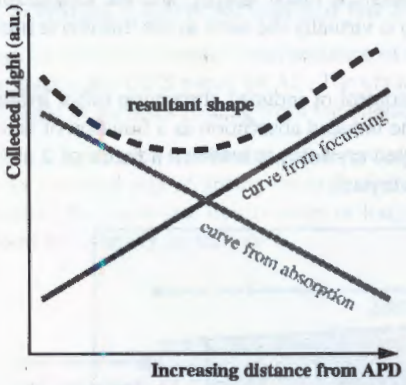


Figure 21: The longitudinal light collection curve - produced from the competing effects of focussing and absorption

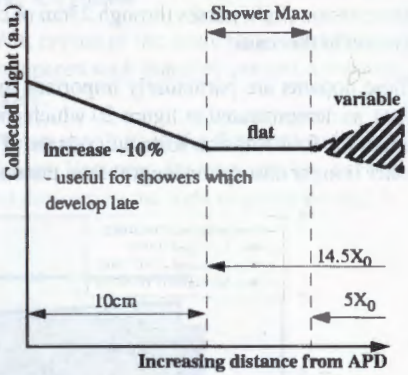


Figure 22: The ideal longitudinal light collection curve

Figures 23 and 24 show the measured light collection curves for a single crystal before and after uniformization at CERN.

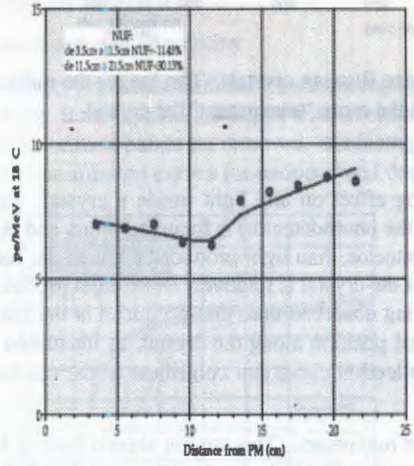


Figure 23: Light collection as a function of distance from the photodetector for a crystal before uniformization

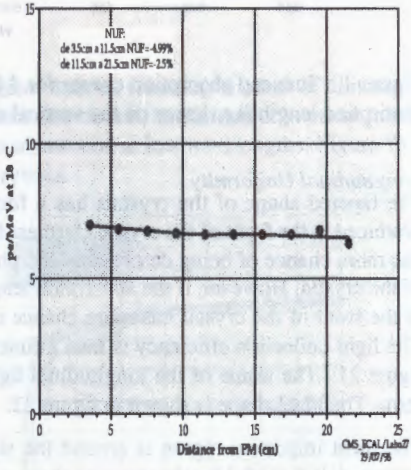


Figure 24: The corresponding light collection curve for the same crystal after uniformization

## 4.3 Radiation Tolerance

As mentioned previously, the radiation environment in CMS is extremely challenging. Lead tungstate crystals have been shown to be radiation hard to high (Mrads) levels, due to the fact that the scintillation mechanism is intrinsically radiation hard. However, some damage has been seen at surprisingly low levels in test beam experiments (few hundred rads, after which it saturates). The effect of radiation damage is to induce colour centres which reduce the transmission, and thus the amount of collected light; the scintillation mechanism remains unaffected. Recent progress has been made with doping and also with the crystal stoechiometry (the ratio between the two principle raw materials - lead oxide and tungsten trioxide). Figure 25 shows the induced absorption at 500nm after 50krad as a function of the stoechiometry. It is clear that there are minima in the induced absorption for certain mixtures.

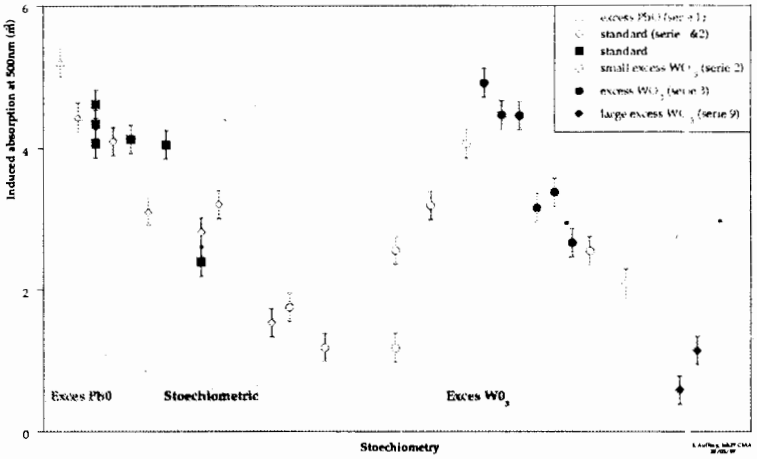


Figure 25: The variation of induced absorption length with stoechiometry for 29 full size Russian $PbWO_4$ crystals

Figure 26 then shows some recent results of low-dose radiation damage on various types of crystal. The light yield of each crystal is also given. The worst crystal is the one with non-optimized stoechiometry and also no doping. Optimizing the stoechiometry increases the radiation hardness and also increases the light yield. Doping with different elements then increases the radiation hardness further, whilst at the same time increasing the light yield.

To summarize, recent progress has shown that optimizing both the doping and stoechiometry not only increases the radiation tolerance but also the light yield of the crystals.

However, even with the best crystals there is still some small amount of low-level radiation damage. This necessitates an accurate in-situ monitoring system using either LED or laser light. This monitoring system can then be used to 'follow' the radiation damage (and recovery) to enable a correction to be applied to the measured energy deposits. Figure 27 shows the correspondance between signals due to an LED calibration pulse and to signals from electrons during test beam irradiation to 650 rads. The inset histogram is of the vertical distances of the

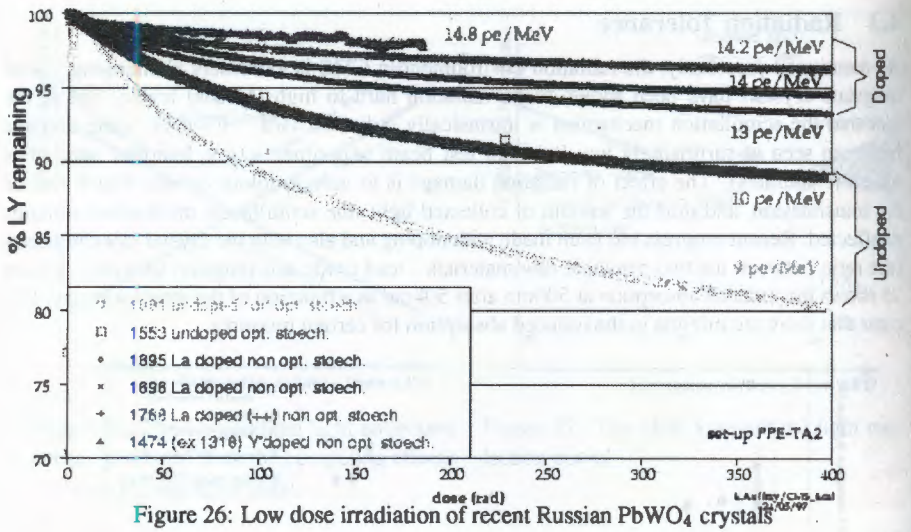


Figure 26: Low dose irradiation of recent Russian $PbWO_4$ crystals

points from the straight line fit, the gradient of which is used to perform the correction to the data. The width of the distribution of this inset histogram essentially gives the calibration error introduced by the use of the LED system, which should be kept to a small (less than 0.5%) level.

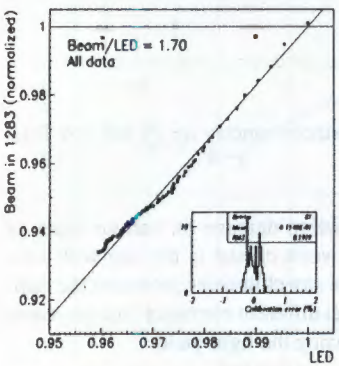


Figure 27: Correspondance between LED and beam signals during testbeam irradiation to 650 rads

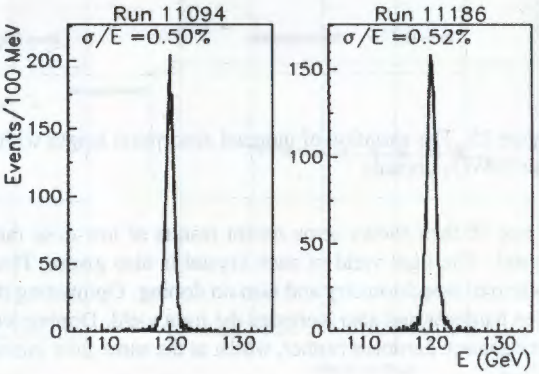


Figure 28: Energy spectra for 120 GeV $e^-$ before (left) and after (right) irradiation to 650 rads

Figure 28 shows the energy spectrum measured by a 3x3 array of crystals due to 120 GeV electrons before and after irradiation to 650 rads. The data taken during and after irradiation

have been corrected using the LED signal. The change in the measured energy resolution is within the experimental uncertainty which suggests that the scintillation mechanism has not been damaged. See [8] for more details.

## 4.4 ECAL Mechanical Structure

The CMS ECAL will contain approximately 120000 units; each unit consists of a lead tungstate crystal, readout device (see section 5) and associated readout electronics and optical/electronic calibration systems. In the ECAL barrel an array of 6 x 2 crystals is assembled inside a hollow 'alveolar' submodule. The alveolar is constructed from a low density two-layer composite material. The first layer (closest to the crystals) is a 25 $\mu$m aluminium foil which acts as a reflector for the light produced in the crystal and also aids mechanical rigidity. The second layer is a glass fibre epoxy resin 75$\mu$m thick. Although the walls of the alveolar are very thin - 100$\mu$m - the composite structure is extremely strong and enables a small inter-crystal gap of 0.4mm to be achieved within a submodule (including tolerances). The gap between crystals in adjacent submodules is a maximum of 0.6mm. Figure 29 shows the mechanical pieces which form a submodule. The alveolar unit is 'closed' by a foam bottom plate, into which fibres for the optical calibration system are mounted, and an aluminium top plate. Plastic cylinders inside the aluminium top plate freeze the crystal positions and allow accurate placement of the APDs.

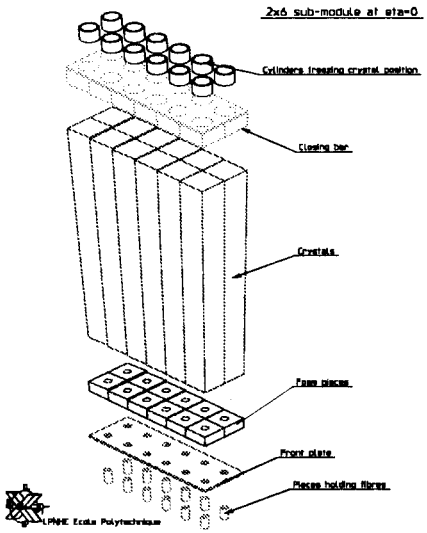


Figure 29: The mechanical structure of a barrel ECAL submodule

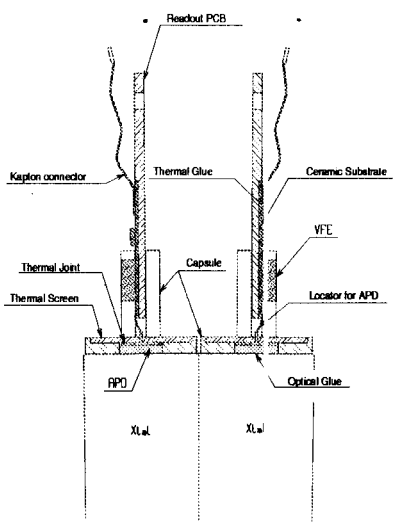


Figure 30: A detailed view of the placement of the APDs on the back of the crystals

Figure 30 shows a detailed view of the back of the crystals showing the placement of the APDs together with the supporting 'capsule' and very-front-end readout electronics.

A group of 12x4 submodules is assembled into a 'supermodule' as shown in figure 31 which provides further mechanical rigidity and includes support and cooling structures. Each supermodule weighs about 600kg. There are 8 supermodules in $\eta$ and 18 in $\phi$. The submodules inside the supermodule are angled by 3° such that the crystals do not point to the interaction vertex, reducing the effect of gaps between crystals.

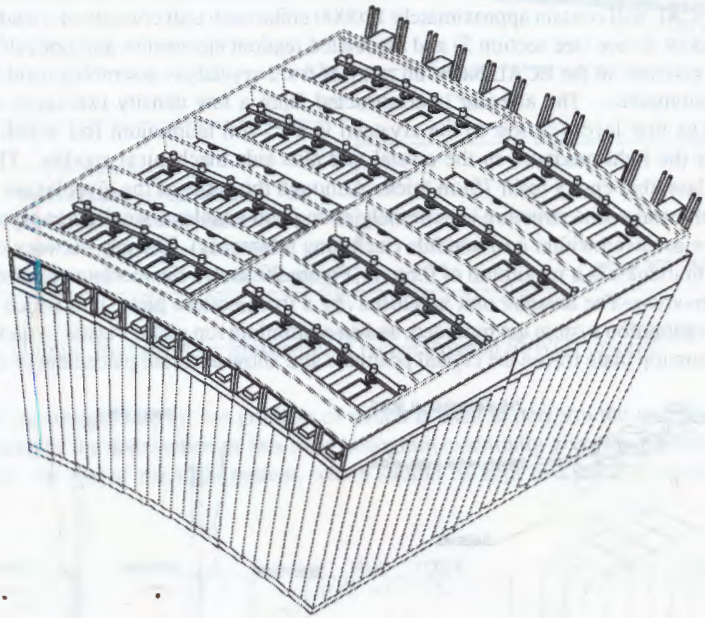

Figure 31: The mechanical structure of a barrel supermodule

The endcap ECAL has a different overall structure to the barrel. The crystals have square front and rear faces which are slightly larger than in the barrel, but are tapered in a different way to the barrel, as shown in figure 32 in order to achieve off-pointing in two dimensions. The presence of the endcap preshower, containing approximately 3 $X_0$ of absorber, allows the crystals to be shorter (by 1cm) than in the barrel. Arrays of 6x6 crystals are placed inside alveolar structures similar to those used in the barrel to form identical 'supercrystals' and these supercrystals are arranged in an 'x-y' grid to cover the majority of the endcap fiducial area - see figure 33. The remaining area, on the outer and inner radii, is covered by dedicated modules.

The overall layout of the CMS ECAL is shown in figure 34 including the endcap preshower.

The barrel ECAL extends up to $\eta = 1.479$, whilst the endcap covers the region $1.479 < \eta < 2.61$. Pileup effects and radiation damage limit the performance of the calorimeter at very high $\eta$ so the 'precision coverage' is defined as the region $|\eta| < 2.5$ (excluding the barrel/endcap interface region).

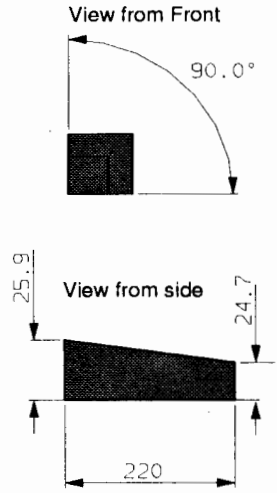


Figure 32: The dimensions of an endcap crystal

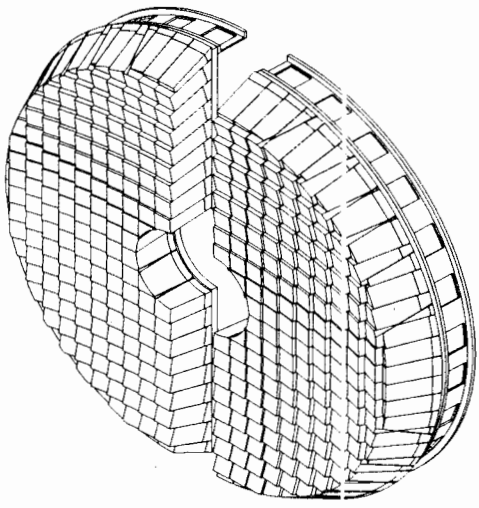

Figure 33: The endcap supercrystal layout

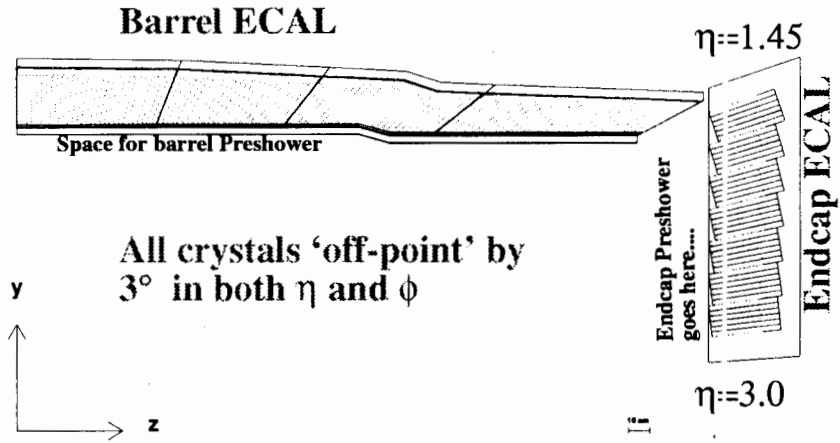


Figure 34: The overall layout of the CMS ECAL. The 'step' in basket 3 of the barrel ECAL enables the barrel preshower to be present if necessary at high luminosity. It should be noted that this design is now obselete: the step is no longer present - it is envisaged that if the barrel preshower is necessary, the final layer of MSGCs in the CMS tracker will be removed to make space (see section 8).

# 5 Photodetectors and Electronics

The relatively low light output of the lead tungstate crystals imposes strict requirements on the type of photodetector used: it must have internal amplification and low noise. Further constraints are the high magnetic field (4T), the compact structure of CMS and the severe radiation environment - particularly in the endcaps. This last constraint has the effect that the photodetectors used in the barrel are not the same as those used in the endcaps.

## 5.1 Avalanche Photodiodes - APDs

The requirements for a compact amplifying photodetector which is able to operate in a high magnetic field are satisfied by a breed of silicon detectors called avalanche photodiodes (APDs). These devices are similar in principle to conventional silicon photodiodes, but they contain a multiplication region which can give a gain of up to a few hundred, depending on how they are constructed. A schematic section through such a device is given in figure 35.

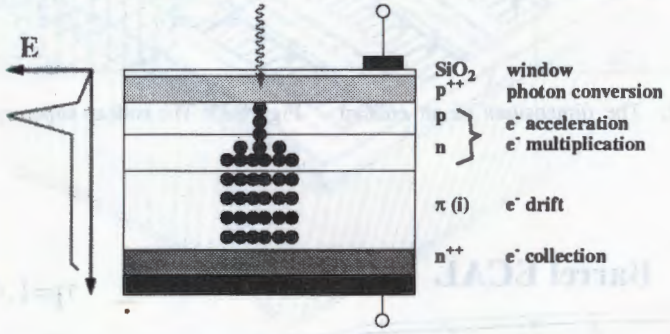


Figure 35: Schematic cross-section of an APD

Essentially, an incident photon is converted to an electron-hole pair in the $p^{++}$ layer, the electron is accelerated (causing multiplication) in the high field p and n regions, and then the 'cloud' drifts in a region of intrinsic silicon and is finally collected.

APDs have some important advantages:

- internal gain of between 50 and 200 - operate at a gain of 50
- low capacitance (due to drift region)
- ability to operate in a high magnetic field
- compact - few tens of microns thick
- sufficiently radiation hard to withstand the neutron flux in the barrel

However, it is relatively difficult to manufacture an APD with a large area: the maximum size of suitable APDs available at present is about $5x5mm^2$. This is a small fraction of the rear surface

of the crystal, so it is planned to use two APDs per crystal in CMS such that the performance of the ECAL is not limited by the photostatistics contribution to the stochastic term. The gain of the devices is sensitive to temperature - approximately 2% per °C. The fluctuations in the leakage current increase with radiation damage such that APDs are unsuitable for use in the endcaps.

One additional disadvantage of APDs is their potential sensitivity to ionizing particles. A minimum ionizing particle ('mip') traversing a conventional PIN silicon detector will deposit, on average, about 100 keV in 300 $\mu$m of silicon. Although APDs are very thin, the amplification region can result in an extremely large signal being produced from a single incident mip, as depicted in figure 36.

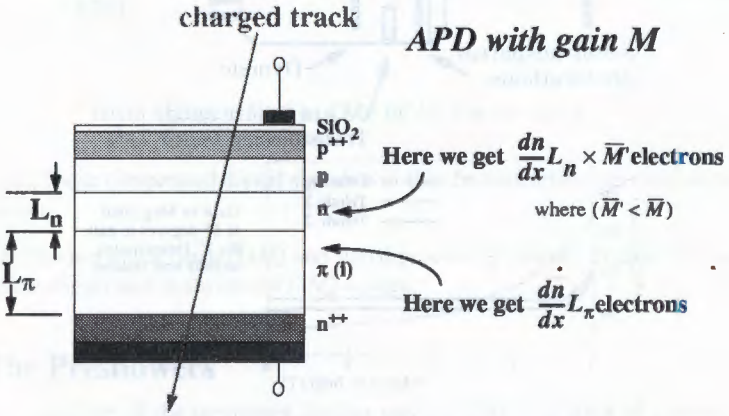


Figure 36: The sensitivity to ionizing radiation of an APD

An effective thickness '$\epsilon$' can be defined as follows:

$$n_e = 100(L_\pi + \epsilon.M) \tag{8}$$

The effective thickness is between about 5$\mu m$ (Hamamatsu) and 12$\mu m$ (EG&G) at a gain of 50. The signal from a mip traversing an APD is then approximately 40 $\times$ $\epsilon$ MeV.

Careful design and manufacture of the various silicon layers can limit this sensitivity (see section 7.3).

## 5.2 Vacuum Phototriodes

As mentioned previously the radiation environment in the endcaps in CMS preclude the use of APDs. Vacuum phototriodes ('VPTs') similar to those used by the OPAL experiment at LEP could be used, but need to be about 1/4 of the size. VPTs have lower gain than APDs but the signal-to-noise requirements in the endcaps are much lower so this is not a problem. The principles of operation of VPTs are similar to conventional photomultiplier tubes. Electrons liberated by a photon incident on a semi-transparent photocathode are accelerated towards an

anode mesh. The electrons can pass through the mesh towards a dynode, where multiplication occurs. The resulting electrons are attracted towards the anode, where they are 'detected'. A schematic diagram of a VPT is shown in figure 37 below. This configuration of electrodes results in the possibility of operation in a high magnetic field, as also demonstrated by the plot in figure 37 which shows the relative output of two phototriodes and one type of phototetrode as a function of magnetic field strength.

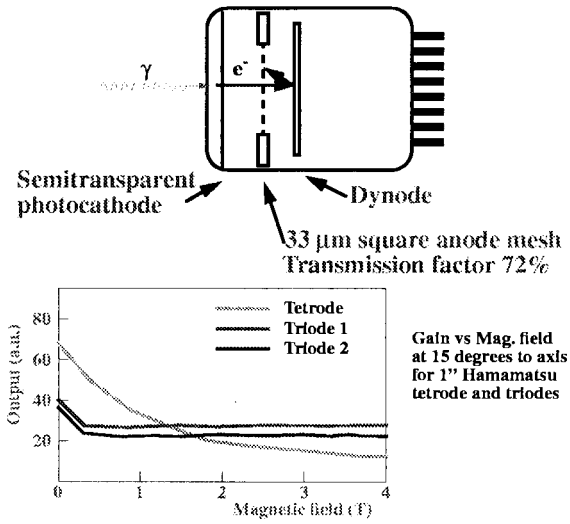


Figure 37: Schematic diagram of a VPT together with a diagram showing their gain response in a magnetic field

These devices are currently under study in Japan, Russia and the UK.

## 5.3 Readout Chain

The requirement for the readout chain is that signals must be output at 40 MHz *without degrading the energy resolution*. This means that a large dynamic range must be allowed (25 MeV $\longrightarrow$ 2 TeV) and that the digitization precision must be better than 0.1%. A schematic representation of the readout chain is given in figure 38.

The readout electronics consist of three principle parts as described briefly below.

**VFE - Very Front End** This shapes and amplifies the analogue signal from APD or VPT. It will be based on either a charge-sensitive or transimpedence low-noise amplifier with the required large dynamic range.

**FE - Front End** This includes a floating-point unit (FPU) for pedestal adjustment and zero suppression. An 11-bit 80 MHz ADC will be incorporated for compression and digitiza-

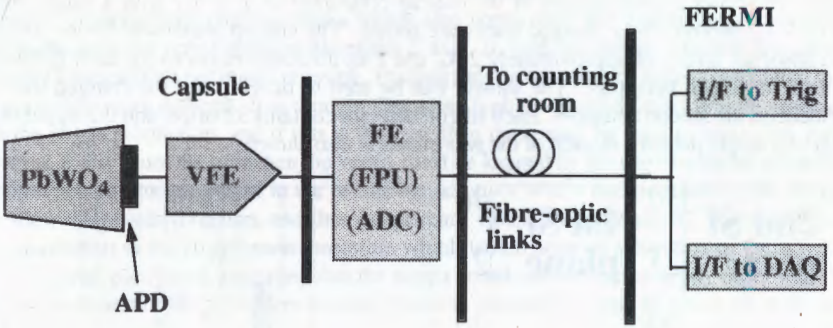


Figure 38: The CMS ECAL readout chain

tion. These compressed digital signals will then be transmitted optically to the counting room.

**FERMI** This is a multichannel DAQ and signal processing module. Digital data are sent both to the trigger and to the central DAQ system.

# 6 The Preshowers

The basic structure of the preshower devices used in CMS is a layer of a dense 'absorber' material followed by a silicon microstrip detector plane. Photons incident on the absorber will start to shower; electrons/positrons generated in the shower will give rise to signals in the silicon detector; these signals enable the position of incidence of the initial photon to be measured. The energy deposited in the absorber must, however, be measured in some way. This means that the signal from the silicon strips must also be used to apply a correction to the energy measured by the crystals. The correction is never perfect, due to fluctuations in the energy deposited in the absorber, so the energy resolution of the ECAL is degraded slightly.

The CMS detector includes two preshower detectors: one in the barrel and one in the endcaps. They are similar in design but have very different functions:

**Barrel Preshower** To measure, in conjunction with the crystals, the angle of incidence of the incoming photons (see section 7.6).

**Endcap Preshower** To distinguish energy deposits in the ECAL caused by single photons and photons from the decay of neutral pions.

In addition to these specialised functions, the preshowers also aid in electron/$\pi^{\pm}$ separation and, due to the absorber material in front of the crystals, reduce rear leakage from high energy showers.

Figure 39 shows a cross-section of the endcap preshower at $\eta = 1.7$ with a single incident 20 GeV $E_t$ photon. Only charged tracks are shown. The endcap preshower device comprises two absorber layers, of approximately 2 $X_0$ and 1$X_0$ thickness respectively, each followed by a plane of silicon detectors. The shower can be seen to develop and the charged tracks are incident on the silicon detectors. Each silicon detector contains 32 strips, and the signal in each strip of a single detector in each of the two planes is also shown.

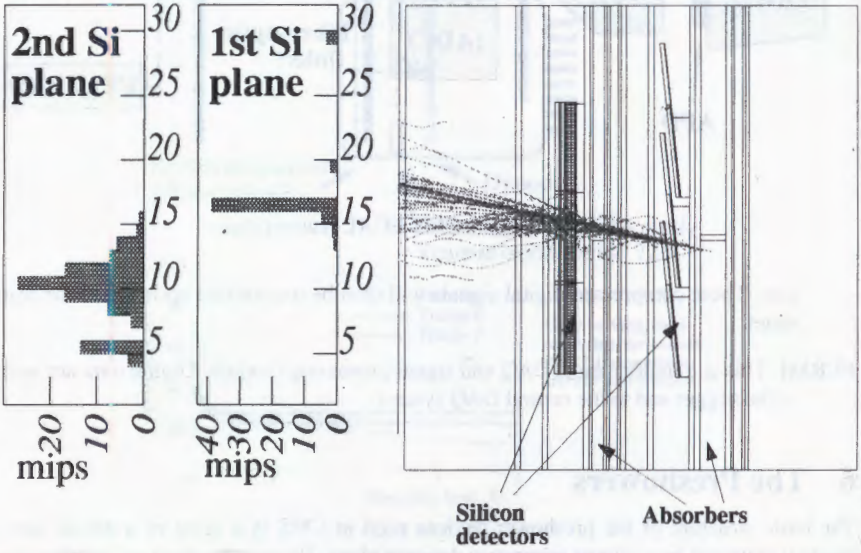


Figure 39: Cross-section of the endcap preshower at $\eta = 1.7$ showing a single incident photon. The signals in each of the two (orthogonal) detector layers is also shown.

The following sections describe the basic functions of the preshowers and present some results obtained from experiment and simulation.

## 6.1 Necessity for Preshowers

### 6.1.1 Barrel Preshower

The principle reason for including a barrel preshower is to measure the angle of incidence of photons. It was mentioned previously (see eqn. 5) that the mass resolution of an intermediate mass Higgs decaying to two photons depends upon both the energy resolution and the accuracy of the measurement of the angle between the two photons. This angle requires a knowledge of the decay point of the Higgs, which due to the short lifetime is essentially the same as the interaction vertex. The bunches of protons in the LHC will be very localized in the transverse plane (r.m.s. spread of about 15 $\mu m$) but the spread longitudinally (along the beam direction) has an r.m.s. width of about 5.3cm. If this vertex position is not known, and we simply use the centre of CMS as an estimate of the vertex position, then an additional contribution to the mass resolution of about 1.5 GeV will result.

In the low luminosity phase of the LHC there are, on average, one or two interactions per bunch crossing. Consequently, charged tracks which also come from the interaction vertex can be used to measure the vertex position along the Z axis. In high luminosity running there are on average 17 interactions per bunch crossing. Finding the correct primary vertex (associated to the Higgs) is thus more difficult. It is thought that some high $p_t$ charged tracks will be associated with the Higgs production, and if this is the case then these may be used to locate the vertex. However, if this is not the case then the vertex must be located by the use of a barrel preshower: a photon position measurement in the preshower, together with a measurement in the crystals, will allow the photon direction, and thus the primary vertex, to be measured. Figure 40 shows the contribution to the Higgs mass resolution which would arise as a function of the coverage in $\eta$ of a barrel preshower, assuming that the vertex could not be located in any other way. The angular resolution of the preshower-crystal system is assumed to scale as either 40 or 50 mrad $/\sqrt{E}$.

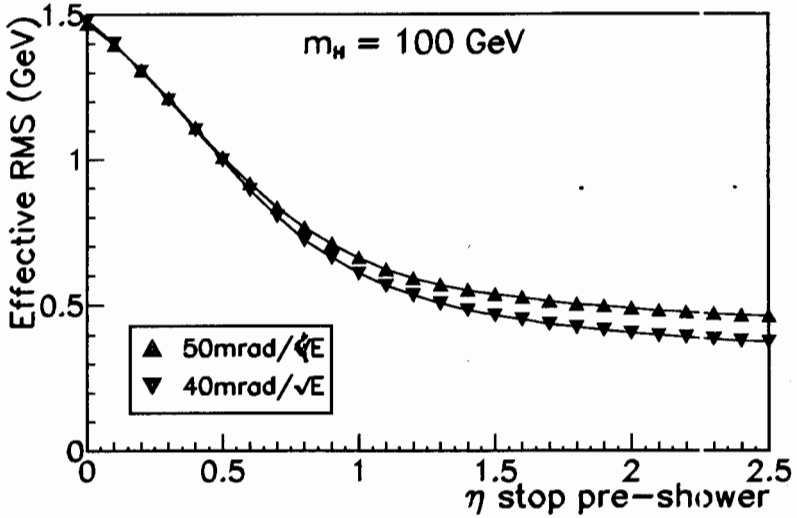


Figure 40: Contribution to the Higgs mass resolution at high luminosity as a function of the $\eta$ coverage of the barrel preshower.

It is apparent that there is no appreciable advantage in having the barrel preshower cover an area greater than about $|\eta| \leq 1$. At present it is unclear as to the necessity of the barrel preshower - it is retained as an option for high luminosity running.

### 6.1.2 Endcap Preshower

One of the major reducible backgrounds to the $H \longrightarrow \gamma\gamma$ channel is from neutral pions in jets which fake single isolated photons. In the barrel the mean separation between the two photons from the decay of a $\pi^0$ is around 1cm at the radius of the ECAL. Consequently the crystals can be used to distinguish between single incident photons and pairs of photons from $\pi^0$s to a great extent. However, in the endcaps the energy of the pions and photons is greater so the separation

between the photons from $\pi^0$s is smaller, of the order of a few mm. A position-sensitive device with sufficient granularity placed upstream of the crystals can be used to identify and reject energy clusters from the photons from $\pi^0$s, as demonstrated in figure 41.

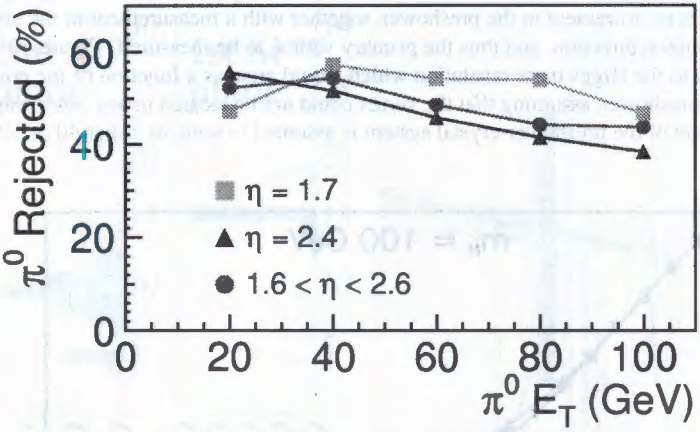


Figure 41: Neutral pion rejection in the endcaps of CMS using either crystals or a preshower, as a function of $\pi^0 E_t$. The efficiency for single photons has been set to 90%.

The $\pi^0$ rejection power of the endcap preshower is rather flat as a function of $E_t$, even at large values of $\eta$ where the separation of the photons is of the order of 1mm. Above an $E_t$ of about 30 GeV, the rejection power of the crystals alone in the endcap is around 20%. The algorithm used to reject photons from $\pi^0$s in the preshower is rather simple; a more sophisticated algorithm, perhaps employing a neural network, should improve the rejection power.

## 6.2 Detector Requirements

The structure of a preshower detector must be chosen carefully.

**Absorber thickness** The absorber must be thick enough (in terms of $X_0$) to initiate photon showers most of the time, but not too thick to excessively degrade the energy resolution. Figure 42 shows the effect that a preshower would have upon the energy resolution of an ECAL, as measured in a testbeam at CERN; the 'added term' should be added in quadrature to the energy resolution of the crystals alone. The preshower used comprised 2.5 $X_0$ of lead absorber followed by a single silicon detector plane - representative of the barrel preshower.

When a 5x5 array of crystals is used to measure the energy the preshower added term is much smaller: the showers initiated in the preshower absorber spread transversally, such that energy may be deposited outside of a 3x3 array.

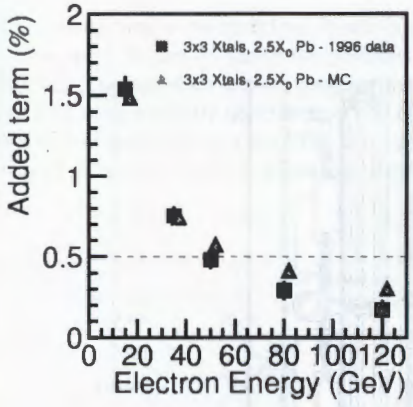


Figure 42: Preshower additional term as a function of electron energy for data and simulation.

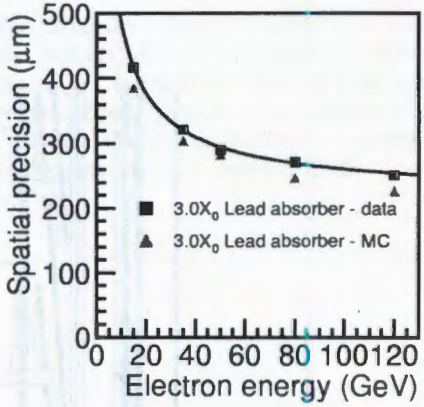


Figure 43: Preshower spatial precision as a function of incident electron energy when 3 radiation lengths of absorber are present

**Compactness** The lateral containment of showers by the crystals is clearly a function of distance between the absorber and the crystals. This is particularly important in the barrel due to the unfavourable direction of the magnetic field. The preshower should thus be as compact and as close to the crystals as possible.

**Strip Pitch** The pitch of the microstrips in the silicon detectors does not have to be too fine as the requirements for position resolution are not too strict. In fact the strips are about 1.9mm x 60mm. The spatial precision obtained from these relatively wide strips is shown in figure 43.

The spatial precision, as measured with the silicon strips following 3 $X_0$ of absorber, may be approximated as:

$$\sigma Y(\mu m) = \frac{1370}{\sqrt{E}} \oplus 260 \qquad (9)$$

## 6.3 Preshower Mechanical Construction

Figure 44 shows a detailed drawing of the endcap preshower mechanical structure. It essentially consists of two layers of lead absorber, each followed by a silicon detector array. The first absorber layer (actually an iron-lead-iron 'sandwich') is about 2 $X_0$ thick whilst the second is about 1 $X_0$ thick. The silicon detectors are about 6cm x 6cm and are supported on aluminium 'wedges' which allow detector overlap in one direction. The two detector layers have their silicon strips aligned in orthogonal directions. The cooling structures, and neutron absorber

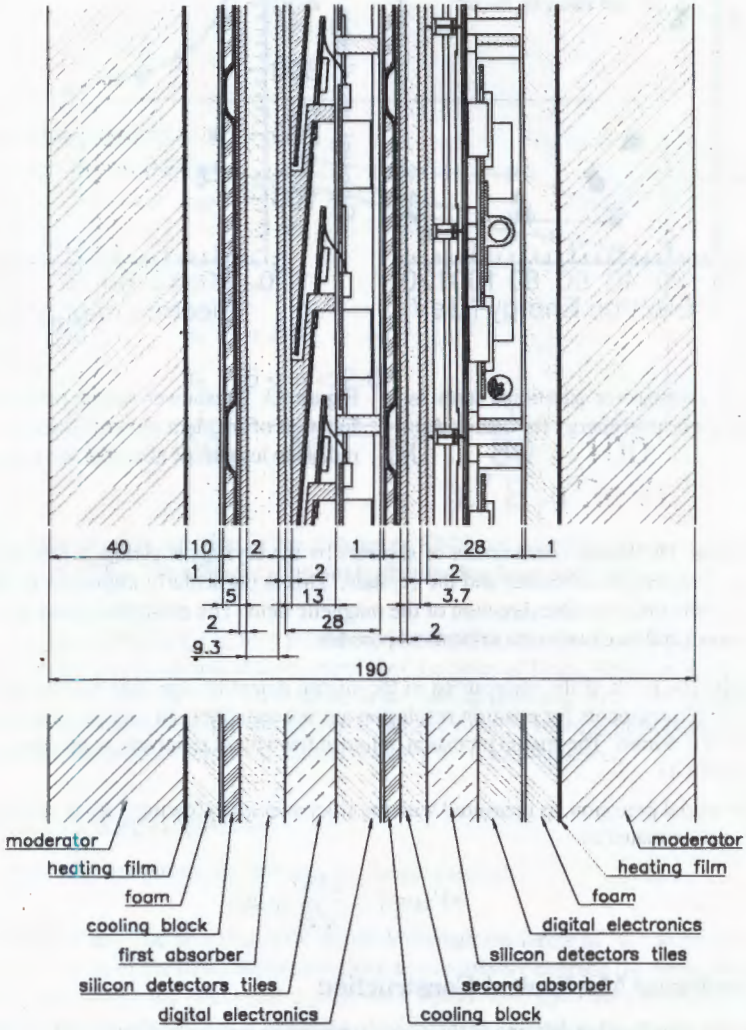


Figure 44: Endcap preshower cross-section: schematic view (bottom) and mechanical design (top). All dimensions are in millimetres.

layers[4], are also shown. Particles are incident from the left.

The construction of the barrel preshower is similar, except that only one absorber layer (2.5 $X_0$) will be used. Figure 45 shows the positions of the endcap ('SE') and barrel ('SB') preshowers in CMS. The barrel preshower, covering the range $|\eta| < 1.1$, will not be included at the startup of CMS as its necessity depends upon the exact nature of both Higgs and minimum-bias events which will not be known until the LHC starts running. The endcap preshower, covering the range $1.479 < \eta < 2.61$, is a baseline item and will be present at the startup of CMS.

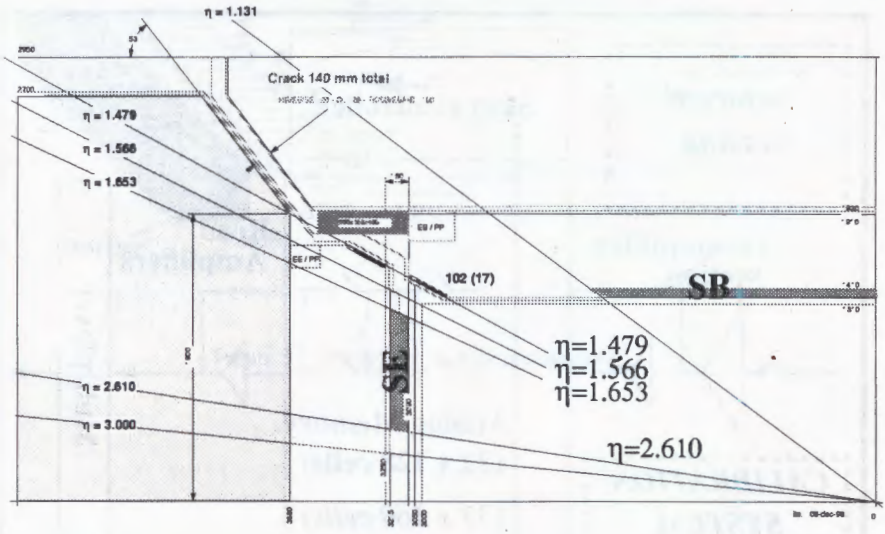


Figure 45: Approximate positions of the endcap and barrel preshowers in CMS

## 6.4 Preshower Electronics

### 6.4.1 Front-end

In contrast to most silicon detectors, particularly those used in tracking devices, the preshower detectors have to operate over a large dynamic range. This is due to the necessity of measuring a m.i.p. signal with an S/N $\approx$ 5 (for calibration) and measuring large signals (equivalent to a few hundred m.i.p.s) due to electron/photon showers with $\approx$ 5% accuracy. To achieve these aims, a custom readout system designated 'PACE' (Preshower Analog CMS Electronics) has been designed at CERN and successfully tested. Each PACE chip will readout signals at 40 MHz from a single 32-channel silicon detector and store these signals for up to 4 $\mu$s. The charge deposited in the silicon due to the passage of a m.i.p. or shower is generally spread over 2 or 3 time samples so the dynamic range does not have to be prohibitively large - a dynamic range of

[4] Neutrons created by nuclear interations in the ECAL crystals can damage silicon detectors, both in the preshower and the tracker .

250 m.i.p.s is sufficient.

Figure 46 shows a block diagram of the PACE chip. Signals from the silicon are stored, after amplification, in the analog memory. If a first-level trigger is received the addresses of the corresponding memory cells are stored in the FIFO. The corresponding second-level trigger may not be received in 4 $\mu sec$ so a 'skip controller' is used such that these memory cells are not overwritten. When the second-level trigger arrives, the addresses of the appropriate memory cells are retieved from the FIFO and the data are passed, via read amplifiers, to a multiplexer.

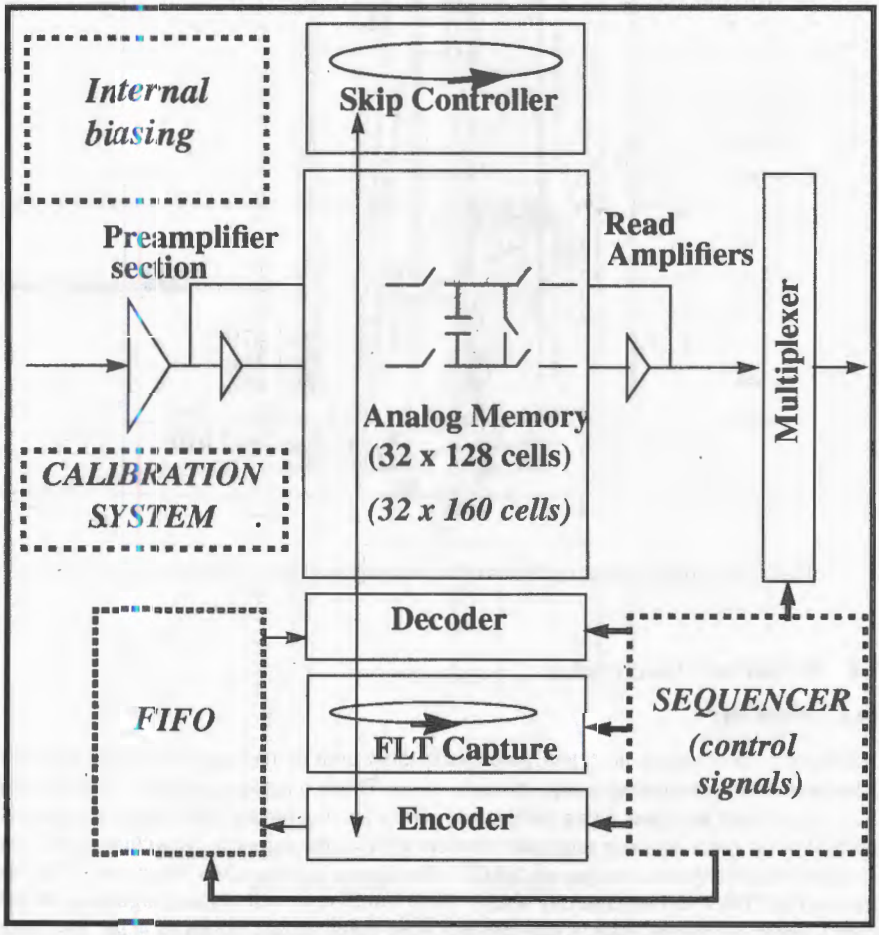


Figure 46: Block diagram showing the layout of the preshower front-end chip - PACE

### 6.4.2 Readout Architecture

The multiplexed analog signals from the front-end are passed to ADC's and then into digital processing units which perform such tasks as pedestal subtraction, suppression of common-mode noise and data sparsification. Much of the electronics, including the optical links, were originally developed for the CMS tracker.

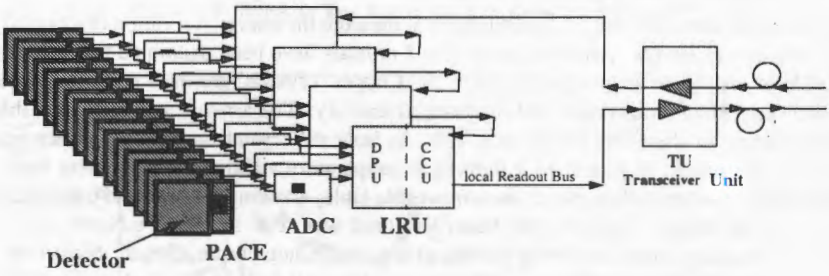


Figure 47: Preshower readout architecture

# 7 Testbeam Results

Many testbeam results, principally concerning energy resolution, have already been presented in this report. This section will show additional results on subjects such as temperature stability, position resolution of crystals and electron/charged-pion separation. The progress achieved with the APD nuclear counter effect is also shown.

## 7.1 Testbeam Setup

The principle aim of the ECAL beam tests is to measure the energy resolution of a crystal array as a function of energy. Arrays of up to 7 × 7 crystals have been examined but the system is capable of testing an array of up to 10 × 10. Copper 'crystals' are used to surround the real crystals providing temperature and mechanical stability. The array is arranged such that it is representative of the CMS ECAL at $\eta = 0$. As both the crystals and APDs are temperature sensitive the matrix is placed in a light-tight temperature stabilized containment box. This containment system is then placed on a moveable table, allowing rotation and translation with respect to the beam. The principle beam line used was 'H4' in CERN's North Area which provides electron, pion and muon beams with a small momentum spread. Most tests were performed with incident electrons, in the energy range 10 GeV to 150 GeV (selectable) with pions and muons being used for some specific tests. In addition, a prototype preshower system was occasionally attached to the containment box. Figure 48 shows a schematic view of the testbeam setup used in 1996 and 1997.

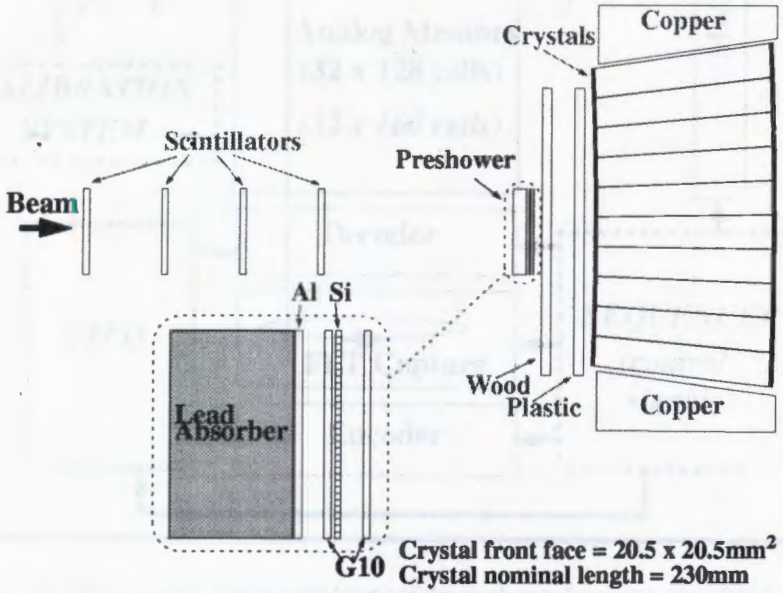


Figure 48: Schematic view of the testbeam setup

Scintillators and wire chambers upstream of the crystal matrix provided triggering and position of incidence information.

## 7.2 Temperature Stability

As mentioned previously, the crystals and APDs are sensitive to temperature variations. The temperature stability of the crystals is thus of utmost importance. In the testbeam the principle source of heat is from the preamplifiers attached directly to the APDs. A water cooling system has been employed to extremely good effect, as shown in figure 49 which illustrates the temperature measured at the back of one crystal over the course of 5 days. A regular cycle is apparent, due to residual day-night temperature variations. However, this fluctuation is of the order of $\pm 0.05^{o}$ which is sufficiently low that it has a negligible effect on the constant term.

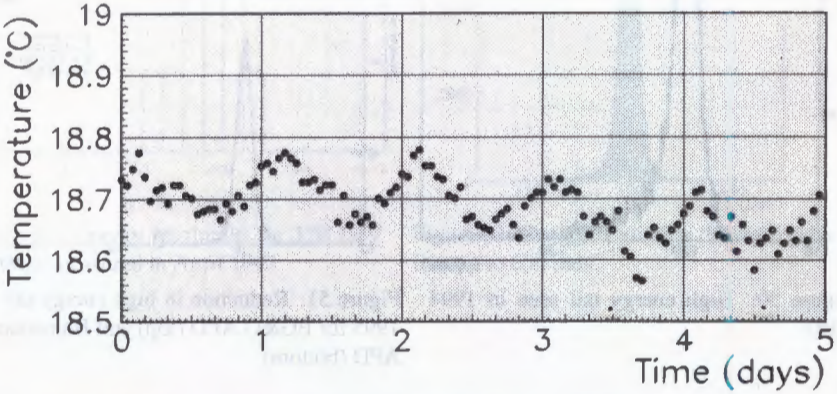


Figure 49: Temperature variation at the back of one crystal during a beam test

## 7.3 Nuclear Counter Effect

Ionizing particles traversing the APDs may cause large signals, as described in section 5, giving rise to a high energy tail in energy spectra. When APDs were first used this effect was considerable, as can be seen in figure 50, but progress was made rapidly such that the tails seen in 1995 with EG&G APDs were quite small, whilst Hamamatsu APDs were better still, as can be seen in figure 51.

APDs from both manufacturers tested in 1996 and 1997 have shown no signs of the nuclear counter effect.

## 7.4 Energy Resolution

The energy resolution obtained from a 3 × 3 matrix of crystals has seen a distinct improvement from the first tests made in 1994 when the stochastic term was around 6% and the constant term about 0.6%. The main improvements have been:

- reduction of the nuclear counter effect
- increase in the light yield of the crystals

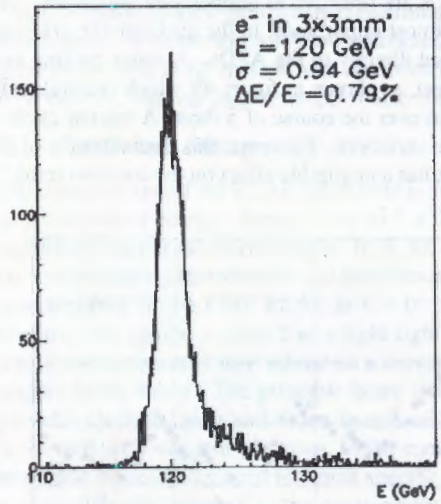


Figure 50: High energy tail seen in 1994 APD

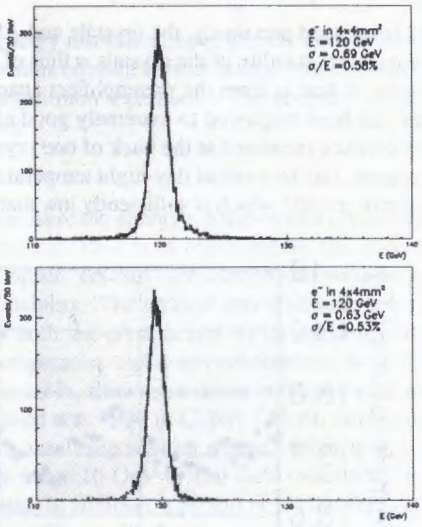


Figure 51: Reduction in high energy tail in 1995 for EG&G APD (top) and Hamamatsu APD (bottom)

- improvement in the temperature stability of the containment system
- increase in crystal radiation hardness
- LED monitoring system to 'follow' low-level radiation damage and correct for it

Figure 52 shows the energy resolution measured for 120 GeV electrons incident on 15 different crystals in 1997. The energy is measured in a $3 \times 3$ array of crystals centred on the struck crystal. The mean stochastic term is about 4.3% and the mean constant term is about 0.4%. One of the largest contributions to the stochastic term is from photostatistics, which will improve when 2 APDs are used on each crystal. Figure 53 shows the overall energy resolution measured during irradiation up to 650 rads at about 25 rads/hour (similar to the barrel dose at high luminosity) with 120 GeV electrons. The LED system was used to correct for any radiation damage.

It should be noted that the energy spectrum in figure 53 is very Gaussian.

## 7.5 Electron/charged-pion separation

Electrons and charged pions have very different energy spectra, as seen in figure 54, resulting in a large separation factor of the order of a few hundred.

A cut on the transverse shower shape, measured by the crystals, can give a further reduction factor. The overall reduction factor, for a 90% electron efficiency, is around 6000.

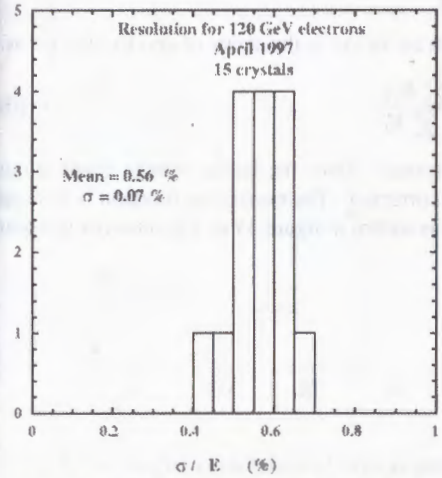


Figure 52: Energy resolution for 120 GeV electrons measured in April 1997

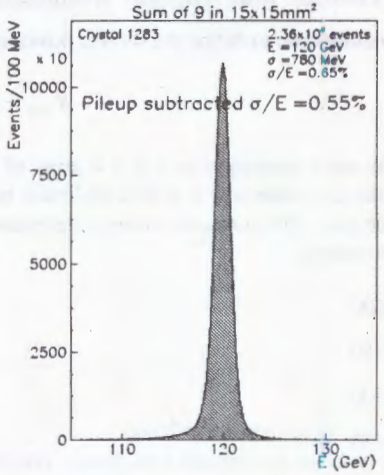


Figure 53: Energy resolution during irradiation up to 650 rads

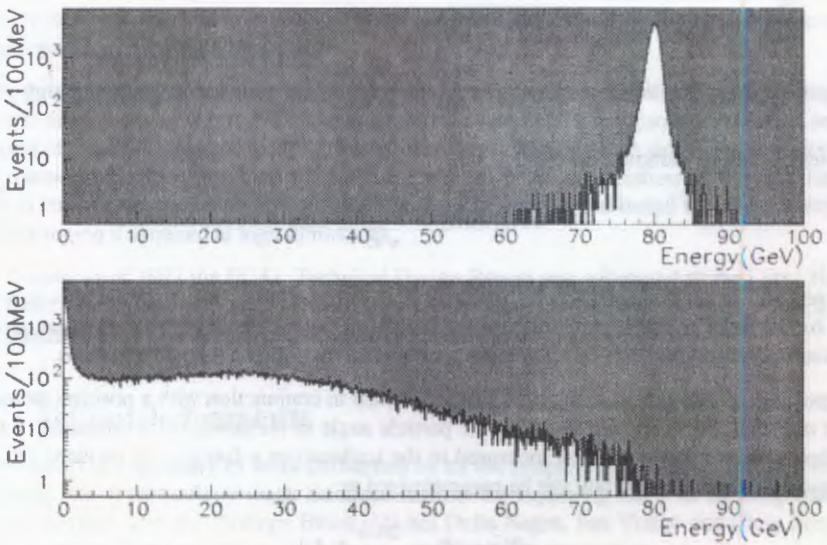


Figure 54: 80 GeV electron (top) and $\pi^-$ (bottom) spectra

## 7.6 Position and Angular Resolution

The quantity used to define the shower position in the ECAL is the centre of gravity, defined as:

$$X_{cog} = \frac{\sum E_i x_i}{\sum E_i} \tag{10}$$

with the sums running over a 3 × 3 array of crystals. Since the lateral shower shape is not triangular this estimator is biased and must be corrected. The correction function is derived from the data. The corrected position resolution is shown in figure 55 as a function of incident electron energy.

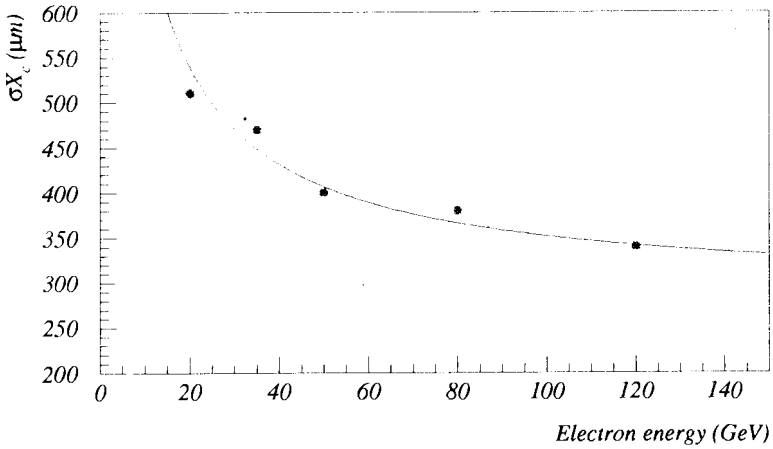


Figure 55: Position resolution of crystals as a function of incident electron energy

The results can be parameterized as:

$$\sigma X_c(mm) = \frac{2.02}{\sqrt{E}} \oplus 0.29 \tag{11}$$

The position resolution for particles incident at an angle relative to the crystal axis is worse than for normally incident particles because fluctuations in the depth of the shower are given a transverse component. This effect is more pronounced for photons than for electrons.

The position measurement in the crystals can be used in conjunction with a position measurement made by the preshower to enable the particle angle of incidence to be estimated. Figure 56 shows the angular resolution measured in the testbeam as a function of incident electron energy. The angular resolution can be parameterized as:

$$\sigma\theta(mrad) = \frac{36.5}{\sqrt{E}} \oplus 4.1 \tag{12}$$

Recent simulation results have confirmed that this order of precision should be obtainable for photons in the barrel of CMS if the barrel preshower is included.

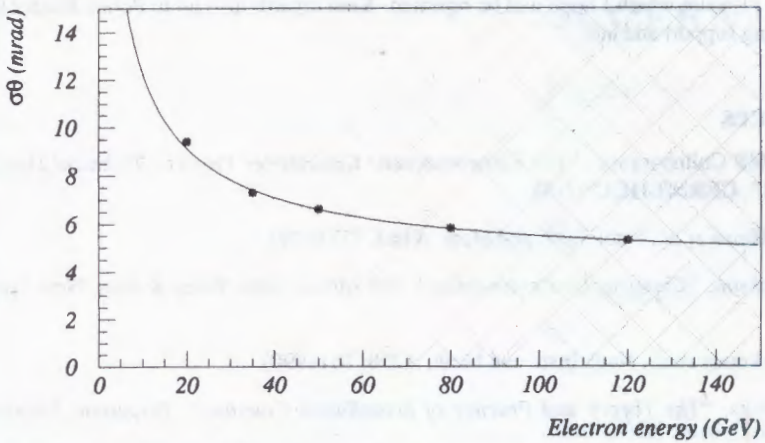


Figure 56: Angular resolution of crystal-preshower system as a function of incident electron energy

# 8 Current Status and Future Work

The latter half of 1997 saw some major changes to the geometrical design of the CMS ECAL, principally imposed due to cost constraints. This has not compromised the physics performance. This report represents the status of the CMS ECAL at the time of the Gomel school, before these changes had been made. Therefore some details, mainly geometrical, presented in this report are now slightly inaccurate.

The principle change has been to reduce the number of crystals in the ECAL by increasing their lateral dimensions by about 20%. The inner radius of the ECAL has also been reduced, and the layout of 'basket 4' (the barrel ECAL basket at the highest $\eta$) has been simplified at the expense of removing the allowed region for the installation of the barrel preshower. Current thoughts are to remove the outermost layer of MSGCs from the tracker and install the barrel preshower in this region if required at high luminosity.

In December of 1997 the ECAL Technical Design Report was submitted to the Large Hadron Collider Committee. The TDR contains the most current ECAL design and performance characteristics, and is generally available from the CMS secretariat at CERN.

# 9 Acknowledgements

This report is a summary of work performed by all the people involved with the CMS ECAL. I would like to particularly thank Etienette Auffray for supplying many of the diagrams used in the 'crystal' section. Philippe Bloch, Michel Della Negra, Jim Virdee and Chris Seez also deserve thanks for their advice and help in compiling this presentation.

Finally, I would like to gratefully acknowledge the wonderful hospitality of our hosts in Gomel, particularly Prof. Nikolai Skatchkov and Prof. Nikolai Shumeiko. It was a pleasure to be invited

to Gomel, a pleasure which I hope will be repeated. Kind regards also go to Polina Kuzhir for her continuing support and aid.

## References

[1] The CMS Collaboration, *"The Electromagnetic Calorimeter Project - Technical Design Report"*, **CERN/LHCC 97-33.**

[2] W. Hoffman *et al.*, Nucl. Instr. and Meth. **A163**, 77 (1979).

[3] J.D.Jackson, *"Classical Electrodynamics"*, 2nd edition, John Wiley & sons, New York, 1975.

[4] M.A.Akrawy *et al.*, Nucl. Instr. and Meth. **A290**, 76 (1990).

[5] J.B. Birks, *"The Theory and Practice of Scintillation Counting"*, Pergamon, London, 1964.

[6] B. Rossi, *"High Energy Particles"*, Prentice-Hall Inc., Englewood Cliffs, NJ, 1952.

[7] The CMS Collaboration, *"The Compact Muon Solenoid - Technical Proposal"*, **CERN/LHCC 94-38.**

[8] A.N.Annenkov et al, *"Systematic Study of the PbWO4 Crystal Short Term Instalibity Under Irradiation"*, **CMS-NOTE/1997-055**

# Results of the CMS End-Cap HCAL module test on the H4 beam at CERN

A.Kurilin, A.Raspereza, S.Sushkov
*NC PHEP, Minsk, Belarus*

V.Kryshkin
*IHEP, Protvino, Russia*

A.Volod'ko, N.Vlasov, V.Tyukov, I.Kossarev
*JINR, Dubna, Russia*

During June, 1996, experimental studies of the CMS End-Cap Hadron Calorimeter module were performed by the RDMS collaboration on beam H4 at CERN.

The following test beam tasks are considered in this paper: calculation of HCAL energy resolution and its dependence on the beam X- and Y-positions; studying of a dead material influence on energy resolution; reconstruction of the beam impact point coordinates.

## 1. Introduction

For the CMS End-Cap Hadron Calorimeter the sampling was chosen 5 and 10 cm of copper [1, 2] . The nonuniform sampling complicates the production and makes two divisions in depth unavoidable. To decrease the production cost but preserving the energy resolution a uniform sampling with 8 cm thick brass was considered. To study the performance of such calorimeter a "hanging file" calorimeter was used with muon, electron and pion beams. An Electromagnetic Calorimeter (introducing a dead material - electronics, cables, cooling, etc.) will be placed in front of the End-Cap Hadron Calorimeter. The impact of this material on energy resolution of the Hadron Calorimeter was also studied. The 2nd section describes the apparatus. The measurements are described in the 3rd section. The data analysis and results are presented in the 4th section. In 5th section the main results and conclusionare given .

## 2. Apparatus and set up

The "hanging file" calorimeter described in details in [2, 3] consists of 8 cm thick brass plates with dimensions 66 cm × 66 cm interspersed with scintillators. Each scintillator (produced in Kharkov) with dimensions 22 × 22 × 0.4 $cm^3$ has a key hole groove in which a wave length shifting fibre (Y11, produced by Kuraray) 0.83 mm diameter is inserted (see fig. 1). One end of the fibre is diamond cutted and aluminized and the other end is spliced to a clear fibre. The clear fibres go to an optical connector. A layer has 9 scintillators forming 9 towers. The scintillators are wrapped into Tyvek and fixed between $Al$ plates 2 and 3 mm thick. To each scintillator a quarts fibre with diameter 0.2 mm feeds UV light through a reflector. There is a hole in the Tyvek opposite to the reflector. The other ends of the fibres are bundled and glued into a tube coupled to a quarts rod which distributes light from the incoming fibre. The optical connector is connected to a ribbon cable consisting of 10 PMMA fibres 0.9 mm diameter and 10 m long (attenuation length about 10 m). The other end of the cable is connected to a photodetector box containing 18 phototubes Phillips 2081 with extended green photocathode. Each phototube is illuminated by a single light emitting diode (LED) light of which is fanned out by optical fibres. The calorimeter is divided longitudinally into two parts : HAC1 containing 9 layers and HAC2 containing 10 layers. Part of the measurements was carried out with varied thickness of absorber (brass plates) placed in front of the calorimeter. The calorimeter was installed on a table moving in horizontal and vertical directions.

### 2.1 Laser control system

The system consists of a nitrogen laser triggered (5 Hz) by a programmable module. The laser light pulse is split, part of the light is fed to a PIN diode to control the pulse amplitude. The other part of the light is fed to a filter wheel to change the light intensity in steps to cover 4 orders of magnitude (about 8 steps) to control the dynamical range of photodetectors and ADC. The position of the wheel is controlled by a programmable module. After the filter wheel the light is distributed among 19 fibres (the number of layers). 19 fibres go to a commutator which allows to illuminate any combinations of layers. The commutator is based on an electrical relay and controlled by the programmable module. After the commutator the fibres feed the light to the calorimeter where the light from each fibre is

split between 9 fibres (number of scintillators). This system allows to feed UV light pulse to each scintillator of the calorimeter.

### 3. Set-up and measurements

The measurements were carried out at H4 beam line at CERN. The beam dimensions were determined by scintillator counter 4 cm × 4 cm and particle coordinates were measured by drift chambers. The pion beam momentum was in the range from 20 up to 375 GeV/c and the electron beam momenta were 20, 50, 100, and 150 GeV/c. To equalize the response of the towers and HAC1 and HAC2 250 GeV muon beam illuminated each tower.

For each measurement the average number of collected events was about $5 \times 10^3$. Between the spills the performance of the apparatus was controlled by the LED and the laser control system.

### 4. Data analysis

Fig. 2 shows the averaged position of the calorimeter pulse height distribution versus horizontal and vertical coordinates of the beam particles (pions with momentum 125 GeV/c). As one can see there is a noticeable momentum spread. To minimize it the results presented below are obtained with conditions that the beam cross-section is 20 mm. This value was chosen after applying various cuts (from 4 up to 50 mm) on the beam size as one can see from figure 3. Corresponding distributions of reconstructed energy are presented in figure 4.

Pion beam had some contamination of muons. To eliminate its contribution there was a requirement that pion energy must be above 5 GeV. Near the experimental apparatus there was a superconducting magnet with very strong stray field. The main goal of the control system (LED and laser) was to monitor the influence of the magnetic field on the phototube and scintillator response. As one can see from figure 5 there are LED pulse height fluctuatuions connected with variation of day temperature (the LED was not temperature stabilized) and no fluctuations for laser. Thus there was no need for gain corrections.

### 5. Results and conclusions

The energy resolution for pions was determined by minimization of the

function:

$$Error = \sum_{E=20}^{E=375} \sum_{n_E=1}^{N_E} (E_{BEAM} - \sum_{j=1}^{18} k_j * A_j),$$

where $k_j$ are weight coefficients; $N_E$ is an events number in certain run (for fixed beam energy value - 20, 50, 125, 200 and 375 GeV). Note that obtained weights $k_j$ are general for the total energy range. So, the reconstructed energy is:

$$E_{REC} = \sum_{j=1}^{18} k_j * A_j.$$

Figure 6 illustrates results on energy reconstruction and the calorimeter resolution *for HCAL center*. Here, the energy distributions for 20, 50, 125, 200 and 375 GeV beams are presented (note that low-energy tails arised from beam contamination by muons have to be excluded from fitting the distribution).

Fig. 7 presents the energy resolution in the form

$$\sigma/E = \sqrt{a^2/E + b^2}.$$

The energy resolution in dependence on the thickness of the absorber placed in front of the calorimeter is shown in the same figure. Quite degradation caused by the dead material is observed.

HCAL test program included investigation of detector characteristics variation with beam position. The calorimeter was exposed with 20, 125 and 375 GeV pions at different coordinates of beam impact point. An example of variation of reconstructed energy and resolution with X coordinate for 125 GeV pion beam is presented in figure 8. Reconstructed energy value is found to increase for towers boundary region of HCAL. This effect is explained by decrease of light transmission losses (from scintillator to fibre) and light relaxation losses (in scintillator) in case when particle strikes HCAL nearby the tower boundary where readout WLS fibers are placed. Resolution vs energy dependences both for the HCAL center and for towers boundary region (X=69.0 cm, Y=45.5 cm) are presented in figure 8.

The simplest method of the beam impact point coordinates estimation was considered [4] . The runs of HCAL X- and Y-scanning by pion beams were used. This reconstruction scheme is illustrated for 375 GeV pions (vertical scanning). First of all, the centers-of-gravity of lateral shower profiles were obtained, subtracting particle coordinates in drift chambers

for every event (fig. 9). In figure 10 such centers-of-gravity are plotted versus the true beam coordinates. These curves can be fitted by the following formula:

$$Y_{cg} = Y_0 + A * sinh((Y_{BEAM} - Y_0)/B)$$

where $Y_{cg}$ is a center-of-gravity coordinate, $Y_0$ corresponds to the HCAL center, $Y_{BEAM}$ is a true beam coordinate and $A$ and $B$ are parameters to be found. Since $A$ and $B$ are found by the fitting, the above written formula can be used to reconstruct the beam coordinates from the $Y_{cg}$ values:

$$Y_{REC} = Y_0 + B * arsh((Y_{cg} - Y_0)/A)$$

assuming this coordinate calibration procedure to be analogous to the energy calibration. To obtain $X_{rec}$ and $Y_{rec}$ distributions the last formula was applied for every event in run (fig. 9).

The deviation of reconstructed coordinates from the true beam positions is shown at the bottom of fig. 10. Dependence of mean reconstructed coordinates uncertainty on the beam energy can be well fitted by the formula [5] :

$$\delta Y = \frac{c}{\sqrt{E}} + d$$

where $c$ and $d$ are parameters found by fitting ($E$ is energy in GeV). In the same figure such deviations of reconstructed coordinates are shown for beam impacting into the HCAL center and for the towers boundary region.

# References


[1] CMS Technical Proposal, CERN/LHCC 94-38, December 1994.

[2] V.Tyukov, N.Vlasov, The effect of the dead zones on energy resolution and response of CMS Endcap Hadron Calorimeter prototype. The analysis of H4 test beam data and simulation results. CMS-TN/96-048, March 1996.

[3] S. Banerjee et. al., HCAL Beam Test August 1995 - Effect of Cu Spacer on Energy Resolution: Data Analysis and Simulation Results, CMS TN/95-189, December 1995.

[4] S.Iwata, Calorimeters (total absorbtion detectors) for High-Energy experiments at accelerators, DPNU-3-79, February 1979.

[5] C.W.Fabjan, R.Wigmans, Energy measurements of elementary particles, Rep. Prog. Phys. 52 (1989) 1519-1580.

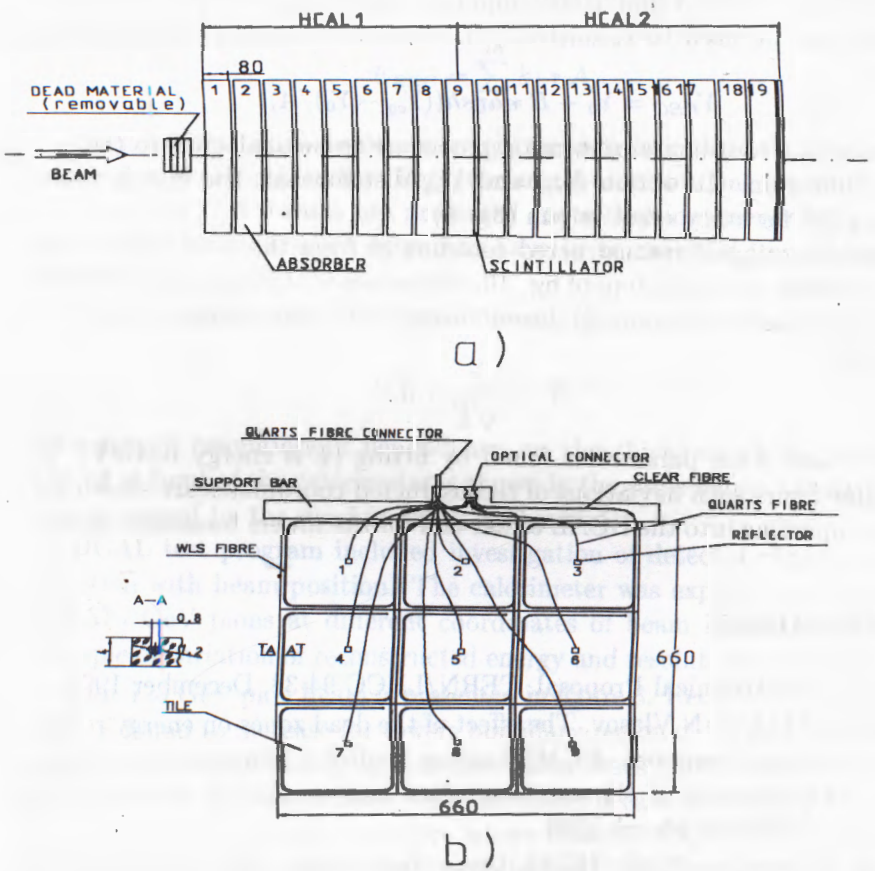


Figure 1: Schematic view of the tested HCAL. The detector consists of 2 sections, each having 3*3 tower matrix structure. During several runs a dead material (Cu plates) was placed in front of the detector.

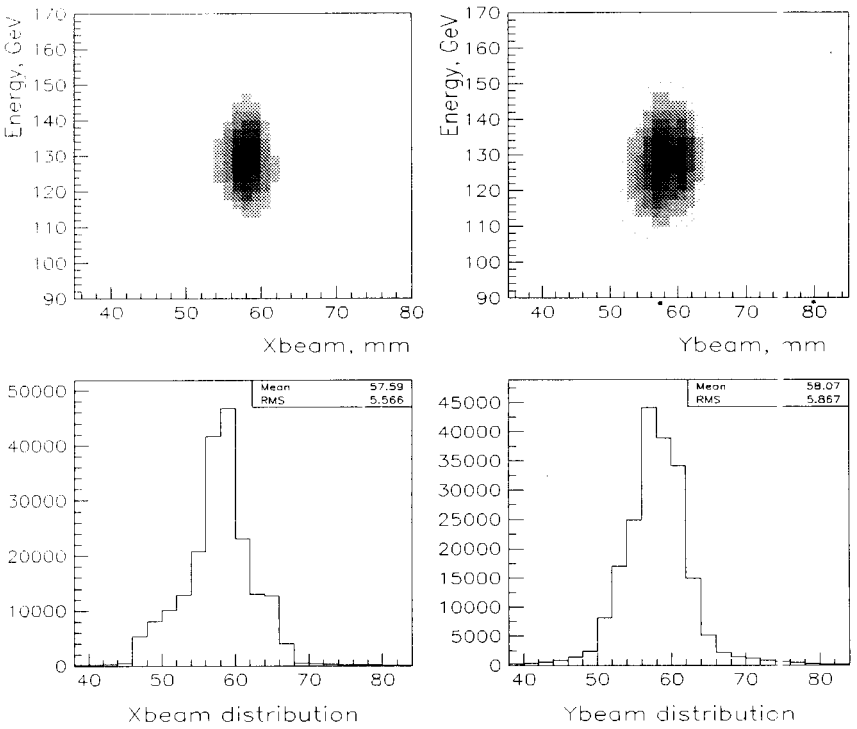


Figure 2: The beam energy profiles and distributions of particle coordinates in drift chambers (Xbeam and Ybeam).

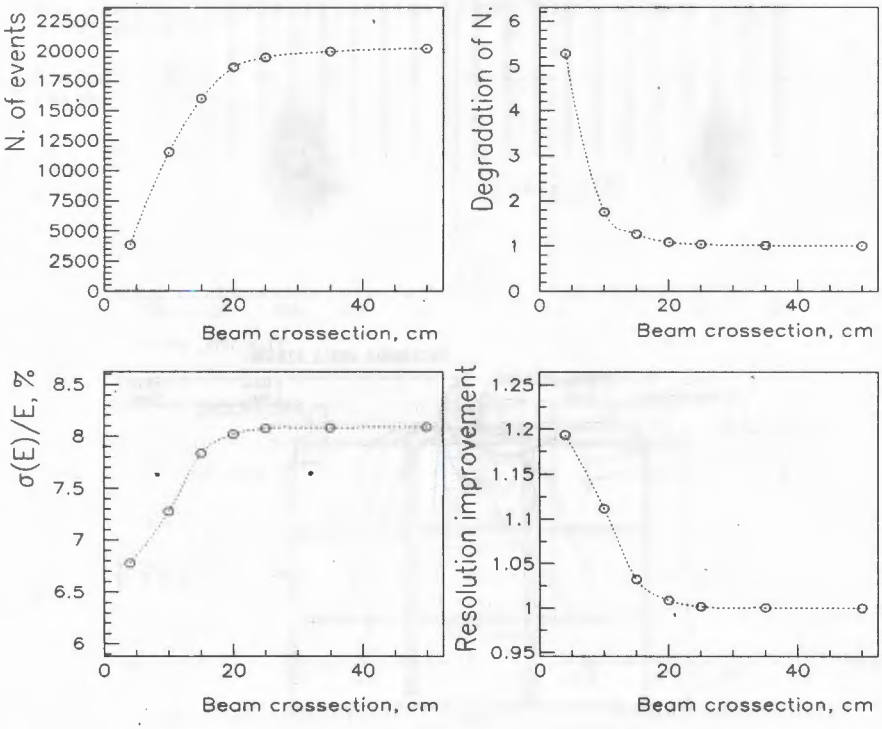


Figure 3: Dependences of events number and energy resolution and its degradation (improvement) on the beam crossection. Boundary between the beam and low-energy halo (20 mm) is observed.

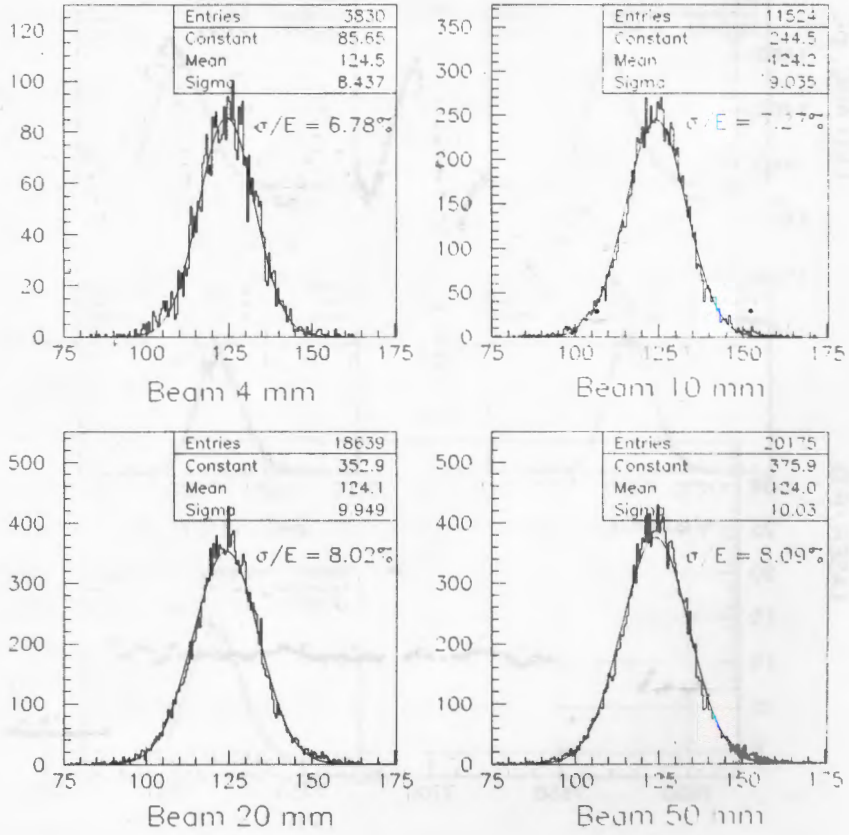


**Figure 4: Distributions of reconstructed energy for various beam sizes (4, 10, 20 and 50 mm). Different energy resolution values were obtained.**

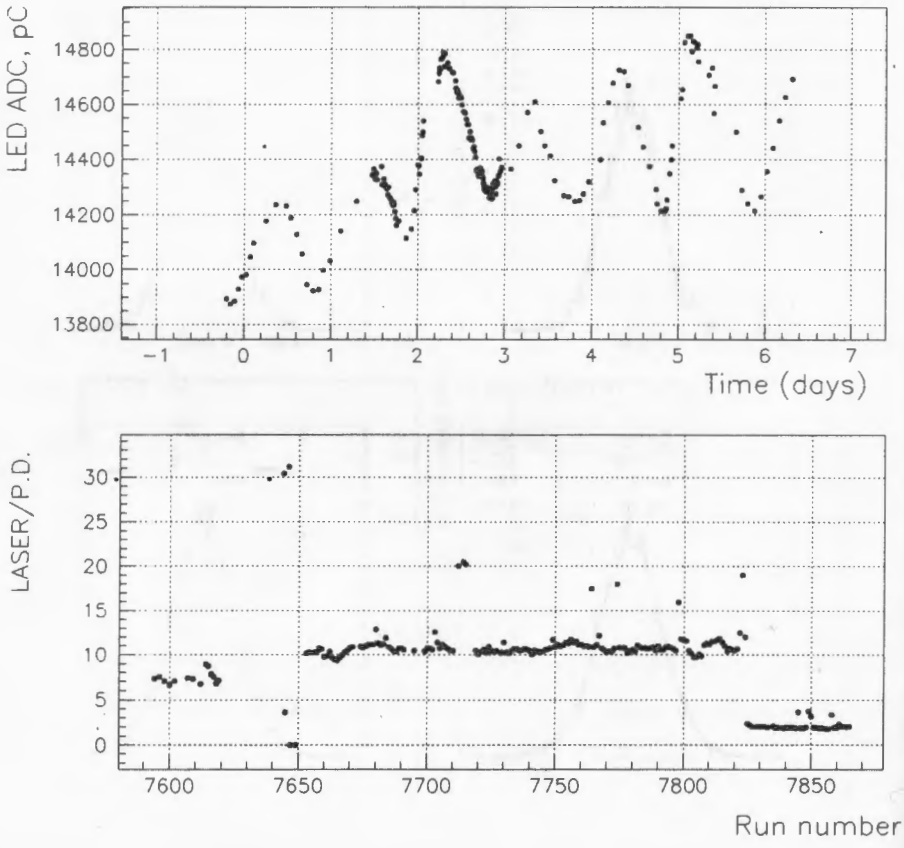


**Figure 5:** Evolution of LED ADC sum with time (top) and evolution of laser-to-P.D. ration with run number (bottom).

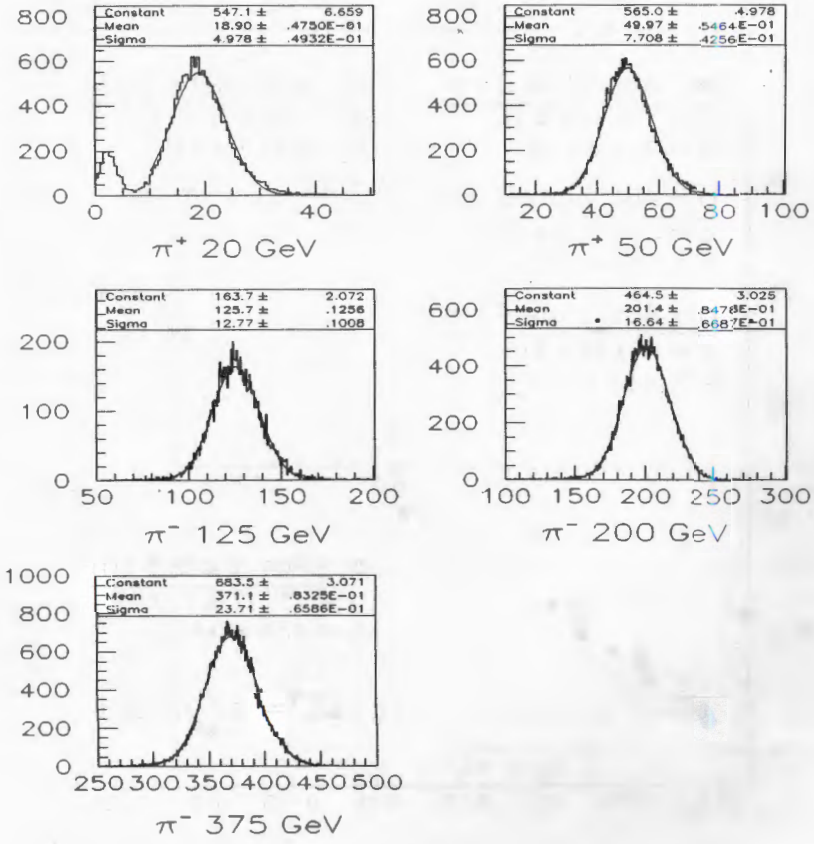


Figure 6: Reconstructed energy distributions for various incident energies. Found ADC-to-$E_{REC}$ weights are general for all beam energy values (20, 50, 125, 200 and 375 GeV).

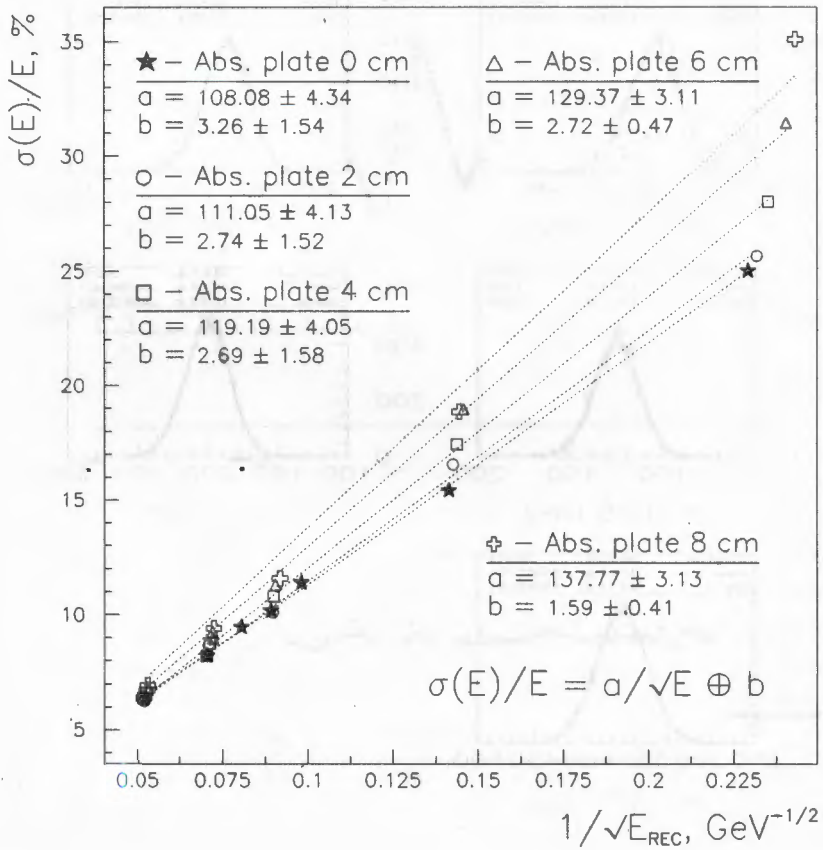


**Figure 7: The dead copper material influence on energy resolution for different plates thicknesses (W = 0 means no dead plate).**

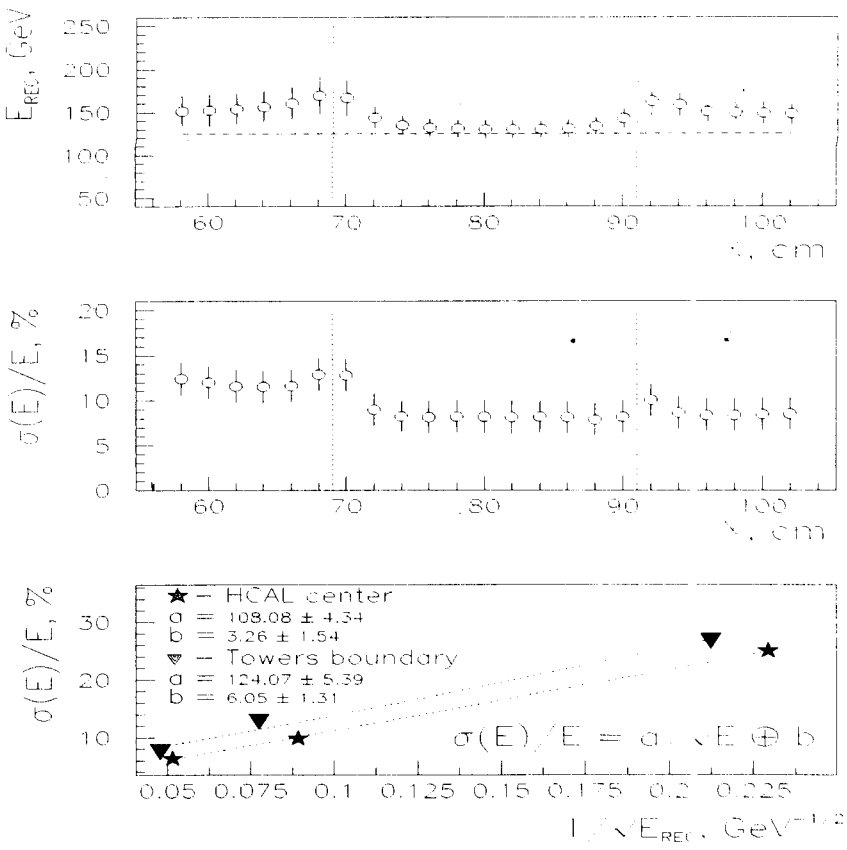


Figure 8: Variation of reconstructed energy and resolution with X coordinate of beam impact point for 125 GeV pions (the top and the middle plots). Energy resolution vs pions beam energy for HCAL center and towers boundary region (the bottom plot).

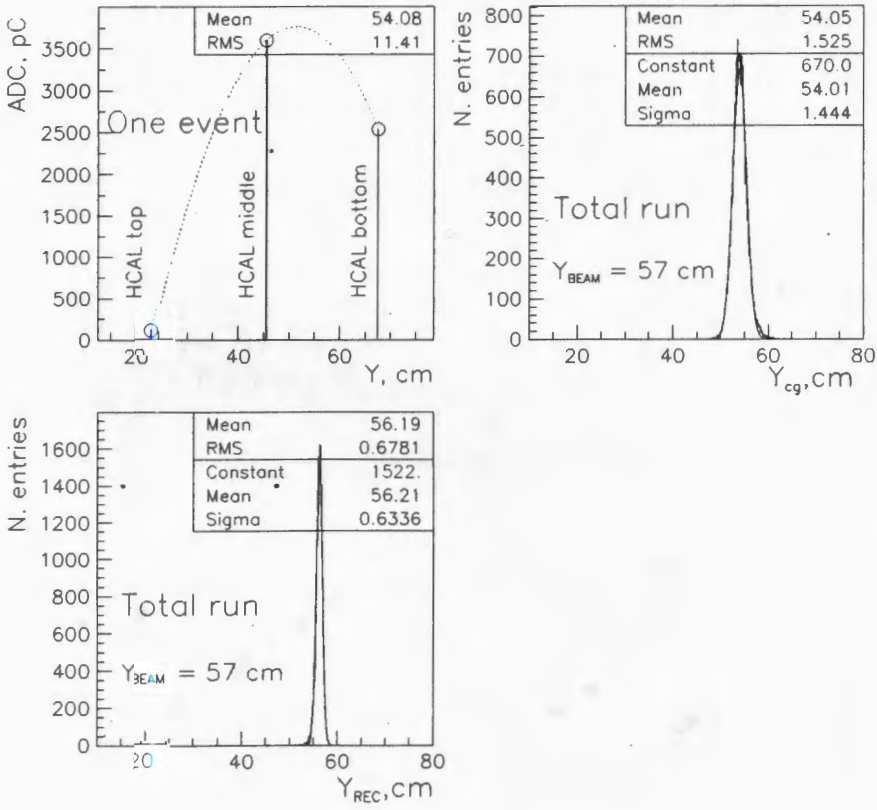


**Figure 9: The centers-of-gravity and reconstruction coordinates distributions for run 7763, 375 GeV pions (particle coordinates in the drift chambers were taken into account).**

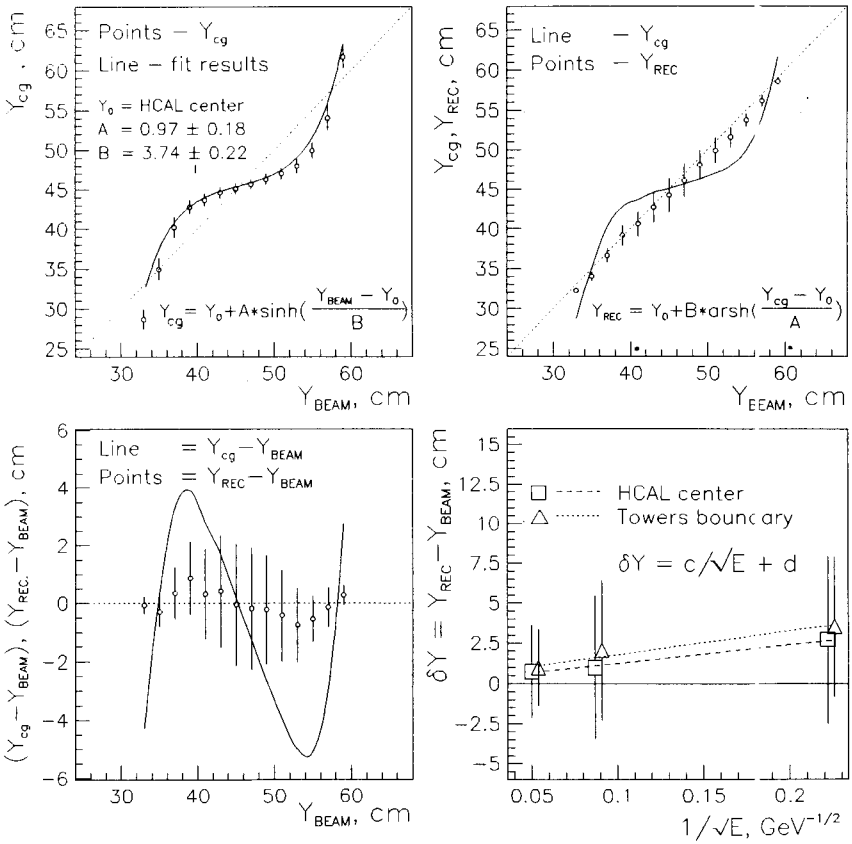


Figure 10: Illustration of used coordinate reconstruction procedure (top). $\pi^-$-beams, 375 GeV. Deviations of $Y_{REC}$ from the true beam positions and its dependence on the beam energy for HCAL center and for the tower boundary (bottom).

# 3. RELATIVISTIC PHYSICS OF HADRONS AND NUCLEI

## The phenomena of the time-violating photon polarization plane and neutron spin rotation by a difraction grating. New methods of measuring of the time-violating interactions.

**V.G.Baryshevsky**

*Nuclear Problems Institute, Bobruiskaya Str 11,*
*Minsk 220080 Belarus.*
*E-mail: bar@inp.belpak.minsk.by*

It is shown, that the new phenomena of the T-violating photon polarization plane and neutron spin rotation appear under diffraction in a noncentrosymmetrical diffraction grating. The equations describing the T-violating photon scattering by a diffraction grating and neutron interaction with noncentrosymmetrical crystal have been obtained. These phenomena may be used for time-violating interactions investigation.

Since the discovery of the CP-violation in decay of K-mesons (Christenson, Cronin, Fitch and Turlay (1964)), a few attempts have been undertaken to observe experimentally this phenomenon in different processes. However, that experiments have not been successful. At the present time, novel more precise experimental schemes are actively discussed: observation of the atom (Lamoreaux (1989)) and neutron (Forte (1983)), Fedorov, Voronin and Lapin (1992)) electric dipole moment; the T(time)-violating atom's (molecule's) spin rotation in a laser wave and the T-violating refraction of a photon in a polarized atomic or molecular gas (Baryshevsky (1993, 1994)).

### 1. P and T-violating photon polarisation plane rotation.

In accordance with Baryshevsky (1993, 1994) the P(parity)- and T-violating dielectric permittivity tensor $\varepsilon_{ik}$ (for case $\varepsilon_{ik} - \delta_{ik} \ll 1$ ) is given by

$$\varepsilon_{ik} = \delta_{ik} + \chi_{ik} = \delta_{ik} + \frac{4\pi\rho}{k^2} f_{ik}(0), \qquad (1.1)$$

where $\chi_{ik}$ is the polarizability tensor of the matter, $\rho$ is the number of atoms (molecules) per $cm^3$, $k$ - the photon wave number. The quantity

$f_{ik}(0)$ is the tensor part of the zero-angle amplitude of elastic coherent scattering of a photon by an atom (molecule) $f(0) = f_{ik}(0)\, e'^{*} e_k$. Here $\vec{e}$ and $\vec{e}\,'$ are the polarization vectors of initial and scattered photons. Indices i=1,2,3 are refered to coordinates x, y, z, respective y, repeated indices imply summations. At zero external electric and magnetic fields, the amplitude $f_{ik}(0)$ can be written as

$$\begin{aligned} f_{ik}(0) &= f_{ik}^{ev}(0) + f_{ik}^{P,T}(0) = f_{ik}^{ev}(0) + \frac{\omega^2}{c^2}[i\beta_s^P \varepsilon_{ikl} n_l \\ &-\beta_v^P \left(\left\langle \vec{J} \right\rangle \vec{n}\right) \delta_{ik} + +i\beta_t^P \varepsilon_{iml} \left\langle \hat{Q}_{mk} \right\rangle n_l \\ &+\frac{1}{2}\beta_t^T \left(\left\langle \hat{Q}_{im} \right\rangle \varepsilon_{mlk} n_l + \left\langle \hat{Q}_{km} \right\rangle \varepsilon_{mli} n_l\right)], \end{aligned} \tag{1.2}$$

where $f_{ik}^{ev}$ is the P, T even (invariant) part of $f_{ik}(0)$, $f_{ik}^{P,T}$ is the P,T-violating part of $f_{ik}(0)$, $\beta_{s,v,t}^{P,T}$ is the scalar (vector, tensor) P,T violating polarizability of an atom (molecule), $\varepsilon_{ikl}$ is the total antisymmetrical unit tensor of the rank three, $\vec{n} = \dfrac{\vec{k}}{k}$, $\left\langle \vec{J} \right\rangle = Sp\rho_J \vec{J}$, $\rho_J$ is the spin density matrix of an atom (molecule) with the spin $\vec{J}$, $\langle Q_{im} \rangle = Sp\rho_J \hat{Q}_{im}$. The second rank tensor $\hat{Q}_{im}$ is given by

$$\hat{Q}_{im} = [2J(2J-1)]^{-1} \left\{ \hat{J}_i \hat{J}_m + \hat{J}_m \hat{J}_i - \frac{2}{3} J(J+1)\, \delta_{in} \right\}$$

In view of (1.1,1.2), the T-violating processes affect upon the dielectric permittivity $\varepsilon_{ik}$ and, as a result, upon the refraction index only in media with polarized atoms (molecules) of the spin equaled or larger than 1. This part of $\varepsilon_{ik}$ is proportional to $\beta_t^T$. If the atoms' (molecules') spins are nonpolarized, only the P-violating term $f_{ik}(0) = \dfrac{\omega^2}{c^2} i\beta_s^P \varepsilon_{ikl} n_l$ exists. The term proportional to $\beta_s^P$ describes the P-violating rotation of a light polarization plane in metallic vapours (Barkov and Zolotariov 1978, Bouchiat and Pottier 1986, Khriplovich 1991).

As it has been shown in (Baryshevsky 1993, 1994), when an atom interacts with two coherent electromagnetic waves, the energy of this interaction depends on the T-violating scalar polarizability $\beta_t^T$. Interaction of an atom (molecule) with two waves can be considered as a process of rescattering of one wave into another and vice versa. Then, as it follows from an expression for the effective interaction energy, the amplitude

$f\left(\vec{k}',\vec{k}\right)$ of the photon scattering by an unpolarized atom (molecule) at a non-zero angle is given by (Baryshevsky 1994):

$$f\left(\vec{k}',\vec{k}\right) = f_{ik}e_i'^{*}e_k = \frac{\omega^2}{c^2}\left(\alpha_s\vec{e}'^{*}\vec{e} + i\frac{1}{2}\beta_s^P\left(\vec{n}'+\vec{n}\right)\left[\vec{e}'^{*}\vec{e}\right]\right. \qquad (1.3)$$
$$\left. +\beta_s^T\left(\vec{n}'-\vec{n}\right)\left[\vec{e}'^{*}\vec{e}\right]\right),$$

where $\vec{k}$ is the wave vector of a scattered photon, $\vec{n}' = \frac{\vec{k}'}{k}$, $\alpha_s$ is the scalar P,T-invariant polarizability of an atom (molecule). Expression (1.3) holds true in the absence of external electric and magnetic fields.

It should be emphasized that expression (1.3) for the elastic scattering amplitude can be derived from the general principles of symmetry. Indeed, there are four independent unit vectors: $\vec{\nu}_1 = \frac{\vec{k}'+\vec{k}}{\left|\vec{k}'+\vec{k}\right|}$, $\vec{\nu}_2 = \frac{\vec{k}'-\vec{k}}{\left|\vec{k}'-\vec{k}\right|}$, $\vec{e}$ and $\vec{e}\,'$, which completely describe geometry of the elastic scattering process. The elastic scattering amplitude $f\left(\vec{k}',\vec{k}\right)$ depends on these vectors and therewith is a scalar. Obviously, one can compose three independent scalars from these vectors: $\vec{e}\,'^{*}\vec{e}$, $\vec{\nu}_1\left[\vec{e}\,'^{*}\vec{e}\right]$, $\vec{\nu}_2\left[\vec{e}\,'^{*}\vec{e}\right]$. As a result, the scattering amplitude can be written as:

$$f\left(\vec{k}',\vec{k}\right) = f_s\left(\vec{k}',\vec{k}\right)\vec{e}\,'^{*}\vec{e} + if_s^P\left(\vec{k}',\vec{k}\right)\vec{\nu}_1\left[\vec{e}\,'^{*}\vec{e}\right] + f_s^T\left(\vec{k}',\vec{k}\right)\vec{\nu}_2\left[\vec{e}\,'^{*}\vec{e}\right], \qquad (1.4)$$

where $f_s$ is the P-,T- invariant scalar amplitude, $f_s^P$ is the P-violating scalar amplitude, and $f_s^T$ is the P-,T- violating scalar amplitude.

It can easily be found from (1.3,1.4) that the term proportional to $\beta_s^T\left(f_s^T\right)$ vanishes in the case of forward scattering $\left(\vec{n}' \to \vec{n}\right)$. Vice versa, in the case of back scattering $\left(\vec{n}' \to -\vec{n}\right)$ the term proportional to $\beta_s^P\left(f_s^P\right)$ gets equal to zero.

Thus, one can conclude that the T-violating interactions manifest themselves in the processes of scattering by atoms (molecules). However, the scattering processes are usually incoherent and their cross sections are too small to hope for observation of the T-violating effect. Another situation takes place for diffraction gratings in the vicinity of the Bragg resonance where the scattering process is coherent. As a result, the intensities of scattered waves strongly increase: for instance, in the Bragg

(reflection) diffraction geometry the amplitude of the diffracted-reflected wave may reach the unity. It gives us an opportunity to study the T-violating scattering processes (Baryshevsky 1994).

In the present paper, equations describing the T-violating scattering by a diffraction grating have been obtained. It has been shown that the photon's refraction index in a non-center-symmetrical grating depends on the T-violating amplitude $f_s^T$ . It can result in a new phenomenon: the T-violating rotation of the photon polarization plane. It has also been shown that the rotation angle rises sharply in the back-scattering diffraction geometry when the conditions of the photon resonance transmission are satisfied.

## The P-,T-violating electromagnetic waves diffraction by a diffraction grating

The phenomenon of P-, T- invariant diffraction of electromagnetic waves by diffraction gratings has been studied in detail for a very wide range of wavelengths (see, for examples, Shih-Lin Chang (1984), Tamir (1988), Maksimenko and Slepyan (1997)). Accoding to these articles equations of the dynamic diffraction can be derived from the Maxwell's equations if the permittivity tensor $\varepsilon_{ik}(\vec{r},\omega)$ of a spatially periodic grating is known.

To include the P, T violating processes into the diffraction theory, let us consider the microscopic Maxwell equations:

$$\begin{aligned} curl\vec{E} &= -\frac{1}{c}\frac{\partial \vec{B}}{\partial t}, \quad curl\vec{B} = \frac{1}{c}\frac{\partial \vec{E}}{\partial t} + \frac{4\pi}{c}\vec{j}, \\ div\vec{E} &= 4\pi\rho, \quad div\vec{B} = 0, \quad \frac{\partial \rho}{\partial t} + div\vec{j} = 0, \end{aligned} \tag{1.5}$$

where $\vec{E}$ is the electric field strength and $\vec{B}$ is the magnetic field induction, $\rho$ and $\vec{j}$ are the microscopic densities of the electrical charge and the current induced by an electromagnetic wave, $c$ is the speed of light. The Fourier transformation of these equations (i.e. $\vec{E}(\vec{r},t) = \frac{1}{2\pi^4}\int \vec{E}\left(\vec{k},\omega\right) e^{i\vec{k}\vec{r}}e^{-i\omega t}d^3kd\omega$ and so on) leads us to the equation for $\vec{E}\left(\vec{k},\omega\right)$ as follows:

$$\left(-k^2 + \frac{\omega^2}{c^2}\right)\vec{E}\left(\vec{k},\omega\right) = -\frac{4\pi i\omega}{c^2}\left[\vec{j}\left(\vec{k},\omega\right) - \frac{c^2k^2}{\omega^2}\vec{n}\left(\vec{n}\vec{j}\left(\vec{k},\omega\right)\right)\right], \tag{1.6}$$

where $\vec{n} = \dfrac{\vec{k}}{k}$ .

In linear approximation, the current $\vec{j}(\vec{r},\omega)$ is coupled with $\vec{E}(\vec{r},\omega)$ by the well-known dependence:

$$j_i(\vec{r},\omega) = \int d^3r' \sigma_{ij}\left(\vec{r},\vec{r}',\omega\right) E_j\left(\vec{r}',\omega\right) \tag{1.7}$$

with $\sigma_{ij}\left(\vec{r},\vec{r}',\omega\right)$ as the microscopic conductivity tensor being a sum of the conductivity tensors of the atoms (molecules) constituting the diffraction grating:

$$\sigma_{ij}\left(\vec{r},\vec{r}',\omega\right) = \sum_{A=1}^{N} \sigma_{ij}^{A}\left(\vec{r},\vec{r}',\omega\right) \tag{1.8}$$

Here $\sigma_{ij}^{A}$ is the conductivity tensor of the A-type scatterers. The summation is over all atoms (molecules) of the grating.

In a diffraction grating, the tensor $\sigma_{ij}\left(\vec{r},\vec{r}',\omega\right)$ is a spatially periodic function. It allows one to derive the expansion of $j_i\left(\vec{k},\omega\right)$ from (1.7) as follows:

$$j_i\left(\vec{k},\omega\right) = \frac{1}{V_0}\sum_{\vec{\tau}} \sigma_{ij}^{c}\left(\vec{k},\vec{k}-\vec{\tau},\omega\right) E_j\left(\vec{k}-\vec{\tau},\omega\right), \tag{1.9}$$

where $\sigma_{ij}^{c}$ is the Fourier transform of the conductivity tensor of a grating's elementary cell, $\vec{\tau}$ is the reciprocal lattice vector of the diffraction grating. Using current representation (1.9), one can obtain a set of equations from (1.6):

$$\left(-k^2 + k_0^2\right) E_i\left(\vec{k},\omega\right) = -\frac{\omega^2}{c^2}\sum_{\vec{\tau}} \hat{\chi}_{ij}\left(\vec{k},\vec{k}-\vec{\tau}\right) E_j\left(\vec{k}-\vec{\tau}\right) \tag{1.10}$$

Tensor of the diffraction grating susceptibility is given by

$$\hat{\chi}_{ij}\left(\vec{k},\vec{k}-\vec{\tau}\right) = \left(\delta_{il} - n_i n_l\right)\chi_{lj}\left(\vec{k},\vec{k}-\vec{\tau}\right) \tag{1.11}$$

with

$$\chi_{lj}\left(\vec{k},\vec{k}-\vec{\tau}\right) = \frac{4\pi i}{V_0\omega}\sigma_{lj}\left(\vec{k},\vec{k}-\vec{\tau}\right) = \frac{4\pi c^2}{V_0\omega^2}F_{lj}\left(\vec{k},\vec{k}-\vec{\tau}\right).$$

Here $F_{lj}\left(\vec{k},\vec{k}-\vec{\tau}\right) = \dfrac{i\omega}{c^2}\sigma_{lj}\left(\vec{k},\vec{k}-\vec{\tau}\right)$ is the amplitude of coherent elastic scattering of an electromagnetic wave by a grating elementary cell from a state with the wave vector $\vec{k}-\vec{\tau}$ to a state with the wave vector $\vec{k}$.

The amplitude $F_{lj}$ is obtained by summation of atomic (molecular) coherent elastic scatterig amplitudes over a grating's elementary cell:

$$F_{lj}\left(\vec{k}'=\vec{k}+\vec{\tau},\vec{k}\right)=\left\langle\sum_{A=1}^{N_c} f_{lj}^{A}\left(\vec{k}'=\vec{k}+\vec{\tau},\vec{k}\right)e^{-i\vec{\tau}\vec{R}_A}\right\rangle, \qquad (1.12)$$

where $f_{lj}^{A}$ is the coherent elastic scattering amplitude by an A-type atom (molecule), $\vec{R}_A$ is the gravity center coordinate of the A-type atom (molecule), $N_c$ is the number of the atoms (molecules) in an elementary cell, angular brackets denote averaging over the coordinate distribution of scatterers in a grating's elementary cell.

The amplitude $f_{lj}$ has been given by equation (1.4,1.3).

¿From (1.11), (1.12) and (1.4) one can obtaine an expression for the susceptibility $\chi_{lj}$ of the elementary cell of an optically isotropic material:

$$\chi_{lj}\left(\vec{k},\vec{k}-\vec{\tau}\right)=\chi_{s\vec{\tau}}\delta_{lj}+i\chi_{s\vec{\tau}}^{P}\varepsilon_{ljf}\nu_{1f}^{\vec{\tau}}+\chi_{s\vec{\tau}}^{T}\varepsilon_{ljf}\nu_{2f}^{\vec{\tau}} \qquad (1.13)$$

where

$$\chi_{s\vec{\tau}}^{(P,T)}=\frac{4\pi c^2}{V_0\omega^2}\left\langle\sum_{A=1}^{N_c} f_{s}^{A(P,T)}\left(\vec{k},\vec{k}-\vec{\tau}\right)e^{-i\vec{\tau}\vec{R}_A}\right\rangle$$

$\chi_{s\vec{\tau}}$ is the scalar P-, T- invariant susceptibility of an elementary cell, $\chi_{s\vec{\tau}}^{P}$ is the P-violating, T- invariant susceptibility of the elementary cell, and $\chi_{s\vec{\tau}}^{T}$ is the P- and T- violating susceptibility of the elementary cell,

$$\vec{\nu}_1^{\vec{\tau}}=\frac{2\vec{k}-\vec{\tau}}{\left|2\vec{k}-\vec{\tau}\right|}\quad,\quad \vec{\nu}_2^{\vec{\tau}}=\frac{\vec{\tau}}{\tau}$$

Then, using (1.10, 1.11,1.13) we can derive a set of equations describing the P and T violating interaction of an electromagnetic wave with a diffraction grating

$$\begin{aligned}\left(-\frac{k^2}{k_0^2}+1\right)E_i\left(\vec{k}\right) &= -\left(\delta_{ij}-n_in_j\right)\chi_{s0}E_j\left(\vec{k}\right)- \qquad (1.14)\\ &-i\chi_{s0}^{P}\left(\delta_{il}-n_in_l\right)\varepsilon_{ljf}n_fE_j\left(\vec{k}\right)-\\ &-\sum_{\vec{\tau}\neq 0}\{\left(\delta_{ij}-n_in_j\right)\chi_{s\vec{\tau}}E_j\left(\vec{k}-\vec{\tau}\right)+\\ &+i\chi_{s\vec{\tau}}^{P}\left(\delta_{il}-n_in_l\right)\varepsilon_{ljf}\nu_{1f}^{\vec{\tau}}E_j\left(\vec{k}-\vec{\tau}\right)+\\ &+\chi_{s\vec{\tau}}^{T}\left(\delta_{il}-n_in_l\right)\varepsilon_{ljf}\nu_{2f}^{\vec{\tau}}E_j\left(\vec{k}-\vec{\tau}\right)\},\end{aligned}$$

where $k_0 = \frac{\omega}{c}$

Assuming the interaction to be P, T invariant $\left(\chi_s^P = \chi_s^T = 0\right)$, equations (1.14) reduce to the conventional set of equations of dynamic diffraction theory (Shih-Lin Chang (1984)).

## The phenomenon of T-violating rotation of the photon polarization plane by a diffraction grating

Let us suppose, first of all, the photon $\omega$ frequency and the wave vector $\vec{k}$ to be such that the Bragg diffraction conditions $\vec{k} = \vec{k} \pm \vec{\tau}$ and $\left|\vec{k}'\right| = \left|\vec{k}\right|$ are not fulfilled exactly, and the inequality $\frac{k_0^2 \left|\hat{\chi}_{lj}\left(\vec{k}, \vec{k} - \vec{\tau}\right)\right|}{\left(\vec{k} - \vec{\tau}\right)^2 - k_0^2} \ll 1$ holds true. In this case, the diffracted wave amplitude is much less comparing with the transmitted one: $\left|\vec{E}\left(\vec{k} - \vec{\tau}\right)\right| \ll \left|\vec{E}\left(\vec{k}\right)\right|$, and the perturbation theory can be applied for the further analysis. As a result in the first approximation of the perturbation theory one can derive from (1.10) that

$$E_j\left(\vec{k} - \vec{\tau}\right) \simeq \frac{k_0^2}{\left(\vec{k} - \vec{\tau}\right)^2 - k_0^2} \hat{\chi}_{jf}\left(\vec{k} - \vec{\tau}, \vec{k}\right) E_f\left(\vec{k}\right) \tag{1.15}$$

$$= \alpha_\tau^{-1} \hat{\chi}_{jf}\left(\vec{k} - \vec{\tau}, \vec{k}\right) E_f\left(\vec{k}\right),$$

where $\alpha_\tau = \frac{\vec{\tau}\left(\vec{\tau} - 2\vec{k}_0\right)}{k_0^2}$, $\vec{k}_0 = \frac{\omega}{c}\vec{n}$, $|\hat{\chi}_{ij}| \ll 1$.

Substitution (1.15) into (1.10) results in the diffraction equations as follows

$$\left(k^2 - k_0^2\right) E_i\left(\vec{k}, \omega\right) - k_0^2 [\hat{\chi}_{if}\left(\vec{k}, \vec{k}\right) \tag{1.16}$$

$$+ \sum_{\vec{\tau} \neq 0} \alpha_\tau^{-1} \hat{\chi}_{ij}\left(\vec{k}, \vec{k} - \vec{\tau}\right) \hat{\chi}_{jf}\left(\vec{k} - \vec{\tau}, \vec{k}\right)] E_f(\vec{k}, \omega) = 0$$

which can be rewritten in more simple form

$$\left(k^2 - k_0^2 \hat{\varepsilon}_{if}\left(\vec{k}, \omega\right)\right) E_f\left(\vec{k}, \omega\right) = 0 \tag{1.17}$$

by introducing the effective permittivity tensor

$$\hat{\varepsilon}_{if}\left(\vec{k}, \omega\right) = \delta_{if} + \hat{\chi}_{jf}\left(\vec{k}, \vec{k}, \omega\right) + \sum_{\vec{\tau} \neq 0} \alpha_\tau^{-1} \hat{\chi}_{ij}\left(\vec{k}, \vec{k} - \vec{\tau}\right) \hat{\chi}_{jf}\left(\vec{k} - \vec{\tau}, \vec{k}\right) \tag{1.18}$$

One can see that even far away from the exact Bragg conditions, where the diffracted wave amplitudes are small, a spatially periodic isotropic medium manifests the optical anisotropy being characterized by the effective permittivity tensor $\hat{\varepsilon}_{ij}\left(\vec{k},\omega\right)$.

Let a photon be incident on a grating normally to its reflection planes. In other words, let the photon wave vector $\vec{k}_0$ be antiparallel to the reciprocal lattice vector $\vec{\tau}$ , i.e. $\vec{k}_0 \uparrow\downarrow \vec{\tau}$ . In this case, the back-scattering diffraction regime can be realized for photons with wave numbers defined by the relation $k \approx \frac{1}{2}\tau$ . If, nevertheless, the inequality $\alpha_\tau \gg \left|\chi_{ij}\left(\vec{k},\vec{k}-\vec{\tau}\right)\right|$ holds true, we can use set of equations (1.16) in which there is only one term satisfying the conditions $\vec{\tau} \uparrow\downarrow \vec{k}$ and $\tau \simeq 2k$ .

Let the coordinate axis $z$ be parallel to $\vec{k}_0$ , $\vec{\tau}$ . In this case, the tensor $\hat{\chi}_{ij}$ has nonzero components at $i$ , $j = 1,2$ only. As a result, set of equations (1.17) can be rewritten in the form as follows:

$$\left(k^2 - k_0^2\varepsilon_{ij}\left(\vec{k},\omega\right)\right) E_j\left(\vec{k},\omega\right) = 0 \tag{1.19}$$

with the permittivity tensor given by

$$\begin{aligned}\varepsilon_{ij}\left(\vec{k},\omega\right) &= \varepsilon_0\delta_{ij} + i\chi_s^P(0)\,\varepsilon_{ij3}n_3 + \\ &+\alpha_\tau^{-1}\left[\chi_s(\vec{\tau})\,\chi_s^T(-\vec{\tau}) - \chi_s(-\vec{\tau})\,\chi_s^T(\vec{\tau})\right]\varepsilon_{ij3}\nu_{23}^{\vec{\tau}}\end{aligned} \tag{1.20}$$

In the above equations we introduced the designations:

$$\chi(\vec{\tau}) = \chi\left(\vec{k},\vec{k}-\vec{\tau}\right), \quad \chi(-\vec{\tau}) = \chi\left(\vec{k}-\vec{\tau},\vec{k}\right), \quad \varepsilon_0 = 1 + \chi_s^{eff},$$

$$\chi_s^{eff} = \chi_s(0) - \alpha_\tau^{-1}\chi_s(\vec{\tau})\,\chi_s(-\vec{\tau}), \quad \vec{n} = \frac{\vec{k}}{\tau}.$$

The term proportional $t_0\ \chi_s^P(0)$ describes the P-violating and T-invariant rotation of the light polarization plane about the direction $\vec{n}$. This term does not depend on a structure of the diffraction grating and exists for any ordinary spatially isotropic media. Unlike to that, the term proportional to $\chi_s^T$ is T-violating and depends on the grating's structure. The term proportional $\chi_s^T$ looks like the term proportional to $\chi_s^P$ and is responsible for the polarization plane rotation about $\vec{\nu}_2^{\vec{\tau}}$.

It is known that the phenomenon of the polarization plane rotation arises when right- and left-circularly polarized photons have different indices of refraction in a medium $n_+$ and $n_-$, respectively. It means that

the tensor $\varepsilon_{ij}$ is diagonal for a given circular polarization and, concequently, the set of equations (1.19) is split into two independent equations. Really, let us write (1.19) in the vector notation:

$$\left(k^2 - k_0^2\varepsilon_0\right)\vec{E} - ik_0^2\chi_s^P(0)\left[\vec{E}\vec{n}\right] \qquad (1.21)$$
$$-k_0^2\alpha_\tau^{-1}\left[\chi_s(\vec{\tau})\chi_s^T(-\vec{\tau}) - \chi_s(-\vec{\tau})\chi_s^T(\vec{\tau})\right]\left[\vec{E}\vec{\nu}_2^\tau\right]$$

and let $\vec{e}_1$ be the unit polarization vector of a linearly polarized photon; $\vec{e}_2 = [\vec{n}\vec{e}_1]$ , $\vec{e}_1 \perp \vec{e}_2 \perp \vec{n}$ . Then, the unit vectors corresponding to the circular polarizations are as follows $\vec{e}_\pm = \frac{\vec{e}_1 \pm i\vec{e}_2}{\sqrt{2}}$. For the right $(\vec{e}_+)$ , left $(\vec{e}_-)$ circularly polarized photons, the field $\vec{E}$ can be represented by $\vec{E} = c_{(\pm)}\vec{e}_{(\pm)}$. As a result, it follows from (1.19, 1.21) that:

$$\left(k^2 - k_0^2\varepsilon_0\right)c_\pm \pm k_0^2\chi_s^P(0)\,c_\pm \pm ik_0^2\alpha_\tau^{-1}\left[\chi_s(\vec{\tau})\chi_s^T(-\vec{\tau}) - \right.$$
$$\left. -\chi_s(-\vec{\tau})\chi_s^T(\vec{\tau})\right]c_\pm = 0 \qquad (1.22)$$

The corresponding refractive indices are obtained from (1.20)

$$n_\pm^2 = \frac{k^2}{k_0^2} = \varepsilon_0 \mp \chi_s^P(0) \mp i\alpha_\tau^{-1}\left[\chi_s(\vec{\tau})\chi_s^T(-\vec{\tau}) - \chi_s(-\vec{\tau})\chi_s^T(\vec{\tau})\right] \qquad (1.23)$$

The angle of the photon polarization plane rotation is defined by :

$$\vartheta = k_0 Re\,(n_+ - n_-)\,L_{ph} \qquad (1.24)$$

where $L_{ph}$ is the photon propagation length in the medium, $Ren_\pm$ is the real part of $n_\pm$. Then, the expression for $\vartheta$ can easily be derived from (1.24,1.23)

$$\vartheta = k_0 Re\frac{n_+^2 - n_-^2}{n_+ + n_-}L \simeq -k_0 Re\chi_s^P(0)\,L - \qquad (1.25)$$
$$-k_0\,Rei\alpha_\tau^{-1}\left[\chi_s(\vec{\tau})\chi_s^T(-\vec{\tau}) - \chi_s(-\vec{\tau})\chi_s^T(\vec{\tau})\right]L$$

One can conclude, thus, that the T-violating interaction results in the phenomenon of the T-violating rotation of the photon polarization plane. The effect manifests itself when the condition

$$Rei\left[\chi_s(\vec{\tau})\chi_s^T(-\vec{\tau}) - \chi_s(-\vec{\tau})\chi_s^T(\vec{\tau})\right] \neq 0$$

holds true.

It follows from (1.13) that the susceptibilities $\chi_s^{P,T}(\vec{\tau})$ can be presented as

$$\begin{aligned}\chi_s^{P,T}(\vec{\tau}) &= \chi_{1s}^{P,T}(\vec{\tau}) - \chi_{2s}^{P,T}(\vec{\tau}) = \\ &= \left\langle \sum_{A=1}^{N_c} f_s^{A(P,T)}\left(\vec{k}, \vec{k}-\vec{\tau}\right) \cos \vec{\tau}\vec{R}_A \right\rangle - \\ &-i\left\langle \sum_{A=1}^{N_c} f_s^{A(P,T)}\left(\vec{k}, \vec{k}-\vec{\tau}\right) \sin \vec{\tau}\vec{R}_A \right\rangle\end{aligned} \tag{1.26}$$

where

$$\chi_{1s}^{P,T}(\vec{\tau}) = \chi_{1s}^{P,T}(-\vec{\tau}) \qquad \chi_{2s}^{P,T}(\vec{\tau}) = -\chi_{2s}^{P,T}(-\vec{\tau}) \tag{1.27}$$

In view of (1.26,1.27) we can rewrite (1.25) as:

$$\vartheta = -k_0 Re\chi_s^P(0)\, L + 2k_0\alpha_\tau^{-1} Re\left[\chi_{1s}(\vec{\tau})\,\chi_{2s}^T(\vec{\tau}) - \chi_{2s}(\vec{\tau})\,\chi_{1s}^T(\vec{\tau})\right] L \tag{1.28}$$

So, the T-violating rotation arises in the case of nonzero odd part of the suscetibility: $\chi_2(\vec{\tau}) \neq 0$. Such a situation is possible if an elementary cell of the diffraction grating does not posses the center of symmetry.

In accordance with (1.28), the angle of the T-violating rotation grows at $\alpha_\tau \to 0$. However, the condition $\alpha_\tau |\chi_s(\vec{\tau})| \ll 1$ violates at $\alpha_\tau^{-1} \to 0$, where the amplitude of diffracted and transmitted waves are comparable: $E\left(\vec{k}-\vec{\tau}\right) \simeq E\left(\vec{k}\right)$ and, consequently, the perturbation theory gets unapplicable. A rigorous dynamical diffraction theory must be applied in this case.

## The T-violating polarization plane rotation in the Bragg diffraction scheme

Let the Bragg condition is fulfilled for the only diffracted wave and is violated for all other possible ones. It allows us to restrict ourselves to the two-wave approximation of the dynamical diffraction theory (Shih-Lin Chang (1984)). In that case, set of equations (1.14) reduces to two coupled equations, which for the back-scattering diffraction scheme $\left(\vec{k}_0 \parallel \vec{\tau}\right)$ take the form as follows:

$$\begin{aligned}\left(\frac{k^2}{k_0^2} - 1\right) E_j\left(\vec{k}\right) &= \chi_s(0)\, E_j\left(\vec{k}\right) + i\chi_s^P(0)\,\varepsilon_{jmf} E_m\left(\vec{k}\right) n_f + \\ &+\chi_s(\vec{\tau})\, E_j\left(\vec{k}-\vec{\tau}\right) + \chi_s^T(\vec{\tau})\,\varepsilon_{jmf} E_m\left(\vec{k}-\vec{\tau}\right) \nu_f,\end{aligned} \tag{1.29}$$

$$\left(\frac{\left(\vec{k}-\vec{\tau}\right)^2}{k_0^2}-1\right)E_j\left(\vec{k}-\vec{\tau}\right)=\chi_s(0)\,E_j\left(\vec{k}-\vec{\tau}\right)+$$

$$i\chi_s^P(0)\,\varepsilon_{jmf}n_f\left(\vec{k}-\vec{\tau}\right)E_m\left(\vec{k}-\vec{\tau}\right)+$$

$$+\chi_s(-\vec{\tau})\,E_j\left(\vec{k}\right)+\chi_s^T(-\vec{\tau})\,\varepsilon_{jmf}\nu_{2f}^{-\vec{\tau}}E_m\left(\vec{k}\right),$$

$$\vec{n}\left(\vec{k}-\vec{\tau}\right)=\frac{\vec{k}-\vec{\tau}}{\left|\vec{k}-\vec{\tau}\right|}.$$

Based on the above consideration, we can conclude that set of equations (1.29) can be diogonalized for the photon of a given circular polarization. Let the right-circularly polarized photon ($\vec{e}_+$) be incident on the diffraction grating. The diffraction process, as it follows from (29), results in the appearance of a back-scattered photon with the left circular polarization ($\vec{e}_-^{\vec{\tau}}$). This is because the momentum of the back-scattered photon $\vec{k}' = \vec{k}-\vec{\tau}$ is antiparallel to the momentum $\vec{k}$ of the incident one. It is obvious that the left-circularly polarized photon will produce a right-circularly polarized back-scattered one.

Thus, for circularly polarized photons set of vector equations (1.29) can be split into two independent sets of scalar equations:

$$\left(\frac{k^2}{k_0^2}-1\right)C_\pm\left(\vec{k}\right)=\left(\chi_s(0)\mp\chi_s^P(0)\right)C_\pm\left(\vec{k}\right)+$$

$$+\left(\chi_s(\tau)\mp i\chi_s^T(\tau)\right)C_\mp\left(\vec{k}-\vec{\tau}\right) \qquad (1.30)$$

$$\left(\frac{\left(\vec{k}-\vec{\tau}\right)}{k_0^2}-1\right)C_\mp\left(\vec{k}-\vec{\tau}\right)=\left(\chi_s(0)\pm\chi_s^P(0)\right)C_\mp\left(\vec{k}-\vec{\tau}\right)+$$

$$+\left(\chi_s(-\vec{\tau})\pm i\chi_s^T(-\vec{\tau})\right)C_\pm\left(\vec{k}\right)$$

Note that equations (1.30) are identical in form to conventional equations of the two-wave dynamical diffraction (Shih-Lin Chang (1984)):

$$\left(\frac{k^2}{k_0^2}-1\right)c_0 = \chi_0 c_0+\chi_\tau c_\tau \qquad (1.31)$$

$$\left(\frac{k_\tau^2}{k_0^2}-1\right)c_\tau = \chi_0 c_\tau+\chi_{-\tau}c_0$$

It allows us to write down a solution immediately, without deriving (see, for example, (Shih-Lin Chang (1984))). As a result, the amplitude of

the transmitted electromagnetic wave at the output is given by

$$\vec{E}_{\pm} = \vec{e}_{\pm} C_{\pm}(L)\, e^{i\vec{k}_0\vec{r}}, \tag{1.32}$$

$$\begin{aligned} C_{\pm}(L) &= 2\left(\varepsilon_1^{\pm} - \varepsilon_2^{\pm}\right) e^{i\frac{1}{2}k_0\varepsilon^{\pm}L}\left[\left(2\varepsilon_1^{\pm} - \chi_0^{\pm}\right) e^{i\frac{1}{2}k_0\left(\varepsilon_1^{\pm}-\varepsilon_2^{\pm}\right)L} - \right. \\ &\left. - \left(2\varepsilon_2^{\pm} - \chi_0^{\pm}\right) e^{-i\frac{1}{2}\left(\varepsilon_1^{\pm}-\varepsilon_2^{\pm}\right)L}\right]^{-1}, \end{aligned} \tag{1.33}$$

where L is the thickness of the diffraction grating,

$$\chi_0^{\pm} = \chi_s(0) \mp \chi_s^P(0),$$

$$\begin{aligned} \varepsilon_1^{\pm} &= \frac{1}{4}\left[\mp 2\chi_s^P(0) + \alpha\right] + \frac{1}{4}\{(2\chi_s(0) - \alpha)^2 - 4\left(\chi_{1s}^2(\vec{r}) + \chi_{2s}^2(\vec{r})\right) \pm \\ &\pm 8\left[\chi_{1s}(\vec{r})\,\chi_{2s}^T(\vec{r}) - \chi_{2s}(\vec{r})\,\chi_{1s}^T(\vec{r})\right]\}^{\frac{1}{2}}, \end{aligned} \tag{1.34}$$

$$\begin{aligned} \varepsilon_2^{\pm} &= \frac{1}{4}\left[\mp 2\chi_s^P(0) + \alpha\right] - \frac{1}{4}\{(2\chi_s(0) - \alpha)^2 - 4\left(\chi_{1s}^2(\vec{r}) + \chi_{2s}^2(\vec{r})\right) \pm \\ &\pm 8\left[\chi_{1s}(\vec{r})\,\chi_{2s}^T(\vec{r}) - \chi_{2s}(\vec{r})\,\chi_{1s}^T(\vec{r})\right]\}^{\frac{1}{2}}, \end{aligned}$$

$$\alpha \equiv \alpha_\tau, \tag{1.35}$$

$$\varepsilon^{\pm} = \varepsilon_1^{\pm} + \varepsilon_2^{\pm} = \mp\chi_s^P(0) + \frac{\alpha}{2},$$

$$\begin{aligned} \varepsilon_1^{\pm} - \varepsilon_2^{\pm} &= \frac{1}{2}\{(2\chi_s(0) - \alpha)^2 - 4\left(\chi_{1s}^2(\vec{r}) + \chi_{2s}^2(\vec{r})\right) \pm \\ &\pm 8\left[\chi_{1s}(\vec{r})\,\chi_{2s}^T(\vec{r}) - \chi_{2s}(\vec{r})\,\chi_{1s}^T(\vec{r})\right]\}^{\frac{1}{2}}. \end{aligned} \tag{1.36}$$

Consider now the diffraction of a photon with linear polarization $\vec{e}_1$ being the superposition of two opposite circular polarizations . In this case

$$\vec{E}(\vec{r}) = \vec{e}_1 e^{i\vec{k}_0\vec{r}} = \frac{\vec{e}_+ + \vec{e}_-}{\sqrt{2}} e^{i\vec{k}_0\vec{r}} \tag{1.37}$$

and the amplitude of the transmitted wave $\vec{E}'(r)$ can be presented by the superposition

$$\begin{aligned} \vec{E}'(\vec{r}) &= \left(\frac{1}{\sqrt{2}}\vec{e}_+ C_+(L) + \frac{1}{\sqrt{2}}\vec{e}_- C_-(L)\right) e^{i\vec{k}_0\vec{r}} = \\ &= \left(\frac{\vec{e}_1 + i\vec{e}_2}{2} C_+(L) + \frac{\vec{e}_1 - i\vec{e}_2}{2} C_-(L)\right) e^{i\vec{k}_0\vec{r}} = \\ &= \left(\frac{C_+ + C_-}{2}\vec{e}_1 + i\frac{C_+ - C_-}{2}\vec{e}_2\right) e^{i\vec{k}_0\vec{r}}. \end{aligned} \tag{1.38}$$

In the case under consideration $c_+ \neq c_-$.As follows from (1.38), this results in changing of the photon polarization at the output.

Let us analyze expression (1.32) for the transmitted wave amplitude more attentively. According to (1.32), the amplitude oscillates as a function of $\alpha$, i.e., as a function of the wavelength, with maximums in points defined by the condition $k_0 Re\left(\varepsilon_1^{\pm} - \varepsilon_2^{\pm}\right) L = 2\pi m$ or $Re\left(\varepsilon_1^{\pm} - \varepsilon_2^{\pm}\right) = \frac{2\pi m}{k_0 L}$ with $m$ as an integer.

Note first of all that the condition $m = 0$ dictates at $\varepsilon_1^{\pm} - \varepsilon_2^{\pm} \to 0$ the limit transition

$$\left\{(2\chi_s(0) - \alpha)^2 - 4\left(\chi_{1s}^2(\vec{r}) + \chi_{2s}^2(\vec{r})\right)\right.$$
$$\left. \pm 8\left[\chi_{1s}(\vec{r})\,\chi_{2s}^T(\vec{r}) - \chi_{2s}(\vec{r})\,\chi_{1s}^T(\vec{r})\right]\right\}^{\frac{1}{2}} \to 0 \qquad (1.39)$$

which determines the thresholds of the total Bragg reflection band where there is a quickly damped inhomogeneous wave inside the diffraction grating. As a result, the transmitted wave amplitude is small.

Let now $m \neq 0$. As we know, the T-violating interactions are very small: $\chi_{s1,2}^T \ll \chi_{s1,2}$. It allows one to expand the square root into the Teylor series truncated beyond the second term:

$$\varepsilon_1^{\pm} - \varepsilon_2^{\pm} \simeq (\varepsilon_1 - \varepsilon_2)_{ev} \pm \frac{\chi_{1s}(\vec{r})\,\chi_{2s}^T(\vec{r}) - \chi_{2s}(\vec{r})\,\chi_{1s}^T(\vec{r})}{(\varepsilon_1 - \varepsilon_2)_{ev}} \qquad (1.40)$$

where $(\varepsilon_1 - \varepsilon_2)_{ev} = \frac{1}{2}\left\{(2\chi_s(0) - \alpha)^2 - 4\left(\chi_{1s}^2(\vec{r}) + \chi_{2s}^2(\vec{r})\right)\right\}^{\frac{1}{2}}$.

Let $Re\chi_{s1,2} \gg Im\chi_{s1,2}$, i.e., the absorption is assumed to be sufficiently small to satisfy the condition $k_0\ Im(\varepsilon_1 - \varepsilon_2)_{ev} L \ll 1$ which admits the consideration of the diffraction grating as an optically transparent medium with $(\varepsilon_1 - \varepsilon_2)_{ev}$ and $\chi_s$ as real functions. Let now the condition $k_0(\varepsilon_1 - \varepsilon_2)_{ev} L = 2\pi m$ be fulfilled at $m \neq 0$. This condition defines the resonance transmission in the grating and allows us to rewrite formula (1.40) in the form as follows

$$\varepsilon_1^{\pm} - \varepsilon_2^{\pm} = \frac{2\pi m}{k_0 L} \pm \frac{k_0\left[\chi_{1s}(\vec{r})\,\chi_{2s}^T(\vec{r}) - \chi_{2s}(\vec{r})\,\chi_{1s}^T(\vec{r})\right] L}{2\pi m} \qquad (1.41)$$

By substituting (1.41) into (1.33,1.32) one can express $\vec{E}_{\pm}$ by

$$\vec{E}_{\pm} = \vec{e}_{\pm}(-1)^m \left(1 - i\frac{k_0(\alpha_{1,2} - 2\chi_s(0))L}{8\pi m} k_0 \Delta^{\pm} L\right) e^{ik_0 \frac{1}{2} e^{\pm}(\alpha_{1,2}) L} \qquad (1.42)$$

where

$$\alpha_{1,2} = 2\chi_s(0) \pm \sqrt{4\left(\chi_{1s}^2 + \chi_{2s}^2\right) + \left(\frac{4\pi m}{k_0 L}\right)^2}$$

$$\varepsilon^{\pm}(\alpha_{1,2}) = \mp\chi_s^P(0) + \frac{1}{2}\alpha_{1,2}$$

In view of that the second term in (1.42) is small and expression (1.42) can be written as

$$\vec{E}_{\pm} = \vec{e}_{\pm}(-1)^m e^{i\varphi_{\pm}} \tag{1.43}$$

where the phase terms are given by

$$\varphi_{\pm} = k_0\left[\frac{1}{2}\varepsilon^{\pm}(\alpha_{1,2}) - \frac{k_0(\alpha_{1,2} - 2\chi_s(0))L}{8\pi m}\Delta^{\pm}\right]L \tag{1.44}$$

Using this equation one can find the angle of the polarization plane rotation:

$$\vartheta = Re(\varphi_+ - \varphi_-) = \vartheta^P + \vartheta_{1,2}^T \tag{1.45}$$

where the first term in the right-hand part defines the P-violating T-invariant rotation angle:

$$\vartheta^P = -k_0 Re\chi_s^P(0)\,L \tag{1.46}$$

and the second one corresponds to the T-violating rotation:

$$\begin{aligned}\vartheta_{1,2}^T(\alpha_{1,2}) &= \mp\frac{k_0^3 L^3}{8\pi^2 m^2}\sqrt{4\left(\chi_{1s}^2 + \chi_{2s}^2\right) + \left(\frac{4\pi m}{k_0 L}\right)^2} \times \\ &\times\left[\chi_{1s}(\vec{\tau})\,Re\chi_{2s}^T(\vec{\tau}) - \chi_{2s}(\vec{\tau})\,Re\chi_{1s}^T(\vec{\tau})\right],\end{aligned} \tag{1.47}$$

the $sign(-)$ is for $\alpha_1$ , the $sign(+)$ is for $\alpha_2$ .

The imaginary part of the T-violating polarizability $Im\chi_{s1,2}^T$ is responsible for the T-violating circular dichroism. Due to that process, a linearly polarized photon gets a circular polarization at the diffraction grating's output. The degree of the circular polarization of the photon is determined from the relation:

$$\begin{aligned}\delta_{1,2} = \frac{\left|\vec{E}_+\right|^2 - \left|\vec{E}_-\right|^2}{\left|\vec{E}_+\right|^2 + \left|\vec{E}_-\right|^2} \simeq Im\varphi_- - Im\varphi_+ = k_0 Im\chi_s^P(0)\,L \pm \\ \pm\frac{k_0^3 L^3}{8\pi^2 m^2}\sqrt{4\left(\chi_{1s}^2 + \chi_{2s}^2\right) + \left(\frac{4\pi m}{k_0 L}\right)^2}\left[\chi_{1s}(\vec{\tau})\,Im\chi_{2s}^T(\vec{\tau})\right. \\ \left. -\chi_{2s}(\vec{\tau})\,Im\chi_{1s}^T(\vec{\tau})\right]\end{aligned} \tag{1.48}$$

It should be pointed out that the resonance transmission condition is satisfied at a given m for two different values of $\alpha$. This is because there is a possibility to approach to the Brilluan (the total Bragg reflection) bandgap both from high and low frequencies. The T-violating parts of the rotation angle are opposite in sign for $\alpha_1$ and for $\alpha_2$. It gives the addition opportunity to distinguish the T-violating rotation from the P-violating T-invariant rotation. Indeed, the P-violating rotation does not depend on the back Bragg diffraction in the general case because the P-violating scattering amplitude equals zero for back scattering (see (1.32-1.35).

In accordance with (1.47,1.48) the T-violating rotation and dichroism grow sharply in the vicinity of the resonance Bragg transmission. At the first glance, one could expect for $\vartheta^T$ the dependence $\vartheta^T \sim k_0 Re\chi^T_{s1,2}(\vec{\tau})\, L$ (see (1.25)). However, in the vicinity of resonance, the rotation angle $\vartheta^T$ turns out to be multiplied by the factor

$$A = (8\pi^2 m^2)^{-1} k_0 \sqrt{4\left(\chi_{1s}^2 + \chi_{2s}^2\right) + \left(\frac{4\pi m}{k_0 L}\right)^2}\, L k_0 \chi_{s1,2} L$$

which provides the above mentioned growth (for example, $A \sim 10^5$ at $\chi_s \simeq 10^{-1}$ , $k_0 \simeq 10^4 \div 10^5 cm^{-1}$ , $L = 1cm$ , $m = 1$ ).

There are different types of diffraction gratings destined for use in optical and more longwave ranges. However, it should be noted that the successful observation of the P-violating rotation has been performed by means of studying of light transmission through gas targets . There are a lot of theoretical calculations for atoms of such gases: see, for example, (Khriplovich (1991)) for $Bi$ , $Tl$ , $Pb$ , $Dy$. From that point of view, it would be preferable to use gases for studying of the T-violating phenomena of polarization plane rotation and dichroism applying the experience accumulated earlier. At the first glance, there is a serious problem how to create such a diffraction grating in a gas. Nevertheless, the problem can be solved if we make use some well-known results of the electromagnetic theory of waveguides (Jackson (1962), Tamir (1988), Maksimenko and Slepyan (1997)). According to this theory, there is a correspondence between wave processes in waveguides with periodically modulated boundaries and homogeneous filling and such processes in regular waveguides filled by a periodic and, generally, anisotropic medium. Let us consider a regular waveguide constituted by two plane-parallel surfaces; for example, two metallic or dielectric mirrors. Let us then place a plane diffraction grating on the surface of the mirror and fill the waveguide

by the studied gas (Figure 1). Because of the above stated correspondence, such a system is equivalent to a regular plane waveguide filled by a gas with a spatially periodic permittivity tensor. The permittivity modulation period is therewith equal to the grating period. As the chosen plane grating has an asymmetric profile (Figure 1), the corresponding virtual volume grating of the permittivity turns out to be noncentrosymmetrical and, thus, satisfies to the above imposed requirements for displaying of the T-violating phenomena.

Let $\hat{\varepsilon}_{ij}(r,\omega) = 1 + \hat{\chi}_{ij}(x,z)$ be the permittivity of the waveguide being considered with as a periodic function with respect to $z$. As it has been stated above , such a waveguide can be modeled by the waveguide with the effective permittivity $\hat{\varepsilon}_{eff}(z,\omega) = 1 + \hat{\chi}_{eff}(z)$ which is a periodic function of $z$ and is independent on $x$. We can show it mathematically starting with the Maxwell equations

$$curlcurl\vec{E}(\vec{r},\omega) - \frac{\omega^2}{c^2}\hat{\varepsilon}(r,\omega)\vec{E}(\vec{r},\omega) = 0 \qquad (1.49)$$

Let an electromagnetic wave propagate in the plane regular waveguide. In this case, the motion along the $z$-axis is free and, thus, it can be described by a plane wave $e^{ikz}$. It results in a set of equations for determining of the stationary states of the waveguide:

$$\frac{d^2\vec{E}_{n\alpha}(x)}{dx^2} + \kappa_n^2\vec{E}_{n\alpha}(x) = 0$$

where $\kappa_n = \dfrac{2\pi n}{d}$ , $\alpha$ notes the polarization state of the wave.

Then, the field $\vec{E}(\vec{r},\omega)$ in the waveguide with the diffraction grating can be presented by the expansion as follows

$$\vec{E}(\vec{r},\omega) = \sum_n c_{n\alpha}(z)\vec{E}_{n\alpha}(x)$$

Substitution of this expansion into (1.50) yields

$$\frac{\partial^2}{\partial z^2}c_{n\alpha}(z) + \left(\frac{\omega^2}{c^2} - \kappa_n^2\right)c_{n\alpha}(z) + \frac{\omega^2}{c^2}\sum_{\tau\alpha}\hat{\chi}^{nn'}_{\tau\alpha\alpha'}e^{-i\tau z}c_{a'}(z) = 0 \qquad (1.50)$$

where $\hat{\chi}^{nn'}_{\tau\alpha\alpha'} = \int \langle E_{n\alpha}(x)|\chi_\tau(x)|E_{n'\alpha'}(x)\rangle\, dx$, $\chi_\tau = \dfrac{1}{a}\int_0^a \chi(z)\,e^{i\tau z}dz$, $a$- is the period of the plane grating.

Assuming the inequality $\frac{\chi^{nn'}\frac{\omega^2}{c^2}}{\kappa_n'^2-\kappa_n^2} \ll 1$ , $\chi_{nn} \ll 1$ to be valid, we can restrict ourselves to a single mode approximation, which allows us to rewrite (1.50) as

$$\frac{\partial^2}{\partial z^2}c_{n\alpha}(z)+\left(\frac{\omega^2}{c^2}-\kappa_n^2\right)c_{n\alpha}(z)+\frac{\omega^2}{c^2}\hat{\chi}_{\alpha\alpha'}(z)\,c_{\alpha'}(z)=0 \qquad (1.51)$$

where $\hat{\chi}_{\alpha\alpha'}(z)=\sum_{\tau}\hat{\chi}^{nn'}_{\tau\alpha\alpha'}e^{-i\tau z}$.

Equations (1.52) are identical with those (see (1.10)) describing the electric field in a volume diffraction grating. So, the goal formulated above has been achieved: we have obtained a volume diffraction grating.

Let us remind (see (1.18)) that the diffraction grating manifests the optical anisotropy (birefringens if the matter of grating possesses optical isotropy). The anisotropy makes difficult to observe the T-violating photon polarization plane rotation. Luckely, however, if the matter of the waveguide or diffraction grating is a dielectric one can change the optical anisotropy characteristics and even decrease the anysotropy sharply by the electric field due to the Kerr or Pockels effect.

Now, let us estimate the effect of the T-violation. To do that we must determine, in accordance with formula (1.47) for $\vartheta^T$, the T-violating susceptibility $\chi^T_{s1,2}$, which, in view of (1.13,1.3,1.4), is proportional to the T-violating atomic polarizability $\beta^T_s$. The estimate carried out by (Baryshevsky (1993,1994), Khriplovich (1991)) gives $\beta^T_s \sim 10^{-3} \div 10^{-4}\beta^P_s$, where $\beta^P_s$ is the P-violating T-invariant scalar polarizability. The polarizability $\beta^P_s$ was studied both theoretically and experimentally (Khriplovich (1991)). Particularly, the theory gives $\beta^P_s \cong 10^{-30}cm^3$ for atoms analogous to Bi, Tl, Pb. It yields the estimate $\cong 10^{-33} \div 10^{-34}cm^3$ for the T-violating atomic polarizability. The polarizabelity $\beta^P_s$ causes the P-violating rotation of the polarization plane by the angle $\vartheta^P = kRe\chi^P_s(0)\,L \cong 10^{-7}$ rad/cm×L for the gas density $\rho = 10^{16} \div 10^{17}$. As a result, in our case the parameter $\varphi = k\chi^T_s(\tau)\,L$ turns out to be $\varphi \cong 10^{-10} \div 10^{-11}$ rad/cm×L and can be even less by the factor h/d, where h is the corrugation amplitude of the diffraction grating while d is the distance between waveguide's mirrors. Assuming this factor to be $\sim 10^{-1}$, we shall find $\varphi \cong 10^{-11} \div 10^{-12}$ rad/cm×L. Thus, the final estimate of the T-violating rotation angle $\vartheta^T$ is

$$\vartheta^T \cong 10^{-11} \div 10^{-12}k_0^2\chi^2_s(\tau)L^3 \qquad (1.52)$$

In real situation the susceptibility of a grating $\chi_s(\tau)$ may exceed the unity. However, our analysis has been performed under the assumption $\chi_s \ll 1$. If, for example, we take $\chi_s = 10^{-1}$ , $k_0 = 10^4$ then $\vartheta^T \simeq 10^{-6} \div 10^{-7} L^3$ and, consequently, for L= 1 cm we will have the rotation angle $\vartheta^T \simeq 10^{-6} \div 10^{-7} rad.$

As it is seen, we have obtained the T-violating rotation angle $\vartheta^T$ of the same order of $\vartheta^P$. It makes possible experimental observation of the phenomenon of the T-violating polarization plane rotation.

It should be noted that the manufacturing of diffraction gratings for the range being more longwave than the visible light one may be simpler. That is why we would like to attract attention to the possibility of studying of the T-violating polarization plane rotation in the vicinity of frequencies of atomic (molecular) hiperfine transitions; for example, for Ce (the transition wavelength is $\lambda = 3.26$ cm) and Tl ( $\lambda = 1.42$ cm).

**Conclusion**

Thus, we have shown that the phenomenon of the T-violating polarization plane rotation appears while the photon is scattered by a volume diffraction grating. The phenomenon grows sharply in the vicinity of the resonance transmission condition. An experimental scheme based on a waveguide, containing a diffraction grating and gas, has been proposed which enables real experiments on observation of the T-violating polarization plane rotation to be performed. The rotation angle has been shown to be $\vartheta^T = 10^{-6} \div 10^{-7} L^3$, where L is the waveguide length (thickness of the equivalent volume diffracting grating). Let there is the electric field in the region of the gas. As a result, the scattering amplitude contains the T-violating term $f_E^T(0) = i\beta_E^T \vec{E}\,[\vec{e}^{\,*} \times \vec{e}]$. The phenomenon of the T-violating photon polarization plane rotation about $\vec{E}$ appeares due to this term. The effect grows sharply in the volume diffraction grating too, but the diffraction grating can be centrisymmetrical. More over the effect can be observed in usual resonator or ring laser because the sign of the photon polarization plane rotation about $\vec{E}$ do not depend from the direction of the photon momentum $\vec{k}$ unlike the P-violating, T-even polarization plane rotation effect which is proportional to $i\beta_v^P \vec{n}\,[\vec{e}^{\,*} \times \vec{e}]$.

## 2. Neutron spin rotation and spin dichroism in media.

Neutron spin rotation and spin dichroism in media caused by parity (P) violation and possible time (T) noninvariance under neutron interaction with nuclei are being actively explored recently (Alfimenkov (1983), Sushkov,Flambaum (1982), Stodolsky (1982), Koster et al (1991), Baryshevsky (1983), Bowman et al (1990), Franke et al (1991)). The mentioned effects are described by the refractive index of neutrons in media

$$\hat{N} = 1 + \frac{2\pi\rho}{k^2}\hat{f}(0), \tag{2.1}$$

where $k$ is the neutron wave number, $\rho$ is the scatters density, $\hat{f}(0)$ is the coherent elastic forward scattering amplitude of neutrons on a nucleus.

M.Forte shows (Forte (1983), Forte, Zayen (1989)) that the T-noninvariant effect of spin rotation arises under neutron diffraction by crystals with nonpolarized nuclei. This effect is determined by coherent elastic scattering amplitude at a non-zero angle $\hat{f}\left(\vec{k}', \vec{k}\right) \sim \vec{\sigma}\left(\vec{k}' - \vec{k}\right)$, where $\vec{\sigma}$ is the Pauli matrix describing neutron spin, $\vec{k}'$ is the wave vector of scattered neutron.

In (Forte (1983), Forte, Zayen (1989), Fedorov, Voronin, Lapin (1992)) the possibility of experimental measurements of this spin rotation effect was considered. One of the main difficulties of the diffraction methods suggested in (Forte (1983), Forte, Zayen (1989), Fedorov, Voronin, Lapin (1992)) is that even for thermal neutrons the beams with very low angular divergence rad and very high degree of monochromaticity $\frac{\Delta k}{k} \sim \frac{\Delta v}{v_B} \sim 10^{-5} \div 10^{-6}$ are needed, where $v_B$ is the angle of Bragg diffraction. Only very small part $\Delta\Phi$ of a neutron flow $\Phi$ can be used to carry out the experiment: $\Delta\Phi \sim \Phi\frac{\Delta k}{k}\Delta v$. The situation is still worse for the range of epithermal neutrons in which $\Delta v \sim 10^{-7}$ rad and even lower.

In (Baryshevsky (1995)) we have shown that there are new effects: the effects of T-noninvariant spin rotation and spin dichroism in the nonpolarized crystals even in case when diffraction conditions are not fulfilled. As a consequence, not only flow $\Delta\Phi$ increases, but the possibility of investigation of in $\hat{f}\left(\vec{k}', \vec{k}\right)$ the range of epithermal neutrons arises.

So, let the neutrons move through a crystal. According to (Baryshevsky (1995), Baryshevsky (1976), Baryshevsky, Cherepitsa (1985)) the Schrodinger equation describing propagation of a coherent neutron wave $\Psi$ in a

crystal with polarized nuclei in the impulse representation has the view

$$\left(k^2 - k_0^2\right)\Psi\left(\vec{k}\right) + \sum_{\vec{\tau}} \frac{2m}{\hbar^2}\hat{U}_{eff}\left(\vec{\tau}\right)\Psi\left(\vec{k} - 2\pi\vec{\tau}\right) = 0, \qquad (2.2)$$

where $k_0$ is the neutron wave number in vacuum, $k$ is the neutron wave number in a crystal. The Fourie transform of neutron effective potential energy in a crystal is

$$\hat{U}_{eff}\left(\vec{\tau}\right) = -\frac{2\pi\hbar^2}{mV_0}\hat{F}\left(\vec{\tau}\right); \hat{F}\left(\vec{\tau}\right) = \sum_j \hat{f}_j\left(\vec{\tau}\right) e^{-w_j(\vec{\tau})} e^{-i2\pi\vec{\tau}\vec{R}_j}, \qquad (2.3)$$

$\hat{F}\left(\vec{\tau}\right)$ is the amplitude of neutron coherent scattering on crystal unit cell in the direction $\vec{k}' = \vec{k} + 2\pi\vec{\tau}$ , where $2\pi\vec{\tau}$ is the vector of crystal reciprocal lattice, $\hat{f}_j\left(\vec{\tau}\right)$ is the amplitude of coherent elastic scattering $\hat{f}_j\left(\vec{k}', \vec{k}\right)$ on the nuclei of j-type in the direction $\vec{k}' = \vec{k} + 2\pi\vec{\tau}$ , $\vec{R}_j$ is the coordinate of the j nucleus in the unit cell, $e^{-w_j(\vec{\tau})}$ is the Debay-Waller factor.

The system of homogeneous equations (2.2) permits to determine the dependence of $k$ on $k_0$, i.e. to determine the neutron refractive index in a crystal.

It is well-known that the area $\Delta v$ of neutron incidence angle on a crystal in which strong diffraction is observed (when the diffracted wave amplitude is comparable with the amplitude of incident wave) is very small $\Delta v \sim 10^{-5} \div 10^{-6}$ rad even for thermal neutrons.

Outside this narrow angle area the diffracted wave amplitude is small and the system of equations (2.2) can be analyzed according to the perturbation theory. As a result, we have

$$\hat{N} = \frac{k}{k_0} \simeq 1 + \frac{1}{2}\hat{g}\left(0\right) + \frac{\hat{g}\left(-\vec{\tau}\right)\hat{g}\left(\vec{\tau}\right)}{2\alpha_B}, \qquad (2.4)$$

where

$$\hat{g}\left(\vec{\tau}\right) = -\frac{2m}{\hbar^2 k_0^2}\hat{U}_{eff}\left(\vec{\tau}\right), \alpha_B = \frac{2\pi\vec{\tau}\left(2\pi\vec{\tau} + 2\vec{k}_0\right)}{k_0^2}$$

As we see, the correction to the neutron refractive index in crystals contains the scattering amplitude at the non-zero angle $\hat{f}\left(\vec{\tau}\right)$.

According to (Baryshevsky (1995)) the expression for $\hat{g}\left(\vec{\tau}\right)$ can be written as a sum

$$\hat{g}\left(\vec{\tau}\right) = \hat{g}_s\left(\vec{\tau}\right) + \hat{g}_{so}\left(\vec{\tau}\right) + \hat{g}_w\left(\vec{\tau}\right), \qquad (2.5)$$

where $\hat{g}_s(\vec{\tau})$ is proportional to the scattering amplitude on the nucleus $\hat{f}_s(\vec{\tau})$ due to strong interactions minus spin-orbital scattering interactions; $\hat{g}_w(\vec{\tau})$ is proportional to the P and T-violating amplitude; $\hat{g}_{so} = \hat{g}_{son} + \hat{g}_{shw}$, $\hat{g}_{son}$ is proportional to the amplitude of spin-orbital neutron scattering on the nucleus due to nuclear forces $\hat{f}_{son}(\vec{\tau}) = f_{son}\vec{\sigma}\left[\vec{k} \times 2\pi\vec{\tau}\right]$, $\hat{g}_{shw}$ is proportional to the amplitude of spin orbital neutron scattering on the nucleus due to neutron magnetic momentum interaction with the nucleus electric field (the so-called Schwinger scattering):

$$\hat{g}_{shw} = i\frac{2m}{V_0\hbar^2 k_0^2}\frac{\mu\hbar}{mc}\sum_j \Phi_j(\vec{\tau})\, e^{-w_j(\vec{\tau})}\vec{\sigma}\left[\vec{k} \times 2\pi\vec{\tau}\right] e^{-i2\pi\vec{\tau}\vec{r}_j}, \tag{2.6}$$

$\mu$ is the magnetic neutron momentum, $\Phi_j(\vec{\tau})$ is the Fourie component of electrostatic potential induced by nucleus $j$.

In case of the target with nonpolarized nuclei $\hat{g}_s(\vec{\tau}) = g_s(\vec{\tau})$ does not depend on neutron spin. Besides, for slow neutrons $g_{so} \ll g_s$ . It allows to write the contribution to caused by diffraction in the following way

$$\delta\hat{N} = \frac{\hat{g}(-\vec{\tau})\,\hat{g}(\vec{\tau})}{2\alpha_B} = \frac{g_s(-\vec{\tau})\,g_s(\vec{\tau})}{2\alpha_B} + \frac{1}{2\alpha_B}g_s(-\vec{\tau})\left[\hat{g}_{so}(\vec{\tau}) + \hat{g}_w(\vec{\tau})\right] + \tag{2.7}$$

$$+\frac{1}{2\alpha_B}g_s(\vec{\tau})\left[\hat{g}_{so}(-\vec{\tau}) + \hat{g}_w(-\vec{\tau})\right].$$

Let the target be nonpolarized. In this case T-noninvariant part of $\hat{g}(\vec{\tau})$ is (Baryshevsky (1995))

$$\hat{g}_w^T(\vec{\tau}) = \frac{4\pi}{k^2 V_0}\sum_j \hat{f}_{jw}^T(\vec{\tau})\, e^{-w_j(\vec{\tau})}e^{-i2\pi\vec{\tau}\vec{R}_j}, \tag{2.8}$$

$$\hat{f}_{jw}^T(\vec{\tau}) = C_j'(\vec{\tau})\,\vec{\sigma}\frac{\vec{\tau}}{\tau}, C_j'(\vec{\tau}) = ReC_j' + ImC_j'.$$

¿From (2.7,2.8) we see that the T-noninvariant contribution to the refractive index in a nonpolarized crystals may occur only in a noncentrosymmetric crystals.

We see also that we have the two effects: the difference of the absorption coefficient of the neutrons with spin parallel and antiparallel to the vector $\vec{\tau}$ (spin dichroism) and the spin rotation around of the direction of $\vec{\tau}$.

Difference $æ_{\uparrow\uparrow} - æ_{\downarrow\uparrow} = k(Im\delta N_{\uparrow\uparrow} - Im\delta N_{\downarrow\uparrow})$

Spin rotation angle $\upsilon = kRe\,(\delta N_{\uparrow\uparrow} - \delta N_{\downarrow\uparrow})\,L$

Difference of the neutrons number $J_{\uparrow\uparrow}$ with spin parallel to $\vec{\tau}$ and the neutrons number $J_{\downarrow\uparrow}$ with spin antiparallel to $\vec{\tau}$ which passed through the crystal is

$$\frac{J_{\uparrow\uparrow} - J_{\downarrow\uparrow}}{J_{\uparrow\uparrow} - J_{\downarrow\uparrow}} = kIm\left(\delta N_{\uparrow\uparrow} - \delta N_{\downarrow\uparrow}\right) L \qquad (2.9)$$

where $L$ is the length of the neutron way in the crystal.

¿From (2.7) it follows that at the constant $\alpha_B$ the angle $\upsilon$ decreases proportionally to $k^{-3}$ and absorption $\sim k^{-1}$ So, at first glance the transfer to the epithermal range only makes worse the situation However, it should be taken into account that in the range of resonances the amplitudes $f_w(\vec{\tau})$sharply increase due to amplification mechanisms, being analogous to the well-known ones for the scattering amplitudes (Forte (1983), Baryshevsky (1995)). According to (Alfimenkov (1983)) there are two amplification mechanisms: dynamical and kinematic. They lead to the increase of the scattering amplitude near resonance in $\sqrt{\frac{\Delta E}{D}} \cdot \sqrt{\frac{\Gamma_{ns}}{\Gamma_{np}}} \simeq 10^5 \div 10^6$, where $\Delta E$ is the averaged distance between the single particle nuclei states, $D$ is the averaged distance between the levels of the compound nucleus, $\Gamma_{ns(p)}$ are the neutron widths of $s(p)$ the neutron state in the incident wave. As a result, for the neutrons with the energies $1 - 10ev$ we can expect the effect increase in $10^3 \div 10^2$ times and as a consequence the decrease in limitation for the detection of T- noninvariant effect. It is very important that neutron part $\Delta\Phi$ even increases as the magnitude $\frac{\Delta k}{k} \sim \frac{\Delta \upsilon_B}{\upsilon_B}$ and for $\Delta\upsilon_B = 10^{-4}$ , $\upsilon_B = \frac{2\pi\tau}{k} \sim 10^{-1}$ we have ten time increase of $\Delta\Phi$. At the same time investigation methods of spin rotation in the field of strong diffraction for the neutrons with such an energy are practically unrealized, since angular range of strong diffraction becomes $\Delta\upsilon_B \sim 10^{-7}$ rad. Two reasons simultaneously spoil the effect: angular spread of crystal mosaic structure ($\Delta\epsilon_m \geq 10^{-6}$ rad) and sharp suppression of flux $\Delta\Phi$ in such a small angular and energetic interval $\Delta\upsilon_B \frac{\Delta k}{k} \sim \frac{\Delta\upsilon_B^2}{\upsilon_B} = 10^{-13}$.

It is very important to say that the difference of absorption coefficient changes with the neutron energy increasing more slowly ($\sim k^{-1}$) than $\upsilon$ and sharply increases in the range of resonances also. As a result the study of the effect of spin dichroism may give the essential advantage in epithermal energy range.

# References


[1] Christenson J.H., Cronin J.W., Fitch V.L. and Turlay R. Phys. Rev. Lett. 13 (1964) 1138

[2] V.G.Baryshevsky Phys. Lett A 177 (1993) 38

[3] V.G. Baryshevsky and D.V.Baryshevsky Journ of Phys. B: At. Mol. Opt. Phys. 27 (1994) 4421

[4] A.M.Barkov and N.S.Zolotariov Lett. J. Exp. Theor. Phys. 118 (1978) 379 (in Russian)

[5] M.A.Bouchiat and L.Pottier Science 234 (1986) 1203

[6] V.V.Fedorov , V.V.Voronin , and E.G.Lapin Journ. of Phys. G: Nucl.Part. Phys. G 18 (1992) 1133

[7] M.J.Forte Journ. of Phys. G.: Nucl. Part. Phys. G 9 (1983) 745

[8] J.D.Jackson Classical electrodinamics (John Wiley & Sons, INC, New York - London) (1962)

[9] I.V.Khriplovich Party Nonconservation in Atomic Phenomena 1991 (London: Gordon and Breach)

[10] S.K.Lamoreaux Nucl. Instrum. Methods A 284 (1989) 43

[11] S.A.Maksimenko, G.Ya.Slepyan Electromagnetics 17 (1997) 147

[12] Shih-Lin Chang Multiple Diffraction of X-rays in Crystals 1984 (Springer-Verlag Berlin Heidelberg New York Tokyo)

[13] T.Tamir Guided-Wave Optoelectronics 1988 (Springer Verlag New York)

[14] V.P.Alfimenkov, Nuclear Physics A398 (1983) 93.

[15] O.Sushkov, V.Flambaum, Usp.Fiz.Nauk 25 (1982) 1.

[16] L.Stodolsky, Phys.Lett. B197 1982) 213.

[17] J.E.Koster et al, Phys.Lett B267 (1991) 23.

[18] V.G.Baryshevsky, Sov.J.Nucl.Phys. 38 (1983) 699.

[19] J.Bowman et al, Phys.Rev.Lett.65 (1990) 1192.

[20] C.Franke et al, Phys. Rev.Lett 67 (1991) 564.

[21] M.Forte, J. of Phys.G 9 (1983) 745.

[22] M.Forte, C.Zayen, Nucl. Instr. Met. A284 (1989) 147.

[23] V.Fedorov, V.Voronin, E.Lapin, J. of Phys. Journ. of Phys. G: Nucl.Part. Phys. G 18, (1992), 1133

[24] V.G.Baryshevsky, Physics of Atomic Nuclei 58 (1995) 1471

[25] V.G.Baryshevsky, J Exp.Theor Phys. 70 (1976) 430

[26] V.G.Baryshevsky, S.V.Cherepitsa, Phys.Stat.Sol (b) 128 (1985) 379

[27] L.I.Lapidus, Rev.Nod.Phys. 39 (1967) 689

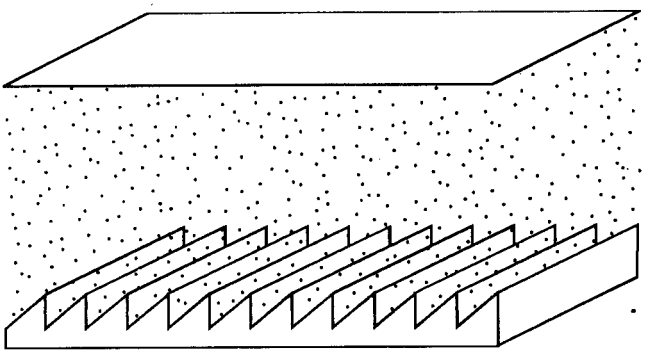

# Electron Spin Precession in a Circularly Polarized Electromagnetic Wave and the Basic Principles of Electron Spin Interaction with Classical Electromagnetic Fields

Victor V. Tikhomirov [1]

*Institute of Nuclear Problems, the Belorussian State University*
*220080, Minsk, Belarus'*

*It is shown that the recently predicted phenomenon of drastic increase of frequency of the electron spin precession in the field of a circularly polarized electromagnetic wave (CPW) indicates the necessity to modify both the Bargmann-Michel-Telegdi (BMT) and Dirac-Pauli (DP) equations as well as the Lagrangians of classical electrodynamics and relativistic quantum mechanics in order to take into consideration both a seagull interaction and off-shell effects accompanying the electron-photon scattering in the low photon energy limit. A patent inadequacy of the most well known derivation of the Low-Gell-Mann-Goldberger limit of the spin dependent part of the Compton scattering amplitude is also demonstrated*

## 1 Introduction

The phenomenon [1] of the electron spin precession in the field of a CPW can, in particular, be readily observed in the region of electron to photon conversion being widely designed at present for measuring a high energy electron beam polarization, investigation of QED effects in strong fields or production of $\gamma$-beams for future $\gamma$-$\gamma$ colliders.

The nature of $e\gamma$ interaction is determined by the photon frequency $\omega$

[1] Electronic mail address: tikh@inp.belpak.minsk.by

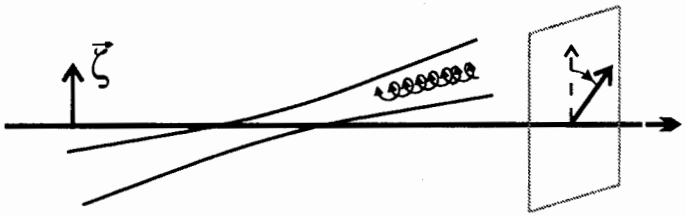

Figure 1: *A drastic increase of frequency of the electron spin precession in a CPW [1] can be observed in the electron-to-photon conversion region.*

in the electron rest frame or the parameter[2]

$$x = 2pk/m^2 = 2\omega/m, \tag{1}$$

where $k = (\omega_0, \omega_0 \mathbf{n}_0)$ and $p = (\varepsilon, \varepsilon \mathbf{v})$ are the photon and electron 4-momenta, respectively. Let us consider a head-on $e\gamma$ collision for which (1) takes the form of $x \simeq 4\omega_0\varepsilon/m^2 \simeq 0.0153\varepsilon(GeV)\omega_0(eV) \simeq 0.019\varepsilon(GeV)/\lambda(\mu m)$ indicating that the typical energies $\omega_0 \simeq 1eV$ and $\varepsilon \sim 100GeV$ allow to reach the quantum region $x \simeq 1$ of maximum increase of angle of the electron spin rotation about the photon wave vector direction in the electron rest frame [1].

In this talk we, however, will consider the classical (nearly Tomson) region $x \ll 1$, in which the phenomenon [1] gives birth to a new view on the basic concepts of electrodynamics of electron spin interaction with classical electromagnetic fields. Indeed, let us analyze the expression [1]

$$\Omega(x \ll 1) = \lambda_2 \frac{\alpha}{\pi} \omega_0 \xi_0^2 \left[ \frac{\alpha}{4\pi} - x^2 \left( \frac{5}{3} \ln \frac{1}{x} - \frac{37}{36} \right) \right] \tag{2}$$

for the electron spin precession frequency in a CPW at $x \ll 1$ which will be reproduced below. The positive spin rotation direction is chosen to look as an anticlockwise from the end of the electron velocity vector. Here $\xi_0 = |e|F/m\omega_0$ is the normalized strength of the CPW field $F = H = E$ and $\lambda_2 = \pm 1$ is the Stokes parameter measuring the degree of its polarization. All the statements discussed below spring from the qualitative change of behaviour of the frequency (2) which occurs in the depth of the classical region, instead of its border.

Indeed, at $x \ll 0.01$ eq. (2) corresponds both to the predictions of the BMT equation and the widely used expression for the low energy limit of

[2]We use the system of units in which $\hbar = c = 1$.

the spin dependent part of the Compton scattering amplitude $f_2'(0)\omega = -2\mu'^2\omega$ obtained by Low [2] and Gell-Mann and Goldberger [3]. Note that both $\Omega(x \ll 1)$ and the LGMG amplitude contain the particle AMM $\mu'$ which plays a key role both in the BMT and DP equations as well as in all the electrodynamics of electron spin interaction with classical electromagnetic fields. However at $x \simeq 0.01$ the frequency (2) changes its sign and at $x = 0.1$ its value exceeds the BMT equation predictions as much as 56 times what indicates that the latter as well as the concept of AMM itself can not describe the electron spin evolution at $x \sim 0.01 - 0.1$ despite a wide-spread opinion [4, §41] that the BMT equation remains adequate in the entire classical region $x \ll 1$ in which a typical length of the electromagnetic field strength variation greatly exceeds the electron Compton wavelength.

As far as the reliability of the predictions of eq. (2) is concerned, it should be noted that the phenomenon [1] is described by the same helicity amplitude as that of increase of an angle of the gamma-ray polarization rotation in a polarized electron target [5] which was observed in [6,7].

The paper is organized as follows. In Sec. 2 the application of the BMT equation to the case of electron spin precession in a CPW is considered. In Sec. 3 we remind the principal role AMM plays in spin interaction with classical electromagnetic fields. The idea of early BMT violation is illustrated in Sec. 4 using a dispersion relation for the scattering amplitude. In Sec. 5 the AMM contribution to the Feynman diagrams describing the phenomenon [1] is separated. In Sec. 6 we find out the nature of other contributions, making necessary to speak about the modification of the BMT and DP equations as well as of the Lagrangians of classical electrodynamics and relativistic quantum mechanics in the region $0.01 \leq x \ll 1$. The necessity to revise the well-known LGMG amplitude derivation is also discussed in Sec. 6. In Sec. 7 we summarize the results.

## 2 Why does the BMT equation predict so small spin precession frequency in a CPW?

A number of reasons exists that make an electromagnetic wave, and, in particular, a CPW, used in combination with an ultrarelativistic electron beam, the best tool to investigate the violation of predictions of the BMT equation. First, it can provide very high field nonuniformity and intensity in the electron rest frame. Second, on the contrary to the case of a linearly

polarized wave, a CPW itself causes an electron spin rotation which allows to study the peculiarities of its evolution in the absence of an additional test field which strength would necessarily be very high [8]. In addition, there is one more fundamental advantage of a CPW use.

Indeed, let us consider the BMT equation [9,4]

$$d\vec{\zeta}/dt = 2\Big(\mu' + \frac{\mu_0}{\gamma}\Big)[\vec{\zeta}\mathbf{H}] + \frac{2\mu'\gamma}{\gamma+1}(\mathbf{vH})[\mathbf{v}\vec{\zeta}] + 2\Big(\mu' + \frac{\mu_0}{\gamma+1}\Big)[\vec{\zeta}[\mathbf{Ev}]], \quad (3)$$

which describes the evolution of the spin vector $\vec{\zeta}$ of an electron (positron) moving with the energy $\varepsilon = \gamma m$ and velocity $\mathbf{v}$ in slowly varying electric $\mathbf{E}$ and magnetic $\mathbf{H}$ fields. Here $m$ and $e = \pm|e|$ are the electron (positron) mass and charge, $\mu_0 = e/2m$ and $\mu'$ are the normal and anomalous parts of their magnetic momenta, respectively ($|\mu_0|$ is equal to the Bohr magnetron). Remind, that if the effects in strong fields 8,10] are not important, than $\mu' \simeq \mu'_0$, where $\mu'_0 = (\alpha/2\pi)\mu_0$ is the celebrated AMM value calculated by Schwinger in 1948.

Substituting the electron velocity induced by the CPW into (3) one obtains [1] for the precession frequency of transverse spin component

$$\begin{aligned}\Omega^{BMT}_{cpw} &= 4\lambda_2\frac{H^2}{\omega_0}\left[\Big(\mu' + \frac{\mu_0}{\gamma}\Big)^2 - \frac{\mu_0}{\gamma}\Big(2\mu' + \frac{\mu_0}{\gamma}\Big)\right] \\ &= 4\lambda_2\mu'^2\frac{H^2}{\omega_0} = \lambda_2\Big(\frac{\alpha}{2\pi}\Big)^2\omega_0\xi_0^2.\end{aligned} \quad (4)$$

Two pairs of parenthesis in (4) separate the contributions which have a different origin. To describe the latter we will proceed from the fact that the BMT equation is only a generalization to the relativistic case of the equation $d\vec{\zeta}/dt = 2\mu[\vec{\zeta}\mathbf{H}]$ of the Larmor precession of a spin of a particle at rest which has a magnetic moment $\mu = \mu_0 + \mu'$. We will consider here the weak CPW field limit $\xi_0^2 \ll 1$ (the opposite one is analyzed in [1]). Let us choose the reference frame in which the electron is on average at rest moving with the Lorenz factor $\gamma = (1+\xi_0^2)^{1/2} \simeq 1$ in a circle under the action of a CPW. In this "average rest frame" the first contribution to (4) corresponds to $\vec{\mu} = \mu\vec{\zeta}$ interaction with a rotating magnetic field described by the first term in (3). The contribution in the second pair of parenthesis corresponds to the third term in (3) (the second one vanishes upon the time averaging in the chosen reference frame) and arises due to the magnetic field induced by the electric one in the instantaneous electron rest frame of rotating electron.

Note that the noninertiality of this reference frame leads to the difference of the numeric coefficients standing by $\mu_0$ and $\mu'$ in the first and third terms in the right hand side of (3). It is this difference, known since the time of "Thomas half" prediction, which provides a cancellation of contributions of two orders in $\alpha = 1/137$. As a result, the frequency (4) acquires the third order in $\alpha$ (in $\alpha/2\pi$, in fact) and becomes at $\gamma = 1$ about six orders lower than each of the two contributions to (4). A nearly complete cancellation of these (and some others, see below) contributions to the frequency (4) constitutes the mentioned above advantage of a CPW use for the purpose of investigation of possible deviations from predictions of the BMT equation. Even a small violation of this cancellation will cause a spin precession frequency increase by several orders of magnitude.

However, one can also easily see from (4) that on the contrary to $\mu_0$, the modification of $\mu'$ can not cause so significant variation of the spin precession frequency. Indeed, even such a considerable modification as $\delta\mu' \sim \mu'$ can cause only the frequency (4) variation by $\delta\Omega \simeq 8\lambda_2\mu'\delta\mu' H^2/\omega_0 \sim \Omega^{BMT}_{cpw}$. Whereas the same modification $\delta\mu_0 \sim \mu'$ of $\mu_0$ will case three order larger variation $\delta\Omega \simeq 8\lambda_2\mu_0\delta\mu' H^2/\omega_0 \sim 2(\mu_0/\mu')\Omega^{BMT}_{cpw} \sim 10^3\Omega^{BMT}_{cpw}$. The aforesaid allows us to conjecture that the AMM modification does not play such an important role in a CPW as it does in strong fields [8,10].

# 3 On the role of AMM

In fact, this role is illustrated by the expression (4), in which all the contributions of $\mu_0$ cancel out making $\mu'$ completely responsible for the effect of electron spin precession in a CPW. The same situation takes place in a uniform magnetic field $\mathbf{H}$ [4, §41]. Indeed, comparing the BMT equation $d\vec{\zeta}/dt = 2(\mu' + \mu_0/\gamma)[\vec{\zeta}\mathbf{H}] = (2\mu' + e/\varepsilon)[\vec{\zeta}\mathbf{H}]$ with that of electron motion $d\vec{v}/dt = (e/\varepsilon)[\vec{v}\mathbf{H}]$ in this case one can easily see that $2\mu_0/\gamma$ gives the same contribution to the precession frequency of particle spin as $e/\varepsilon$ to that of its velocity. As a result, the frequency $2\mu' H$ of spin rotation in respect with the particle velocity, naturally manifested in the case of *moving* particles, is again completely determined by $\mu'$. This statement remains valid even in the case of a very strong field [8,10] in which all the specifics of its action can be described by introduction of the AMM depending on the field strength into the BMT equation [11].

As is known, both the BMT equation and that of the Larmor precession describe the phenomena of both *Nuclear Magnetic* and *Electron Paramag-*

*netic Resonance* as well as the electron spin evolution in various devices used in accelerators with a very high accuracy. More general description of the spin evolution taking into consideration the quantum features of electron motion in a bound state can be developed [8] using the Dirac-Pauli (DP) equation

$$\left[\gamma^{\mu}\left(\frac{\partial}{\partial x_{\mu}} - ieA_{\mu}\right) - im - \frac{1}{2}\mu'\sigma_{\mu\nu}F^{\mu\nu}\right]\psi = 0. \qquad (5)$$

Like (3) the last does not implement other specific physical concepts than that of AMM. No wonder that in the case of classical motion the DP equation predictions do not differ from that of the BMT equation. In particular, it was shown independently by S.Cherkas and P.Zarzhitsky that the frequency (4) also follows from (5). As a consequence, the discussed violation of the BMT equation in a CPW also indicates that of the DP equation as well.

Up to now there were no doubt that the concept of AMM embodied in equations (3) and (5) describes well the electron spin evolution in a classical field. As far as the AMM of electron is calculated in QED, the classical electrodynamics of electron spin evolution can, in general, be considered as a *low energy effective theory* with respect to QED. We are going to prove that the drastic increase of frequency (2) indicates that this conventional theory is valid only in the region $x \ll 0.01$ whereas there is a reason to develop some *another effective theory* of electron spin interaction with classical electromagnetic field in the region $0.01 \leq x \ll 1$. In addition to AMM, this effective theory has to include some other *new characteristics of electron*. In addition, since the most refined way to obtain the BMT and DP equations is to use, respectively, the Lagrangians of classical electrodynamics and relativistic quantum mechanics, their modification can also be forecasted.

# 4 Dispersion relation and the spin precession

Going to the quantum theory of the phenomenon [1] we would remind that the subtracted dispersion relation [12]

$$\mathrm{Re}f_2(\omega) = f_2'(0)\omega + \frac{2\omega^3}{\pi}\,\mathrm{P}\int_0^{\infty}\frac{\mathrm{Im}f_2(\omega')}{\omega'^2(\omega'^2-\omega^2)}d\omega' \qquad (6)$$

for the spin dependent part $f_2(\omega)$ of the forward $\gamma e$ scattering amplitude $f(\omega) = f_1(\omega) - \lambda_2(\vec{\zeta}\mathbf{n})f_2(\omega)$ was used to predict the phenomenon [4-6] of gamma-ray polarization rotation in a polarized electron target. In fact, the electron spin precession in a CPW can be considered [13] in the same way using the amplitude $f(\varepsilon) = f_1(\varepsilon) - \lambda_2(\vec{\zeta}\mathbf{n})f_2(\varepsilon)$ of the forward $e\gamma$ scattering in a moving "photon target" with photon density (a number of photons in a cubic centimeter) $\rho_\gamma = H^2/4\pi\omega_0$.

When the electron is in rest or moves with the velocity $\mathbf{v} = -v\mathbf{n}$ $(v > 0)$ antiparallel to the photon with a frequency $\omega_0$, the amplitudes of $\gamma e$ and $e\gamma$ scattering are connected via simple equation [13,1]

$$f(\varepsilon) = \frac{\varepsilon v}{\omega} f(\omega), \tag{7}$$

where $\omega = \omega_0(1+v)\varepsilon/m = xm/2$ (see eq. (1)) is the photon frequency in the electron rest frame. Following the theory of Faraday effect one can introduce the refraction tensor $n = 1 + 2\pi f(\varepsilon)\rho_\gamma(1+v)/p^2 v$ containing the refraction indexes for electrons with opposite helicities allowing to calculate the angle of electron spin rotation and its precession frequency

$$\Omega = -\frac{2H^2}{\varepsilon\,\omega_0}\lambda_2 f_2(\varepsilon). \tag{8}$$

Even a brief analysis of eqs. (6)-(8) allows one to predict the phenomenon [1]. First, in the soft photon energy limit[3] one may neglect the integral term in (6) and get as a result the LGMG amplitude [2,3]

$$f_2^{(3)} = f_2'(0)\omega = -2{\mu_0'}^2\omega = -\frac{\alpha^3 x}{16\pi^2 m}. \tag{9}$$

Substituting the latter into (7) and (8) one obtains the spin rotation frequency (4) following from the BMT equation.

However the disregard of the integral term in (6) turnes out to be valid only at such small values of parameter (1) as $x = 2\omega/m \ll 0.01$. Indeed, the LGMG amplitude (9) is of order $\alpha^3$, whereas, according to the optical theorem, both $\mathrm{Im} f_2$ and the integral term in (6) are, in general, of order $\alpha^2$. As a result, with the increase of parameter $x$ the integral contribution to

[3]The unsubtracted dispersion relation taken in the same limit is called the Gerasimov-Drell-Hearn sum rule. It contains the widely discussed below LGMG amplitude and represents a considerable fundamental interest.

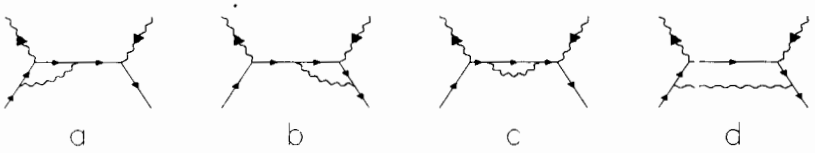


Figure 2: *Feynman diagrams contributing to the lowest order radiative correction to Compton scattering and describing both the phenomena [1] and [5].*

(6) begins to exceed (9) as soon as $x$ reaches 0.01, providing the sign change and drastic increase of the frequency (2). Since this increase manifests itself already in the depth of the classical region, the question arises why it is not described by the BMT and DP equations widely used to describe with a great precision the electron spin interaction with classical electromagnetic fields characterized by $x \ll 1$. Since both (3) and (5) are based on the concept of AMM, in order to answer this question we should first analyze the role which AMM plays in the Compton scattering.

# 5 The AMM contribution to the amplitude of Compton scattering

The most conventional way to introduce the electron AMM is based on the Feynman diagrams. It has just been pointed out that the phenomenon [1] is described by the contribution of order $\alpha^2$ to the Compton scattering amplitude which corresponds to the fourth-order Feynman diagrams shown in Fig.2. It should also be mentioned that the amplitude $M$ evaluated according to the Feynman rules is connected with the amplitude $f(\omega)$, determining the refraction index, by the relation [1]

$$f(\omega) = \frac{M}{8\pi m}. \tag{10}$$

Since the time of Schwinger it is well-known that the AMM of electron and, more general, its magnetic form factor is described by the vertex diagrams of the third and higher orders. This statement, however, is valid only when both electron lines connected to the vertex diagram are external while the photon one is internal. If, on the contrary, at list, one electron line connected to the vertex diagram is internal, as in the case of the real photon Compton scattering, a relation of this vertex diagram to the AMM

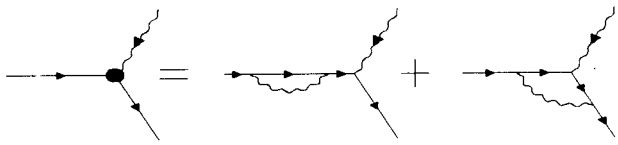

Figure 3: *The third order effective vertex operator which allows to introduce the concept of AMM in the case of a real photon.*

is not so direct. Indeed, let us consider the third-order vertex operator of absorption of a real photon by an electron

$$\Gamma^{(3)}_{\mu} - \gamma_{\mu} \equiv \Lambda^{(3)}_{\mu}(p,p') = \frac{\alpha}{2\pi}\left(A\gamma_{\mu} - B\frac{\hat{q}\gamma_{\mu}}{m} - C\frac{p_{\mu}}{m} - D\frac{\hat{q}p_{\mu}}{m^2}\right) \qquad (11)$$

evaluated [14] in the Feynman gauge. Here $\hat{q} \equiv \gamma q = \gamma^{\mu}q_{\mu} \equiv \gamma^0 q_0 - \vec{\gamma}\vec{q}$, $\mu = 0,1,2,3$, $\gamma_{\mu}$ are the Dirac matrices, $p$ and $p' = p + q$ are the electron 4-momenta before and after absorption of a real photon with 4-momentum $q$ ($p^2 = m^2, q^2 = 0$). The coefficients $A, B, C$ and $D$ are functions of electron virtuality $\rho = 1 - p'^2/m^2 = -2pq/m^2$, $\rho = -x$ for the photon absorption and $\rho = x$ for its emission.

In order to introduce the concept of AMM in the case of electron transitions between the states on a mass shell, the amplitude $-e\bar{u}\Gamma_{\mu}uA^{\mu}$ should be considered [4]. However, if, say, the final electron is not on the mass shell, this amplitude will contain the term proportional to $\ln|\rho|$ [14] which has no finite limit at $\rho \to 0$. To introduce the magnetic form factor which has the limit corresponding to the Schwinger's value $\mu'_0$ of AMM in the case of a static uniform magnetic field, the external virtual electron line should be described by the multiplier [4, §110]

$$U(p') = u(p') + S(p')M(p')u(p') \qquad (12)$$

instead of the usual wave function amplitude $u$. $S(p')$ in (12) is the precise electron propagator and $M(p') = \hat{p}' - m - S^{-1}(p')$ is the mass operator. We will show that the amplitude $\bar{U}(p')\Gamma_{\mu}u(p) = \bar{u}(1 + MS)\Gamma_{\mu}u$ has the same limit at $q \to 0$ as the well-known Schwinger's amplitude of virtual photon absorption accompanying the electron transition between the states on the mass shell. This amplitude allows to determine the effective vertex operator of the electron interaction with a real photon (see Fig.3)

$$\Gamma_\mu^{eff}(\rho) = (1 + MS)\Gamma_\mu \approx \left(1 + M\frac{1}{\hat{p}' - m}\right)(\gamma_\mu + \Lambda_\iota^{3)}) \\ = \gamma_\mu f(\rho) + \frac{\hat{q}\gamma_\mu}{2m}g(\rho) - \frac{\alpha}{2\pi}\frac{\hat{q}p_\mu}{m^2}D(\rho), \tag{13}$$

where

$$f(\rho) = 1 - \frac{\alpha}{4\pi}\rho D(\rho), \qquad g(\rho) = \frac{\alpha}{2\pi}\Big[C(\rho) - 2B(\rho)\Big]. \tag{14}$$

Though these functions of the electron virtuality $\rho$ have no such interpretation as the more usual form factors $f(q^2)$ and $g(q^2)$ do in the Breit system [4], we will also call them the electric and magnetic form factors, respectively, leaving the argument $\rho = \pm x$ to mark their specifics. Since, according to eq. (14) and the expressions [14] for the coefficients $B, C$ and $D$, one has $f(0) = 1$, $g(0) = \alpha/2\pi = \mu_0'/\mu_0$ and $D(0) = 0$, the effective vertex operator (13) indeed transforms at $\rho \to 0$ to the well known expression

$$\Gamma_\mu^{eff}(\rho \to 0) = \gamma_\mu - \frac{\alpha}{2\pi}\frac{1}{2m}\sigma_{\mu\nu}q^\nu \tag{15}$$

describing the interaction of a particle with charge $e$ and AMM $\mu_0' = (\alpha/2\pi)\mu_0$ with a weak static uniform electromagnetic field [4,8,14].

The vertex operator (13) will allow us below both to show that the magnetic form factor variation does not play any significant role in the spin precession frequency (2) increase and to establish the factors really causing this phenomenon. Namely, the regular contribution to the Copmton scattering amplitude described mainly by the box diagram *d* from Fig.2 and the contribution of the off-shell effects described by the electric form factor $f(\rho)$. As far as the phenomenon [1] is closely connected with the LGMG amplitude (9), it has also to appear in our consideration. Furthermore, we will show that the well known evaluation of this amplitude [2,4] is oversimplified and must be substantially revised.

# 6 The nature of the BMT equation violation

In fact, the LGMG amplitude (9) represents a really fundamental interest in application to the Compton scattering on a *nucleon*. In its turn a much more transparent considered case of $e\gamma$ scattering, allowing to evaluate both the vertex operator (13) and the regular contribution to the

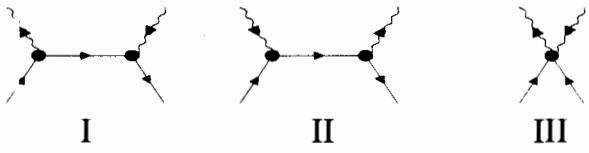


Figure 4: *The diagrams representing to the pole (I, II) and regular (III) contributions to the Compton scattering amplitude.*

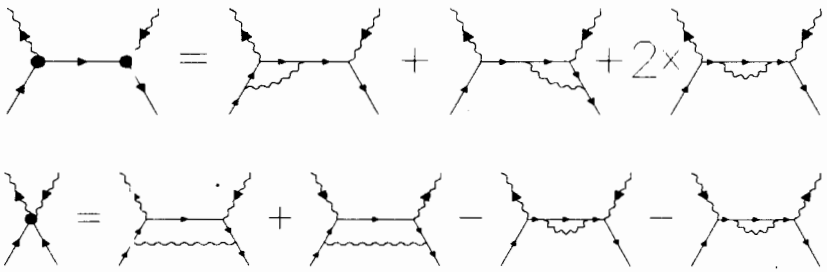

Figure 5: *A connection of the diagrams I and III describing the pole and regular contributions to the Compton scattering amplitude, respectively, with the diagrams a – d describing the first correction to the Compton scattering. The similar connection for the diagram II discribing the remaining part of the pole contribution is obtained from that for the diagram I above by changing the order of photon emission and absorption.*

Compton scattering amplitude, will allow us to verify the validity of several principal assumptions made in the most traditional approach [2,4] to the derivation of the LGMG amplitude.

Indeed, let us follow the simplest way of [4] and represent the Compton scattering amplitude as a sum of pole and regular contributions described, respectively, by the diagrams $I, II$ and $III$ given in Fig. 4. Since the fourth-order Feynman diagrams describe the essence of the phenomenon [1], it will be sufficient to use the third-order effective vertex operator (13) (see Fig. 3) for the vertexes of the diagrams $I$ and $II$ in order to express in accordance with Fig.5 the contributions of diagrams $I, II$ and $III$ from Fig. 4 through that of diagrams $a - d$ from Fig.2. As far as $\rho = -x$ for emission and $\rho = x$ for absorption of the photon, we will express the summary contribution of the diagrams with the opposite order of these processes through the single positive parameter $x = |\rho|$. In order to follow the details of the LGMG amplitude derivation in [2,4] let us first

substitute the low energy limit (15) of the vertex operator (13) to the forward scattering amplitudes, corresponding to the pole diagrams *I* and *II*. As a result we deceptively easy (see below) obtain the expression

$$M_{LGMG} = 2\pi\alpha x g^2(0)\lambda_2(\zeta\mathbf{n}) = 16\pi\omega m{\mu'_0}^2\lambda_2(\zeta\mathbf{n}) = \frac{\alpha^3\omega}{\pi m}\lambda_2(\zeta\mathbf{n}), \qquad (16)$$

which, according to (10), exactly corresponds to the LGMG amplitude (9). However, if we use a precise expression (13) for the vertex operator instead of its on-shell limit (15), we obtain

$$\mathrm{Re}M_{I+II} = \pi\alpha\Big\{4\Big[f^2(-x) - f^2(x)\Big] + x\Big[g^2(-x) + g^2(x)\Big]\Big\}\,\lambda_2(\zeta\mathbf{n}) \qquad (17)$$

for the real part of the Feynman amplitude (it is the real part which describes spin rotation). From the low energy expansion of (17)

$$\mathrm{Re}M_{I+II}(x \ll 1) \approx 4\alpha^2\frac{\omega}{m}\Big[1 + \frac{7}{4}x^2 + \Big(4 + 7x^2\Big)\ln x + \frac{\alpha}{4\pi}\Big]\lambda_2(\zeta\mathbf{n}) \qquad (18)$$

one can easily see that, in addition to the latter term in the brackets which corresponds to the amplitude (16), eq. (18) contains the contribution

$$4\alpha^2\frac{\omega}{m}\Big(1 + 4\ln x\Big)\lambda_2(\zeta\mathbf{n}) \qquad (19)$$

which was, in fact, overlooked in [2,4] though it exceeds the LGMG amplitude (16) more than $4\pi/\alpha \sim 10^3$ times in the low energy limit. We should stress that this contribution takes its origin from the completely neglected in [2,4] *off-shell effects* described mainly by the electric form factor $f(\rho)$, whereas the role of the magnetic form factor $g(\rho)$ is much smaller. This circumstance makes the phenomenon [1] principally different from that of the BMT equation modification in the strong uniform [8] and wave [10] fields since both of them completely reduce to the AMM modification which can, in fact, be quite naturally incorporated to the BMT equation.

Equations (7)-(10) and (19) show that the pole contribution to the Compton scattering amplitude leads to the spin precession frequency thousands times exceeding that of (4) following from the BMT equation. If this prediction was true, both the BMT equation and all the concept of AMM would be completely inapplicable in any field which Fourier expansion contains even a small component with circularly polarization.

Since this is not the case, the problem of compensation of the combination (19) arises which can be resolved applying to the regular contribution

$$\mathrm{Re}M_{III} = 2\alpha^2\left\{\left(\frac{4}{x}-1\right)\left[F(x-1)+\frac{\pi^2}{6}\right]\right.$$
$$\left.-\left(\frac{4}{x}+1\right)\left[F(x)-\ln x\ln(1+x)\right]-\frac{x}{1-x^2}-\frac{2x\ln x}{(1-x^2)^2}\right\}\lambda_2(\zeta\mathbf{n}) \qquad (20)$$

described by the diagram *III* (see Figs. 4 and 5) and contributing to the total spin dependent part of the Compton scattering amplitude $M = M_{I+II} + M_{III}$ which through the eqs. (10), (7) and (8) leads to the basic formulae (2) of this paper. A low energy expansion of (20)

$$\mathrm{Re}M_{III}(x \ll 1) \approx -4\alpha^2\frac{\omega}{m}\left[1+\frac{13}{18}x^2+\left(4+\frac{16}{3}x^2\right)\ln x\right]\lambda_2(\zeta\mathbf{n}) \qquad (21)$$

indeed contains the combination (19) with the minus sign. In other words, one can state that it is the compensation of (19) in (18) and (21) which leads to the LGMG amplitude (9).

It should be mentioned that both the off-shell effects and their cancellation with the regular part of the scattering amplitude, restored with the help of Ward identity, were, *in principle*, taken into account in [3]. However the complex case of the Compton scattering by a nucleon made it impossible to realize that the combination $\rho\ln\rho$ appearing in (13) in the soft limit can not be treated in such a way on the contrary to the term proportional to $\rho$ which, in fact, was implied in [3].

The regular contribution to the Compton scattering amplitude described by the diagram *III* reduces to the purely spin dependent *effective seagull* $e\gamma$ *interaction* in the classical limit. As is well-known, such type of interaction is completely absent in the *spinor* QED. The situation with this interaction as well as with the effective Lagrangian which can be introduced to take this interaction into account, reminds that with the effective $\gamma$-$\gamma$ interaction corresponding to the Heisenberg-Euler theory [15].

In fact, the regular contribution will be really important only if it is unremovable by the gauge transformation. The simple straightforward calculations being possible in the case of $e\gamma$ scattering show that the *virtual photon* gauge transformation does not change neither pole $I+II$ nor regular *III* contribution. On the other hand the *real photon* gauge transformation will change the contributions of both $I+II$ and *III* by terms proportional to

the combination $\bar{u}\gamma^{\mu}\hat{q}u[f(x)g(x) - f(-x)g(-x)]$. The latter does not vanish if the off-shell effects are taken into consideration by means of electron magnetic form factor $g(x)$ completely refuting by this the demonstration of possibility to neglect the allegedly gauge invariant regular contribution *III* in [4]. However, despite the latter is changed under this gauge transformation, this change can not, in fact, remove the combination (19) which cancellation in (18) and (21) leads to the LGMG amplitude.

On the other hand the evident absence of cancellation of the terms proportional both to $\alpha^2 x^2$ and $\alpha^2 x^2 \ln x$ in (18) and (21) provides the fast exceeding of the spin dependent part $M = M_{I+II} + M_{III}$ of the forward Compton scattering amplitude over the LGMG limit describing through eqs. (7)-(10) the fast increase of the spin precession frequency (2) leading to the complete violation of the BMT equation predictions at quite classical photon frequencies $\omega \sim 1\text{keV}$.

All the aforesaid allows to argue that to describe the electron spin interaction with a CPW in the classical photon energy region $0.01 \leq x \ll 1$ the $e\gamma$ seagull interaction as well as the off-shell effects have to be taken into consideration in order to modify all the known methods used to describe the electron spin evolution in *an arbitrary* classical electromagnetic field.

# 7 Conclusions

In conclusion, our investigation have shown that the BMT equation as well as the obtained by Low [2] and Gell-Mann and Goldberger [3] low energy limit of the spin dependent part of the Compton scattering amplitude adequately describe the electron spin precession in the field of a CPW only in the depth of the classical photon frequency region $\omega \ll 1keV$ or $x = 2\omega/m \ll 0.01$.

To describe the electron spin precession in a CPW in the upper part $0.01 \leq x \ll 1$ of the classical region $x \ll 1$ some purely spin dependent $e\gamma$ *seagull interaction* as well as the *off-shell effects* described mainly by the electric form factor have to be taken into consideration in order to modify the BMT and DP equations as well as the Lagrangians of classical electrodynamics and relativistic quantum mechanics.

In addition, the transparent QED consideration made it possible to revile the drawbacks of the LGMG amplitude derivation based on the disregard of both the *off-shell effects* and the *regular part* of the Compton scattering amplitude in the low photon energy limit. Namely, it was shown that particularly the cancellation of the contributions of these two features,

each of which exceed the LGMG amplitude a thousand times and more, constitute a basic foundation of the LGMG theorem which, thus, can not be considered as well-grounded in the most interesting case of $\gamma$-*nucleon* scattering.

The author is indebted to Prof. V.G.Baryshevsky and Prof. I.B.Khriplovich for valuable discussions as well as to D.N.Matsukewich for the help in calculations.

# References

[1] V. V. Tikhomirov. Phys. Rev. D **53** (1996) 7213.
[2] F. E. Low, Phys. Rev. **96**, (1954) 1428.
[3] M. Gell-Mann, and M. L. Goldberger, Phys. Rev. **96**, (1954) 1433.
[4] V. B. Beteistetsky, E. M. Lifshits, and L. P. Pitaevsky, *Quantum Electrodynamics*, Pergamon, Oxford 1982.
[5] V. G. Baryshevsky, and V. L. Lyuboshits, Yad. Fiz. **2**, (1965) 666.
[6] V. M. Lobashov *et al.*, Pis'ma Zh. Eksp. Teor. Fiz. **14**, (1971) 373.
[7] P. Bock, and P. Luksch, Lett. Nuovo Cim. **2**, (1972) 1081.
[8] I. M. Ternov, V. R. Khalilov, and V. M. Rodionov, Zh. Eksp. Teor. Fiz. **71**, (1976) 871; *Interaction of Charged Particles with an Intense Electromagnetic Field* (in Russian), Izd. MGU, Moscow, 1982.
[9] V. Bargmann, L. Michel, V. L. Telegdi, Phys.Rev.Lett. **2**, (1950) 935.
[10] V. I. Ritus, Zh. Eksp. Teor. Fiz. **57**, (1969) 2176; Proc. (Tr.) P. N. Lebedev Phys. Inst. Acad. Sci. USSR **111**, (1979) 3.
[11] V. N. Baier, V. M. Katkov, and V. S. Fadin, *Radiation by Relativistic Electrons* (in Russian), Atomizdat, Moscow, 1973.
[12] M. Gell-Mann, M. L. Goldberger, and W. E. Thirring, Phys. Rev. **95**, (1954) 1612.
[13] V. G. Baryshevsky, Yad. Fiz. **48**, (1988) 1063.
[14] A. I. Akhieser and V. B. Berestetsky, *Quantum Electrodynamics* (Interscience, New York, 1965).
[15] A.V.Manohar, *Effective Field Theories*, hep-ph/9606222.

# Nonorthogonality Of Refraction Operator Eigenstates For Nucleons (Antiprotons) Moving In Polarized Target And The Possibility Of Extraction Of Information About Real Part Of Forward Coherent $pp$, $np$ and $\bar{p}p$ Scattering Amplitude

V.G.Baryshevsky[1], A.V.Raspereza[2]

[1] *Research Institute For Nuclear Problems, Bobruiskaya str. 11, 220050 Minsk, Belarus*

[2] *National Scientific and Educational Center of Particle and High Energy Physics attached to Byelorussian State University, Bogdanovich str. 153, 220040 Minsk, Belarus*

It is shown that refraction operator eigenstates are not orthogonal for nucleons and antiprotons moving in polarized target. It leads to the appearence of a specific interference term in the expression describing beam intensity evolution. This effect can be used for extraction of information about real part of amplitude of forward coherent $pp$, $np$ and $\bar{p}p$ scattering.

# 1 Introduction

It is known that for relativistic nucleons travelling in polarized media the effect of spin rotation takes place [1],[2]. This effect is the consequence of the fact that nucleon wave is characterized by two refractive indicies corresponding to two different spin states of nucleon, and can be interpreted as the result of interference of such states [3]. Measuring angle of spin rotation one can find real part of forward coherent $NN$ scattering amplitude $\hat{f}(0)$. The description of such experiment can be found in [2]. Pronounced effect opens the possibility for investigation of wide spectrum of phenomena arising in $np$ and $pp$ scattering. For example, information on both real and imaginary parts of $\hat{f}(0)$ may clarify the question concerning the existence of dibaryon resonances [4] - [6]. So far the dispersion analysis has been the only indication of existence of such exotic baryon states [5], [6]. However theoretical results presented in these papers need detailed experimental verification. Knowledge of real part of $\hat{f}(0)$ is also necessary for investigation of inelastic channels of $pp$ and $pn$ scattering.

Since refraction operator isn't hermitian, eigenstates of refraction operator

may not be orthogonal. In this case the specific interference term arises in the expression describing the evolution of beam intensity, which becomes sensitive to the real part of $\hat{f}(0)$. It allows us (it is shown below) to extract additional information about real part of $\hat{f}(0)$ by direct measurement of intensity of nucleon (antiproton) beam propagating through polarized target.

The paper is organized as follows. In second section we give theoretical background for the effect of interference of refraction operator eigenstates, and consider conditions upon which this effect arises. Moreover, the expression for intensity evolution of nucleon beam in mixed state for arbitrary geometry of scattering is deduced. Third section is devoted to numerical analysis carried out on the basis of theoretical background. Brief description of the proposed experiment is presented in this section. The expected statistical accuracy of measurement is estimated.

Though experiment, proposed in present paper, doesn't imply complete determination of real part of forward scattering amplitude, it's simpler in comparison with the experiment described in [2], because it doesn't require measurement of polarization of particles passed through polarized target. Such experiment can be considered as the first step to research programme, aimed at complete measurement of forward coherent $pp$ $pn$ $\bar{p}p$ scattering amplitude, and can be used as independent test for further generation of related experiments.

# 2 Theoretical background

## 2.1 Nonorthogonality of refraction operator eigenstates

Let us consider the beam of nucleons (antiprotons) propagating through polarized target. Wave function of nucleons propagating in medium is described by plane wave:

$$\mid \Psi(z)\rangle = \exp\left(ik\hat{N}z\right) \mid \Psi(0)\rangle, \tag{1}$$

where $k$ - wave number, $\mid \Psi(0)\rangle$ - initial wave function, $\hat{N}$ - refraction operator. The latter can be expressed using amplitude of forward scattering of nucleons on polarized nuclei [7]:

$$\hat{N} = 1 + \frac{2\pi\rho}{k^2}\hat{f}(0), \tag{2}$$

where $\rho$ is density of polarized nuclei in the target. In its turn P- and T-invariant amplitude of coherent forward scattering of particles with spin 1/2 on polarized target can be written as follows:

$$\hat{f}(0) = A + B(\vec{P}_t\hat{\vec{\sigma}}) + C(\vec{P}_t\vec{n})(\vec{n}\hat{\vec{\sigma}}), \tag{3}$$

where $\vec{P}_t$ - vector of target polarization, $\vec{n}$ - unit vector in the direction of beam propagation, $\hat{\vec{\sigma}}$ - vector composed of Pauli matricies, $A$, $B$, $C$ - complex constants. Let us represent refraction operator in the following form:

$$\hat{N} = G + (\vec{G}\hat{\vec{\sigma}}),$$

$$G = 1 + \frac{2\pi\rho}{k^2}A, \tag{4}$$

$$\vec{G} = \frac{2\pi\rho}{k^2}(B\vec{P}_t + C(\vec{n}\vec{P}_t)\vec{n}) = \vec{G}_1 + i\vec{G}_2,$$

where $\vec{G}_1$ and $\vec{G}_2$ are real and imaginary parts of vector $\vec{G}$. Let us introduce refraction operator eigenfunctions $\mid n_1\rangle$ and $\mid n_2\rangle$, normalized to the unit. It should be noted that normalized eigenfunctions of linear operator are defined with the accuracy of phase factor $\exp(i\alpha)$. Therefore we can choose $\mid n_1\rangle$ and $\mid n_2\rangle$ in such a way that their product is real value:

$$\langle n_1 \mid n_2\rangle = \langle n_2 \mid n_1\rangle. \tag{5}$$

In this case the product of $\mid n_1\rangle$ and $\mid n_2\rangle$ can be expressed in terms of vectors $\vec{G}_1$, $\vec{G}_2$ and value $G$ as follows:

$$\langle n_1 \mid n_2\rangle = \langle n_2 \mid n_1\rangle = \frac{d}{\sqrt{\mid n_1 - n_2 \mid^2 + d^2}}, \tag{6}$$

where

$$d = sign(\vec{G}_1\vec{G}_2)\sqrt{2\left(\vec{G}_1^2 + \vec{G}_2^2 - \sqrt{(\vec{G}_1^2 - \vec{G}_2^2)^2 + 4(\vec{G}_1\vec{G}_2)^2}\right)}, \tag{7}$$

and

$$n_{1,2} = G \pm \sqrt{\vec{G}^2} = G \pm \sqrt{\vec{G}_1^2 - \vec{G}_2^2 + 2i(\vec{G}_1\vec{G}_2)}. \tag{8}$$

$n_1$ and $n_2$ are refractive indicies of nucleons moving in target. From expressions (4 - 8) It directly follows from expressions (4 - 8), that vector $\vec{G}$ is representable in the form:

$$\vec{G} = \frac{n_1 - n_2}{2}\vec{g}, \tag{9}$$

where $\vec{g}$ - unit complex vector : $\vec{g}^2 = 1$. Analysis of relations (6 - 8) shows that orthogonality of refraction operator eigenstates is possible in three cases:

1) when vector $\vec{P}_t$ is parallel to vector $\vec{n}$;
2) when vector $\vec{P}_t$ is perpendicular to vector $\vec{n}$;

3) when the following relation is satisfied:

$$\Delta = \begin{vmatrix} \Re(B) & \Re(C) \\ \Im(B) & \Im(C) \end{vmatrix} = 0, \tag{10}$$

where $\Re(Z)$ and $\Im(Z)$ are real and imaginary parts of complex number $Z$ respectively. In all other cases refraction operator eigenstates are not orthogonal.

## 2.2 Interference of refraction operator eigenstates

Initial wave function can be written as superposition of $\mid n_1\rangle$ and $\mid n_1\rangle$ states:

$$\mid \Psi(0)\rangle = C_1 \mid n_1\rangle + C_2 \mid n_2\rangle \tag{11}$$

Wave function of nucleon at the depth $z$ in the target can be written in the following way:

$$\mid \Psi(z)\rangle = C_1 \exp(ikn_1 z) \mid n_1\rangle + C_2 \exp(ikn_2 z) \mid n_2\rangle. \tag{12}$$

Expression for beam intensity $I(z) = \langle \Psi(z) \mid \Psi(z)\rangle$ has the following form:

$$\begin{aligned} I(z) = &\mid C_1 \mid^2 \exp(-2\Im(n_1)kz) + \mid C_2 \mid^2 \exp(-2\Im(n_2)kz) + \\ &+2\Re(C_2^* C_1 \langle n_2 \mid n_1\rangle \exp(i(n_1 - n_2^*)kz)) \end{aligned} \tag{13}$$

Introducing the definitions:

$$\begin{aligned} \mid C_i \mid^2 &= I_i, \\ C_2^* C_1 &= \sqrt{I_1 I_2}\exp(i\alpha), \\ -2k\Im(n_i) &= \sigma_i \rho, \end{aligned} \tag{14}$$

where $\sigma_i$ has the sense of cross section of absorbtion for particle in state $\mid n_i\rangle$, we finally obtain:

$$\begin{aligned} I(z) = &I_1 \exp(-\sigma_1 \rho z) + I_2 \exp(-\sigma_2 \rho z) + \\ &+2\sqrt{I_1 I_2}\langle n_2 \mid n_1\rangle \exp(-\frac{1}{2}(\sigma_1 + \sigma_2)\rho z)\cos(\Re(n_1 - n_2)kz + \alpha) \end{aligned} \tag{15}$$

The latter term in expression (15) describes the interference of refraction operator eigenstates $\mid n_1\rangle$ and $\mid n_2\rangle$. One should note that in the case of the orthogonality of these states interference term is equal to zero. Interference is also absent when initial state of nucleon is $\mid n_1\rangle$ or $\mid n_2\rangle$.

## 2.3 Intensity evolution in the case of arbitrary geometry of scattering

Let us consider the beam of nucleons in mixed state. In such a case beam is described by density matrix:

$$\hat{\chi} = \frac{I}{2}\Big(1 + \vec{P}\hat{\vec{\sigma}}\Big), \tag{16}$$

where $I$, $\vec{P}$ - intensity of beam and vector of beam polarization respectively. Kinematic equation for density matrix has the form:

$$\hat{\chi}(z) = \exp\left(i\hat{N}kz\right)\hat{\chi}(0)\exp\left(-i\hat{N}^{+}kz\right) \tag{17}$$

Using the relation directly following from (9):

$$\exp\left(i\vec{G}\hat{\vec{\sigma}}kz\right) = \cos\left(\frac{n_1 - n_2}{2}kz\right) + i(\vec{g}\hat{\vec{\sigma}})\sin\left(\frac{n_1 - n_2}{2}kz\right), \tag{18}$$

and well known relation for Pauli matricies:

$$\hat{\sigma_i}\hat{\sigma_j} = \delta_{ij} + i\epsilon_{ijk}\hat{\sigma_k} \tag{19}$$

one obtain the following expression for intensity $I(z) = Tr(\hat{\chi}(z))$ of nucleon beam, propagating through polarized medium:

$$I(z) = I_1(z) + I_2(z), \tag{20}$$

where

$$I_1(z) = \frac{I_0}{2}\exp\left(\sigma_0 n_m z\right)\left(\cosh\left(\sigma_s\rho z\right)\Big(1 + \frac{|\vec{q}|^2 + |\vec{l}|^2}{4} - (\vec{m}\vec{P}_0)\Big) - \sinh\left(\sigma_s\rho z\right)(\vec{q}\vec{P}_0)\right),$$

$$I_2(z) = \frac{I_0}{2}\exp\left(\sigma_0 n_m z\right)\left(\cos\left(\eta kz\right)\Big(1 - \frac{|\vec{q}|^2 + |\vec{l}|^2}{4} + (\vec{m}\vec{P}_0)\Big) - \sin\left(\eta kz\right)(\vec{q}\vec{P}_0)\right) \tag{21}$$

are noninterference and interference terms respectively. $I_0$ and $\vec{P}_0$ are initial intensity and polarization vector of nucleon beam, $n_m$ - molecular density of target substance. Values $\sigma_0$ and $\sigma_s$ have the sense of absorbtion cross section and spin-dependent part of total cross section of nucleons (antiprotons) scattering on polarized nuclei respectively:

$$\begin{aligned}\sigma_0 &= \frac{\Im(n_1 + n_2)k}{n} = \frac{1}{2}(\sigma_1 + \sigma_2),\\ \sigma_s &= \frac{\Im(n_1 - n_2)k}{\rho} = \frac{1}{2}(\sigma_1 - \sigma_2).\end{aligned} \tag{22}$$

Value $\eta$ and vectors $\vec{q}$, $\vec{l}$, $\vec{m}$ can be expressed in terms of refractive indicies and vector $\vec{g}$:

$$\eta = \Re(n_1 - n_2),$$
$$\vec{q} = \vec{g} + \vec{g}^*, \vec{l} = i(\vec{g} - \vec{g}^*), \vec{m} = i[\vec{g}, \vec{g}^*]. \tag{23}$$

Note that vectors $\vec{q}$, $\vec{l}$, $\vec{m}$ are orthogonal to each other. In the case when interference arises, real part of forward coherent $pp$, $np$ or $\bar{p}p$ scattering amplitude affects the evolution of beam intensity. It gives us tool for extraction of information about real part of $\hat{f}(0)$.

# 3 On possibility to extract information about real part of forward coherent $pp$, $np$ and $\bar{p}p$ scattering amplitude

Let us introduce parameter

$$A_s = \frac{i(\vec{P}_0) - i(-\vec{P}_0)}{i(\vec{P}_0) + i(-\vec{P}_0)}, \tag{24}$$

where $i = I/I_0$ - normalized intensity. This parameter characterizes assymetry of $pp$, $pn$ and $\bar{p}p$ scattering for opposite orientations of spin of scattered particles. The value $2\pi\rho z f(0)/k$ ($f(0)$ is expected to be sufficiently less than 1 ($(\sim 10^{-2} \div 10^{-1}) \cdot z[m]$), therefore we can neglect terms of order greater than 2 in expansion of $I(z)$ on this parameter, and obtain the following approximated expression for $A_s$ :

$$A_s = -2\Big(kz(\vec{P}_0\vec{G}_2) + k^2z^2([\vec{G}_1\vec{G}_2]\vec{P}_0)\Big). \tag{25}$$

In the case when polarization vector of primary beam is orthogonal to vector $\vec{n}$ and vector $\vec{P}_t$ first term in (25) disappeares, and parameter $A_s$ is expressed in the following way :

$$A_s = -\left(\frac{2\pi\rho l}{k}\right)^2 P_0 P_t \Delta \sin 2\theta, \tag{26}$$

where $\Delta$ is defined in accordance with (10), $\theta$ - angle, constituted by vectors $\vec{P}_t$ and $\vec{n}$, $l$ - target length, $P_0$ and $P_t$ - polarizations of target and primary beam respectively. It can be seen from (26) that absolute value of $A_s$ reaches maximum at $\theta = \pi/4$. Measuring parameter $A_s$ one can found parameter $\Delta$ and therefore extract information about real part of $pp$, $np$ and $\bar{p}p$ forward coherent scattering amplitude.

Precise measurement of parameter $\Delta$ requires long target with high density of polarized nuclei. Moreover target polarization should be measuread with good accuracy so that to decrease possible systematic error of measurement. Solid state targets fabricated at CERN and used in SMC experiment [8], [9] seem to suit these requirments. They all consist of two cell sections (60-65 cm) polarized in opposite directions. These two sections can be unified in order to increase effective length of polarized target. Thus total length of 120-130 cm can be achieved. Our goal is to estimate possible statistical and systematic errors of parameter $\Delta$ measured in proposed experiment with pronounced targets for $pp$ $pn$ and $\bar{p}p$ scattering Let us roughly estimate the value of parameter $A_s$ which can be observed in real experiment. Of course, we can't forecast value of parameter $\Delta$. It should be determined experimentally. But we can suggest that $\Delta \sim \gamma^2 f_B^2$ ($f_B$ - amplitude of $NN$ scattering in Born approximation, $f_B \sim 10^{-13} \div 10^{-12}$ cm, $\gamma$ - Lorentz-factor). Density of polarized nuclei in target can be found from the relation :

$$\rho = \frac{\rho_g N_a P D}{M}, \tag{27}$$

where $\rho_g$ - mass density of target substance, $N_a$ - Avogadro number, $P$ - packing factor (targets under consideration have granular structure), $D$ - dilution of polarized nuclei, $M$ - mass of one mole of target substance. Using data from table 1 we obtain the following rough estimation for parameter $A_s$:

$$A_s \sim (10^{-1} \div 10^{-3}) \cdot \frac{\gamma^2 l^2 [m^2]}{p^2 [GeV^2/c^2]}, \tag{28}$$

where $p$ - momentum of incident beam. Necessary statistics $S$ (number of protons, neutrons or antiprotons entered the target) which provides the relative statistical accuracy $\epsilon(A_s)$ of measured value $A_s$ can be found under suggestion that number of particles passed through the target has Poisson distribution. Then for $S$ we obtain:

$$S = 2(A_s \epsilon(A_s))^{-2} \exp(\sigma(p) n_m l), \tag{29}$$

where $\sigma(p)$ - absorbtion cross section of incident particles with momentum $p$ in target substance. The latter can be roughly estimated as follows :

$$\sigma_a(p) = N_p \sigma_{ap}(p) + N_n \sigma_{an}(p), \tag{30}$$

where $a$ - type of incident particles ($a = p, n, \bar{p}$), $N_p$ and $N_n$ - number of protons and neutrons in the molecule of target substance respectively, $\sigma_{ap}$ and $\sigma_{an}$ - total cross section of incident particle on proton and neutron respectively.

| Material (chemical formula) | $NH_3$ (solid) | $C_4H_9OH$ (solid) |
|---|---|---|
| Density, g/cm$^3$ | 0.853 | 0.985 |
| Dilution | 3/17 | 10/74 |
| Packing factor | 0.58 | 0.63 |
| Target length, cm | 65(130) | 60(120) |
| Target polarization | 90%±2.5% | 84%±2.5% |

Table 1: Characteristics of targets used in SMC experiment (CERN). [8],[9]

Let us briefly describe the proposed experiment. Schematic layout of experimental setup is presented in figure 1. Polarimeter placed in front of target provides us with information about initial polarization of beam. Monitors are used for measuring flux of nucleons or antiprotons in front of and behind polarized target. Measurements shoul be done for the following cases of scattering geometry :

1) Vector of primary polarization of beam is orthogonal to plane constituted by vectors $\vec{n}$ and $\vec{P}_t$. Angle between $\vec{n}$ and $\vec{P}_t$ is $45^o$.

2) Geometry is the same except for the circumstance that vector of beam polarization has the opposite orientation with respect to previous case.

Measuring the flux of nucleons (antiprotons) in front of and behind target in these two cases one can found parameter $A_s$ and calculate $\Delta$.

Figure 2 summarizes our calculation of $A_s$ to $\Delta$ ratio as function of momentum of incident particles (two targets - $NH_3$ and $C_4H_9OH$ - are considered). Parameter $S(A_s\epsilon(A_s))^2$ (see eq. (29)) dependence on beam momentum is presented in figure 3. Data on $pp$, $np$ and $\bar{p}p$ total cross sections are taken from Review of Particle Properties [10]. Calculations were made for beam momentum ranging from 1 GeV/c up to 10 GeV/c for this range of energies is the matter of interest in the light of dibaryon resonance problem.

*Inaccuracies in measuring of beam and target polarization are expected to* be main sources of systematic error in determination of parameter $A_s$. Table 1 indicates lower limit of systematic error connected with inaccuracy in measuring of target polarization.

# 4 Conclusions

Let us briefly summarize the obtained results:

1) It is shown that real part of spin-dependent term of forward coherent

$pp$, $np$ and $\bar{p}p$ scattering amplitude affects the evolution of beam intensity in polarized target. It allows us to extract information about real part of forward coherent scattering amplitude.

2) The experiment on measurement of parameter $\Delta = \Re(B)\Im(C) - \Im(B)\Re(C)$ is proposed. Necessary statistics providing desirable accuracy is estimated.

3) Targets used in SMC experiments are shown to suit the proposed experiment.

# References


[1] V.G.Baryshevsky, *Phys. Lett. A171(1992)431*

[2] V.G. Baryshevsky, A.G.Shekhtman, *Nucl. At. Phys. (In Russian) 57(1994) 8 1370*

[3] V.G.Baryshevsky, D.V.Baryshevsky, *J. Phys. B27(1994)3277*

[4] A.Yokosawa, *Phys. Rep., 64 No. 2 (1980) 47-86*

[5] W.Grein, P.Kroll *Nucl. Phys. B137 (1978) 173-188*

[6] W.Grein, P.Kroll, *Nucl. Phys. A377 (1982) 505-517*

[7] V.G.Baryshevsky, *Nuclear Optics of Polarized Media, Moscow, Energoatomizdat, 1995 (In Russian)*

[8] SMC collaboration, *Nucl. Instr. Meth. A356(1995), 79-82*

[9] SMC collaboration, *CERN-PPE-97-066, Jun 1997*

[10] Review of Particle Properties, *Phys. Rev. D50 No3 (1994)*

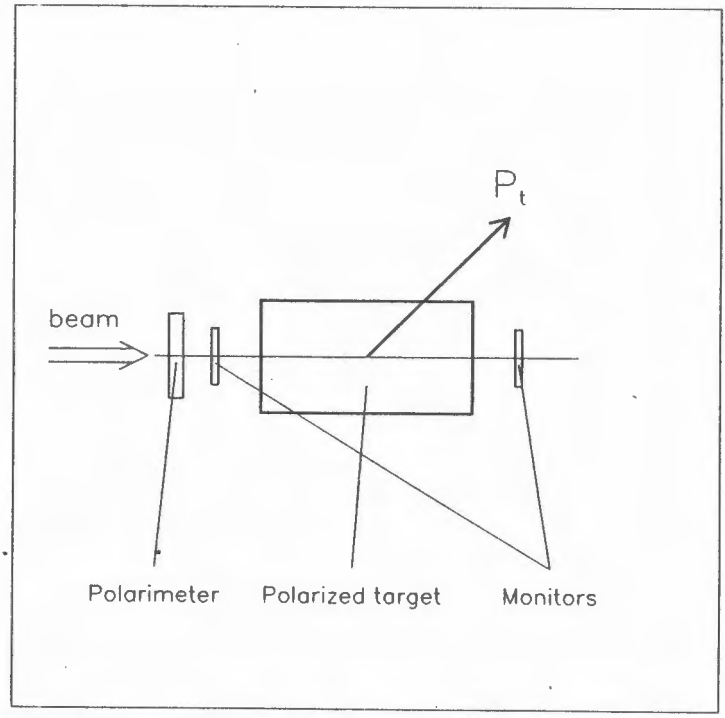


Figure 1: Schematic layout of the proposed experiment.

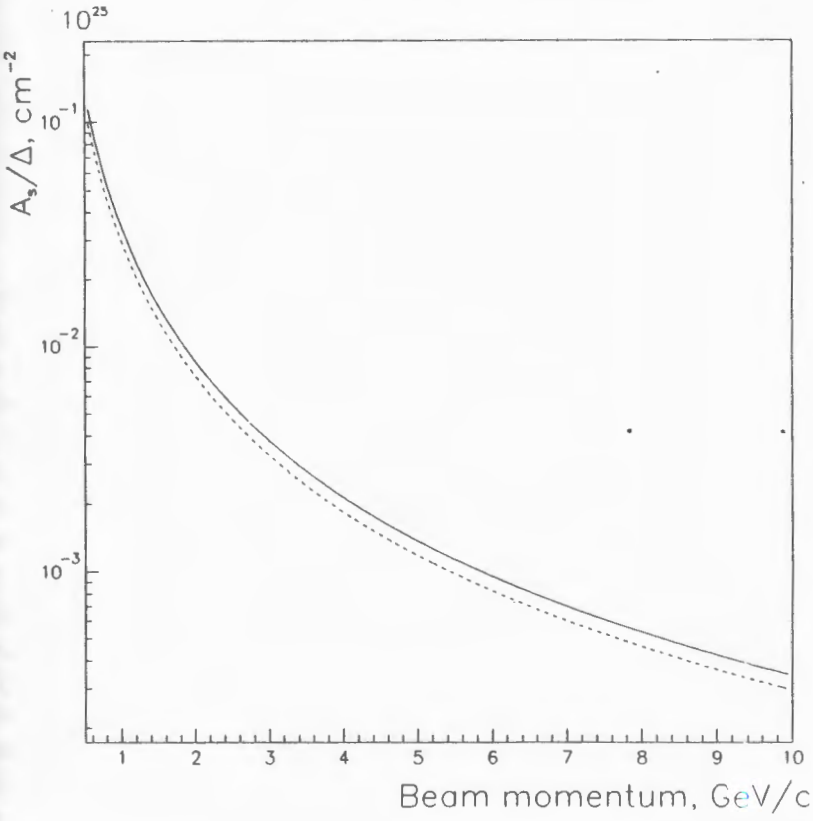


Figure 2: Parameter $A_s$ in units of $\Delta$ vs beam momentum. Dashed line - butanol target; solid line - ammonia target. Target lenght - 1m.

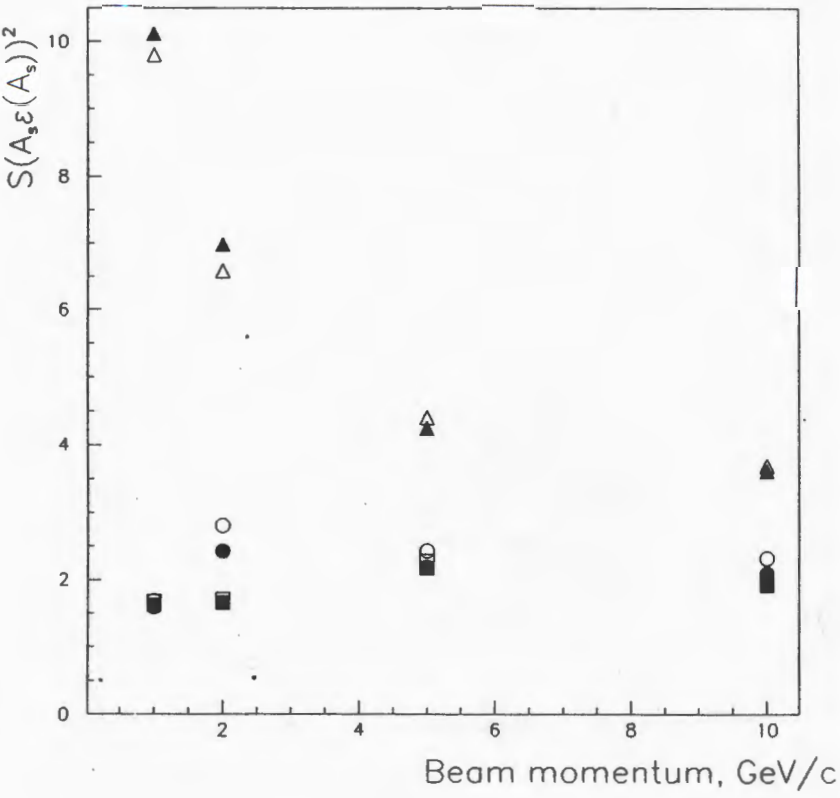


Figure 3: Product $S(A_s\epsilon(A_s))^2$ (see eq. (29)) vs beam momentum. Target length - 1m. Circles stand for proton beam; squares - neutron beam; triangles - antiproton beam. Filled marks - ammonia target; Open marks - butanol target.

# Manifestation of nonnucleon degrees of freedom in nuclei in reaction of the cumulative particle production.

**A.Litvinenko**
Laboratory of High Energy
of Joint Institute for Nuclear Research Dubna,141980,Moscow region,Russia
E-mail: litvin@moonhe.jinr.ru

## Introduction

It is well known that the many properties of nuclei are described in the framework of the nucleon models. These models are used at low energy (for description static properties of nuclei and nuclear reaction) as well as at high energy (different variants of cascade models). However the limited region of validity of nucleon models is evident even from the fact that a nucleon is a composite particle. From this fact it is natural to expect the manifestation of non–nucleon degree of freedom for configuration with short internucleon distances. The situation looks the same, as in molecular or solid state when the overlapping electron levels are reorganized. But at present time it is impossible to say what has happened when the distance between nucleon became smaller, than nucleon size. It is natural to expect the deviation from nucleon models predictions for reactions where high internal momentum ($k_{int.} > 0.2GeV/c$) is essential (short internucleon distances correspond to the high internal momentum). In deep inelastic scattering of leptons this internal momentum corresponds to the region of the Bjorken variable $x_b \geq 1$, where the cross sections are too small [1]. In this article the possibility to use the reactions of cumulative particles production for studying non–nucleon degree of freedom is discussed.

## Cumulative particle production

### Definition

The particle (c) produced in reaction

$$A_I + A_{II} = c + X \tag{1}$$

is called cumulative if the following two conditions is implemented [2]:

1. the particle (c) is produced in kinematic region forbidden for free nucleon collision;

2. the particle (c) is produced in fragmentation region one of the colliding particle (for example I)

$$|Y_I - Y_c| < |Y_I - Y_{II}| \tag{2}$$

Where $Y_I$ is rapidity.

For description of cumulative particle spectrum the scale cumulative variable (cumulative number) $X_c$ is often used [2],[3]. In the rest frame of particle $A_I$ it means the minimum necessary from kinematic target mass in nucleon mass units and for pions is equal to:

$$X_c = \frac{(P_{II}P_c) - m_\pi^2/2}{(P_I P_{II}) - (P_I P_c) - m_N^2} \quad , \tag{3}$$

where $P_I, P_{II}$, $P_c$ are four-momentum of colliding and detected particles respectively, $m_\pi$ and $m_N$ are masses of pion and nucleon. In the first approximation the differential cross-section for cumulative particle is proportional to the exponent of cumulative number:

$$E\frac{d\sigma}{d\mathbf{p}} \sim \exp(-X_c/ < X_c >) \quad . \tag{4}$$

The slope parameter $< X_c >$ is the same for all kinds of cumulative particles and weakly depends on sort of particle $II$ and collision energy starting from 3 - 4 GeV/nucleon [4, 5, 6] (see Fig.1).

## Models

A lot of models have been proposed for description of cumulative particle production [7]. In the simplest models the cumulative particles appear as a result of rescattering of primary or secondary particle on target nucleon. However, it was shown that this mechanism can't describe the cross section for cumulative particle production even for small cumulative number ($X_c \geq 1.2$) [9]. The other models can be divided in two classes [7]. In the model with so called hot fluctон a cumulative particle emitted by object arising from during collision (very hot fireball). It is very difficult in this approach to describe the cumulative particle production in collisions

of lepton with nuclei or cumulative particle production in collisions of proton with deuteron. At present moment the more persuasive is the models with cold fluctons. In this model cumulative particle produced by high momentum tail in nuclei wave function. On the other hand this model can be divided on models based on nucleon component and models based on non-nucleon component. Two kinds of these models are discussed below.

### Experiments with non-polarized particles

Because the hadron probe is not so simple in interpretation then leptonic it is natural to compare the data obtained using these two probes. This comparison is presented in Fig.2 where the square of deuteron wave function obtained from electron scattering on deuteron and deuteron break-up reaction $D + p = p(0^o) + X$ is presented. One can see that agreement between this set of data is rather well. In impulse approximation the cross section for the reaction (1) is given by integral of square of wave function with elementary cross-section $\sigma_{el}(c)$) :

$$E\frac{d\sigma}{d\mathbf{p}} = \int \sigma_{el}(c)|\Psi(k)|^2 G(k) \qquad (5)$$

Were $\Psi(k)$ is one particle wave function, k is the constituent (nucleon, quarks) momentum, and G(k) is some smooth function depending on concrete variant model. For nucleon models the $\sigma_{el}(c)$ is equal to cross section of particle $c$ production in NN collision. In Fig.3 the experimental data on the ratio of particles yield for cumulative ($X > 1$) and noncumulative ($X < 1$) is presented. These data clear indicate that mechanism of particle production is different for cumulative and noncumulative region. It is very difficulty in the framework of nucleon models to explain this data. It is necessary to assume that cross section ratio for different particle production changes in order of magnitude for cumulative and noncumulative region. These data clearly show that mechanism of particle production is different for cumulative and noncumulative region.

### Experiments with polarized deuteron

It is obvious, that the study of the spin degree of freedom in cumulative particle production can give more detailed information about nuclear matter at short distances and about reaction mechanisms. First experiments of such kind were the measurements of cumulative proton polarization for

fragmentation of unpolarized nuclei [10]. The most precise experiments have shown that this value is small (5-10 %) [11] and can be explained by produced proton rescattering [11, 12]. However, for the nuclear structure investigation experiments on nuclear fragmentation in a definite spin state i.e. experiments on studying spin effects on polarized nuclei fragmentation into cumulative hadrons seem more adequate. Experiments with polarized deuterons allow us to separate contribution from the S and D components in the deuteron wave function. In particular, it is clearly seen from the expressions (valid for the nucleon model via an impulse approximation) for the tensor analyzing power ($T_{20}$) and polarization transfer coefficient ($\kappa$) for tensor and vector polarized deuteron fragmentation into proton (at an angle of 0°):

$$T_{20} = \frac{2u(k)w(k) - w(k)^2/\sqrt{2}}{u^2(k) + w^2(k)} \tag{6}$$

$$\kappa = \frac{u^2(k) - w^2(k) - u(k)w(k)/\sqrt{2}}{u^2(k) + w^2(k)} \tag{7}$$

In these equations, u and w denotes S and D waves in the deuteron and $k$ is its internal momentum

The values of $T_{20}$ and $\kappa$ for protons as a secondary particle have been studied at Saclay and at Dubna. The data obtained is shown in Fig.4 and Fig.5. A simple correlation between $T_{20}$ and $\kappa$ following from (2) and (3) is not confirmed by the these data [13]. The final state interaction was taken into account to describe these data [14], but a full agreement with the experimental data was not achieved. In the region $k \geq 0.8$ $GeV/c$ the value of $T_{20}$ is more close to the asymptotic predicted by the model [15] taking into account non-nucleon degree of freedom in deuteron wave function. The more evident deviation from nucleon model prediction follows from the experimental value of $T_{20}$ for tensor polarized deuteron fragmentation into pion (at angle of 0°) Fig.6 [16].

## Conclusions

The revue of some features of the experimental data of cumulative particle production has been performed. It was shown that some of these features can not be explained in the framework of nucleon model.

For obtaining more detail information about manifestation of non-nucleon degree of freedom in cumulative particle production additional experiments are necessary. For example experiment with extraction hadron

formation length from $A_t$–dependence of deuteron fragmentation on different targets as it was done for pions in [17] and so on.

This work was performed with the support of the Russian Found for Fundamental Research, Grant 96-02-17207.

# References

[1] BCDMS Collaboration - *Preprint JINR* **E1-93-133** (1993) Dubna.

[2] Baldin A.M., it Proc. of the Int. Conf. on Extreme States in Nuclear Systems. Dresden: **V.2**, P.35, 1980.

[3] A.G.Litvinenko, A.I.Malakhov, P.I.Zarubin. *JINR Rapid Communications*, **No 1(58)-93**, p.27, Dubna, 1993.

[4] V.S.Stavinsky - *Part. and Nucl.* **10(6)** (1979) p.949 (in Russian).

[5] N.A.Nikiforov, Y.D.Bayukov, V.I.Efremenko et al. - *Phys. Rev.***C22, No.2** (1980) p.700.
S.V.Boyarinov et al.- *Yad. Fiz.***50(6)** (1989) p.1605 (in Russian).
S.V.Boyarinov et al.- *Yad. Fiz.***54(1)** (1991) p.119 (in Russian).

[6] K.V.Alanakyan et al.- *Yad. Fiz.***25** (1977) p.545 (in Russian).

[7] Efremov A.V. *Sov. J. Part. and Nucl.* **V.13(5)**, p.613, (1982).

[8] V.S.Stavinsky, In.Proceedings of the IX Int.Sem. on High Enrgy Physics Problems, **V.1**, p.190, Dubna, 1988

[9] V.K.Lukyanov, A.I.Titov, Part. and Nucl. **10(4)**, 815 (1979).

[10] S.L.Belostozky et al. - *Phys. Lett* **B124** (1983) p.469.

[11] O.P.Gavrishchuck et al. - *Phys. Lett* **B255** (1991) p.327. I.M.Belyaev et al. - *JINR Rapid Comm.***No.2[28]-88** (1988) p.1427 Dubna.

[12] O.P.Gavrishchuck, L.S.Zolin,I.G.Kosarev - *Comm. of JINR* **P1-91-528** (1991) Dubna.

[13] L.S.Azhgirey et al. - *Preprint JINR* **E1-94-155** (1994) Dubna.

[14] G.I.Lykasov - *Part. and Nucl.* **24** (1993) p.475.

[15] A.P.Kobushkin - *J.Phys.G: Nucl. Part. Phys.* **19** (1993) p.1993.

[16] T.Iwata et al., In.Proceedings of the 12th Int.Sem. on High Enrgy Spin Physics, p.371, Amsterdam, 1996

[17] Yu.S.Anisimov et al., Elementary Particles and Fields, **60**, p.957, 1977.

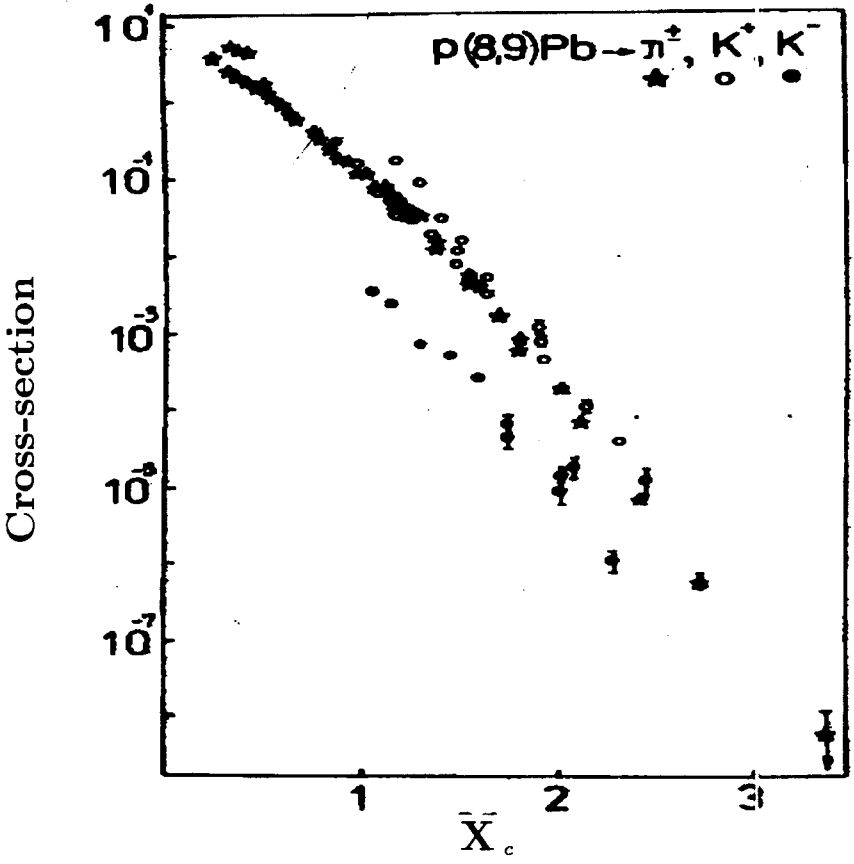


Figure 1:

The cross section for cumulative particles production as a function of cumulative number [4].

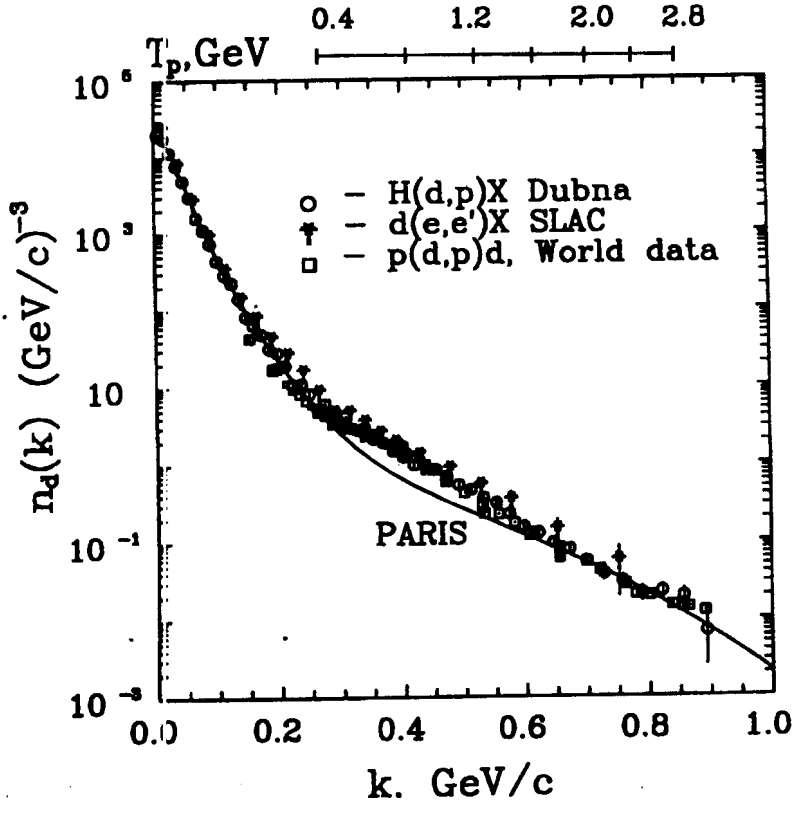


Figure 2:

The square of deuteron wave function extracted from different reactions. (See A.P.Kobuschkin Proceedings of Int. Symp. "DEUTERON-93", Dubna, 1994)

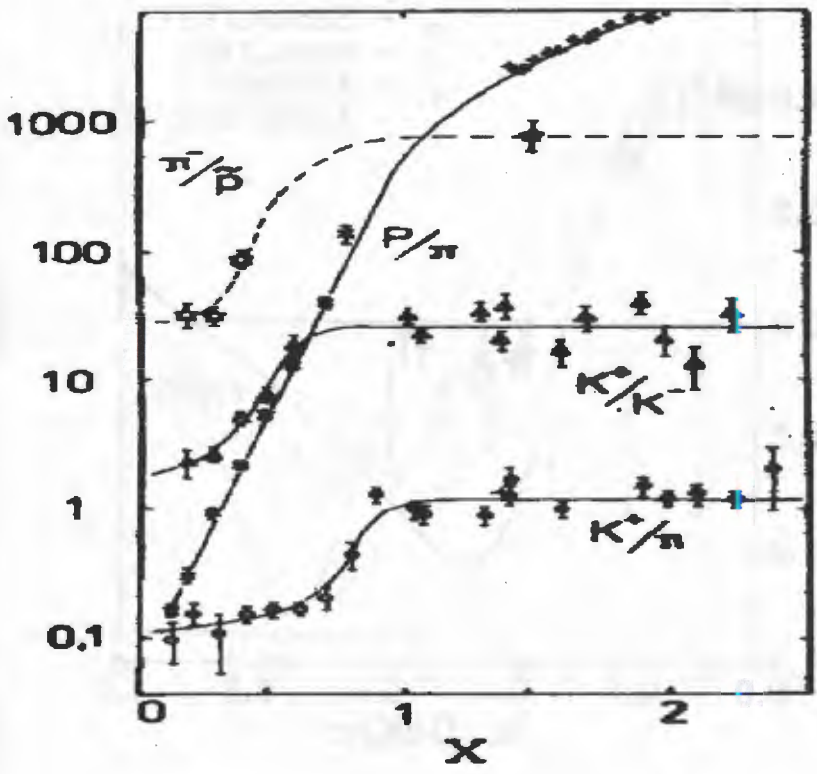


Figure 3:

The ratio of particle yeild in cumulative ($X > 1$) and non-cumulative ($X < 1$) region [4].

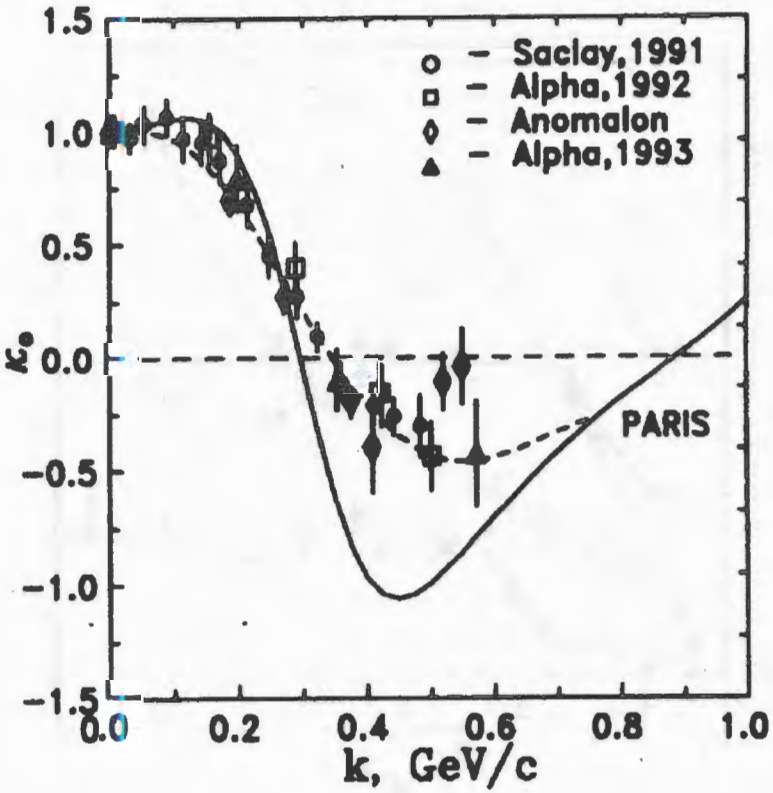


Figure 4:

Deuteron-to-proton polarization transfer $\kappa_0$ (See L.S.Azhgirei at al. Proceedings of Int. Symp. "DEUTERON-95",p.337, Dubna, 1996)

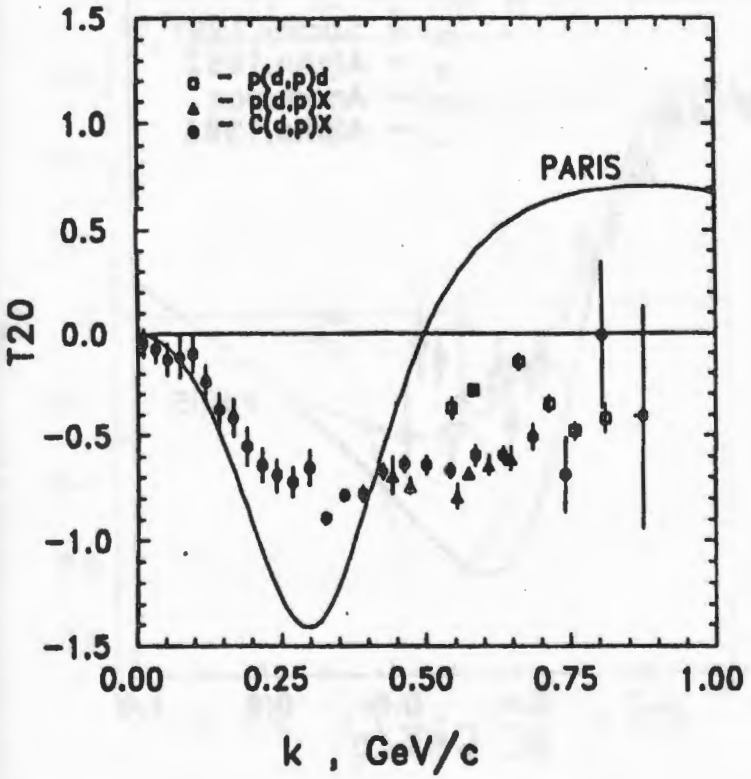


Figure 4:

The tensor analyzing power for deuteron break-up reaction [13].

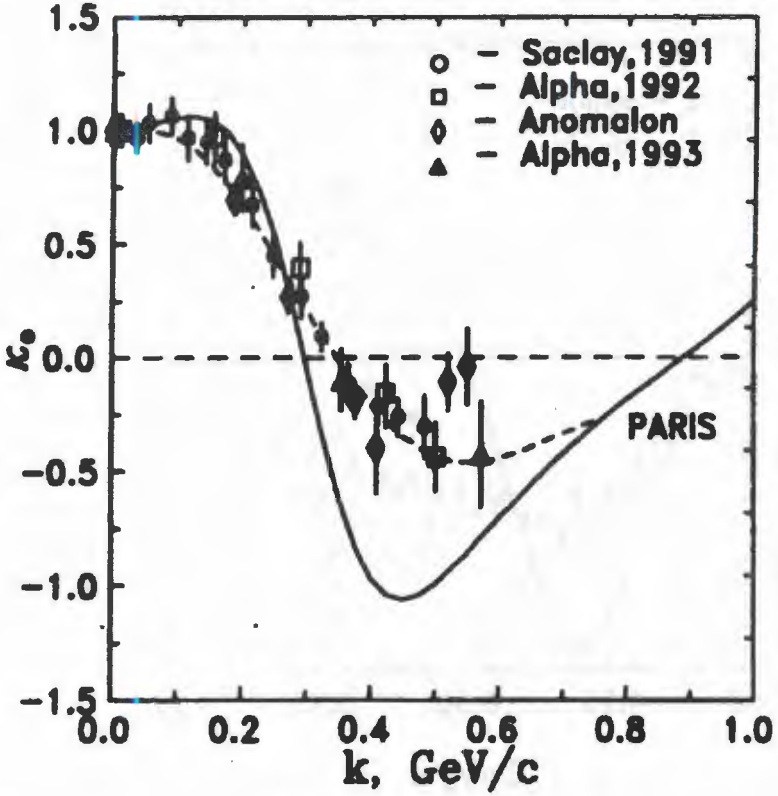


Figure 5:

Deuteron-to-proton polarization transfer $\kappa_0$ (See L.S.Azhgirei at al. Proceedings of Int. Symp. "DEUTERON-95",p.337, Dubna, 1996)

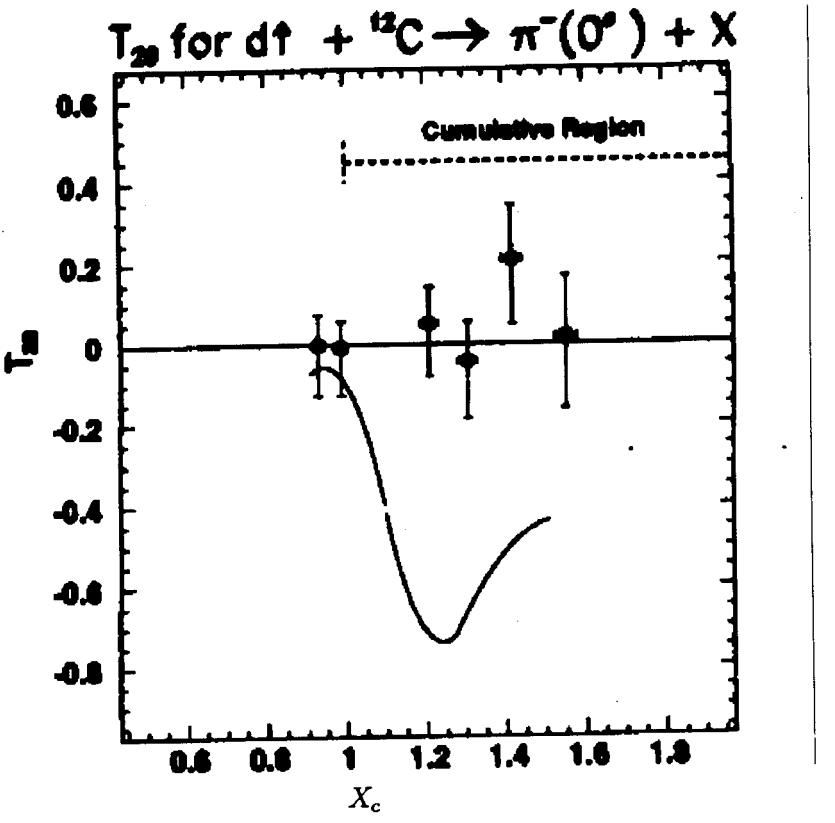


Figure 6:

The tensor analyzing power for deuteron fragmentation into pions [16].

# THE STUDY OF K-MESON DECAYS WITH THE HYPERON SPECTROMETER

NADEJDA RUSSAKOVICH
Joint Institute for Nuclear Reserch, Dubna, Russia
SERPUKHOV-167 COLLABORATION

## 1 Introduction

We present here some interesting results obtained with the HYPERON spectrometer in the framework of K-decay investigation program in close collaboration with our belorussian colleagues from Minsk and Gomel.

Though main interests of present particle physics are concentrated now on high energies recently reached with new colliders and on heavy flavours, the Kaon physics still maintains its interest unaltered and can provide very imported information on fundamental problem. The origin of the CP-violation is not yet well identified. K-decays offer a unique way to study sources of the CP- violation, a point which is of crucial importance. Also $\Delta I = 1/2$ rule is still difficult to account for from theoretical point of view. Moreover effects beyond the Standart Model could manifest itselves in low energy processes such as K-decays.

The theoretical description of K-decays necessarily involves non- perturbative long-distance QCD. Clearly these low energy QCD effects must be taken into account to make realistic predictions. The basic idea is represented by an assumed $SU(3)_L \times SU(3)_R$ chiral symmetry of strong interactions, valid in the zero masses of lightest quarks ($u$, $d$ and $s$) limit. A spontaneous symmetry breaking is supposed to occur in this limit, giving rise to an octet of massless Goldstone bosons which are associated to the usual pseudoscalar octet of the lowest lying mesons. It is possible to obtain from the basic QCD Lagrangian the effective Lagrangian of four-quark

interaction. Then by means of bozonisation one can derive the effective non- linear chiral Lagrangians in terms of pseudoscalar meson fields, the photon and the lepton fields with the desired symmetry properties. Great progress has been achieved in the framework of chiral perturbation theory which allows a systematic expansion of the hadronic matrix elements in power of meson momenta. Such an expansion is just suitable to K-decays where the energy release is small and the decay products are very slow in the kaon rest frame. The general form of the $\Delta S = 1$ non-leptonic weak Hamiltonian accounting for the orders $O(p^2)$ and $O(p^4)$ was worked out [1] and attempts to account for $O(p^6)$ processes, and to incorporate vector meson resonances and the notion of the vector meson dominance in the chiral Lagrangian formalism appeared recently [2, 3, 4].

One can predict by means of the effective Lagrangian a multitude of transition amplutudes involving pions and kaons in terms of a reduced number of constants which are established by fit to experimental data. For this reason such an approach is extensively applied to semileptonic and non-leptonic decays. Actually, certain decays turn to be quite sensitive to a hadronization model used to evaluate hadronic matrix elements and therefore can be considered as stringent tests of the chiral Lagrangian approach. In this aspect new accurate experimental studies of K-decays with improved systematics and high statistics should be performed at present and future facilities.

## 2 Experimental procedure

The HYPERON spectrometer was designed for the study of hypercharge exchange reactions and after the K-decay program had been accepted was substantially modified [5]. The present layout of the spectrometer is shown in figure 1.

We used the unseparated secondary beam of 10 GeV/c positive particles from the U-70 accelerator. The total beam intensity was about $10^6$ particles per spill. The contamination of K-mesons in the beam was about 5% and K-mesons were picked out by the threshold gas Cherenkov counters Č1–Č3.

The momentum spread in the beam was about 1.5% but we could mesure it more precisely ($\Delta p/p = 0.5\%$) with the beam spectrometer based on the analysing magnet MAGNET1 with a very uniform field ($\Delta H/H \leq 0.1\%$) and a set of 2mm multiwire proportional chambers PC1–PC4. The

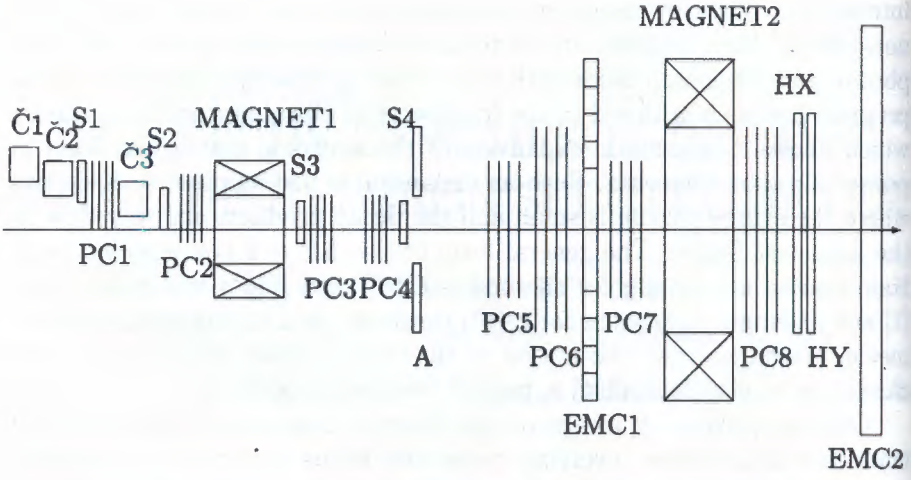


Figure 1: Layout of the HYPERON-2 spectrometer

scintillation counters S1–S4 were used for counting kaons entering the two meter decay region between the chambers PC4 and PC5 The scintillation counter $A$ with a hole in the center was in anticoincidence to suppress K-decays in the beam spectrometer area at the trigger level.

Secondary charged particles were registered in the secondary spectrometer by the magnet MAGNET2 and a set of 2-mm proportional chambers PC5–PC8. The reconstructed momentum range was $1.5 \div 10 GeV/c$ and the relative momentum resolution over this region was $1 \div 3\%$.

$\gamma$-quanta from $K^+$- and $\pi^0$-decays were registered by two electromagnetic calorimeters EMC1 and EMC2. Both detectors are lead glass cherenkov hodoscope calorimeters. The cell sizes are $100 \times 100 mm^2$ in EMC1 and $85 \times 85 mm^2$ in EMC2. The central zone of EMC2 consists of smaller cells $42.5 \times 42.5 mm^2$. To let forward photons and charged particles pass through the spectrometer, EMC1 has a $50 \times 50 cm^2$ hole in the center. The energy resolutions were $\simeq 0.1/\sqrt{E}$ for EMC1 (see [6] for details) and $\simeq 0.08/\sqrt{E}$ for EMC2. $\gamma$-quanta impact positions were reconstructed from the shower energy distribution in the calorimeter cells [7, 8]. The mean reconstruction accuracies are $\Delta x \simeq \Delta y \simeq 9mm$ in EMC1 [6] and $\Delta x \simeq \Delta y \simeq 7mm$ and $\Delta x \simeq \Delta y \simeq 4.5mm$ in EMC2 for cell sizes $85mm$ and $42.5mm$ respectively [8]. A part of the data were taken with two scintillation hodoscopes HX and HY to increase the track reconstruction efficiency.

# 3 Mesurement of the $K^+ \to e^+\pi^0\nu$ decay formfactors

The first result we obtained is a determination of the formfactors in the $K^+ \to e^+\pi^0\nu$ semileptonic decay [9].

## 3.1 Introduction

The most general form of the matrix element of $K_{l3}$ decays is given by [10, 11]:

$$\begin{aligned} M \;\propto\; & \bar{\psi_\nu}(1-\gamma_5)[m_K f_S \\ & +\frac{i}{2}(f_+ p_\alpha + f_- q_\alpha)\gamma^\alpha \\ & +i\frac{f_T}{m_K} p_K^\alpha p_\pi^\beta \sigma_{\alpha\beta}]\psi_l \end{aligned} \tag{1}$$

where $\psi_\nu$, $\psi_l$ are leptonic spinors, $m_K$ - K-meson mass, $p_K$ and $p_\pi$ are $K$ and $\pi$ four momenta, $p = p_K + p_\pi$, $q = p_K - p_\pi$ is momentum transfer to dilepton system, $f_+$, $f_-$ are vector formfactors, $f_S$, $f_T$ - scalar and tensor formfactors. If only the V-A interaction exists the scalar and tensor formfactors should be zero. The vector formfactors depend on the $q^2$ variable only and are usually represented by the linear parametrisation

$$f_\pm(q^2) = f_\pm(0)\left(1 + \lambda_\pm \frac{q^2}{m_{\pi^0}^2}\right). \tag{2}$$

In the case of the $K_{e3}$ decay the $f_-$ - term is negligible due to small lepton mass. So this decay yields information on the slope parameter $\lambda_+$, the scalar and tensor couplings $f_S$, $f_T$, and their relative phase $\Phi_{ST}$. The $K_{e3}$ decays are relevant in testing the CKM matrix element $V_{us}$ which one can calculate knowing the decay probability and the vector formfactor.

Also the interest in the V-A current structure testing increased recently. The experimentally obtained [12] branching ratio of the $\pi^- \to \pi^0 e^- \nu$ decay

$$B^{exp} = (1.61 \pm 0.23) \cdot 10^{-7}$$

does not agree with the Standart Model prediction

$$B^{th} = (2.41 \pm 0.07) \cdot 10^{-7}.$$

This fact can be explained in particular by possible existence of tensor interaction [13]. Inserting of tensor fields in a standart decay amplitude induces nonzero scalar and tensor formfactors.

## 3.2 Experiment and data procesing

This experiment was performed before the HYPERON reconstruction with the part of the spectrometer up to the first electromagnetic calorimeter EMC1. There was also the decay volume filled with Helium between the chambers PC4 and PC5 (see figure 1).

The main trigger requirement was registration of at least three showers in the EMC1. It was done to suppress a main background process – the $K_{\pi 2}$ decay. To determine the shower number at the trigger level all EMC1 cells were joint into 5 groups. Summed energies in at least three groups of cells must be above a definite threshold (adjustable). In this experiment it was about $800MeV$.

Events were accepted if the following criteria were satisfied:

1. there are one beam track and one secondary track;
2. the reconstructed decay point is in the decay volume;
3. the distance between the charge particle impact point in the EMC1 and the nearest shower axis is less than 60mm;
4. there are three showers with the energies above 1GeV.
5. the event is not the $K_{\pi 2}$ decay (they were selected by the kinematical fit at the confidence level 0.99);
6. the event fits the $K_{e3}$ hypothesys at the confidence level 0.95.

After all data processing we obtained about 32000 reconstructed decays. In the figure 2 you can see the $e^+\gamma\gamma\nu$ effective mass distribution. The solid line shows the experimental spectrum, the dashed line - the spectrum simulated by the Monte-Carlo method. They are in good agreement and the mean values of the distributions coincide with the kaon mass.

To obtain the matrix element we should calculate the acceptance with the constant matrix element and analyze the ratio of the experimental distribution and the simulated one. The acceptance was calculated by the Monte-Carlo method. A sample of $1.5 \times 10^7$ decays was simulated

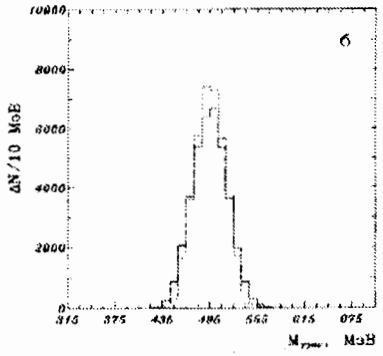


Figure 2: The distribution of the $(e^+\gamma\gamma\nu)$ effective masses for the $K_{e3}$ decay.

and reconstructed by the same analysis program as the real events. The simulation took into account the detector performance, the trigger and reconstruction criteria. The acceptance dependence on the momentum transfer $q^2$ is shown in figure 3. The dependence is smooth in all region of the $q^2$ variation.

## 3.3 Results

The resulting vector formfactor dependence on $q^2$ is shown in figure 4. It was fitted with the linear function (2) and the result for the vector formfactor slope parameter is:

$$\lambda_+ = 0.0284 \pm 0.0027 \pm 0.002$$

with $\chi^2 = 27$ for 22 degrees of freedom. This is the most precise measurement known by now and as you can see from the figure 5 it is in good agreement with all previous experiments. The systematic error was estimated from the dependence of the result on selection criteria and does not exceed 0.002.

We performed independent analysis of the Dalitz plot density distribution using only the vector term of the matrix element. The obtained

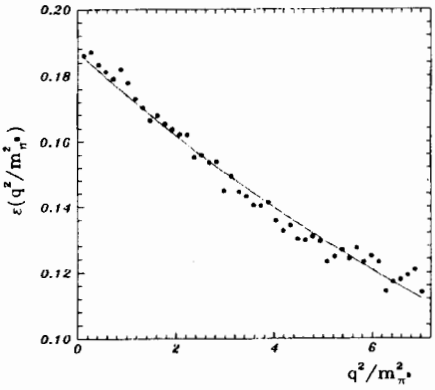


Figure 3: The acceptance dependence on the momentum transfer $q^2$.

parameter value is:

$$\lambda_+ = 0.0283 \pm 0.0029.$$

The effect of radiative corrections to the Dalitz plot increases the value up to $\lambda_+ = 0.0296$.

Using the matrix element in its general form we fitted again the Dalitz plot density distribution to obtain the scalar and tensor formfactors and their relative phase. The results of the approximation are given in table 1 (coloumn 4). The results of the experiment [11] are shown in the column 3 to compare. It was the only experiment before us where nonzero formfactor values were obtained. In the column 2 the world averages [14] are presented. The obtained values of the scalar and tensor formfactors differ significantly from zero. So our result also points to the possible existence of tensor interaction.

New determination of the CKM matrix element $|V_{us}|$ was also done in this experiment [15]. Using the obtained $\lambda_+$ value, the well known decay width and the theoretical value for $f_+(0)$ one can obtain the $|V_{us}|$ value from the relation for the decay rate:

$$\Gamma = \frac{G_F^2}{768\pi^3} m_K^5 |V_{us}|^2 |f_+(0)|^2 (0.579 + 2.140\lambda_+ + 3.166\lambda_+^2)$$

Our result is

$$|V_{us}| = 0.2195 \pm 0.0027.$$

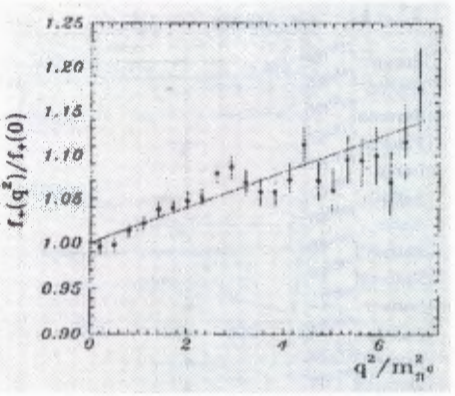


Figure 4: The dependence of the vector formfactor $f_+$ on the momentum transfer $q^2$.

This result is in very good agreement with the best-known measurement $|V_{us}| = 0.2196 \pm 0.0023$ [16] and its precision is almost the same.

# 4 Experiment with the new layout of the HYPERON spectrometer

After the HYPERON reconstruction new experimental data containing different modes of $K^+$-decays were collected. Our facilities allow us to measure all kinematic parameters of all involved particles, as charged as netral. The specific feature of our trigger, like in the $K_{e3}$ experiment, was a requirement of at least three showers in both calorimeters. The $K^+ \to \pi^+\pi^0$ decay which was not completely suppressed by the trigger gave us a very good possibility of calibrating the e/m-calorimeters with tagged $\pi^0$, using $\pi^+$-energy in the K-rest system distribution (figure 6) where one can see the sharp peak at 248MeV from the binary $K_{\pi 2}$ decay. Selecting $K_{\pi 2}$ events we required $238MeV \leq E^{\pi^+}_{CM} \leq 258MeV$ and two $\gamma$ - quanta in both calorimeters. The calibration was done by fitting two $\gamma$-quanta effective mass to the $\pi^0$-mass.

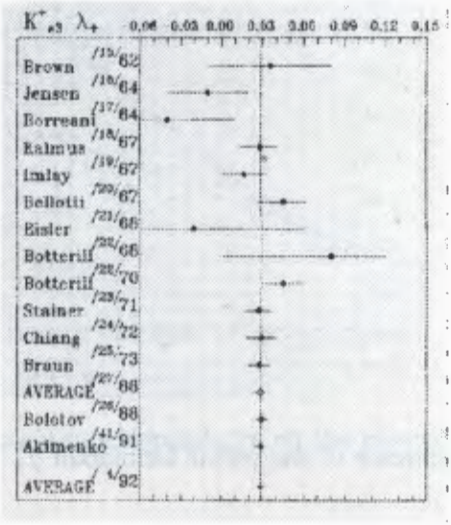


Figure 5: All results of mesurement of the slope parameter $\lambda_+$

Table 1: The values for the parameters $\lambda_+$, $|f_S/f_+(0)|$, $|f_T/f_+(0)|$ and $\Phi_{ST}$ in the $K_{e3}$ decay.

| Parameter | World average value | Experiment Steiner et.al | Our results |
|---|---|---|---|
| $\lambda_+$ | | $0.012^{+0.011}_{-0.014}$ | $0.024^{+0.003}_{-0.003}$ |
| $\left\|\frac{f_S}{f_+(0)}\right\|$ | $0.084^{+0.023}_{-0.023}$ | $0.14^{+0.03}_{-0.04}$ | $0.070^{+0.016}_{-0.016}$ |
| $\left\|\frac{f_T}{f_+(0)}\right\|$ | $0.38^{+0.11}_{-0.11}$ | $0.24^{+0.16}_{-0.14}$ | $0.53^{+0.09}_{-0.10}$ |
| $\Phi_{ST}$ | | $0.00^{+0.95}_{-0.95}$ | $0.00^{+0.52}_{-0.52}$ |

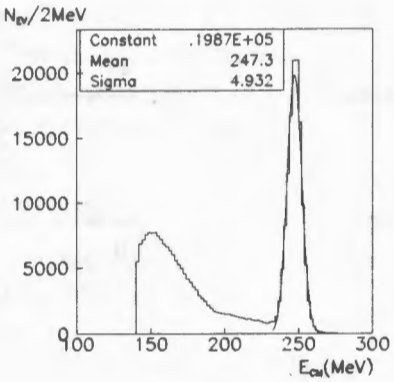


Figure 6: Charge particle energy in the K-rest frame. The peak is fitted with the Gaussian.

# 5 Study of the $K^+ \to \pi^+\pi^0\pi^0$ decay

## 5.1 Introduction

The first process we studied was the $K^+ \to \pi^+\pi^0\pi^0$ decay. The Dalitz plot slope parameters of these decays attracted new theoretical interest recently concerning the effective chiral Lagrangian approach to K-decays [17, 18, 19, 20]. The nonleptonic weak Lagrangian has the form

$$L_W^{|\Delta S|=1} = \tilde{G}_F \sum_{i=1}^{8} C_i(\mu) O_i(\mu),$$

where $\tilde{G}_F = \sqrt{2} G_F \sin\Theta_C \cos\Theta_C$, $\Theta_C$ – Cabibbo angle, $C_i(\mu)$ – Wilson coefficients, $O_i(\mu)$ – four-quark operators. The reliable evaluation of the contribution of the "penguin" diagrams (figure 7) is of primary interest here. According to modern theoretical models not only the enhancement of the $|\Delta I| = 1/2$ transitions but also the direct CP-violation in nonleptonic K-decays are conditioned by "penguin" diagram contribution, in particular by the imaginary parts $ImC_5$ and $ImC_8$.

Due to the small energy release the $K_{\pi 3}$ decay amplitudes can be ex-

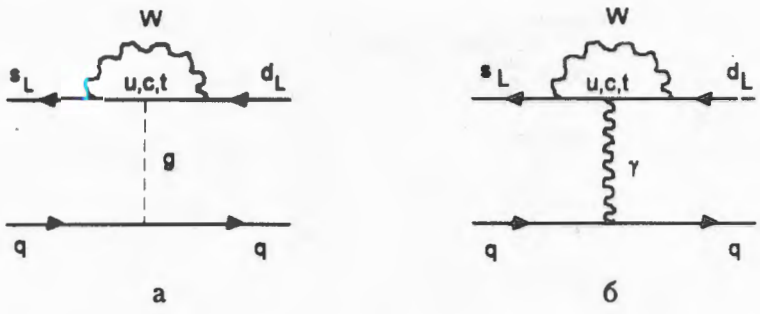


Figure 7: Gluon (a) and electromagnetic (b) "penguin" diagrams

panded in powers of the Mandelstam variables X and Y:

$$M = \sum \left[A_{IJ} + B_{IJ}X + C_{IJ}\left(X^2 + Y^2/3\right) + D_{IJ}\left(X^2 - Y^2/3\right)\right],$$

where

$$X = \frac{(s_3 - s_0)}{m_\pi^2}, \quad Y = \frac{s_2 - s_1}{m_\pi^2};$$

$s_i = (p_K - p_i)^2$, $i = 1, 2, 3$ (i=3 for odd meson); $s_0 = (s_1 + s_2 + s_3)/3$; $p_i$ – four momenta, $I$ – isospin of final state, $J$ – double isospin changing. Experimentally observed slope parameters $g$, $h$ and $k$ from the squared matrix element dependence on $X$ and $Y$

$$|M|^2 = C\left(1 + gX + hX^2 + kY^2\right) \tag{3}$$

are related to the amplitude coefficients:

$$g = 2\frac{Re(AB^*)}{|A|^2}, \quad h = \frac{|B|^2 + 2Re\left[A(C^* + D^*)\right]}{|A|^2}, \quad k = \frac{2}{3}\frac{Re\left[A(C^* - D^*)\right]}{|A|^2}$$

The coefficients in the decay amplitude cannot be calculated now using only theoretical principles. They can be obtained as a result of fitting a theoretical model to experimental data on nonleptonic K-decays (including decay probabilities and slope parameters $g$, $h$, $k$ in (3).

But one cannot make the reliable fit with the existing experimental data, because the quadratic coefficients $h$ and $k$ are measured with too low precision.

All three slope parameters $g$, $h$, $k$ have to be measured to find out how different dynamic mechanisms contribute to the decay amplitude. Moreover, the asymmetry in $g$ parameters of CP-conjugated charged kaon decays would be manifest evidence for the direct CP-violation.

## 5.2 Data processing

For data processing we used some methods that are described in [6, 7, 8, 21]

To get the most unambigous sample we chose events that satisfied the following requirements:

1. one beam track and one secondary track are detected;
2. the decay point is in the region between PC4 and PC5 (see figure 1);
3. the angle of the beam track with the secondary one is more than 4mrad;
4. four gammas with energies higher than 500 MeV are detected in both calorimeters;
5. the $\pi^+$ momentum is measured;
6. the chosen event fits the $K^+ \to \pi^+\pi^0\pi^0$ hypothesis at the $CL(\chi^2) \geq 3\%$ (6C-fit).

Using these criteria we have collected slightly more than 33000 events of the $K^+ \to \pi^+\pi^0\pi^0$ decay. Figure 8(left) shows the $(\gamma\gamma)$ - effective mass spectrum for the chosen events (both pairs of gammas in each event are presented). The spectrum of $(\pi^+\gamma\gamma\gamma\gamma)$ effective masses is shown in figure 8(right). The experimental data are well described by the normal distribution which illustrates a good quality of the $K_{\pi 3}$ decay reconstruction and extremely low background level (about 0.5%).

## 5.3 Background

Under the above listed conditions we have no contribution of other K decays. The only process that could give a marked contribution to the experimental sample was the $K^+N \to K^+N\pi^0\pi^0$ diffraction scattering that occurs through a wide resonance $(K^+\pi^0\pi^0)$ with small momentum transfer to a nucleon. To study this background we simulated this process

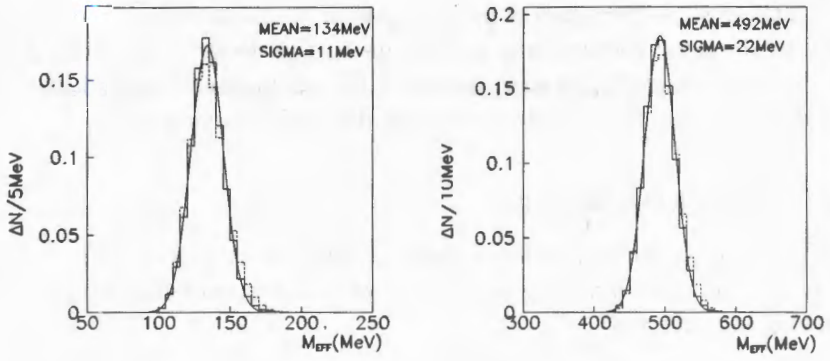


Figure 8: $(\gamma\gamma)$ - effective mass distrbution (left), $(\pi^+\gamma\gamma\gamma\gamma)$ - effective mass distribution (right) for the $K^+ \to \pi^+\pi^0\pi^0$ events. Solid line – experiment, dashed line – Monte-Carlo simulation, solid curve – fit of the experimental spectrum with a Gauss distribution.

with our data processing requirements and found that the contribution to our sample is 0.5 %, that is practically negligible. To test this effect experimentally we studied the dependence of final results on the amount of matter in the beam. We changed the decay region length, so that in one case it contains only air and in other case it also included the scintillator counter S4 and some proportional chambers, increasing in the amount of matter at about 7 times. Comparing two sets of the slope parameters obtained as a result of analysis of the Dalitz plots for two decay regions we found out that these sets coincide within one statistical error. One can also see no underlayer in the effective mass spectrum, that is in very good agreement with a Gaussian.

## 5.4 Acceptance

To obtain the matrix element dependence on X and Y we simulated $K^+ \to \pi^+\pi^0\pi^0$ acceptance with the constant matrix element. The Monte-Carlo simulation took into account the detector performance and the same trigger and reconstruction criteria as for the real events. The acceptance depen-

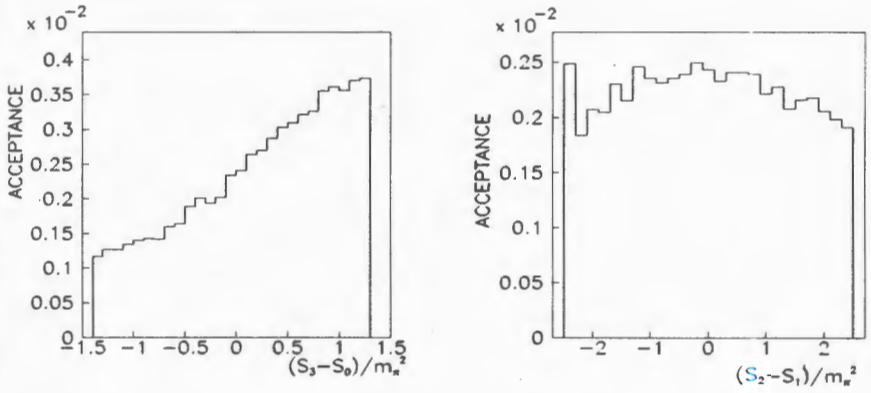


Figure 9: Dependence of the acceptance on the X-variable (left) and on Y-variable (right).

dencies on the X and Y variables are shown in figure 9. The total physical range of the X and Y variables is presented ($-2.7 \leq Y \leq 2.7 \quad -1.4 \leq X \leq 1.3$). The acceptance is smooth and does not change rapidly at the edge of the Dalitz plot. Distributions of $(\gamma\gamma)$ and $(\pi^+\gamma\gamma\gamma\gamma)$ effective masses for the accepted Monte-Carlo events are shown in figure 8 by dashed lines and are in good agreement with the experimental spectra. The number of accepted Monte-Carlo events was about five times larger than the number of experimental events.

The resulting Dalitz plot (figure 10) represents the experimentally observed density of distribution over the simulated one.

## 5.5 Results

Approximating the Dalitz plot with the expression

$$F_1(X,Y) = C_1(1 + gX + hX^2 + kY^2) \tag{4}$$

we obtained [22]

$$\begin{aligned} g &= 0.736 \pm 0.014 \pm 0.012, \\ h &= 0.128 \pm 0.015 \pm 0.024, \\ k &= 0.0197 \pm 0.0045 \pm 0.0029, \qquad \chi^2 = 1.5/ndf \end{aligned} \tag{5}$$

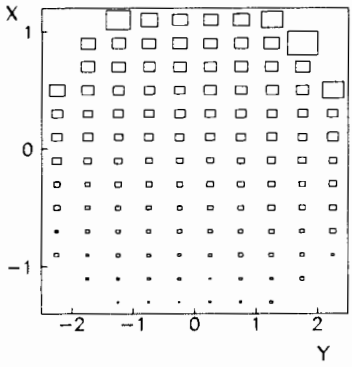


Figure 10: Resulting Dalitz plot for the $K^+ \to \pi^+\pi^0\pi^0$ decay.

Here the first errors are statistic and the second ones are systematic (see below). Note that the constant $C$ in (3) and the constant $C_1$ in (4) are different. The constant $C$ disappears due to normalizing of the experimental and simulated distributions.

In most of the previous experiments only the $\pi^+$ - energy spectrum was measured. To compare we analysed the matrix element dependence on the X variable (figure 11) fitting it with the expression $F_2(X) = C_2(1 + gX + hX^2)$. The obtained parameter values

$$g = 0.703 \pm 0.012,$$
$$h = 0.106 \pm 0.013, \qquad \chi^2 = 0.91/ndf$$

agree with (5) and also exceed substantially the world averages.

## 5.6 Systematic errors

To estimate systematic errors we investigated several independent issues.

1. We separately fitted three sample of events which were taken in different runs. These runs were comparable in statistics but data were taken under different trigger conditions with respect to the group thresholds in the calorimeters and in the third run two hodoscopes HX and HY (figure 1) were included.

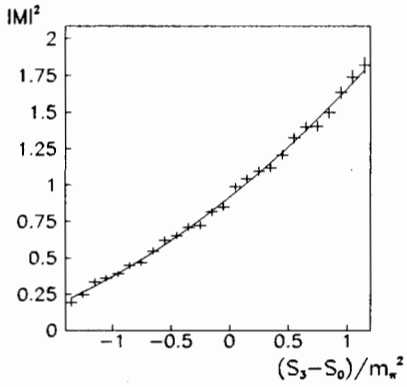


Figure 11: Matrix element dependence on the X variable for the $K^+ \to \pi^+\pi^0\pi^0$ decay. Solid curve – fit with the function $F_2(X) = C_2(1 + gX + hX^2)$

2. We set one of the variables in the kinematic fit to be "unknown", for instance $\pi^+$ or photon energy (5C-fit), and compared with 6C-fit results (5).

3. We cut exreme bins at the edge of the Dalitz plot (bin size is 0.2x0.5 (XxY)) to avoid large uncertanties in this range.

4. We rejected events where $\gamma$-quanta hit EMC1 near the hole in the center because of possible leakage of an electromagnetic shower, though this leakage should be on the average compensated by the calibration method.

5. We also increased the lower $\gamma$ - quantum energy limit from 500MeV to 1000MeV.

6. A test of systematic errors can be done in the kinematic fit by checking "pulls" [23] for each variable. If one has no systematic errors and sets correct experimental uncertainties, these "pulls" should follow the standardized Gaussian distribution with the mean value 0 and the standard deviation 1. Our "pulls" are in good agreement with this distribution. As an example, a "pull" for the $\pi^+$ - momentum

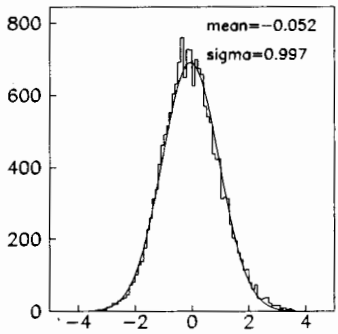


Figure 12: "Pull" for $\pi^+$*momentum* in $K^+ \to \pi^+\pi^0\pi^0$ decay.

is presented in figure 12 where the fit by normal distribution is also shown.

7. We also took into account the possibility of incorrect $\gamma$-quantum pairing. The influence of this effect was studied by simulation. These events amount to about 1 % and practically do not affect the result.

In the above cases, the maximum deviations of the slope parameter values from (5) are 0.012, 0.024 and 0.003 for $g$, $h$ and $k$ respectively. We take these values as the systematic errors for the slope parameters.

## 5.7 Discussion of the results

The quadratic parameter $k$ was previously measured only in three experiments [24, 25, 26] where the Dalitz plot was studied. The most precise value was $k = 0.011 \pm 0.007$ [24]. The world average for this parameter is not determined. It should be mentioned that all three previous results for the parameter $k$ are compatible with zero while our value is more than $3\sigma$ larger.

The results of all previous experiments on $K^\pm \to \pi^\pm\pi^0\pi^0$ decays [24, 25, 26, 27, 28, 29, 30, 31, 32, 33, 34], our results and the world averages [14] are presented in figures 13 and 14. One more measurement for the

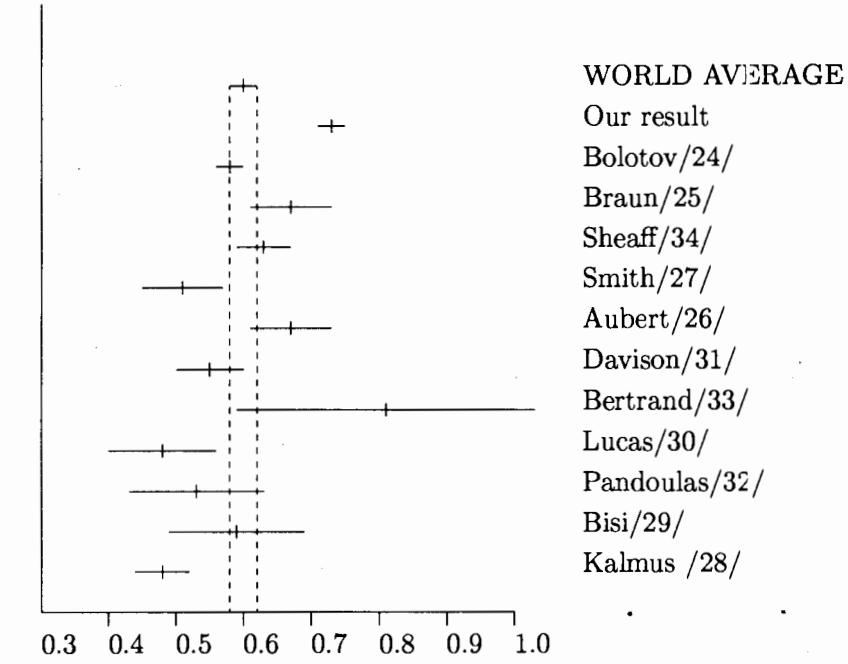


Figure 13: Linear slope $g$ for the $K^+ \to \pi^+\pi^0\pi^0$ decay.

linear slope $g = 0.705 \pm 0.018 \pm 0.016$ (fit with $h = 0$) was reported at the ICHEP'96 conference in Warsaw [35] but it is not shown in fig. 13 because the authors consider it as preliminary. One can see that our data are $5.5\sigma$ for $g$ and $3\sigma$ for $h$ larger than their world averages ($g = 0.594 \pm 0.019$, $h = 0.035 \pm 0.015$). Compairing with the other experiments one can see that the most significant difference is between our results and those given in [24]. There is agreement within one or two errors with the results [25, 26, 33, 34] for the linear slope $g$ and large values for $h$ which agree with our result were obtained in [25, 33]. Disagreement with other results is not too significant. Concerning these discrepancies we would like to make some observation.

We should emphasize that our experiment is the only electronic one where all involved particle momenta were measured. In [24] the $\pi^+$ - momentum was unmeasured. Two other experiments, where the Dalitz plot was studied and all kinematics parameters were measured, were carried out

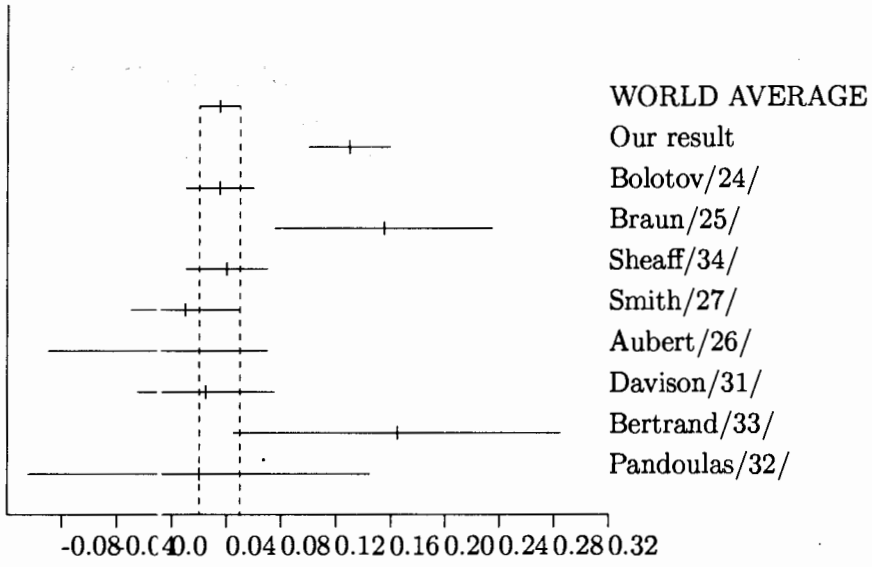


Figure 14: Quadratic parameter $h$ for the $K^+ \to \pi^+\pi^0\pi^0$ decay.

with bubble chambers and our results agree with them within one or two errors. In the other experiments also with bubble chambers (except [27] where wire chambers and hodoscopes were used), only the $\pi^+$ - momentum was measured and neither photon energy nor two pairs of $\gamma$ - quanta were detected. Experiment [27] suffered a large uncertainty in number of $\gamma$ - quanta determination. Thus in these cases one expects more background sources contrary to our experiment where there was practically no background.

The preliminary result [35] for the linear slope $g$ is in very good agreement with our result and stresses the existing discrepancy in the world data.

As we mentioned in the introduction, the slope parameters cannot be calculated theoretically due to strong model dependence and large theoretical uncertainties. Strictly speaking, we have no theoretical predictions about the parameter values. Any estimations of the slope parameters were obtained from the theoretical fit to the experimental data. Thus the discrepancy in the experimental results must be clarified in future experiments.

# 6 Conclusion

To conclude I briefly remind the main results presented in this report.

The K-decay study program is performed with the HYPERON spectrometer at the Serpukhov accelerator in close collaboration with belorussian scientists. Some interesting physical results are already obtained in the framework of this program.

The most precise value of the $K_{e3}$ vector formfactor slope parameter was obtained.

Nonzero values of the tensor and scalor formfactors were measured in the $K_{e3}$ decay, that points to possible existence of tensor interaction.

New measurement of the CKM matrix element $V_{us}$ was done. The obtained value agree well with the best known result and has almost the same precision.

The matrix element coefficients for the $K^+ \to \pi^+\pi^0\pi^0$ decay were measured with the precision higher than in the previous experiments. Nonzero value for the $k$ parameter was obtained. Values obtained for the linear slope $g$ and the quadratic coefficient $h$ substantially exceed the world-averages but there is agreement with some of the previous results.

I would like to thank our Belorussian collegues, who collaborate with us. Their contribution to our job at all stages is really invaluable. And I am gratefull to all organizers of this school for their hospitality.

# References

[1] J.Kambor, J.Missimer and D.Wyler, *Nucl.Phys.* B346 (1990) 17.

[2] M.Bando, T.Kugo, K.Yamawaki, *Phys.Rep.* vol.164, (1988) 217.

[3] G.Ecker, J.Gasser, A.Pich, E. de Rafael, *Nucl.Phys.* B321 (1989) 311.

[4] A.Bel'kov, A.Laniov, G.Bohm, A.Shaale, *Physica elementarnykh chastits i atomnogo iadra (russian)*, vol.26, No3 (1995) 562.

[5] A.Asmolov *et al.*, *Instrum. and Experim. Techniques (translated from Pribori i Tekhnika Experimenta, Russia)*, vol.37, No3, (1994) 263.

[6] Yu.Budagov *et al. Preprint JINR E13-92-219* Dubna, 1992.

[7] N.Cherr.ov *et al.*, *Matemeticheskoe modelirovanie (russian)*, vol.2, No.10, p.132, 1990.

[8] V.Batusov and N.Russakovich, *Instrum. and Experim. Techniques (translated from Pribori i Tekhnika Experimenta, Russia)*, vol.39, No.5, (1996) 55.

[9] S.Akimenko et al., *Phys.Lett.* B259 (1991) 225.

[10] H.Braun et al.,*Nucl.Phys.* B89 (1975) 220.

[11] H.Stainer et al., *Phys.Lett.* B36 (1971) 521.

[12] V.N.Bolotov et al., *Phys.Lett.* B243 (1990) 308.

[13] M.Chizhov *Modern Phys.Lett.* A8, No29 (1993) 2753.

[14] Particle Data Group, *Phys.Rev.* D54, No1, 1996.

[15] G.Velev *JINR Communication*, E1-93-305, Dubna, 1993.

[16] H.Leutwyler and M.Ross, *Z.Phys.* C25 (1984) 91.

[17] J.Kambor, J.Missimer and D.Wyler, *Phys.Lett.* B261 (1991) 496.

[18] A.Bel'kov *et al.*, *Internal Bericht DEZY-Zeuten* 93-05, 1993.

[19] A.Bel'kov *et al.*, *International Journal of Modern Physics* A7, No.20 (1992) 4757.

[20] L.Maiani and N.Paver in *The DAΦNE Physics Handbook*, vol.I, p.191, Fraskati, Italy, 1991.

[21] G.Velev *et al.*, *Instrum. and Experim. Techniques (translated from Pribori i Tekhnika Experimenta, Russia)*, vol.34, No.5 (1991) 65.

[22] V.Batusov *et al, in Proceedings of 28th International Conference on High Energy Physics*, Warsaw, World Scientific, 1997, p.1200.

[23] V.Blöbel *"Least Square Methods"* in "Formulae and Meth. in Experim. Data Evaluation with Special Emphasis on High Energy Physics", vol.3, European Physical Society, CERN, 1984.

[24] V.Bolotov *et al.*, *Sov. Journ. of Nucl. Phys.*, 44 (1986) 73.

[25] H.Braun *et al.*, *Lett. al Nuovo Chim.*, 17 (1976) 521

[26] B.Aubert *et al.*, *Nuovo Chim.*, 12A (1972) 509.

[27] R.M.Smith *et al, Nucl.Phys. B91, (1975) 45, Nucl.Phys. B60 (1973) 411.*

[28] G.E.Kalmus, *et al.*, *Phys.Rev.Lett. 13 (1964) 99.*

[29] V.Bisi *et al. Nuovo Chim., 35 (1965) 768.*

[30] P.W.Lucas *et al. Phys.Rev. D8 (1973) 727.*

[31] D.Davison *et al. Phys.Rev. 180 (1969) 1333.*

[32] D.Pandoulas *et al. Phys.Rev. D2 (1970) 1205.*

[33] D.Bertran *et al, Nucl. Phys.* B114 (1976) 387

[34] M.Sheaff, *Phys. Rev.* D12 (1975) 2570.

[35] J.Bähr *et al, in Proceedings of 28th International Conference on High Energy Physics*, Warsaw, World Scientific, 1997, p.1204.

# Elastic and Inelastic Photon Scattering by the Deuteron Below Pion Threshold as Tools to Study Polarizabilities of the Neutron

M.I. Levchuk

*B.I.Stepanov Institute of Physics, Belarusian Academy of Sciences,*
*F. Skaryna prospect 70, 220072 Minsk, Belarus*

**Abstract**

In this lecture our recent calculations for the reactions $\gamma d \to \gamma np$ and $\gamma d \to \gamma d$ are briefly summarized and discussed in relation with possibilities to determine polarizabilities of the neutron.

Since 1956 the electric polarizability of the neutron was probed in experiments on low-energy neutron scattering by heavy nuclei. The best and the only positive result was reported as [1]

$$\alpha_n = 12.0 \pm 1.5\ (stat.) \pm 2.0\ (syst.) \tag{1}$$

(henceforth we use the units of $10^{-4}$ fm$^3$ for the polarizability and disregard a small ~5% difference between the so-called polarizability-zero and polarizability-bar). Such a high precision, however, has later been questioned, and more recent experiments, which gave the values

$$\alpha_n = 0 \pm 5\ [2], \qquad \alpha_n = 7 \sim 19\ [3], \tag{2}$$

found sources of larger uncertainties.

Still less is known experimentally about the magnetic polarizability of the neutron, $\beta_n$. Meanwhile both the quantities $\alpha_n$ and $\beta_n$ are invaluable for testing models of hadrons and understanding the hadron structure [4, 5]. To compare polarizabilities of the proton and neutron, an accuracy at least as good as in Eq. (1) is really needed.

Some time ago a method was proposed [6] to measure $\alpha_n$ and $\beta_n$ in the reaction

$$\gamma d \to \gamma' np. \tag{3}$$

The amplitude of (3) in the kinematics of quasi-free scattering was calculated and analyzed in framework of the diagrammatic approach. Most important diagrams are shown in Fig. 1. They correspond to photon scattering on quasi-free nucleons, a $NN$-rescattering correction (or final state interaction, FSI), and the 1-loop contribution of mesonic exchange currents (MEC) and isobar configurations (IC). Omitted in Fig. 1 are FSI corrections to the MEC-IC diagrams and corrections due to intermediate state interaction (ISI) which is $NN$-rescattering in between photon absorption and emission. All these corrections are expected to be marginal in the quasi-free kinematics. When the momentum $\vec{p}_\gamma - \vec{p}_{\gamma'}$ transferred from photons to hadrons is mostly carried out by the neutron, whereas

the spectator proton gets a small momentum $p_p \sim p_F \ll p_n$ with $p_F \simeq 66$ MeV/c, the reaction amplitude is dominated by the neutron-pole diagram 1*a*. Correspondingly, the differential cross section of (3) has a peak at small $p_p$ (that is the neutron quasi-free peak, NQFP) and, in the peak region, is proportional to the differential cross section of neutron Compton scattering [6].

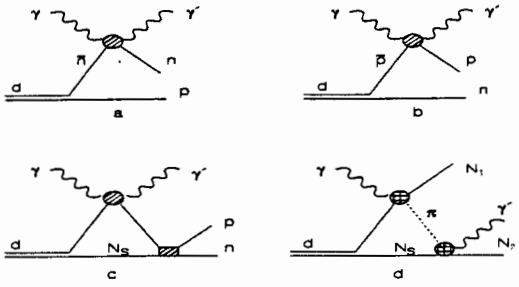


Figure 1: Diagrams of the reaction (3). A diagram with a contact $\gamma\gamma\pi n$ vertex is not shown but is taken into account.

To evaluate the diagrams in Fig. 1, we use the following physical input for the $\gamma\gamma NN$, *dpn*, *NNNN* and $\gamma\pi NN$ blocks there:

(i) Nucleon Compton scattering amplitudes found from a dispersion theory [7, 8] and reasonably extrapolated off the mass shell. They depend on electric and magnetic polarizabilities of the nucleons which, in practical calculations, are taken to be

$$\alpha_p + \beta_p = 14.2 \pm 0.5, \quad (4)$$

$$\alpha_n + \beta_n = 15.8 \pm 0.5, \quad (5)$$

$$\alpha_p - \beta_p = 10.0 \pm 3.0. \quad (6)$$

The difference of the polarizabilities of the neutron, $\alpha_n - \beta_n$, is assumed to be a free parameter which has to be determined from the experiment. A model dependence in thus determined Compton scattering amplitudes is discussed in [7, 8, 9]. We mention here that, owing to a very large $t$-channel $\pi^0$-exchange contribution to the neutron Compton scattering amplitude, uncertainties in the experimental values of the $\gamma\gamma\pi^0$ and $\pi NN$ coupling constants prevent determining $\alpha_n$ better than $\pm 2$, provided $\alpha_n \sim 12$ [6].

(ii) The deuteron wave function and the half-off-shell $NN$-scattering amplitude given by realistic $NN$ potentials. To explore model dependence, we have tried three nonrelativistic versions of the Bonn OBE potential (OBEPR) [10] and a separable approximation [11] to the Paris potential [12].

(iii) Off-shell pion photoproduction amplitudes. They determine the MEC and IC contributions and are evaluated by using the standard Blomqvist-Laget model [13].

As a typical example we discuss here the differential cross section $d^3\sigma/d\Omega_{\gamma'}d\Omega_n dE_n$ calculated in the on-plane kinematics at the photon energy $E_\gamma = 100$ MeV for a large photon angle $\theta_{\gamma'} = 135°$, which provides almost optimal sensitivity of the neutron Compton scattering amplitude to $\alpha_n - \beta_n$. The corresponding neutron angle $\theta_n$ is taken close to the NQFP value, $\theta_n \simeq -(\pi - \theta_{\gamma'})/2$. Relative significance of the diagrams 1*a*, 1*b*, 1*c*, and 1*d* is shown in Fig. 2. The diagram 1*b* is completely negligible at NQFP, or, at the above specified angles and $E_\gamma$, when $E_n \simeq 15$ MeV. The FSI (diagram 1*c*) contributes a lot and reduces the cross section by ~27% at NQFP. The MEC-IC correction (diagram 1*d*) is relatively small and is only $\sim -7\%$ in the kinematics considered. Beyond the NQFP region all these and some other corrections can be more important.

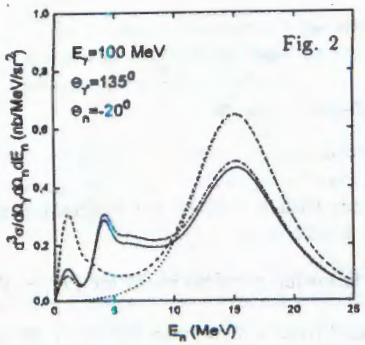


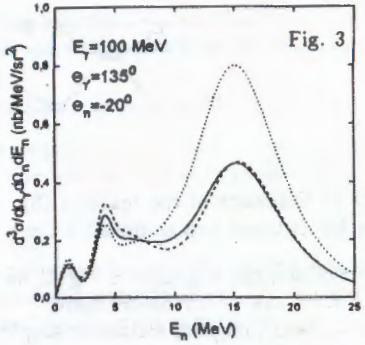


Figure 2: Contributions of different diagrams to the differential cross section of (3). $\alpha_n = 10$. Dotted line: the neutron pole diagram 1*a*. Dash, dash-dotted, and solid lines: contributions of the diagrams 1*a*, *b* (PWIA), 1*a*, *b*, *c* (DWIA), and 1*a*, *b*, *c*, *d* (DWIA+MEC+IC), respectively.

Figure 3: Dependence of the differential cross section on $\alpha_n$. Dash, solid, and dotted lines: $\alpha_n = 0$, 10, and 20, respectively.

Using different *NN* potentials and varying such parameters as off-shell cut-off in meson-baryon vertices we estimate theoretical uncertainties in the predicted cross sections coming through various binding effects (FSI, MEC-IC) to be about 4%.

Figure 3 illustrates how the differential cross section depends on the neutron electric polarizability. Predictions are given for $\alpha_n = 0$, 10, and 20, while $\alpha_n + \beta_n$ is fixed according to (5). The cross sections with $\alpha_n = 0$ and 10 are hardly distinguishable, whereas a prominent effect is seen when $\alpha_n$ changes between 10 and 20. Such a behavior of the differential cross section of the inelastic reaction (3) perfectly corresponds to the polarizability dependence of the differential cross section of elastic $\gamma n$ scattering. The latter is mainly linear in $(\alpha_n - \beta_n)^2 \simeq (15.8 - 2\alpha_n)^2$ [8]. We may conclude that measurements of the process (3) at energies below pion threshold are well suited to establish an upper limit

for $\alpha_n$ and less appropriate to find the lower limit. The very first and rapid measurement of the differential cross section of (3) in the NQFP region at energies $E_\gamma \simeq 80-130$ MeV has led to the bounds [14]

$$\alpha_n = 10.7^{+3.7}_{-10.7} \tag{7}$$

which are similar to or even stricter than those in (2). Further more extensive measurements would be certainly desirable. To determine a lower limit for $\alpha_n$ from the reaction (3) it might be profitable to do measurements at higher energies around 200−300 MeV, as is discussed in [6, 8].

Another option for studying polarizabilities of the neutron is deuteron Compton scattering,

$$\gamma d \to \gamma' d'. \tag{8}$$

Due to isospin conservation, diagrams with $t$-channel $\pi^0$-exchange do not contribute to the amplitude of (8) and, therefore, do not inflate uncertainties in extracted polarizabilities. On the other hand, the elastic reaction (8) can give only the isospin-averaged polarizabilities of the nucleon, so that one has to learn very well polarizabilities of the proton from independent experiments. Fortunately, nowadays that seems to be not a major problem. Studies of elastic $\gamma p$ scattering have already given the polarizabilities of the proton, $\alpha_p = 12.1 \pm 1.0$ and $\beta_p = 2.1 \mp 1.0$ ("global average" of [9] constrained to Eq. (4)), and some other experiments are under way which may improve the accuracy.

To calculate the amplitude of the reaction (8) we use again the diagrammatic approach. The total scattering amplitude consists of two pieces which are the so-called resonance and seagull amplitudes [15]. The resonance piece comes from low-lying intermediate excitations of the deuteron and corresponds to two-step scattering via photon absorption followed by photon emission and vice versa or, said differently, from iteration of the electromagnetic current operator $\vec{J}$. This piece can have and generally has an imaginary part. The seagull amplitude is real and corresponds to processes in which the absorption and emission happens at the same moment, as seen at the considered energy scale. At energies below ~100 MeV only two-nucleon intermediate states must be included in the resonance amplitude. Meson exchanges between photon interaction points can be treated in the unretarded approximation (with an important correction found in [16]) and, therefore, be included in the seagull amplitude. Both the current $\vec{J}$ and the seagull operator $S_{ij}$ have to be consistent with the nuclear Hamiltonian $H_0$ of the $NN$ system and satisfy conditions of the gauge invariance [15].

The resonance amplitude is given by two diagrams in Fig. 4 involving off-shell vertices $\Gamma_d$ of the deuteron photodisintegration. The diagram 4*a* corresponds to free propagation of intermediate nucleons. The diagram 4*b* takes into account $NN$ rescattering in the intermediate state (i.e. ISI) and contains, in particular, the deuteron pole contribution. In the case of the OBEPR potentials the nuclear Hamiltonian $H_0$ used to find the deuteron wave function and off-shell $NN$-scattering amplitudes reads

$$H_0 = T + V = \sum_{i=1}^{2} \frac{p_i^2}{2m} + \sum_{\alpha=\pi,\eta,\delta,\sigma,\omega,\rho} V^\alpha_{\rm OBE}\ , \tag{9}$$

where the potentials $V^\alpha_{\rm OBE}$ depend on the nucleon momenta $p_i$ and include meson exchanges with $\alpha = \pi$, $\eta$, $\delta$, $\sigma$, $\omega$, and $\rho$. The vertex $\Gamma_d$ includes the same exchanges and is given by two diagrams in Fig. 5 describing the one- and two-body (MEC-IC) contributions, respectively. The latter diagram is determined by $\gamma$-meson-nucleon-nucleon

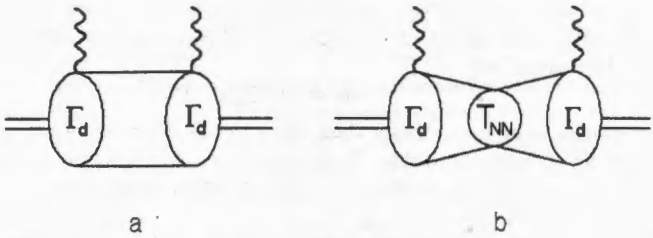


Figure 4: Resonance parts of the deuteron Compton scattering amplitude: (a) without and (b) with $NN$ rescattering.

vertices $J^\alpha$ disclosed in Fig. 6. To avoid misunderstanding we remark that the OBEPRs were originally constructed with the PS-version of the $\pi NN$-interaction, and the same PS-vertices are implied in Fig. 6, so that the diagram 6c is absent in the case of $\alpha = \pi$. The diagram 6c contributes to $J^\rho$, since the $\rho NN$ interaction is momentum dependent. Explicit formulas for $J^\alpha$ and $\Gamma_d$ in case of the OBEPRs are given in [17]. In the present calculation we also take into account the leading relativistic (spin-orbit) correction to the one-nucleon current $\vec{J}_N$ which determines the first diagram in Fig. 5.

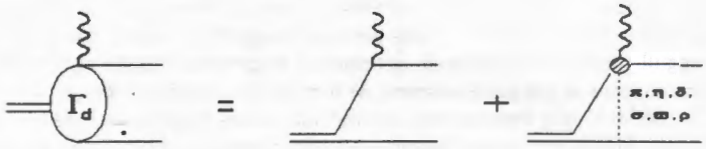


Figure 5: The deuteron photodisintegration vertex $\Gamma_d$.

The second, seagull, part of the total scattering amplitude can also be split into one- and two-body components. The one-body piece $S^{[1]}$ of the seagull operator comes from the kinetic-energy part of $H$ (thus giving the so-called Thomson term), the momentum-dependent spin-orbital interaction, and internal structure of nucleons (polarizabilities). In particular, the Thomson term reads

$$e'_i S^{[1]\mathrm{Th}}_{ij}(\vec{k}', \vec{k}) e_j = \frac{e^2}{m} \vec{e}' \vec{e}, \tag{10}$$

and the contribution of the polarizabilities is equal to

$$e'_i S^{[1]\mathrm{pol}}_{ij}(\vec{k}', \vec{k}) e_j = -2 \times 4\pi \Big[ \alpha_N E_\gamma E_{\gamma'} \vec{e}' \vec{e} + \beta_N (\vec{k}' \times \vec{e}')(\vec{k} \times \vec{e}) \Big], \tag{11}$$

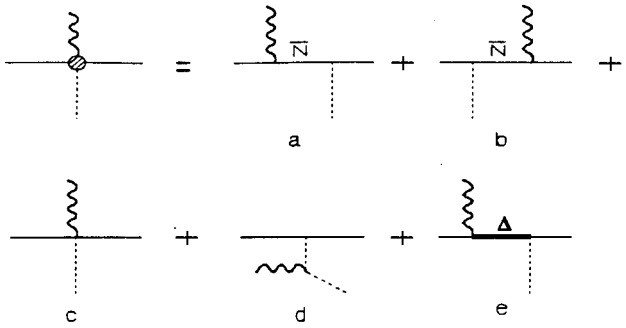


Figure 6: $\gamma$-meson-nucleon-nucleon vertices. The symbol $\bar{N}$ stands for the antiparticle part of the nucleon propagator.

where $\alpha_N = \frac{1}{2}(\alpha_p + \alpha_n)$ and $\beta_N = \frac{1}{2}(\beta_p + \beta_n)$ are isospin-averaged polarizabilities of the nucleon. In accordance with Eqs. (4)–(5) we adopt

$$\alpha_N + \beta_N = 15. \tag{12}$$

The value of $\alpha_N - \beta_N$ cannot be predicted so precisely, and for the sake of illustration we have tried a few values between 9 and 15 in the present calculation.

The two-body seagull operator $S^{[2]}$ is given by diagrams in Fig. 7 which include the same one-boson exchanges $\alpha$ as stand in the $NN$ potentials $V^{\alpha}_{\rm OBE}$. Lengthy specific details cannot be given here and will appear elsewhere [18]. At low energies $E_\gamma^2 \lesssim m_\pi^2$ the spin-independent part of the operator $S^{[2]}$ yields a contribution to the Compton scattering amplitude described by the enhancement parameter $\kappa$ in the TRK sum rule [19]. As may be expected, the largest contribution to $S^{[2]}$ comes from the pion exchange, whereas the main effect of other bosons is reduced to a $\sim$8% increase in $\kappa$.

A complete calculation of all terms described above involves diagrams up to 4 loops, and it is technically not easy to evaluate appropriate integrals. At the present stage we do not compute directly the ISI diagram in Fig. 4. Instead, we have evaluated it in frames of a simplified minimal model [20] which agrees quite well with the complete calculation as for other diagrams are concerned. We believe that such a procedure does not introduce large errors or inconsistencies because the rescattering contribution itself is not large (cf. dash-dotted and solid lines in Fig. 8). As an additional check of consistency we have verified that the found ISI term brings the total $\gamma d$ scattering amplitude to the correct Thomson limit of $-e^2/2m$ at zero energy.

Role of separate diagrams is demonstrated in Fig. 8. To avoid for a moment uncertainties related with unknown polarizabilities of the neutron we disregard there the polarizability contribution (11). Generally the resonance amplitude, the one-body seagull, and the two-body seagull are found to be of the same order. The full seagull gives

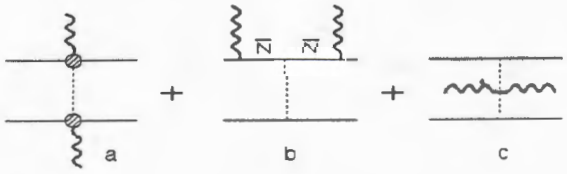


Figure 7: The two-body seagull operator $S^{[2]}$.

more than 70% of the differential cross section in the considered energy region. Meanwhile the ISI contribution is rather small. It decreases the forward differential cross section by 7% to 9% at energies 50 to 100 MeV, and this feature perfectly agrees with findings of other calculations [20, 22, 23]. Both our calculation and calculations from [20, 23] show a positive ISI contribution at backward angles which is small but certainly bigger than that found in [22].

Polarizabilities of the nucleon essentially affect the differential cross section, and that gives hopes to find them from accurate data on elastic $\gamma d$ scattering. As is directly seen from Eqs. (10)--(11), the electric polarizability decreases the Thomson term and hence the differential cross section. This decrease is determined by $\alpha_N + \beta_N$ at the forward angle and $\alpha_N - \beta_N$ at the backward one. Numerically, when $\alpha_N - \beta_N$ changes between 9 and 15 we observe a decrease in the predicted $d\sigma(180°)/d\Omega_\gamma$ by 4% at 50 MeV and 20% at 100 MeV. Using $\alpha_N - \beta_N \simeq 9$ we get a reasonable agreement with the preliminary data of [21].

New precise measurements of the differential cross section of (8) in a wide angular region at energies above 50 MeV are certainly desired. Predictions at forward angles are almost free from uncertainties in polarizabilities, and, therefore, models might be tested very well in that region. Data at backward angles interpreted with right models can then be used to extract $\alpha_N - \beta_N$. To the moment predictions of cited and present calculations of elastic $\gamma d$ scattering differ too much to be used for uncritical extracting the polarizabilities. A further work is needed to understand weak points in different calculations.

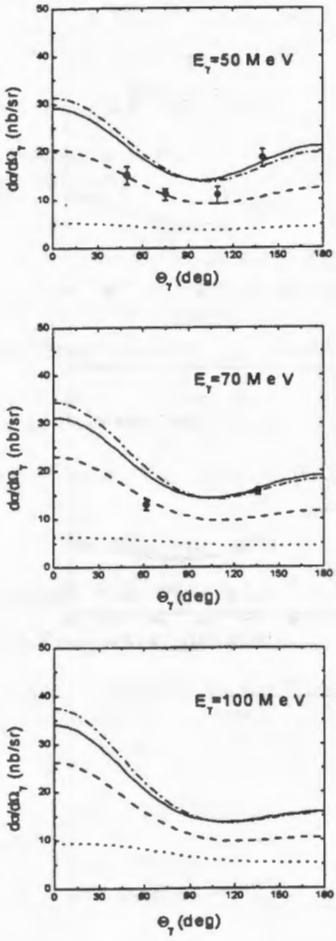


Figure 8: Contributions of different diagrams to the differential cross section of $\gamma d$ scattering at 50, 70 and 100 MeV vs. the c.m. scattering angle $\theta_\gamma$. Dotted lines: resonance amplitude only. Dash, dash-dotted, and solid lines: the one-body seagul., the two-body seagull, and the rescattering contribution are successively added. Polarizabilities are switched off ($\alpha_N = \beta_N = 0$). Data are from [21].

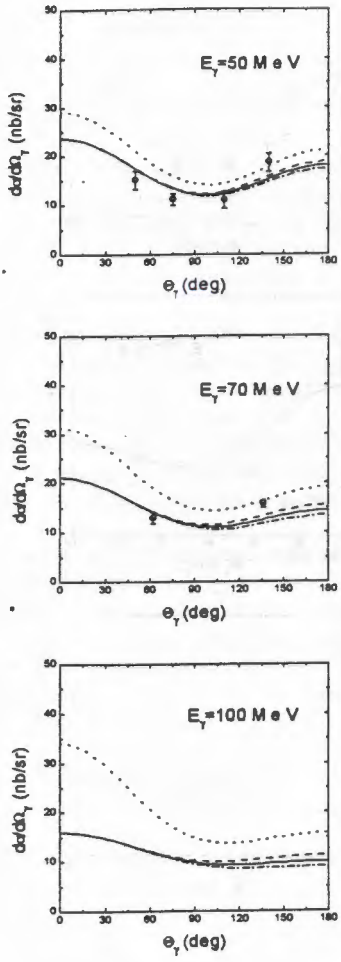


Figure 9: Differential cross sections at various polarizabilities. $\alpha_N + \beta_N = 15$ is fixed. Dash, solid, and dash-dotted lines: $\alpha_N - \beta_N = 9$, 12, and 15, respectively. Dotted lines: $\alpha_N = \beta_N = 0$. Data are from [21].

## References


[1] J. Schmiedmayer, P. Riehs, J. Harvey, and N. Hill: Phys. Rev. Lett. **66**, 1015 (1991)

[2] L. Koester et al.: Phys. Rev. **C51**, 3363 (1995)

[3] T.L. Enik et al.: Sov. J. Nucl. Phys. **60**, 567 (1997)

[4] V.A. Petrun'kin: Sov. J. Part. Nucl. **12**, 278 (1981)

[5] A.I. L'vov: Int. J. Mod. Phys. **A8**, 5267 (1993)

[6] M.I. Levchuk, A.I. L'vov, and V.A. Petrun'kin: Preprint FIAN #86, Moscow 1986; Few-Body Systems **16**, 101 (1994)

[7] A.I. L'vov: Sov. J. Nucl. Phys. **34**, 597 (1981);
A.I. L'vov, V.A. Petrun'kin, and M. Schumacher: Phys. Rev. **C55**, 359 (1997)

[8] A.I. L'vov: Sov. J. Nucl. Phys. **42**, 583 (1985)

[9] B.E. MacGibbon et al.: Phys. Rev. **C52**, 2097 (1995)

[10] R. Machleidt, K. Holinde, and Ch. Elster: Phys. Rep. **149**, 1 (1987);
R. Machleidt: Adv. Nucl. Phys. **19**, 196 (1989)

[11] J. Haidenbauer and W. Plessas: Phys. Rev. **C30**, 1822 (1984); ibid. **C32**, 1424 (1985)

[12] M. Lacombe et al.: Phys. Rev. **D12**, 1495 (1975)

[13] I. Blomqvist and J.M. Laget: Nucl. Phys. **A280**, 405 (1977)

[14] K.W. Rose et al.: Nucl. Phys. **A514**, 621 (1990)

[15] H. Arenhövel, in: New Vistas in Electro-Nuclear Physics, Eds. E.L. Tomusiak, H.S. Caplan, and E.T. Dressler, Plenum Press 1986

[16] M.-Th. Hütt and A.I. Milstein: Nucl. Phys. **A609**, 391 (1996)

[17] M.I. Levchuk: Few-Body Systems **19**, 77 (1995)

[18] M.I. Levchuk and A.I. L'vov: in preparation

[19] P. Christillin and M. Rosa-Clot: Nuovo Cim. **28A**, 29 (1975)

[20] M.I. Levchuk and A.I. L'vov: Few-Body Systems Suppl. **9**, 439 (1995)

[21] M.A. Lucas: PhD Thesis, Univ. Illinois at Urbana-Champaign, 1994

[22] M. Weyrauch: Phys. Rev. **C41**, 880 (1990)

[23] T. Wilbois, P. Wilhelm, and H. Arenhövel: Few-Body Systems Suppl. **9**, 263 (1995)

# Electroweak characteristics of mesons in the relativistic quark model

**V.V. Andreev and N.V. Maksimenko**

*Gomel State University, Gomel, 246699 Belarus*
*E-mail:root@tpf.gsu.gomel.by*

**Introduction.**

Relativistic few body problem has attracted a great attention in hadronic and nuclear physics. The most complete results are in the case of two particles. Description of the bound system within the relativistic quantum field theory is founded on the basis of four-dimensional covariant Bethe-Salpeter equation [1]. However, this equation gives series of difficulties when the practical calculations are made.

There are various reductions of two-body Bete-Salpeter equation. Different forms of these reductions were discussed by Logunov-Tavkhelidze [2], Kadyshevsky [3], Todorov [4], Gross [5], Poluzou,Keister,Lev [6]-[7] and many others.

The relativistic two-body systems were analyzed by Weinberg [8], Frankfurt - Strikman [9], Kondratyuk-Terent'ev [10] in infinite-momentum frame. Some authors use diagram approach, i.e. they select leading diagrams and project them onto three-dimensional space. Others use effective Hamiltonians, Fadeev equation.

More general covariant pertubation theory with spurions was proposed by Kadyshevsky [11]. Different forms of the quasi-potential equation can be derived using this approach [11]-[12]. The quasipotential approach and the method of the contact interaction as the consequences of the Bethe-Salpeter equation are widely recognized in the practical application [13].

Last years accuracy of measurement of the hadron electromagnetic characteristics improves considerably. This fact permits better to analyze the field-theoretical and model conception of the hadron interaction with the electromagnetic field: that is why we investigate some electroweak properties of the mesons.

In the paper [14] within the framework of the quasipotential approach [2], relativistic composite models for computation of the electric polarizability and the mean square radius of charge distribution and radial excitations of mesons as bound systems of valence quarks are proposed. The electromagnetic radius and mesons polarizability are obtained with the use of the effective Lagrangians [15]-[17], which are constructed taking into account on the one hand the general principles of the relativistic

quantum field theory and on the other hand the compound relativistic model of meson representation. Also using a relativistic constituent quark model based on point form of Poincare-covariant quantum mechanics we calculate the electromagnetic radius and the decay constants of the mesons with spinor quarks.

## Effective Lagrangian approach

Consider the scalar bound system involving the charged scalar particles. The effective Lagrangian of electromagnetic field interaction with the hadrons is represented as covariant expansion in terms of tensor of the electromagnetic field $F_{\mu\nu}$ and potential $A_\mu$

$$L_{eff} = \frac{1}{8M^2}\left(\partial_\mu\varphi^+\right)\left(\partial_\nu\varphi\right) + \left(\partial_\mu\varphi\right)\left(\partial_\nu\varphi^+\right) -$$

$$- \left(\varphi^+\partial_\mu\partial_\nu\varphi + \varphi\partial_\mu\partial_\nu\varphi^+\right)\left[(\alpha+\beta)F^{\mu\sigma}F^{\nu}_{\sigma} - \frac{1}{2}\beta g_{\mu\nu}F^{\rho\sigma}F_{\sigma\rho}\right] +$$

$$+ e^2A_\mu^2\varphi^+\varphi + ie\left[\varphi^+\overleftrightarrow{\partial_\mu}\varphi\right]A^\mu, \qquad (1)$$

where $\varphi$ is the field function of scalar charged structural particle, $\alpha$ and $\beta$ are the electric and magnetic static polarizabilities. Let us consider generating functional

$$exp(iS_{eff}) = Z(A). \qquad (2)$$

For calculation $S_{eff}$ in (2) we have restricted to the model with two vertex $\Gamma$. As a result we have

$$iS_{eff} = \langle\Delta(A; Z_1 - Z_1')\Gamma(A; Z_1', Z_2'; Z)\Delta(A; Z_2 - Z_2')\Gamma(A; Z_1, Z_2; Z)\rangle, \quad (3)$$

where $\Delta(A; Z_1 - Z_2)$ is propagator of scalar particle in the electromagnetic field, $\Gamma(A; Z_1, Z_2; Z)$ is the three-point vertex function in the electromagnetic field. Using the reduction technique methods, one can relate Bethe-Salpeter function and the vertex function

$$\chi_{\mathcal{P}}(Z_1,Z_2) = i\left\langle\exp\left(-i\mathcal{P}Z\right)\Delta\left(Z_1 - Z_1'\right)\Gamma\left(Z_1', Z_2'; Z\right)\Delta\left(Z_2' - Z_2\right)\right\rangle, \quad (4)$$

where $\mathcal{P}$ is the total momentum of the compound system. The brackets in this equation mean the integration with respect to $Z_1'$, $Z_2'$ and $Z$ variables. The function (4) obeys to the homogeneous Bethe-Salpeter equation [18].

$$\chi_{\mathcal{P}}(Z_1, Z_2) = i\langle\Delta(Z_1 - Z_1')\chi_{\mathcal{P}}(Z_1', Z_2')\Delta(Z_2' - Z_2)V(Z_1' - Z_2')\rangle, \qquad (5)$$

where $V$ is the interaction potential. In the contact interaction approximation and in the momentum representation the equation (5) is:

$$\Delta_1^{-1}(p_1)\Delta_2^{-1}(p_2)\chi_{\mathcal{P}}(p) = i\frac{g}{(2\pi)^4}\int dq\chi_{\mathcal{P}}(q), \tag{6}$$

where $p = p_1 + p_2, \mathcal{P} = \frac{1}{2}(p_1 - p_2)$. When (6) integrated over $dp_0$, we obtain

$$\chi_{\mathcal{P}}(\vec{p}) = N\frac{E_1 + E_2}{E_1E_2[(E_1 + E_2)^2 - E^2]}, \tag{7}$$

where $E_i = \sqrt{\vec{p}_i^2 + m_i^2};\ i = 1,2;\ E = \sqrt{\vec{\mathcal{P}}^2 + M^2}$, $N$ is the normalizing factor, $M$ is the compound system mass. Using the relativistic covariant normalization [19, 20] .

$$\frac{i}{(2\pi)^4}\int dpdp'\chi_{\mathcal{P}}(p)[\frac{\partial}{\partial E}(K - V)]\chi_{\mathcal{P}}(p') = 2E, \tag{8}$$

where

$$K(p,p';\mathcal{P}) = \Delta_1^{-1}(p_1)\Delta_2^{-1}(p_2)\delta(p - p'),$$

we obtain

$$N^2 = \frac{1}{(\frac{2m^2}{M\beta}atan\frac{M}{2\beta} - 1)},$$

where $\beta = \sqrt{m^2 - \frac{M^2}{4}}$.

**Electromagnetic radius and the polarizabilities .**

Using (7), the pion $\langle r^2\rangle$ is calculated as

$$\langle r^2\rangle = \frac{1}{8\beta^2M^2}\frac{M^2 + \frac{M^4+4\beta^4}{2M\beta}atan\frac{M}{2\beta} - 12\beta^2}{\frac{2m^2}{M\beta}atan\frac{M}{2\beta} - 1}. \tag{9}$$

It follows from (9), when the binding energy is low (the compound system is non-relativistic)

$$\langle r^2\rangle \sim \frac{1}{8\beta^2}, \tag{10}$$

and when the binding energy is high (the compound system is relativistic)

$$\langle r^2\rangle \sim \frac{0.3}{m^2}. \tag{11}$$

The numerical analysis of (9) is adequate to the experimental value $\langle r^2 \rangle$ [21] when $\pi$-meson mass is $M = 140\ MeV$ and quark mass is $m = 210\ MeV$. This result is in accordance with (11). Consequently, $\pi$-meson is the strong-bound relativistic quark system. In order to calculate the electrical polarizability of $\pi$-meson we have restricted to the model of the electromagnetic field interaction. It follows from the equations (1), (3) and (7), that the electrical polarizability of $\pi$-meson is defined by

$$\alpha = (\frac{e^2}{4\pi})\frac{16\pi N^2}{M^3}\mathcal{I}. \tag{12}$$

Here

$$\mathcal{I} = \int\limits_0^1 dx\{(\hat{Q}^2 + \hat{\bar{Q}}^2)\frac{\frac{1}{4}x^2 - \frac{1}{3}x^3 + \frac{1}{8}x^4}{[x(1-x) - \eta^2]^2} - \hat{Q}\hat{\bar{Q}}\frac{\frac{1}{4}x^2(1-x)^2}{[x(1-x) - \eta^2]^2} -$$

$$- (\hat{Q}^2 + \hat{\bar{Q}}^2)\frac{x^3(1-x)^2(\frac{2}{3} - \frac{1}{2}x)}{[x(1-x) - \eta^2]^3} + \hat{Q}\hat{\bar{Q}}\frac{x^3(1-x)^3}{[x(1-x) - \eta^2]^3}\}, \tag{13}$$

where $\hat{Q}$ and $\hat{\bar{Q}}$ are the values of quark and antiquark charges, $\eta = \frac{m}{M}$. Within the strong coupling we obtain

$$\alpha = \frac{e^2}{4\pi}\frac{96\pi}{m^2 M}\{(\hat{Q}^2 + \hat{\bar{Q}}^2)(\frac{1}{40} + \frac{2M^2}{315m^2}) - (\hat{Q}\hat{\bar{Q}})(\frac{1}{120} + \frac{M^2}{140m^2})\}. \tag{14}$$

The numerical estimations of (14), when $m = 210 \leq MeV$, give value $\alpha$, which agrees with the experiment [22] . We shell explain how the polarizability can be calculated in the quasipotential approach [2] . Let us assume, that

$$\Gamma(A|Z_1 Z_2 Z) = \tilde{\Gamma}(A)\delta(Z_{10} - Z_0)\delta(Z_{20} - Z_0).$$

Then one can derive the equation

$$iS_{eff} = \langle \tilde{\Gamma}(A)\tilde{\mathcal{G}}^{(0)}(A)\tilde{\Gamma}(A)\rangle, \tag{15}$$

where $\tilde{\mathcal{G}}^{(0)}(A)$ is the three-dimensional Green function in the external electromagnetic field. Let us introduce the wave function, that will obey the quasipotential equation

$$\tilde{\mathcal{G}}^{(0)-1}(A)\tilde{\Phi}(A) = \tilde{V}(A)\tilde{\Phi}(A), \tag{16}$$

where $\tilde{V}(A)$ is the quasipotential of system in the electromagnetic field. Then (15) takes the form

$$iS_{eff} = \langle \tilde{\Phi}(A)\tilde{\mathcal{G}}^{(0)-1}(A)\tilde{\Phi}(A)\rangle. \tag{17}$$

Consider a particular case when the system interacts with the constant electric field. Restricting to the first order of field $\vec{E}$ in the left- and right-hand side of (17) we get the electric radius of the system

$$\langle r^2 \rangle = \int d\vec{q}\varphi_n(\vec{q})(-\frac{i}{2}\vec{\partial}_q)^2\varphi_n(\vec{q}) + \frac{3}{16}\int d\vec{q}\mid \varphi_n(\vec{q}) \mid^2 \frac{\vec{q}^2}{E_q^4}, \qquad (18)$$

where $\varphi_n(\vec{q})$ is the wave functions (18) of the relative movement of the quark in the rest frame system, $E_q = \sqrt{\vec{q}^2 + m^2}$, $m$ is the quark mass. Comparing in (17) the structures proportional to the second order of field $\vec{E}$, we obtain the expression for the electric polarizability [14]

$$\alpha = \frac{1}{\mid \vec{E} \mid^2}\{\sum_\xi \int d\vec{q}\varphi_n(\vec{q})\chi_n^+(\xi)i(\widehat{Q}_1 - \widehat{Q}_2)(\vec{E}\vec{\partial}_q)\varphi_n^{(1)}(\vec{q},\xi) -$$

$$-\frac{1}{M}\sum_\xi \int d\vec{q}\varphi_n(\vec{q})\chi_n^+(\xi)\Gamma^{(2)}(\vec{q})\chi_n(\xi)\varphi_n(\vec{q}) -$$

$$-\frac{1}{M}\sum_\xi \int d\vec{q}\varphi_n(\vec{q})\chi_n^+(\xi)[\frac{1}{2}(\widehat{Q}_1 - \widehat{Q}_2)(\vec{E}\vec{\partial}_q)]^2\chi_n(\xi)\varphi_n(\vec{q})\}. \qquad (19)$$

In the equations (18) and (19) the functions $\chi_n(\xi)$ are the flavour wave function of the quarks,

$$\Gamma^{(2)}(\vec{q}) = (\hat{Q}_1^2 + \hat{Q}_2^2)(M^2 - 10E_q^2)\frac{\vec{E}^2}{8E_q^4} +$$

$$+(\hat{Q}_1^2 + \hat{Q}_2^2)(53E_q^2 - 5M^2)\frac{(\vec{E}\vec{q})^2}{16E_q^6} - 3\hat{Q}_1\hat{Q}_2\frac{(\vec{E}\vec{q})^2}{8E_q^4}.$$

The wave functions $\varphi_n^{(1)}(\vec{q},\xi)$ obey the quasipotential equation in the first order of the external field. The interaction of the dipole moment with the electric field yields the first term of (19) ($\alpha_{dip}$). All other terms of (19) are determined by the relativistic interaction of the quarks with the external field ($\alpha_{rel}$). The quasipotential equation (16) for the system of scalar quarks in the first order of the field $\vec{E}$ has the form

$$[\vec{\nabla}_r^2 - \tilde{V}(r) - m^2 + \frac{M_n^2}{2}\frac{(\hat{Q}_2 - \hat{Q}_1)}{2e}(e\vec{E}\vec{r})]\varphi_n^{(1)}(\vec{q},\xi) = 0.$$

We shall consider the model with Coulomb and oscillator quasipotential ($C = const$)

$$V_{coul} = -\frac{g}{r} - C,$$

$$V_{osc} = -gr^2 - C. \qquad (20)$$

The wave function for the quasipotentials (20) has the form ($n = 0$)

$$\varphi_0^{coul}(r) = Aexp(-\beta_0^{coul} r), \quad \varphi_0^{osc}(r) = Aexp(-\frac{1}{6}\beta_0^{osc} r^2).$$

The parameters of wave functions $\varphi_0(r)$ are determined by the condition of the energy quantization

$$\beta_n^{coul} = \frac{g^2}{4(n+1)^2}, \quad \beta_n^{osc} = -\sqrt{g}(n + \frac{3}{2}),$$

where

$$\beta_n^{coul} = m^2 - C - \frac{M_n^2}{4}, \quad \beta_n^{osc} = \frac{M_n^2}{4} - m^2 + C.$$

The parameters $g$ and $C$ are in agreement with the masses $\pi'(1300)$ and $K'(1400)$. For $\pi$-mesons $m = 330MeV$, for $K$-mesons - $m = 420MeV$. Under these parameters the averaged squared radiuses of $\pi$- and $K$-mesons (18) have the same order both in Coulomb and oscillator models:

$$\sqrt{\langle r_\pi^2\rangle^{coul}} = 0.25 f_m, \quad \sqrt{\langle r_\pi^2\rangle^{osc}} = 0.21 f_m,$$

$$\sqrt{\langle r_K^2\rangle^{coul}} = 0.26 f_m, \quad \sqrt{\langle r_K^2\rangle^{osc}} = 0.23 f_m.$$

We obtain the same order for polarizability in Coulomb and oscillator models (the numerical values are given in units of $10^{-4} f_m^3$).

$$\alpha_{coul}^{\pi^0} = 1.83, \quad \alpha_{coul}^{\pi^\pm} = 3.63, \quad \alpha_{coul}^{K^0} = 0.24, \quad \alpha_{coul}^{K^\pm} = 0.93;$$

$$\alpha_{osc}^{\pi^0} = 1.68, \quad \alpha_{osc}^{\pi^\pm} = 4.02, \quad \alpha_{osc}^{K^0} = 0.27, \quad \alpha_{osc}^{K^\pm} = 1.05.$$

Due to the factor $\frac{1}{M}$ in (19), the relativistic correction to the polarizability ($\alpha_{rel}$) makes the essential contribution comparable with an ordinary polarizability ($\alpha_{dip}$).

## RQM formalism for $q\bar{q}$ bound states

The formulation of relativistic quantum mechanics (RQM) differs from nonrelativistic quantum mechanics by the replacement of invariance under Galilean transformations with invariance under Poincare transformations. The dynamics of many-particle system in the RQM is specified by expressing ten generators of Poincare group $\hat{M}_{\mu\nu}$ and $\hat{P}_\mu$ in terms of dynamical variables. In the constructing generators for interacting systems it is

customary to start with the generators of the corresponding noninteracting system (**we shall write this operators without "a hat"** ) and then add interactions in the way, that is consistent with Poincare algebra. In the relativistic case it is necessary to add an interaction $V$ to more than one generator in order to satisfy the commutation relations of the Poincare algebra. Dirac [23] observed, that there is no unique way of separating the generators into dynamical subset ( the generators including interaction $V$ ) and kinematical subset. Kinematical subset must be associated with some subgroup of Poincare group, usually called stability group [24] or kinematic subgroup [25].

There are three forms of the dynamics in the relativistic quantum mechanics, called "instant","point","light-front" forms [23]. The description in the instant form implies that the operators of three-momentum and angular momentum do not depend on interactions, i.e. $\hat{\vec{P}} = \vec{P}$ and $\hat{\vec{J}} = \vec{J}$ $(\hat{\vec{J}}=(\hat{M}^{23}, \hat{M}^{31}, \hat{M}^{12}))$ and interactions may be presented in operator $\hat{P}^0$ and generators of the Lorentz boosts $\hat{\vec{N}} = (\hat{M}^{01}, \hat{M}^{02}, \hat{M}^{03})$. The description in the point form implies that the operators $\hat{M}^{\mu\nu}$ are the same as for noninteracting particles, i.e. $\hat{M}^{\mu\nu} = M^{\mu\nu}$, and thus interaction terms can be presented only in the four-momentum operators $\hat{P}$. In the front form with the marked $z$ axis we introduce + and - components of the four-vectors as $p^+ = (p^0 + p^z)/\sqrt{2}$, $p^- = (p^0 - p^z)/\sqrt{2}$. We require that in the front form the operators $\hat{P}^+, \hat{P}^j, \hat{M}^{12}, \hat{M}^{+-}, \hat{M}^{+j}$ $(j = 1, 2)$ are the same as the corresponding free operators, and interaction terms may be presented in the operators $\hat{M}^{-j}$ and $\hat{P}^-$. It is significant that four-momentum of the two-particle bound system $P$ is not conserved i.e. $P \neq p_1 + p_2$, where $p_1$ and $p_2$ are four-momenta of the particles of noninteracting system.

Three-momenta $\vec{p}_1$, $\vec{p}_2$ of the particles (in our case, the quarks ) with the masses $m_1$ and $m_2$ of relativistic system can be transformed to the total $\vec{P}$ and relative momenta $\vec{k}$ to facilitate the separation of the center of mass motion:

$$\vec{P}_{12} = \vec{p}_1 + \vec{p}_2,$$

$$\overrightarrow{k} = \overrightarrow{p_1} + \frac{\overrightarrow{P_{12}}}{M_0}\left(\frac{\left(\overrightarrow{P_{12}}\overrightarrow{p_1}\right)}{\omega_{M_0}\left(\overrightarrow{P_{12}}\right) + M_0} + \omega_{m_1}\left(\overrightarrow{p_1}\right)\right), \qquad (21)$$

where

$$M_0 = \omega_{m_1}\left(\overrightarrow{k}\right) + \omega_{m_2}\left(\overrightarrow{k}\right), \omega_{m_1}\left(\overrightarrow{p_1}\right) = \sqrt{\overrightarrow{p_1}^2 + m_1^2}. \qquad (22)$$

The eigenvalue problem for the mass of $q\bar{q}$ system can be expressed in two equivalent forms [26]:

$$\hat{M} \mid \Psi > \equiv (\hat{M}_0 + \hat{V}) \mid \Psi > = M \mid \Psi >,$$
$$(k^2 + \hat{W}) \mid \Psi > = \eta \mid \Psi >, \tag{23}$$

where the masses of bound $q\bar{q}$ system $M$ and $\eta$ are given by the relation:

$$M^2 = 2\eta + m_1^2 + m_2^2 + 2\sqrt{\eta(\eta + m_1^2 + m_2^2) + m_1^2 m_2^2}$$

and $k \equiv \left|\vec{k}\right|$.

The solution of any above eigenvalue problems will lead to eigenfunctions of the form

$$_0\left\langle \vec{V}_{12}\mu, [J\,k], (ls) \left| \vec{V}\,\mu, [J\,M] \right\rangle = \right.$$
$$= \left(\frac{M}{M_0}\right)^{3/2} \delta_{JJ'}\delta_{\mu\mu'}\delta(\vec{V} - \vec{V}_{12})\Psi^{J\mu}(k\,l\,s\,;M) \tag{24}$$

with the velocities of bound system $\vec{V} = \vec{P}/M$ and noninteracting system $\vec{V}_{12} = \vec{P}_{12}/M_0$. The function $\Psi^{J\mu}(k\,l\,s\,;M)$ satisfies in the point form a following equation [26]:

$$\sum_{l's'} \int_0^\infty < k\,l\,s \parallel W^J \parallel k'\,l'\,s' > \Psi^J(k'\,l'\,s';\,M)k'^2 dk' +$$
$$+ k^2\Psi^J(k\,l\,s;M) = \eta\Psi^J(k\,l\,s;M) \tag{25}$$

with reduced matrix element of operator $\hat{W}$.

The state vector $\left|\vec{V}_{12}\,\mu,\,[J\,k]\,,\,(l\,s)\right\rangle_0$ is the eigenstate of operators $\vec{V}_{12}$, $\hat{J}^2$ (angular momentum), $\hat{J}_3$ and also $\hat{L}^2$, $\hat{S}^2$ , where $\vec{L}$ and $\vec{S}$ are relative orbital momentum and total spin momentum accordingly. This vector of the noninteracting $q\bar{q}$ system transforms irreducibly under Poincare transformations. The vector $\left|\vec{V}\,\mu, [J\,M]\right\rangle$ is eigenstate of the interacting system, that also transforms irreducibly.

In this approach the meson state is defined as state of on-shell quark and antiquark with the wave function $\Psi^{J\mu}(k\,l\,s\,;M)$

$$\left|\vec{P}\,\mu\,[JM]\right\rangle = \sum_{ls}\sum_{\lambda_1\lambda_2}\int d^3k \sqrt{\frac{\omega_{m_1}\left(\vec{p_1}\right)\omega_{m_2}\left(\vec{p_2}\right)M_0}{\omega_{m_1}\left(\vec{k}\right)\omega_{m_2}\left(\vec{k}\right)\omega_{M_0}\left(\vec{P_{12}}\right)}}$$
$$\Psi^{J\mu}(kls;M)\sum_{m\lambda}\sum_{\nu_1\nu_2}\langle s_1\nu_1, s_2\nu_2|\, s\lambda\rangle\,\langle lm, s\lambda|\, J\mu\rangle$$
$$Y_{lm}(\theta,\phi)\,D^{1/2}_{\lambda_1\nu_1}\left(\vec{n}\,(p_1, P_{12})\right)D^{1/2}_{\lambda_2\nu_2}\left(\vec{n}\,(p_2, P_{12})\right)$$
$$|p_1\lambda_1\rangle\,|p_2\lambda_2\rangle \tag{26}$$

where $\langle s_1\nu_1, s_2\nu_2 |\, s\lambda\rangle$, $\langle lm, s\lambda |\, J\mu\rangle$ are Clebsh-Gordan coefficients of $SU(2)$-group, $Y_{lm}(\theta,\phi)$ - spherical harmonic with spherical angle of $\vec{k}$. Also, in Eq.(26 )

$$D^{1/2}\left(\overrightarrow{n}\right) = \frac{1 - i\left(\overrightarrow{n}\,\overrightarrow{\sigma}\right)}{\sqrt{1+\overrightarrow{n}^2}}$$

is $D$-function of Wigner rotation, which is determined by vector-parameter

$$\overrightarrow{n}\left(p_1,p_2\right) = \frac{\overrightarrow{u_1}\times\overrightarrow{u_2}}{1-\left(\overrightarrow{u_1}\,\overrightarrow{u_2}\right)}$$

with $\overrightarrow{u} = \overrightarrow{p}/\left(\omega_m\left(\overrightarrow{p}\right)+m\right)$.

## Basic Requirements for Current Operator

Current operators $\hat{J}^\mu(x)$ of bound systems are required to calculate the decay constants, the charge form factors and the other properties of relativistic particles. Since $\hat{J}^\mu(x)$ is four-vector operator, it has the same transformation properties as the four-momentum $\hat{P}_\mu$ under Poincare transformation. It implies that the commutation relations between $\hat{J}^\mu(x)$ and Poincare generators $\hat{M}^{\rho\sigma}$, $\hat{P}_\mu$ are identical to the commutation relations between the generators of the Poincare group and four momentum:

$$\left[\hat{M}^{\rho\sigma}, \hat{J}^\mu(x)\right] = i\left(g^{\mu\sigma}\hat{J}^\rho(x) - g^{\mu\rho}\hat{J}^\sigma(x)\right) - i\left(x^\rho\frac{\partial\hat{J}^\mu(x)}{\partial x_\sigma} - x^\sigma\frac{\partial\hat{J}^\mu(x)}{\partial x_\rho}\right) \tag{27}$$

$$\left[\hat{P}_\mu, \hat{J}_\gamma(x)\right] = -i\frac{\partial\hat{J}_\mu(x)}{\partial x^\gamma} \tag{28}$$

The translational invariance of the current operators implies that

$$\hat{J}_\mu(x) = \exp\left(i\hat{P}x\right)\hat{J}_\mu(0)\exp\left(-i\hat{P}x\right) \tag{29}$$

This relation makes it possible to reduce problem of seeking $\hat{J}_\mu(x)$ to the problem of seeking $\hat{J}_\mu(0)$ (see, for example [27], [6] ). The requirements of Lorentz invariance (27) reduces to

$$\left[\hat{M}^{\rho\sigma}, \hat{J}^\mu(0)\right] = i\left(g^{\mu\sigma}\hat{J}^\rho(0) - g^{\mu\rho}\hat{J}^\sigma(0)\right) \tag{30}$$

If the theory is invariant under the space reflection and time reversal, and $\hat{U}_P$,$\hat{U}_T$ are the corresponding representation operators, then the current

operator should be satisfied the following conditions:

$$\hat{U}_P(\hat{J}^0(x^0,\vec{x}),\hat{\vec{J}}(x^0,\vec{x}))\hat{U}_P^{-1} = (\hat{J}^0(x^0,-\vec{x}),-\hat{\vec{J}}(x^0,-\vec{x})),$$
$$\hat{U}_T(\hat{J}^0(x^0,\vec{x}),\hat{\vec{J}}(x^0,\vec{x}))\hat{U}_T^{-1} = (\hat{J}^0(-x^0,\vec{x}),-\hat{\vec{J}}(-x^0,\vec{x})) \qquad (31)$$

In addition to these equations continuity equation $\partial\hat{J}^\mu(x)/\partial x^\mu = 0$ can be used. As follows from (28) this requirements can be written in the form

$$\left[\hat{P}_\mu, \hat{J}_\nu(0)\right] g^{\mu\nu} = 0. \qquad (32)$$

Finally, the operator $\hat{J}_\mu(x)$ should be also satisfied the cluster separability [26, 6, 7, 28] for many-particle system.

For calculations many authors assume that the mathematical expressions of current operators for bound system and for the noninteracting system are equivalent. This condition (so called, impulse approximation)

$$\hat{J}_\mu(0) = J_\mu(0) \qquad (33)$$

is reasonable only in point form of the Poincare relativistic mechanics ([29]). This result is evident from Eq.(30).

## Decay constants and charge radius of pseudoscalar mesons in RQM formalism

The decay constant $f_p$ for $\pi^\pm$ is defined by

$$\left\langle 0\left|\hat{J}^\mu(0)\right|\overrightarrow{P},M\right\rangle = i(1/2\pi)^{3/2}\frac{1}{\sqrt{2\omega_M\left(\overrightarrow{P}\right)}}P^\mu f_p, \qquad (34)$$

where $\hat{J}^\mu(0)$ is the operator of axial-vector part of the charged weak current once Cabibbo-Kobayashi-Maskawa mixing matrix element $V_{qq'}$ has been removed. The state vector is normalized by $\left\langle\vec{P},M\left|\vec{P}',M\right.\right\rangle = \delta(\vec{P}-\vec{P}')$.

The meson current operator can be defined by the axial-vector current of the free quarks fields:

$$\hat{J}^\mu(0) = \hat{d}(0)\gamma^\mu\gamma_5\hat{u}(0).$$

Using Eq.(26) and Eq.(34) we found, that

$$f_p = \frac{\sqrt{2}m\,N_c}{\pi\sqrt{M}}\int_0^\infty \frac{dk\,k^2}{\omega_m\left(\overrightarrow{k}\right)}\Psi(k,M), \qquad (35)$$

where $N_c$-number of colors and the wave function of pseudoscalar meson is normalized as

$$\int_0^\infty dk\, k^2\, N_c\, |\Psi\,(k, M)|^2 = 1$$

For pion we assume, that the masses of $u$ and $d$-quarks are equal i.e. $m_u = m_d \equiv m$. In the nonrelativistic quark model, when $k^2 \ll m^2$, meson decay constants are given by

$$f_p \sim \frac{1}{\sqrt{M}} \Psi\,(r = 0) \tag{36}$$

with $\Psi\,(r = 0) \sim \int d^3k\, \Psi(k)$.

The amplitude of decay $\pi \to \gamma + \gamma$ can be parametrized as

$$M_{\pi^0 \to \gamma\gamma}(k_1, k_2) = (-1)\frac{4\pi\alpha}{(2\pi)^{3/2}}\, g_{\pi\gamma\gamma}\, \epsilon_{\mu\nu\rho\sigma}\, k_1^\mu\, k_2^\nu\, \xi^\rho\,(k_1)\, \xi^\sigma\,(k_2)\,, \tag{37}$$

where $k_1, k_2$ are momenta of photons having polarization vectors $\xi^\rho\,(k_1)$ and $\xi^\rho\,(k_2)$. The calculations of the matrix element $M_{\pi^0 \to \gamma\gamma}(k_1, k_2)$ for real photons in the lowest order implies that

$$g_{\pi\gamma\gamma} = \frac{m\, N_c}{\pi\, M^{3/2}} \int_0^\infty \frac{dy\, y}{\sqrt{y^2+1}} \ln \left| \frac{\sqrt{y^2+1} + y}{\sqrt{y^2+1} - y} \right| \Psi\,(y\, m, M) \tag{38}$$

The equation of the bound $q\bar{q}$ states motion (25) within the RQM is relativistic one with appropriate effective potential $W$ (or $V$ ). However, it is a problem to obtain wave function $\Psi(k, M)$ as solution of this equation. Therefore, we use simple model wave function depending on length scale parameter $\beta$:

$$\Psi(k\,, M) \equiv \Psi(k\,, \beta) = 2/(\sqrt{N_c}\beta^{3/2}\pi^{1/4}) exp(-\frac{k^2}{2\beta^2}). \tag{39}$$

And second parameter of this model is the constituent quark mass $m$. It is fixed by fitting the relevant experimental data. We use the following values for decay constant $f_p = 130.7 \pm 0.1 \pm 0.36 \;\; MeV$ [30] and for coupling constant $g_{\pi\gamma\gamma} = 0.0839 \pm 0.0013 \;\; MeV^{-1}$, which are determined by radiative widths $\Gamma(\pi \to \gamma + \gamma) = 7.25 \pm 0.13 \;\; eV$ [31] . From these values we obtain the allowed region for the mass $m$ of quark and the parameter $\beta$ in wave function (39):

$$m = 155 \pm 5 \quad MeV, \qquad \beta = 150 \pm 5 \quad MeV. \tag{40}$$

Our optimal value of light quark mass $m = 155\ MeV$ is not in agreement with result of $m = 250\ MeV$ (see, [32] , [33] ), but is roughly in agreement with result of $m = 170\ MeV$ [34] .

The most general form of the hadronic matrix element of the vector current must be represented in terms of two form factors

$$\left\langle \vec{P}', M' \middle| \bar{q}(0)\gamma^{\mu} q(0) \middle| \vec{P}, M \right\rangle = \frac{1}{2 * (2\pi)^3 \sqrt{\omega_M\left(\vec{P}\right)\omega_{M'}\left(\vec{P}'\right)}} (F_+(t)(P\mu' + P_\mu) + F_-(t)\left(P'_\mu - P_\mu\right)),$$

where $t = -(P' - P)^2$ , $q(x)-$ operator of the quark field. In the case of pion we shall consider only $F_+(t)$. On rearrangements, as a result we obtain the following expression for the form factor:

$$F_+(t) = \frac{1}{2}\int_0^{\infty} dk k^2 \Psi(k) \int_0^1 dx [\Psi(k_1) + \Psi(k_2) - \frac{k\left|\vec{V}\right|}{\omega_m\left(\vec{k}\right)} x(\Psi(k_1) - \Psi(k_2))],$$

where $k_i^2 = k^2 + \Delta_i$, $\Delta_i = 4\gamma^4[\left|\vec{V}\right|^2\left(\omega_m^2\left(\vec{k}\right) + k^2x^2\right) + (-1)^i\left|\vec{V}\right|k\ (1 + \left|\vec{V}\right|^2)$, $\gamma = 1/\left(1 - \left|\vec{V}\right|^2\right)$, $\left|\vec{V}\right|^2 = t/(t + 4\ M^2)$.

Using the definition mean square radius : $\langle r^2\rangle = -6\ dF_+(t)/dt$ at $t = 0$ we obtain the final relativistic pion charge radius for the wavefunction (39) in a simple form:

$$\left\langle r^2 \right\rangle = \frac{3}{M^2}\left(\frac{m^2}{2\beta^2} + \frac{5}{4}\right). \tag{41}$$

Unfortunately for authors, numerical calculation of the mean square radius is not in agreement with experimental result $\langle r^2\rangle = 0.44\ fm^2$ for pion. But we think, that more appropriate form of the wavefunction $\Psi(k)$ should give the desired result.

## ACKNOWLEDGMENTS

This work was supported by grant **N. F96-326 (17.02.97)** from the Foundation for Fundamental Research of Republic Belarus.

# References


[1] N.Nakanichi, Progr. Theor. Phys. Suppl., N43 (1969); E.E.Salpeter, H.A.Bethe, Phys. Rev. **84** , p.232 (1951).

[2] A.A.Logunov, A.N.Tavkhelidze, Nuovo Chimento, **29**, p.380 (1963).

[3] V.G.Kadyshevsky, Nucl.Phys. B, **6** p.125 (1968).

[4] I.T.Todorov, Phys.Rev. D, **10**, p.2351 (1971).

[5] F.Gross , Phys.Rev., **186**, p.1448 (1969); Phys. Rev. D, **10**, p.223 (1974).

[6] B.D.Keister, W.N.Polyzou in Advances in Nuclear Physics, edited J.W.Negele and E.Vogt (Plenum, New York, 1991).

[7] F.M.Lev Annals of Physics **237**, p.355 (1995).

[8] S.Weinberg, Phys.Rev. **150**, p.1313 (1966).

[9] L.L.Frankfurt, M.I.Strikman Phys.Rep., **76**, p.215 (1981).

[10] L.A.Kondratyuk, M.V.Terent'ev Yad.Fiz., **31**, p.1087 (1980).

[11] V.G.Kadyshevsky, Zh. Eksp. Teor. Fiz., **46**, p.654, p.872 (1964); V.G.Kadyshevsky, R.M.Mir-Kasimov, N.B.Skachkov Yad. Fiz., **9**,p.219, p.462 (1969).

[12] V.G.Kadyshevsky, R.M.Mir-Kasimov, N.B.Skachkov Part. Nucl., **2**, p.635 (1972).

[13] R.N.Faustov, Nuovo Cimento.,**69A**, p.37-46, (1970); M.K.Volkov. Part. and Nuclei, **24**, p.81 (1993); T.Ino. Progr. Theor. Phys., **89**, p.895 (1993).

[14] N.V.Maksimenko, S.G.Shulga, Yad. Fiz., **56**, p.201 (1993).

[15] N.V.Maksimenko, L.G.Moroz, In Proc. 2 Intern. School of Young Scientists on High Energy Physics and Relativistic Nucl. Phys., Gomel, 1979. Dubna JINR,D2-11707, p.533-543 1979.

[16] A.I.L'vov, Preprint FIAN. N344, Moscow. 1987.

[17] N.V.Maksimenko, L.G.Moroz, O.M.Deryuzhkova. Proceeding of the Academy of Sciences of Belarus, Phys-math. series, 1995, N4, p.118-122

[18] A.A.Arkhipov,V.I.Savrin, Fiz. Elem. Chast. and Atom. Yad. (Sov. J. Part. Nucl.), **16**. p.1091 (1985).

[19] C.Itzykson, J.B.Zuber. Quantum field theory. Moskow: "Peace", v.1,2. 1984 (In russian).

[20] D.Lurie, A.Macfarlane, Y.Takahashi., Phys. Rev., **140B**, p.1091 (1965).

[21] S.R.Amendolia et. al. , Phys. Lett. , **B178**, p.435 (1986).

[22] Yu.M.Antipov et. al., Z. Phys. ,**C26**. p.495 (1985).

[23] P.A.M. Dirac Rev.Mod.Phys., **21**, p.392 (1949)
[24] H. Leutwyler and J. Stern, Annals of Phys. **112**,94 (1978).
[25] F. Coester and W.N. Polyzou, Phys.Rev. D, **26**,1348, (1982).
[26] W.N. Polyzou, Annals of Physics **193**, p.367 (1989).
[27] F.M.Lev "Forms of Relativistic dynamics, current operators and deep inelastic lepton-nucleon scattering" hep-ph/9505373.
[28] F.M.Lev , Rivista del Nuovo Cimento, **16,** N2 , p.1 (1993)
[29] F.M. Lev " Effect of binding in deep inelastic scattering revisited ", hep-ph/9501348.
[30] Review of Particle Properties, Phys. Rev.D, **50**, p.1271 (1994).
[31] H.Atherton et al. Phys. Lett. B .**158**, p.1 (1985).
[32] W.Jaus Phys.Rev. D, **44**, N.9, p.2851 (1991)
[33] H.Ito, W.W.Buck and F.Gross Phys. Rev.C, **45**, p.1918 (1992)
[34] C.R. Münz, J. Resag, B.C. Metsch and H.R. Petry Phys. Rev. C **52** N.4, p.2110 (1995).

# Poincare-covariant quark model of decay constant in the heavy mass limit

**V.V. Andreev**

*Gomel State University, Gomel, 246699 Belarus*
*E-mail: Andreev@tpf.gsu.gomel.by*

**Introduction.**

The phenomenology of electroweak decays of the hadrons has always been a source of information about the interactions of quarks. Today, electroweak decays of hadrons containing heavy quarks are employed for tests of the Standard Model and measurements of its parameters.

According to the structure of the current interaction, electroweak decays of hadrons can be divided into the following classes: leptonic decays, in which the quarks of the decaying hadron annihilate each other and only leptons appear in the final state; semileptonic decays, in which both leptons and hadrons appear in the final state; photons decays, in which the final state consists of photons only; radiative transitions between hadrons, in which hadrons and photon are caused by hadron decays, non-leptonic decays, in which the final state consists of hadrons only. Over the last decade, a lot of information on hadron decays has been collected in experiments at $e^+e^-$ and hadron colliders. This has led to a rather detailed knowledge of the flavour sector of the Standard Model and many of the parameters associated with it.

In this work the leptonic decay constant of the pseudoscalar mesons is calculated with the use of the relativistic constituent quark model constructed on the point form of Poincare-covariant quantum mechanics. We investigate the decay constant of the mesons with spinor quarks in the heavy mass limit.

## $q\bar{q}$ bound state in the point form of RQM .

There are three forms of the dynamics in the relativistic quantum mechanics (RQM), called "instant","point","light-front" forms [1]. In this work we use point form of the RQM [2]. The description in the point form implies that the generators of the Poincare group $\hat{M}^{\mu\nu}$ are the same as for noninteracting particles and bound systems. Interaction terms can be presented only in the four-momentum operators $\hat{P}_\mu$, but the four-velocities of bound and free-particle systems are equal.

The momenta $\vec{p}_1$, $\vec{p}_2$ of the quarks with the masses $m_1$ and $m_2$ of relativistic system can be transformed to the total $\vec{P}$ and relative momenta $\vec{k}$ to facilitate the separation of the center of mass motion:

$$\vec{P}_{12} = \vec{p}_1 + \vec{p}_2,\ \overrightarrow{k} = \overrightarrow{p_1} + \frac{\overrightarrow{P_{12}}}{M_0}\left(\frac{\left(\overrightarrow{P_{12}}\overrightarrow{p_1}\right)}{\omega_{M_0}\left(\overrightarrow{P_{12}}\right) + M_0} + \omega_{m_1}\left(\overrightarrow{p_1}\right)\right), \qquad (1)$$

where $M_0 = \omega_{m_1}\left(\overrightarrow{k}\right) + \omega_{m_2}\left(\overrightarrow{k}\right), \omega_{m_1}\left(\overrightarrow{p_1}\right) = \sqrt{\overrightarrow{p_1}^2 + m_1^2}$.

The solution of the eigenvalue problem will lead to eigenfunction of the form

$$_0\left\langle \vec{V}_{12}\mu, [J\,k], (ls) \middle| \vec{V}\mu, [J\,M] \right\rangle =$$

$$= \left(\frac{M}{M_0}\right)^{3/2} \delta_{JJ'}\delta_{\mu\mu'}\delta(\vec{V} - \vec{V}_{12})\Psi^{J\mu}(k\,l\,s\,;M) \qquad (2)$$

with the velocities $\vec{V} = \vec{P}/M$ and $\vec{V}_{12} = \vec{P}_{12}/M_0$ of bound and noninteracting systems respectively. The function $\Psi^{J\mu}(k l s\,;M)$ satisfies in the point form the following equation [4]:

$$\sum_{l's'} \int_0^\infty < k\,l\,s \parallel W^J \parallel k'\,l'\,s' > \Psi^J(k'\,l'\,s';\,M)k'^2dk' +$$

$$+ k^2\Psi^J(k\,l\,s;M) = \eta\Psi^J(k\,l\,s;M) \qquad (3)$$

with reduced matrix element of operator $\hat{W}$.

In the point form the meson state is defined as the state of on-shell quark and antiquark with the wave function $\Psi^{J\mu}(k\,l\,s\,;M)$

$$\left|\overrightarrow{P}\mu\,[JM]\right\rangle = \sqrt{\frac{M}{\omega_M\left(\overrightarrow{P}\right)}} \sum_{ls\lambda_1\lambda_2} \int d^3k \sqrt{\frac{\omega_{m_1}\left(\overrightarrow{p_1}\right)\omega_{m_2}\left(\overrightarrow{p_2}\right)}{\omega_{m_1}\left(\overrightarrow{k}\right)\omega_{m_2}\left(\overrightarrow{k}\right)}}\Psi^{J\mu}(kls;M)$$

$$\sum_{m\lambda}\sum_{\nu_1\nu_2} \langle s_1\nu_1, s_2\nu_2|\, s\lambda\rangle \langle lm, s\lambda|\, J\mu\rangle\, Y_{lm}(\theta,\phi)$$

$$D^{1/2}_{\lambda_1\nu_1}\left(\overrightarrow{n}\,(p_1,P)\right) D^{1/2}_{\lambda_2\nu_2}\left(\overrightarrow{n}\,(p_2,P)\right) |p_1\lambda_1\rangle\,|p_2\lambda_2\rangle \qquad (4)$$

where $\langle s_1\nu_1, s_2\nu_2|\, s\lambda\rangle$, $\langle lm, s\lambda|\, J\mu\rangle$ are Clebsh-Gordan coefficients of $SU(2)$-group, $Y_{lm}(\theta,\phi)$ - spherical harmonic with spherical angle of $\vec{k}$.

Also, in Eq.(4 ) $D^{1/2}\left(\overrightarrow{n}\right) = 1 - i\left(\overrightarrow{n}\,\overrightarrow{\sigma}\right)/\sqrt{1+\overrightarrow{n}^2}$ is $D$ -function of Wigner rotation, which is determined by vector-parameter $\overrightarrow{n}(p_1,p_2) = \overrightarrow{u_1}\times\overrightarrow{u_2}/(1-\left(\overrightarrow{u_1}\overrightarrow{u_2}\right))$ with $\overrightarrow{u} = \overrightarrow{p}/\left(\omega_m\left(\overrightarrow{p}\right)+m\right)$.

**Leptonic decay constant.**

The leptonic decay constant for pseudoscalar meson is defined by

$$\left\langle 0\left|\hat{J}^{\mu}(0)\right|\overrightarrow{P},M\right\rangle = i\,(1/2\pi)^{3/2}\frac{1}{\sqrt{2\omega_M\left(\overrightarrow{P}\right)}}P^{\mu}f_p, \qquad (5)$$

where $\hat{J}^{\mu}(0)$ is the operator of axial-vector part of the charged weak current. Using Eq.(4) and Eq.(5) we found in the point form dynamics, that [5]

$$f_p = \frac{N_c}{\pi\sqrt{2M}}\int_0^{\infty} dk\,k^2\sqrt{\frac{M_0^2-(m_1-m_2)^2}{\omega_{m_1}\left(\overrightarrow{k}\right)\omega_{m_2}\left(\overrightarrow{k}\right)}} * \frac{(m_1+m_2)}{M_0}\Psi\,(k,M)\,, \qquad (6)$$

where $N_c$ is the number of colors, $m_1$ and $m_2$ are the respective masses of two quarks. The wave function for pseudoscalar meson has the normalization

$$\int_0^{\infty} dk\,k^2\,N_c\,|\Psi\,(k,M)|^2 = 1.$$

When $m_1 = m_2 = m_Q$, the leptonic decay constant is defined by

$$f_p = \frac{2N_c\sqrt{2}m_Q}{\pi\sqrt{M}}\int_0^{\infty}\frac{dk\,k^2\Psi\,(k,M)}{\omega_{m_Q}\left(\overrightarrow{k}\right)}. \qquad (7)$$

The equation for the bound $q\bar{q}$ states (3) in the RQM is relativistic equation with effective potential $W$. However, it is hard problem to obtain wave function $\Psi(k,M)$ as solution of this equation. Therefore, we use simple model of wave function depending on length scale parameter $1/\beta$:

$$\Psi(k\,,M) \equiv \Psi(k\,,\beta) = 2/(\sqrt{N_c}\beta^{3/2}\pi^{1/4})exp(-\frac{k^2}{2\beta^2}). \qquad (8)$$

Using the equations (7) and (8), one can see that

$$f_p = \frac{2\sqrt{2N_c}m_Q}{\pi^{5/4}\sqrt{M}\beta^{3/2}}\int_0^\infty \frac{dkk^2}{\omega_{m_Q}\left(\overrightarrow{k}\right)} exp(-\frac{k^2}{2\beta^2}) =$$

$$= \frac{\sqrt{2N_c}\beta^{3/2}}{\pi^{3/4}\sqrt{M}V} U\left(\frac{1}{2}, 0, \frac{1}{2V^2}\right) \tag{9}$$

with $V = \beta/m_Q$ and Kummer's hypergeometric function $U\left(\frac{1}{2}, 0, z\right)$.

We now consider the heavy mass limit of (6). This limit is defined as $m_1, m_2 \longrightarrow \infty$, $V = P/M$ is fixed. The starting point in the construction of the effective theory with the heavy quarks (HQET) is the observation that a heavy quark bound inside a hadron moves more or less with the hadron's velocity $V$. Its momentum can be written as

$$p_Q = m_Q V + \tilde{k}, \tag{10}$$

where the components of so-called residual momentum $\tilde{k}$ are much smaller than $m_Q$. Interactions of the heavy quark with light degrees of freedom change the residual momentum by an amount of order $\tilde{k} \sim \Lambda_{QCD} \simeq 1/R_{Hadron}$, but the corresponding changes in the heavy-quark velocity vanish as $\Lambda_{QCD}/m_Q \longrightarrow 0$. In the center of mass system we obtain, that relative momentum $\overrightarrow{k}$ (1) and residual momentum $\overrightarrow{\tilde{k}}$ are equal and therefore, the heavy mass limit in the point form is given by

$$\left|\overrightarrow{k}\right| \leq \Lambda_{QCD} \ll m_Q. \tag{11}$$

The nonrelativistic variant furnishes the following relation for leptonic decay constant (6):

$$f_{nonrel} = \frac{N_c\sqrt{2}}{\pi\sqrt{M}}\int_0^{\Lambda_{QCD}} dk\, k^2(1 - \frac{k^2}{2m_Q^2} + \frac{3k^4}{8m_Q^4})\Psi_{nonrel}\,(k, M)\,, \tag{12}$$

where $\Psi_{nonrel}\,(k, M)$ is normalized as

$$\int_0^{\Lambda_{QCD}} dk\, k^2\, N_c\, |\Psi_{nonrel}\,(k, M)|^2 = 1.$$

The parameter $\beta$ can be estimated with mean square radius (MSR) $\langle r^2 \rangle_{nonrel} = 1/\Lambda^2_{QCD}$ of the meson with the heavy quarks. In the nonrelativistic approximation the MSR is $\langle r^2 \rangle_{nonrel} = 3/8\beta^2$ and we obtain the relationship between $\beta$ and $\Lambda_{QCD}$:

$$\Lambda_{QCD} = \sqrt{\frac{8}{3}}\beta. \tag{13}$$

The nonrelativistic wave function can be chosen in the form:

$$\Psi_{nonrel}(k, M) \sim \Psi(k, M) \sim exp(-\frac{k^2}{2\beta^2}), \tag{14}$$

since the model wave function (8) does not have the small parameter $\Lambda_{QCD}/m_Q$ (or $V = \beta/m_Q$).Using (12),(13) and ( 14) we obtain the following result for $f_{nonrel}$:

$$f_{nonrel} \approx \frac{\sqrt{N_c}\beta^{3/2}}{\sqrt{M}}(1.02 - 0.69V^2 + 0.89V^4). \tag{15}$$

Let us discuss briefly the role of relativistic corrections in leptonic decay constant of pseudoscalar meson with heavy quarks. This effect can be extracted easily. Using asymptotic limit for Kummer's function ($1/V \longrightarrow \infty$) we found, that decay constant (9) can be written as

$$\begin{aligned} f_p &\approx \frac{2\sqrt{N_c}\beta^{3/2}}{\pi^{3/4}\sqrt{M}}\left(1 - \frac{3}{2}V^2 + \frac{45}{8}V^4\right) \\ &\approx \frac{\sqrt{N_c}\beta^{3/2}}{\sqrt{M}}(0.85 - 1.27V^2 + 4.77V^4). \end{aligned} \tag{16}$$

When the serieses (16) and (15) are compared, it is apparent that their second and third terms diverge. Namely these terms are relativistic corrections for heavy-quark effective theory. If it is granted that the parameter $\Lambda_{QCD} = a\beta$ with $a = \sqrt{2}$ then the first terms of series are approximately equal, i.e.

$$f_{nonrel} \approx \frac{\sqrt{N_c}\beta^{3/2}}{\sqrt{M}}(0.84 - 0.45V^2 + 0.45V^4), \tag{17}$$

but the next terms diverge considerably. Based on this model analysis of decay constants we formulated a supposition, that large momentum

(relativistic effects) are of great importance in power corrections in the heavy mass limit.


## ACKNOWLEDGMENTS

This work was supported by grant **N. F96-326 (17.02.97)** of the Foundation for Fundamental Research of Republic Belarus.


# References


[1] P.A.M. Dirac Rev.Mod.Phys., **21**, p.392 (1949)

[2] F.Gross Phys.Rev., **186**, p.1448 (1969); Phys. Rev. D, **10**, p.223 (1974). F.M.Lev "Forms of relativistic dynamics, current operators and deep inelastic lepton-nucleon scattering" hep-ph/9505373.

[3] F. Coester and W.N. Polyzou, Phys.Rev. D, **26**,1348, (1982).

[4] W.N. Polyzou, Annals of Physics **193**, p.367 (1989).B.D.Keister, W.N.Polyzou in Advances in Nuclear Physics, edited J.W.Negele and E.Vogt (Plenum, New York, 1991).

[5] V.V. Andreev Proc. 3-d Annual Seminar NPCS'94. Editors V.I.Kuvshinov&G.Krylov,Minsk 1995.P.141-145.

# The electromagnetic characteristics of pions in the diagram quark model

**O.M.Deryuzhkova, N.V.Maksimenko.**

*Skaryna University, Sovietskaya Str., 104, 246699, Gomel, Belarus*

The effective phenomenological action function of the electromagnetic field interaction with the structural particle has been obtained on the basis of general requirements of the relativistic quantum theory. It is determined by the electromagnetic structural parameters of the hadrons. Using the method of functional integration the electromagnetic characteristics of $\pi$-meson are calculated in the diagram quark model.

Last years an accuracy of measurements of the hadron electromagnetic characteristics has been improved considerably. This fact permits to analyse more profoundly the field-theoretical and model conceptions of hadrons interaction with an electromagnetic field.

In the present work the electrical polarizability and $\langle r^2 \rangle$ of $\pi$-meson are calculated within the diagram quark model.

The effective Lagrangians of the electromagnetic field interaction with structural particles of the spin 0, 1/2, 1 are obtained in refs [1] - [4] . For hadrons of zero spin it is represented as a covariant expansion in terms of tensor of the electromagnetic field $F_{\mu\nu}$ and potential $A_\mu$:

$$L_{eff} \doteq \frac{1}{8M^2}[(\partial_\mu\varphi^+)(\partial_\nu\varphi) + (\partial_\mu\varphi)(\partial_\nu\varphi^+) - (\varphi^+\partial_\mu\partial_\nu\varphi + \varphi\partial_\mu\partial_\nu\varphi^+)]*$$

$$* [(\alpha + \beta)F^{\mu\sigma}F^{\nu}_{\sigma} - \frac{1}{2}\beta g_{\mu\nu}F^{\rho\sigma}] + e^2A^2_\mu\varphi^+\varphi + ie[\varphi^+ \overleftrightarrow{\partial}_\mu \varphi]A^\mu, \qquad (1)$$

where $\varphi$ is the field function of the scalar charged structural particle, $\alpha$ and $\beta$ are the $\pi$-meson polarizabilities. The expansion constants are the electromagnetic characteristics of the hadrons.

Let us consider a generating functional

$$exp(iS_{eff}) = Z(A). \qquad (2)$$

For calculation $S_{eff}$ in (2) we have restricted to the diagram model with two pion-quark vertexes. For definition of $\langle r^2 \rangle$ and the pion-quark coupling constant $g$ we shall consider the matrix element of the current (Fig. 1).

$$g^2 = \frac{8\pi^2 M}{\frac{2m^2}{M\beta}atan\frac{M}{2\beta} - 1},$$

$$\langle r^2\rangle = \frac{1}{8\beta^2 M^2}\,\frac{M^2 + \frac{M^4+48\beta^4}{2M\beta}atan\frac{M}{2\beta} - 12\beta^2}{\frac{2m^2}{M\beta}atan\frac{M}{2\beta} - 1}, \tag{3}$$

where $\beta = \sqrt{m^2 - \frac{M^2}{4}}$, $m$ is the constituent quark mass.

It follows from (3), when the binding energy is small (the compound system is non-relativistic)

$$\langle r^2\rangle \sim \frac{1}{8\beta^2}, \tag{4}$$

and when the binding energy is high (the compound system is relativistic)

$$\langle r^2\rangle \sim \frac{0.3}{m^2}. \tag{5}$$

Let us consider $iS_{eff}$ in the diagram model with two pion-quark vertexes and restrict to the second order of the field $A_\mu$. Then we obtain

$$iS_{eff} = -\frac{1}{2}g^2\{(\varphi^+(x_1)\Delta^{(2)}(x_1,x_2)\varphi(x_2)\Delta^{(0)}(x_2,x_1)+$$

$$+\varphi^+(x_1)\Delta^{(0)}(x_1,x_2)\varphi(x_2)\Delta^{(2)}(x_2,x_1)+$$

$$+\varphi^+(x_1)\Delta^{(1)}(x_1,x_2)\varphi(x_2)\Delta^{(1)}(x_2,x_1))\}. \tag{6}$$

Here $\Delta^{(0)}$, $\Delta^{(1)}$, $\Delta^{(2)}$ are the propagators of the scalar quarks and they are as follows

$$\Delta_0(x,y) = \frac{1}{(2\pi)^4}\int dq\frac{e^{-iq(x-y)}}{q^2-m^2},$$

$$\Delta^{(1)}(x,y) = \left\langle \Delta^{(0)}(x,x')\, j_\mu(x')\,\Delta^{(0)}(x',y)\, A^\mu(x')\right\rangle, \tag{7}$$

$$\Delta^{(2)}(x,y) = -e^2\left\langle \Delta^{(0)}(x,x')\,\Delta^{(0)}(x',y)\, A^2(x')\right\rangle +$$

$$+\left\langle \Delta^{(0)}(x,x')\, j_\mu(x')\, A^\mu(x')\,\Delta^{(0)}(x',x'')\, j_\nu(x'')\, A^\nu(x'')\,\Delta^{(0)}(x'',y)\right\rangle,$$

where $j_\mu(x)$ is the scalar quark current.

Let us consider the action (6) in the case when $\pi$-meson interacts with the constant electric field

$$A^\mu(k) = \{(-i)(2\pi)^4\delta(k_0)(\vec{E}\vec{\partial}_k)\delta(\vec{k}),\vec{O}\}.$$

Using (7) we can rewrite (6) in the form

$$iS_{eff} = \frac{(-1)e^2g^2}{2[(2\pi)^4]^2}\langle\delta(p_1-p_2)\varphi^+(p_2)\varphi(p_1)[f_1+f_2+f_3]\rangle, \tag{8}$$

where

$$f_1 = (E_i E_j)\left[\frac{(-2)\,\delta_{ij}}{D^3(q_1')\,D(q)} - \frac{8q_{1i}'q_{1j}'}{D^4(q_1')\,D(q)}\right],$$

$$f_2 = (E_i E_j)(-8)\left[\frac{\delta_{ij}\,(q_{10}')^2}{D^4(q_1')\,D(q)} + \frac{6\,(q_{10}')^2\,q_{1i}'q_{1j}'}{D^5(q_1')\,D(q)}\right],$$

$$f_3 = (E_i E_j)\,\frac{16q_0q_jq_{10}'q_{1i}'}{D^3(q_1')\,D^3(q)}.$$

In the equation (8) the brackets mean the integration with respect to $p_1, p_2$ and $q$ variables, $D(q) = q^2 - m^2$, $q_1' = q + p^2$.

Note that the action (8) contains the contribution of the diagrams in Fig.2. It can be calculated using the method of dimensional regularization.

For the action (8) we obtain

$$iS_{eff} = \left(\frac{e^2g^2\vec{E}^2}{2\left[(2\pi)^4\right]^2}\right)\left(\frac{4i\pi^2}{M^4}\right)\langle\delta(p_1 - p_2)\,\varphi^+(p_2)\,\varphi(p_1) * .$$

$$* \int_0^1 dx\{(\hat{Q}^2 + \hat{\bar{Q}}^2)\frac{\frac{1}{4}x^2 - \frac{1}{3}x^3 + \frac{1}{8}x^4}{[x(1-x) - \eta^2]^2} - \hat{Q}\hat{\bar{Q}}\frac{\frac{1}{4}x^2(1-x)^2}{[x(1-x) - \eta^2]^2} -$$

$$-(\hat{Q}^2 + \hat{\bar{Q}}^2)\frac{x^3(1-x)^2(\frac{2}{3} - \frac{1}{2}x)}{[x(1-x) - \eta^2]^3} + \hat{Q}\hat{\bar{Q}}\frac{x^3(1-x)^3}{[x(1-x) - \eta^2]^3}\}\rangle, \qquad (9)$$

where $\hat{Q}$ and $\hat{\bar{Q}}$ are the values of quark and antiquark charges, $\eta = \frac{m}{M}$. In the case when the binding energy is high (the compound system is relativistic) the electrical polarizability has been obtained using (1) and (9)

$$\alpha = \frac{96\pi}{137}\frac{1}{m^2M}\{(\hat{Q}^2 + \hat{\bar{Q}}^2)(\frac{1}{40} + \frac{2}{315\eta^2}) - (\hat{Q}\hat{\bar{Q}})(\frac{1}{120} + \frac{1}{140\eta^2})\}. \qquad (10)$$

The numerical estimations of (9), when $m = 500MeV$ and $M = 140MeV$ are consistent with the experiment

$$\alpha_{exp} = (6.8 \pm 1.4)\cdot 10^{-43}cm^3\ [5]\ .$$

In the case, when the binding energy is high, the value $\alpha$ agrees with the experiment, when $m = 700MeV$ and $M = 140MeV$.

The numerical estimations of $\langle r^2\rangle$ (see (3)) are in agreement with the experiment [6] , when $m = 210MeV$ and $M = 140MeV$.

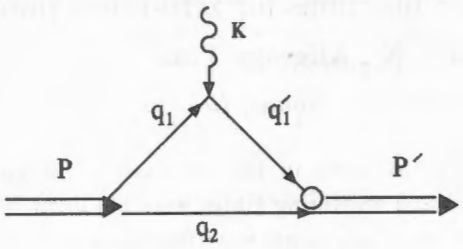


Figure 1: The diagram for definition of the matrix element of the current.

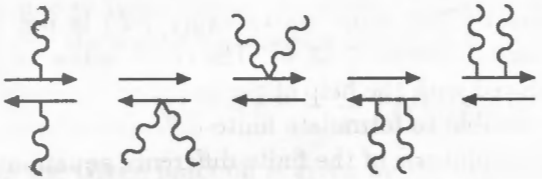

Figure 2:

# References

[1] G.Feinberg, J.Sucher.// Phys. Rev. 1970. V.A2. P.2395.
[2] N.V.Maksimenko, L.G.Moroz.// In Proc. 2 Intern. Scool of Young Scientists on High Energy Physics and Relativistic Nucl. Phys., Gomel, 1997. Dubna: JINR. D2-11707. 1979. P.533.
[3] A.I.L'vov. Phenomenon of electric and magnetic polarizability of particles in relativistic theory: Preprint FIAN. N344. Moscow. 1987.
[4] N.V.Maksimenko.// Rep. of Acad. of Sciences of Byelorussia. 1992. V.36. P.508.
[5] Yu.M.Antipov et. al.// Z. Phys. 1985. V.C26. P.495.
[6] S.R.Amendolia et. al.// Phys. Lett. 1986. V.B178. P.435.

# Green functions in the relativistic configurational representation and wave functions for zero-range potential

**Kapshai V.N., Alferova T.A.**

*Skaryna University, Gomel, Belarus*

The explicit forms of Green functions in the relativistic configurational representation (RCR) for bound and scattering states were obtained. For zero-range potential $V(r) = -V_0\delta(r)$ one-dimensional wave functions of bound states with the quantum conditions and the wave functions of scattering states with the reflection and penetration coefficients were found.

In the momentum representation the quasipotential equations [1, 2] are analogous to the nonrelativistic Lippman-Schwinger and Schrödinger integral equation (IE). It is well known that in the nonrelativistic theory solution of the Schrödinger equation can be found well in the coordinate representation, not in the momentum one. In the coordinate representation this equation is differential. However for the relativistic equations the Fourier analysis with nonrelativistic plane waves $\exp(i\ \vec{p}\vec{x})$ is not too useful, since equations become differential [3, 4]. The construction of the RCR [5, 6], which is introduced with the help of the harmonic analysis on the Lorentz group, makes possible to formulate finite-difference equations for a wave function. However solutions of the finite-difference equations in the general case could be found within "$i$ - periodical constants". There is a possibility to preserve the attractive construction of the RCR with its physically evident behavior of local potentials $V(r)$ and wave functions $\Psi_{\vec{q}}(\vec{r})$, and at the same time to get rid from the ambiguity of solutions, that is to formulate IE in the RCR [7].

Constructing of IE in the RCR makes possible to examine zero radius potentials, that are videly used in the nonrelativistic theory [8-10]. The exact solutions of the differential Schrödinger equation with $\delta$- potentials [9, 10] have received the most study. In this connection it is interesting to take a further look at the relativistic equations with this potentials. It is obvious that studying the difference equations with the $\delta$-potentials is difficult since it is impossible to formulate their boundary conditions similar to quantum-mechanical boundary conditions for differential equations. And IE in the RCR, on the contrary, are well suited for the study $\delta$-potentials. In the present paper with the help of the IE explicit fomrs we obtain the spectrum, the wave functions of bound states and wave functions

of scattering states with the reflection and penetration coefficients.

For simplicity's sake in this paper we will consider the one-dimensional equations, begining with the nonrelativistic IE. For bound states with the energy $E_{nr} < 0$ the IE in the coordinate space can be written in the form

$$\Psi(x) = -\frac{m}{\pi} \int G(w; x, y) V(y) \Psi(y) \, dy, \tag{1}$$

where $w^2 = -2mE$, and Green function

$$G(w; x, y) = \int \frac{e^{ip(x-y)}}{p^2 + w^2} dp = \frac{\pi}{w} e^{-w|x-y|}. \tag{2}$$

For the potential $V(x) = -V_0 \delta(x)$ from (1) we obtain

$$\Psi(x) = \frac{mV_0}{w} \Psi(0) \, e^{-w|x|}. \tag{3}$$

The quantum condition $E = -mV_0^2/2$ follows from (3), and the constant $\Psi(0)$ is defined from the normalization condition. Note here, while the parameter $V_0$ increases, the energy $E$ decreases beyond all bounds.

For the scattering states with $E_{nr} > 0$ the equation takes the form

$$\Psi(x) = e^{iqx} - \frac{m}{\pi} \int G(q; x, y) V(y) \Psi(y) \, dy, \tag{4}$$

and the Green function is given by the expression

$$G(q; x, y) = \int \frac{e^{ip(x-y)}}{p^2 - q^2 - i0} dp = \frac{\pi i}{q} e^{iq|x-y|}. \tag{5}$$

The wave function in case of the potential $V(x) = -V_0 \delta(x)$ is

$$\Psi(x) = e^{iqx} + Be^{iq|x|}; \quad B = \frac{imV_0}{q - imV_0}. \tag{6}$$

The reflection and penetration coefficients are

$$R = |B|^2 = \frac{m^2 V_0^2}{q^2 + m^2 V_0^2}; \quad P = |A|^2 = |1 + B|^2 = \frac{q^2}{q^2 + m^2 V_0^2}.$$

And now let us turn our attention to the relativistic equations in the RCR for the bound states when $E = m \cos x < m$ $(0 < x < \frac{\pi}{2})$:

$$\Psi_i(r) = -\int g_i(x; r, r') V(r') \Psi_i(r') \, dr'. \tag{7}$$

The explicit forms of Green functions for different quasipotential equations [11] are following

$$g_1\left(x;r,r'\right)=\int\frac{e^{i\chi\left(r-r'\right)}}{\cosh^2\chi-\cos^2 x}d\chi=\frac{2\pi}{\sin 2x}\cdot\frac{\sinh\left[\left(r-r'\right)\left(\frac{\pi}{2}-x\right)\right]}{\sinh\left(\frac{\pi}{2}r-\frac{\pi}{2}r'\right)}, \tag{8}$$

$$g_2\left(x;r,r'\right)=\int\frac{e^{i\chi\left(r-r'\right)}}{\cosh\chi\left(\cosh\chi-\cos x\right)}d\chi=$$

$$=\frac{2\pi}{\sin 2x}\cdot\left[\frac{2\sinh\left[\left(r-r'\right)\left(\pi-x\right)\right]}{\sinh\left(\pi r-\pi r'\right)}-\frac{\sin x}{\cosh\left(\frac{\pi}{2}r-\frac{\pi}{2}r'\right)}\right], \tag{9}$$

$$g_3\left(x;r,r'\right)=\int\frac{e^{i\chi\left(r-r'\right)}\cosh\chi}{\cosh^2\chi-\cos^2 x}d\chi=\frac{\pi}{\sin x}\frac{\cosh\left[\left(r-r'\right)\left(\frac{\pi}{2}-x\right)\right]}{\cosh\left(\frac{\pi}{2}r-\frac{\pi}{2}r'\right)}, \tag{10}$$

$$g_4\left(x;r,r'\right)=\int\frac{e^{i\chi\left(r-r'\right)}}{\cosh\chi-\cos x}d\chi=\frac{2\pi}{\sin x}\frac{\sinh\left[\left(r-r'\right)\left(\pi-x\right)\right]}{\sinh\left(\pi r-\pi r'\right)}. \tag{11}$$

Solutions of the equations (7) with the Green functions (8)-(11) for the potential $V(r)=-V_0\delta(r)$ can be found in the following form:

$$\Psi_i(r)=V_0 g_i(x;r,0)\Psi_i(0). \tag{12}$$

The quantum conditions are definited from (12) when $r=0$:

$$V_0 g_i(x;0,0)=\lim_{r\to 0}V_0 g_i(x;r,0)=1. \tag{13}$$

Their explicit forms:

$$1)\ \frac{4V_0\left(\frac{\pi}{2}-x\right)}{\sin 2x}=1;\quad 2)\ \frac{4V_0\left(\pi-x\right)}{\sin 2x+2\pi V_0\sin x}=1, \tag{14}$$

$$3)\ \frac{\pi V_0}{\sin x}=1;\quad 4)\ \frac{2V_0\left(\pi-x\right)}{\sin x}=1. \tag{15}$$

In these cases, when $V_0$ increases, the parameter $x$ increases monotonously, and the energy $E=m\cosh x$ decreases monotonously. When $V_0$ ranges up to a critical value $V_0^{cr}$ the energy $E$ is equal to zero. If the parameter $V_0$

goes on to increase then the energy level disappears. There is this effect for four our equations, and

$$V_{01}^{cr} = V_{02}^{cr} = 1/2; \quad V_{03}^{cr} = V_{04}^{cr} = 1/\pi.$$

The curves for the potential parameter $V_0$ as a function of energy parameter $x$ are given in Fig.1

Let us consider the nonhomogeneous integral equations in the RCR for the scattering states with $E = m\cosh b > m$:

$$\Psi_i(r) = e^{ixr} - \int g_i(b; r, r')\, V(r')\, \Psi_i(r')\, dr'. \tag{16}$$

The associated Green functions of continuous spectrum are

$$g_1(b; r, r') = \int \frac{e^{ix(r-r')}}{(\cosh\chi - i0)^2 - \cosh^2 b} d\chi = \frac{2i\pi}{\sinh 2b} \frac{\sinh\left[\left(r-r'\right)\left(\frac{\pi}{2}+ib\right)\right]}{\sinh\left(\frac{\pi}{2}r - \frac{\pi}{2}r'\right)}, \tag{17}$$

$$g_2(b; r, r') = \int \frac{e^{ix\left(r-r'\right)}}{\cosh\chi\,(\cosh\chi - \cosh b - i0)} d\chi =$$

$$= \frac{2\pi}{\sinh 2b}\left[\frac{2i\sinh\left[\left(r-r'\right)(\pi+ib)\right]}{\sinh\left(\pi r - \pi r'\right)} - \frac{\sinh b}{\cosh\left(\frac{\pi}{2}r - \frac{\pi}{2}r'\right)}\right], \tag{18}$$

$$g_3\left(b; r, r'\right) = \int \frac{e^{ix\left(r-r'\right)}\cosh\chi}{(\cosh\chi - i0)^2 - \cosh^2 b} d\chi = \frac{i\pi}{\sinh b} \frac{\cosh\left[\left(r-r'\right)\left(\frac{\pi}{2}+ib\right)\right]}{\cosh\left(\frac{\pi}{2}r - \frac{\pi}{2}r'\right)}, \tag{19}$$

$$g_4\left(b; r, r'\right) = \int \frac{e^{ix\left(r-r'\right)}}{\cosh\chi - \cosh b - i0} d\chi = \frac{2i\pi}{\sinh b} \frac{\sinh\left[\left(r-r'\right)(\pi+ib)\right]}{\sinh\left(\pi r - \pi r'\right)}. \tag{20}$$

For the potential $V(r) = -V_0\delta(r)$ the solutions of equations (16) have the form

$$\Psi_i(r) = e^{ibr} + \frac{V_0}{1 - V_0 g_i(b; 0, 0)} g_i(b; r, 0). \tag{21}$$

For example, for the wave function $\Psi_1(0)$ we have the following expression:

$$\Psi_1(r) = e^{ibr} + B_1 \cdot \frac{\sinh\left(\frac{\pi}{2}r + ibr\right)}{\sinh\left(\frac{\pi}{2}r\right)} =$$

$$=: e^{ibr} + \frac{B_1}{2}(1 + \coth\frac{\pi}{2}r)e^{ibr} + \frac{B_1}{2}(1 - \coth\frac{\pi}{2}r)e^{ibr}, \qquad (22)$$

where

$$B_1 = \frac{2i\pi V_0}{\sinh 2b + 4bV_0 - i2\pi V_0}. \qquad (23)$$

By analogy, we obtain the explicit forms for $\Psi_{2,3,4}(r)$ and in all our cases there are the following asymptotic formulae

$$\Psi_i(r) \;_{r\to-\infty}= e^{ibr} + B_i e^{-ibr}; \quad \Psi_i(r)\,|_{r\to\infty}= e^{ibr}(1 + B_i), \qquad (24)$$

where

$$B_2 = \frac{i4\pi V_0}{\sinh 2b + 2\pi V_0 \sinh b + 4bV_0 - i4\pi V_0};$$

$$B_3 = \frac{i\pi V_0}{\sinh b - i\pi V_0}; \quad B_4 = \frac{2i\pi V_0}{\sinh b + 2bV_0 - 2i\pi V_0}. \qquad (25)$$

From the asymptotic expressions for $\Psi_i(r)$ (24) we define the reflection and penetration coefficients

$$R_i = |B_i|^2, P_i = |1 + B_i|^2. \qquad (26)$$

It is not difficult to see that in all cases there is the relation

$$R_i + P_i = |B_i|^2 + |1 + B_i|^2 \equiv 1.$$

The curves for the reflection coefficients as a function of rapidity $b$ ($E = m\cosh b$) are given in Fig.2. The reflection coefficient $R_1$ as a function of $b$ when parameter $V_0$ is positive is given in Fig.3, when parameter $V_0$ is negative it is given in Fig.4.

# References


[1] A.A.Logunov, A.N.Tavkhelidze// Nuovo Cimento. 1963. V.29. P.380.

[2] V.G.Kadyshevsky // Nucl.Phys. 1968. V.B6. N1. P.125.

[3] O.A.Khrustalev // Preprint IHEP 69-24. Serpukhov. 1969.

[4] A.A.Arhipov, V.I.Savrin// Preprint IHEP 82-21. Serpukhov. 1982.

[5] V.G.Kadyshevsky, R.M.Mir-Kasimov, N.B.Skachkov// Nuovo Cimento. 1968. V.55A. N2. P.233.

[6] V.G.Kadyshevsky, R.M.Mir-Kasimov, N.B.Skachkov// Sov. Journ. Part. and Nucl. 1972. V.2. N.3 P.638.

[7] V.N.Kapshai, N.B.Skachkov // Sov. Journ. Theor. Math. Phys. 1983. V.55. N1. P.26.

[8] A.I.Baz', Y.B.Zeldovich, A.M.Perelomov. Scattering, Reactions and Decay in Nonrelativistic Quantum Mechanic (In Russian). Moskva. Nauka. 1971.

[9] Y.N.Demkov, V.N.Ostrovskii. The Use of Zero-range Potentials in atomic Physics (In Russian). Moskva. Nauka. 1975.

[10] S.Alberio, F.Gesztesy, R.Hoegh-Krohn, H.Nolden. Solvable Models in Quantum Mechanics Springer-Verlag. New-York. 1988.

[11] V.N.Kapshai, T.A.Alferova // In: "Covariant methods in theoretical physics". Minsk. IPh ANB. 1997.

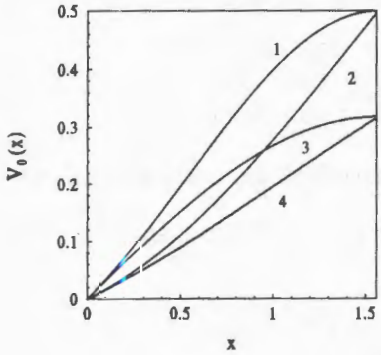


Fig.1

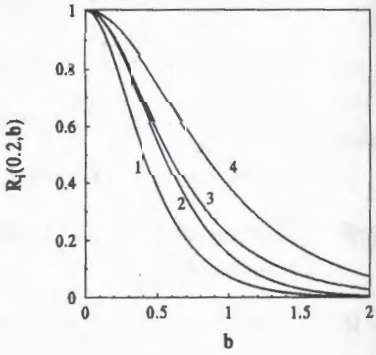


Fig.2

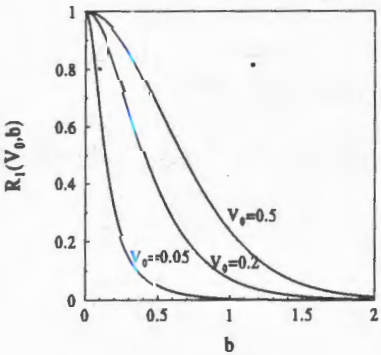


Fig.3

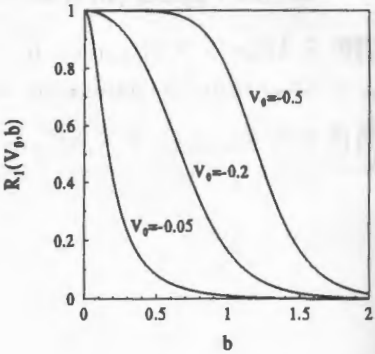


Fig.4

## List of participants

| First name, Family name | Institution, Country | E-mail |
|---|---|---|
| Tatyana Alferova | GSU Belarus | root@tpf.gsu.gomel.by |
| Viktor Andreev | GSU Belarus | root@tpf.gsu.gomel.by |
| Tamara Andreeva | GSU Belarus | root@tpf.gsu.gomel.by |
| Akram Artykov | JINR, Russia | akram@nusun.jinr.ru |
| Sergey Avakyan | GPI Belarus | avakyan@ gpi.gomel.by |
| Alexander Babich | GPI Belarus | babich@gpi.gomel.by |
| Natalia Babich | GPI Belarus | babich@gpi.gomel.by |
| Dmitry Bandurin | JINR, Russia | dmv@cv.jinr.ru |
| David Barney | CERN | David.Barney@cern.ch |
| Alfred Bartl | Vienna Univ. Austria | bartl@pap.univie.ac.at |
| Walter Bartl | IHEP Austria | Walter.Bartl@oeaw.ac.at |
| Vladimir Baryshevsky | INP BSU Belarus | bar@inp.belpak.minsk.by |
| Helmut Boettcher | DESY Germany | hboett@ifh.de |
| Andrey Bogush | IP NAS Belarus | bogush@dragon.bas-net.by |
| Nicholas Brook | Glasgow Univ. GB | brook@v2.ph.gla.ac.uk |
| Valery Burov | JINR, Russia | burov@thsun1.jinr.dubna.su |
| Sergey Chatrchan | JINR, Russia | chatrch@cv.jinr.ru |
| Sergey Chekanov | IP NAS Belarus<br>HEFIN Univ. of Nijmegen | sergei@hef.kun.nl |
| Natalia Chekhlova | NC PHEP Belarus | cheh@hep.by |
| Sergey Cherkas | INP BSU Belarus | cherkas@inp.belpak.minsk.by |
| Yuri Chernichenko | GPI Belarus | chernich@gpi.gomel.by |
| Dmitry Demin | JINR, Russia | demin@nusun.jinr.ru |
| Oksana Deryuzhkova | GSU Belarus | root@tpf.gsu.gomel.by |
| Evgeny Dey | GSU Belarus | root@tpf.gsu.gomel.by |
| Tatyana Donskova | JINR, Russia | donskova@ypr.jinr.dubna.su |
| Valery D'yachenko | JINR, Russia | dyachenko@lhe.jinr.ru |
| Sergey Dymov | JINR, Russia | dymov@nusun.jinr.ru |
| Ilias Efthymiopoulos | CERN | i.efthymiopoulos@cern.ch |
| Mikhail Galynsky | IP NAS Belarus | galynski@dragon.bas-net.by |
| Batmunh Ganhuyag | JINR, Russia | gana@sunhe.jinr.ru |
| Valentin Gilewsky | IP NAS Belarus | gilewsky@dragon.bas-net.by |
| Georgy Gogiberidze | JINR, Russia | goga@sunse.jinr.ru |
| Vladimir Gritsev | IP NAS Belarus | lfve@dragon.bas-net.by |
| Alexander Ilyichev | NC PHEP Belarus | ily@hep.by |
| Valery Kapshay | GSU Belarus | root@tpf.gsu.gomel.by |
| Vladimir Kashkan | IP NAS Belarus | ltf@dragon.bas-net.by |
| Sergey Kruglov | NC PHEP Belarus | kruglov@hep.by |

| | | |
|---|---|---|
| Yuri Kulchitsky | JINR, Russia | kulchits@vxcern.cern.ch |
| Alexander Kurilin | NC PHEP Belarus | kurilin@hep.by |
| Yuri Kurochkin | IP NAS Belarus | yukuroch@dragon.bas-net.by |
| Andrey Kutov | JINR, Russia | kutov@sunse.jinr.ru |
| Rim Kutuev | JINR, Russia | kutuev@sunse.jinr.ru |
| Vyacheslav Kuvshinov | IP NAS Belarus | kuvshino@dragon.bas-net.by |
| Polina Kuzhir | NC PHEP Belarus | kuzhir@hep.by |
| Mikhail Levchuk | IP NAS Belarus | levchuk@dragon.bas-net.by |
| Anatoly Litvinenko | JINR, Russia | litvin@moonhe.jinr.ru |
| Sergey Lobastov | JINR, Russia | natbug@sunse.jinr.ru |
| Viktor Lysan | JINR, Russia | lyssan@sunse.jinr.ru |
| Nikolai Maksimenko | GSU Belarus | root@tpf.gsu.gomel.by |
| Vladimir Maslennikov | BSU Belarus | |
| Dmitry Matsukevich | INP BSU Belarus | mats@inp.belpak.minsk.by |
| Igor Meshkov | JINR, Russia | meshkov@nusun.jinr.ru |
| Dmitry Mirkarimov | JINR, Russia | mirkarim@sunse.jinr.ru |
| Natalia Molokanova | JINR, Russia | molokan@sunse.jinr.ru |
| Miroslav Nagy | IP NAS Slovak Repub. | fyzinami@nic.savba.sk |
| Alexander Pankov | GPI Belarus | pankov@gpi.gomel.by |
| Yuri Pleskachevsky | IMPS NAS Belarus | plesk@polymer.gomel.by |
| Mikhail Pletyukhov | IP NAS Belarus | plet@dragon.bas-net.by |
| Vladimir Pletykhov | Parliament Belarus | plet@dragon.bas-net.by |
| Alexander Prokhorov | JINR, Russia | prohorov@sunhe.jinr.ru |
| Fedor Prokoshin | JINR, Russia | prokosyn@nusun.jinr.ru |
| Valery Prokoshin | GKNT Belarus | science@leo.bas-net.by |
| Alexey Raspereza | NC PHEP Belarus | rasp@hep.by |
| Rui Ribeiro | CERN | rui.ribeiro@cern.ch |
| Viktor Rumyantsev | JINR, Russia | rumyantsev@lnpnw1.jinr.ru |
| Nadezhda Russakovich | JINR, Russia | ruso@nusun.jinr.ru |
| Nikolai Sahno | GSU Belarus | root@tpf.gsu.gomel.by |
| Andrey Saprykin | IP NAS Belarus | saprykin@dragon.bas-net.by |
| Maria Savina | JINR, Russia | savina@lhe.jinr.ru |
| Sergey Scherbakov | GTU Belarus | |
| Valery Shaporov | IP NAS Belarus | shaporov@dragon.bas-net.by |
| Vitaly Shevtsov | JINR, Russia | sandal@sandal.jinr.ru |
| Sergey Shmatov | JINR, Russia | shmatov@lhe.jinr.ru |
| Sergey Shulga | GSU Belarus | root@tpf.gsu.gomel.by |
| Roman Shulyakovsky | IP NAS Belarus | ltf@dragon.bas-net.by |
| Nikolai Shumeiko | NC PHEP Belarus | shum@hep.by |
| Nikolai Skachkov | JINR, Russia | skachkov@vxcern.cern.ch |
| Vladimir Skalozub | Dnepropetrovsk Univ. Ukraine | skalozub@ff.dsu.dp.ua |
| Gregory Snow | Univ. of Nebraska USA | gsnow@unlinfo.unl.edu |

| | | |
|---|---|---|
| Igor Solovtsov | JINR, Russia | solovtso@thsun1.jinr.dubna.su |
| Sergey Son | GPI Belarus | son@gpi.gomel.by |
| Pavel Starovoitov | NC PHEP Belarus | star@hep.by |
| Vasily Strazhev | Min. of Education Belarus | Stragau@minedu.unibel.by |
| Juan Suarez | NC PHEP Belarus | suarez@hep.by |
| Sergey Sushkov | NC PHEP Belarus | svs@hep.by |
| Igor Suslov | JINR, Russia | suslov@nusun.jinr.ru |
| Alina Suzko | JINR, Russia | suzko@thsun1.jinr.dubna.su |
| Viktor Tikhomirov | INP BSU Belarus | tikh@inp.belpak.minsk.by |
| Sergey Timoshin | GPI Belarus | timoshin@gpi.gomel.by |
| Arkady Tolkachev | NC PHEP Belarus | tol@hep.by |
| Evgeny Tolstopyatov | IMPS NAS Belarus | plesk@polymer.gomel.by |
| Lev Tomilchik | IP NAS Belarus | lmt@dragon.bas-net.by |
| Irene Vichou | CERN | i.vichou@cern.ch |
| Vladimir Vinogradov | JINR, Russia | vinogradov@main1.jinr.dubna.su |
| Mikhail Volkov | JINR, Russia | volkov@thsun1.jinr.dubna.su |
| Alexander Yarchak | Gomel Executive Committee | |
| Vladimir Zykunov | GPI Belarus | zykunov@gpi.gomel.by |

**Труды Международной школы-семинара «Актуальные проблемы физики частиц»**

**Proceedings of International School-Seminar «Actual Problems of Particle Physics»**

Ответственный за подготовку сборника к печати
В.С.Румянцев

**E1,2-98-307**

Том I

Макет Н.А.Киселевой

Рукопись сборника поступила 27.10.98. Подписано в печать 18.11.98
Формат 60 × 90/16. Офсетная печать. Уч.-изд. листов 23,0
Тираж 170. Заказ 50995. Цена 45 р.

Издательский отдел Объединенного института ядерных исследований
Дубна Московской области